©2017

Chengyu Chen

AGGREGATION AND ADSORPTION PROCESSES

OF CARBONACEOUS NANOPARTICLES

IN AQUEOUS ENVIRONMENTS

by

CHENGYU CHEN

A dissertation submitted to the

Graduate School-New Brunswick

Rutgers, The State University of New Jersey

In partial fulfillment of the requirements

For the degree of

Doctor of Philosophy

Graduate Program in Environmental Sciences

Written under the direction of

Dr. Weilin Huang

And approved by

_____

_____

_____

_____

New Brunswick, New Jersey

October, 2017

ABSTRACT OF THE DISSERTATION

AGGREGATION AND ADSORPTION PROCESSES

OF CARBONACEOUS NANOPARTICLES

IN AQUEOUS ENVIRONMENTS

By **CHENGYU CHEN**

Dissertation Director:

Dr. Weilin Huang

Carbonaceous nanoparticles (NPs), which are intentionally manufactured or originate from incomplete combustion, reach aqueous environments continuously through direct input, surface runoff, wastewater treatment plants, and atmospheric deposition. Upon release into aqueous environments, carbonaceous NPs will likely undergo aggregation and adsorption processes depending on the local solution chemistries and ambient species. Understanding the physiochemical interactions governing these two fundamental processes of carbonaceous NPs is crucial for evaluating their fate, transport, and potential applications in aqueous environments.

The first part of this work focused on the aggregation and adsorption behaviors of a new class of manufactured carbonaceous NPs, nanosized activated carbons (NACs), in an effort to evaluate the applicability of NACs as adsorbents to be injected into groundwater systems for remediation purpose. Investigation on aggregation kinetics of four types of NACs demonstrated that, under solution chemistries typical of freshwater environments, NACs should remain stable as dispersed NPs with diameter below 200 nm. Such strong colloidal stability of NACs may enable long distance travel of these NPs to reach target pollutants when injected into groundwater systems. Study on the adsorption processes of NACs for two model aromatic pollutants, 4-chlorophenol (4-CP) and aniline, showed rapid removal of contaminants from water. More importantly, the equilibrium adsorption indicated that the adsorption capacities of NACs were 10-100 times greater than other nanosized adsorbents. The combined strong colloidal stability and adsorption capacity of NACs suggested their potential application as superior adsorbents for groundwater remediation.

The second part of this dissertation investigated the aggregation process of soot NPs in aqueous environments. These carbonaceous NPs are produced unintentionally from incomplete combustion, are ubiquitously distributed, and are of serious environmental concerns. Results showed that aggregation kinetics of soot NPs were strongly influenced by solution chemistries including electrolyte compositions and concentrations as well as pH. The presence of macromolecules such as humic acid and proteins significantly enhance the colloidal stability of soot NPs. The aggregation behavior of soot NPs could be predicted by the classic Derjaguin-Landau-Verwey-Overbeek (DLVO) theory using the Hamaker constant determined in this study. Soot NPs should remain stable against

aggregation in typical freshwater environments and neutral rain droplets, but are likely to aggregate under saline (e.g., estuaries and oceans) and/or acidic (e.g., acid rain droplets) conditions.

Results from this work imply that NACs with strong colloidal stability and high adsorption capacities may enable benign NP design and applications, whereas the toxic soot NPs having such high colloidal stability they could endanger human and environment health. In summary, this dissertation has furthered our understanding of the aggregation and adsorption processes of carbonaceous NPs, which may facilitate the prediction of their fate and transport in aqueous environments.

ACKNOWLEDGEMENTS

My journey as a Ph.D. student at Rutgers was valuable, productive, and rewarding thanks to the generous help from many great people that I have encountered in my life. First and foremost, I would like to express my deepest gratitude to my dissertation advisor, Dr. Weilin Huang, for his tremendous support, extensive guidance, and valuable connections for my study, research, career development, and personal life. I sincerely thank Dr. Huang for providing me this treasured opportunity to study abroad in the U.S. for 2 years as an exchanged undergraduate student and 5 years for my doctoral degree. Dr. Huang has trained me everything essential to become a scientific researcher that will accompany me throughout my professional career. His expertise and experience in physiochemical processes in environmental sciences have instilled me interests and knowledge in this research area which I will be continuously working on. Dr. Huang's patience and enthusiasm have encouraged me whenever I encounter difficulties, frustrations, and confusions in my research, careers, and personal life. For me, Dr. Huang is also my life mentor, faithful friend, and loving parent who has given me greatest support and caring and also to my family. I was truly fortunate and honored to have Dr. Huang being the most important part of my graduate study.

My deepest appreciation is extended to my committee members, Dr. Gediminas Mainelis, Dr. John Reinfelder, and Dr. Paul Takhistov for their valuable input and advice on various aspects of my research work. Dr. Mainelis and Dr. Reinfelder have given me helpful guidance whenever I encounter difficulties in interpreting my experimental results related to their expertise. It was Dr. Takhistov's lecture class that had introduced me to

years I have spent here give me a great opportunity to meet many wonderful friends, experience the American culture, and have such a precious memory in my life.

Finally, I want to express my biggest thanks and love to my families. I owe a deep sense of gratitude to my parents and parent-in-law for their unconditional love and support. Their devotion and love have helped me achieve the work that is accomplished today. I am also indebted to my wife, Muwen Lu, who provides endless support and love particularly during the down days of my life. She is such a cheerful person whom I could share my happiness and every wonderful moment of my life. It was our precious memory to experience our graduate study and obtain our Ph.D. degrees together at Rutgers. Specially, we are now excitedly looking forward to the upcoming birth of our first baby, Kevin Chen, who will arrive in the world in May 2017.

TABLE OF CONTENTS

LIST OF TABLES

LIST OF ILLUSTRATIONS

LIST OF EQUATIONS

1. CHAPTER I. INTRODUCTION

1.1. Background Information

1.1.1. Carbonaceous Nanoparticles

Nanotechnology is the study and manipulation of materials at atomic, molecular, and macromolecular scales [1]. Nanoparticles (NPs) defined as particles with at least one dimension less than 100 nanometers are considered to be the building blocks for nanotechnology [2]. Carbonaceous nanomaterials composed entirely or mainly of carbon atoms are one of the seven major classes of NPs, drawing exclusive awareness in the era of nanotechnology [3-6]. Carbonaceous nanomaterials could be divided into two operationally defined categories, depending on their sources and origin [7]. Intentionally produced (engineered, manufactured) carbonaceous NPs originate from industrial activities with well-controlled properties for specific applications; whereas unintentionally produced (or incidental) carbonaceous NPs originate from incomplete combustion of biomass and fossil fuels as undesired byproducts [8].

Carbon's unique hybridization and tunable properties allow for tailored manipulation into a variety of engineered carbonaceous nanomaterials in different dimensions. The manufactured carbon-based NPs include nanosized activated carbons (NACs), carbon nanotubes (single-walled, SWCNTs or multi-walled, MWCNTs), fullerene (C_{60}), graphene and derivatives (graphene oxides, GO or reduced graphene oxides, RGO), nanodiamond, carbon nanofibers, and amorphous carbonaceous composites [3-5, 9, 10]. Owing to their size-endowed unique physiochemical features, manufactured carbonaceous NPs find use in a variety of scientific and industrial areas, such as

environmental, electronic, energy, pharmaceutical, catalytic, agricultural, and materials applications [3, 9, 11]. Manufactured carbonaceous NPs have been cited as one of the top 50 industrial chemicals manufactured worldwide, with 9.8 million tons of production in 2008 [8]. The growing production and use of engineered carbonaceous NPs will lead to their increased exposure to the environment [2, 6, 12]. These nanomaterials are sometimes deliberately introduced into the environment, such as by direct injection of NPs into the sub-surface for remediation purpose [9, 13]. Another entry route for the engineered carbonaceous NPs to the environment could be accidental release during the manufacturing process.

In contrast to manufactured nanomaterials with well-controlled properties, carbonaceous NPs such as soot may be produced unintentionally from incomplete combustion of fuels and biomass. Soot NPs are produced as undesired byproduct each year at approximately 8 million tons from combustion [14]. The massive production of soot from numerous burning sources as well as the global cycling of these carbonaceous NPs have resulted in their ubiquitous distribution in the environment and their routine exposure to human [8].

Due to the ubiquity and special nano-dimension features of carbonaceous NPs, environmental researchers are actively exploring the environmental and health concerns of these NPs as contaminants of emerging concerns [6, 11, 15, 16]. Numerous previous studies have demonstrated the toxic potentials of carbonaceous NPs during interactions with biological systems [1, 15-19]. Recent studies also indicated that the presence of carbonaceous NPs such as soot NPs in the environment could significantly impact the marine ecosystems and the global carbon cycle [20, 21]. Although carbonaceous NPs find

use in a variety of applications, their potential impacts to human health and the environment have also raised serious public and scientific concerns. Therefore, the broad applications and environmental concerns of carbonaceous NPs necessitate a systematic understanding of their fate and transport in the environment.

1.1.2. *Aggregation and Adsorption Processes of Nanoparticles*

To optimize applications of carbonaceous NPs as well as to gain better understanding of their potential environmental hazards, it is crucial to study the fundamental physiochemical processes that these NPs may undergo as they enter the environment. Upon release into aqueous systems, carbonaceous NPs will likely exist in various aggregation states and adsorb to chemicals depending on the solution chemistries and ambient species [22]. Both aggregation and adsorption processes of NPs governed by physiochemical interactions may alter their size and surface properties, which could strongly influence the fate and transport of these NPs in the environment.

Carbonaceous NPs entering aqueous environments will exist in various aggregation states. The ability of NPs to remain stable against aggregation in aqueous systems is termed colloidal stability, which is typically governed by the interplay between electrostatic repulsion and van der Waals attraction according to the classic Derjaguin-Landau-Verwey-Overbeek (DLVO) theory [23, 24]. It is known that for most colloidal NPs, variation of solution chemistries including electrolyte composition or concentration and pH condition will have strong influence on surface properties of NPs, and thus, their colloidal stability [24, 25]. Meanwhile, the presence of environmental macromolecules

(e.g., natural organic matter, NOM) and biological macromolecules (e.g., proteins and polysaccharides) may impact the aggregation behavior of NPs [26, 27]. Study of effects from these environmental factors on colloidal stability of NPs is critical for elucidation and prediction of their fate and transport in aqueous environments.

Carbonaceous NPs typically are highly adsorptive towards organic molecules that are prevalent in the environment. This is because carbonaceous NPs characteristically have exceptionally high specific surface area (SSA), and the surfaces of these carbonaceous materials are inherently hydrophobic. Therefore, these NPs can be functionalized as ideal candidates for adsorption of target pollutant in aqueous environment [9, 28, 29]. On the other hand, environmental (macro)molecules (e.g., NOM) [30], bacteria and viruses [20, 31, 32], and toxic pollutants [33-35] may passively adsorb onto hydrophobic carbon particles such as black carbon. The adsorbed species onto NPs can modify their surface properties and travel along with the mobile NPs in the environment. Toxic chemicals associated with carbonaceous NPs may be released during the interactions of NPs with aquatic organisms and cause biological damage. Understanding the adsorption behavior of carbonaceous NPs is hence critical for evaluation of their applicability as adsorbents as well as understanding their impact on aquatic environments.

Two types of carbonaceous NPs are selected for study of their aggregation and adsorption processes: nanosized activated carbons (NACs) as a new class of engineered NPs and soot NPs as a ubiquitous contaminant in the environment. Despite of the great importance of these two types of carbonaceous NPs in the environment, their aggregation processes in aqueous systems have never been quantitatively studied. In addition, there

have been no studies to date that systematically investigate the adsorption behavior of NACs, which may be ideal candidates for adsorption of pollutants in contaminated water.

1.1.3. Nanosized Activated Carbons

There have been a number of studies focusing on the fate and transport of several manufactured carbonaceous nanomaterials such as fullerenes [36-38], carbon nanotubes [39-41], and graphene oxide [42] in aquatic systems. However, such information is less available for NACs, which are a new class of manufactured carbonaceous nanomaterials. Compared to conventional activated carbon (AC) as its bulk counterpart, NAC possesses unique nano-dimension feature along with enormous porosity and great SSA as well as insignificant cytotoxicity [43, 44]. Therefore, NACs are potential candidates for catalyst support [45], drug carriers [43], disease tracers [46], and adsorbents for water reclamation [47]. A key step for evaluating the fate, transport, and applicability of NACs will be determining their colloidal stability in aqueous solutions, as it indicates the mobility of NPs once they enter natural or engineered aquatic systems. Study of the adsorption behavior of NACs will also be of great importance to predict their removal efficiencies when used as water remediation agents and to design their carrying capacity when used as drug carriers.

One scenario for the application of NACs in environmental remediation is to be injected into groundwater systems as superior nanosized adsorbent for in situ removal of organic pollutants. So far other manufactured nanomaterials such as CNTs [48-52] and nano zero valent iron (nZVI) have been proposed for achieving such purpose [13, 53],

however, they are prevented from practical applications due to some major roadblocks. For example, CNTs have low adsorption affinity attributed to their low SSA, and more importantly, they are prone to aggregation because of the strong hydrophobic surfaces leading to mutual attraction [52, 54-56]; although nZVI is highly reactive, it has very limited mobility beyond a few centimeters because it readily forms aggregates in water [57]. Clearly, injected NPs for groundwater remediation must not only be highly reactive, but also must remain suspended and mobile in polluted aquifers over days [57, 58]. We propose NACs as a new class of manufactured NPs meeting such criteria for applications in groundwater remediation. Questions to be examined experimentally include whether NACs are both highly adsorptive towards organic pollutants as well as highly stable against aggregation under solution conditions typical of groundwater systems. Study of the aggregation kinetics as well as adsorption behavior of NACs in aquatic environments is critical for both filling the knowledge gap in colloidal science and evaluating the technical applicability of NACs for groundwater remediation.

1.1.4. Soot Nanoparticles

In addition to the manufactured NAC nanomaterials, soot NPs produced from incomplete combustion of fuels and biomass constitute of a major portion of the unintentionally produced carbonaceous NPs in the environment. Upon release to the atmosphere, soot NPs have been identified as contributing to various adverse effects on human health [17, 19, 59, 60], visibility reduction [61], soiling of buildings [62], agricultural productivity [63], and global climate change [64-66]. Soot NPs may

eventually reach water bodies via atmospheric dry and wet deposition or fluvial discharge [67-69], resulting in strong impacts on the aquatic ecosystems [20, 21] and global carbon cycle [68].

To evaluate the environmental fate and transport of these soot NPs and their potential interactions with the ambient environment, it is crucial to understand the factors governing their aggregation behavior under both atmospheric and aquatic conditions, which controls their size and interactions with the ambient environment [22]. Most studies to date have focused on the aggregation behavior of manufactured carbonaceous NPs (e.g., CNTs, fullerenes, and graphene) in aquatic environments. However, the fundamental aggregation kinetics of soot particles in aqueous phase is poorly characterized, despite the fact that the concentration of black carbon (i.e., soot) NPs is indeed 10^4 to 10^7 times higher than MCNPs in the water column and aquatic sediments [7]. Due to the great significance of soot NPs in the atmosphere, there are numerous studies on their aggregation behavior under dry [70-73] and humid [74-76] atmospheric conditions. However, there have been no studies to date that focus systematically on the aggregation kinetics and colloidal stability of soot NPs under aqueous conditions where water is the dominant phase. Such study may have significant implications for fate, transport, and toxicity of soot NPs in wet environments, which include cloud water, rain droplets, and aquatic environments, where soot NPs are ubiquitously distributed.

1.2. Research Objectives and Hypotheses

The overarching goal of this dissertation is to investigate the aggregation and adsorption processes of carbonaceous NPs for understanding their fate, transport, and applications in aqueous environments. Factors influencing the colloidal stability of NACs and soot NPs against aggregation under aqueous conditions are the major focuses of this study. In addition, the adsorption behavior of NACs for organic pollutants will be investigated with the aim to evaluate the potential application of injecting NACs as mobile nano-adsorbents for groundwater remediation purpose.

Specifically, NACs as a new class of manufactured carbonaceous NPs and soot NPs as a prevalent group of unintentionally produced carbonaceous NPs are selected for study. The major objectives are to quantify and predict the colloidal stability of NACs and soot NPs against aggregation under various solution chemistry conditions and in the presence of different environmental and biological macromolecules. The experimental aggregation kinetics data will be collected using time-resolved dynamic light scattering (TRDLS) technique to construct stability curves based on the attachment efficiency data, allowing for determination of their critical coagulation concentrations (CCC). The experimental results are compared with the classic DLVO theory to derive physiochemical parameters including the Hamaker constants for the tested NPs. The characterized properties of nanomaterials coupled with computational fitting practices are employed to elucidate and predict the aggregation mechanisms and charge acquisition of NPs based on fundamental theories involving intermolecular forces and particle interaction energies. In addition, the adsorption behavior of NACs towards typical organic pollutants will be characterized using high performance liquid chromatography (HPLC) for evaluation of their

applicability as superior adsorbents to be injected into groundwater systems for in situ water remediation.

There are two major hypotheses for this thesis work: (1) NACs possess both high colloidal stability and strong adsorbability that could be utilized as nanosized adsorbents for in situ groundwater remediation; (2) diesel soot NPs are potentially hazardous nanomaterials that could remain relatively stable against aggregation in typical wet environments such as freshwater and rain droplets.

1.3. Organization of This Dissertation

This dissertation is composed of an overall introduction (Chapter 1), four independent papers each presented in one chapter (Chapters 2 to 5), and a final chapter on major conclusions and future work (Chapter 6).

In Chapter 1, the background information of nanotechnology and the crucial needs for understanding NPs colloidal stability and adsorption behavior on evaluating their fate and transport as well as applications in aqueous environments are briefly introduced. Research objectives, organization of the dissertation, and important contributions are also outlined.

In Chapter 2, the influence of solution chemistries on the colloidal stability of NACs was investigated. Four types of NACs manufactured from different plant materials were obtained for this study. Effects of background electrolytes and pH on the aggregation kinetics of NACs were quantified and compared with the DLVO theory. The derived Hamaker constants for each NAC nanomaterial have important implications for

prediction of colloidal stability of NACs as well as interfacial interactions involving AC materials such as adsorption processes. Results demonstrated NACs have strong colloidal stability against aggregation under solution conditions typical of freshwater environments.

In Chapter 3, four types of NACs from Chapter 2 and one commercial powdered activated carbon (PAC) as comparison were used to study their adsorption behavior for two model aromatic pollutants, 4-chlorophenol (4-CP) and aniline in aqueous solution. The pore structures, adsorption rates, adsorption equilibrium isotherms, and adsorption mechanisms were characterized for the NAC adsorbents. More importantly, comparisons showed that the adsorption capacities of NACs were 10-100 times greater than other reported nanosized carbonaceous adsorbents (e.g., CNTs, graphene, and fullerene), and were similar with conventional AC adsorbents (e.g., PAC and granular AC, GAC). Results from this chapter indicated that NACs possess much strong adsorption capacity compared to other potential nanosized adsorbents. Coupled with results from Chapter 2 which demonstrated the high colloidal stability of NACs, results from these two chapters confirmed the hypothesis that NACs are superior nanosized adsorbents simultaneously having high mobility and strong adsorptivity to be injected into groundwater systems for in situ remediation of organic pollutants.

In Chapter 4, a standard reference soot particulate matter collected from diesel engine was employed for studying the aggregation kinetics influenced by electrolyte composition and concentration and pH conditions typically present in wet environments such as cloud water, rain droplets, and aquatic environments. Comparison of the experimental aggregation kinetics data with the classic DLVO theory demonstrated that soot NPs aggregate similarly with other common colloidal particles, with the Hamaker

constants derived for the first time for soot NPs in aqueous medium. Results indicated that soot NPs may be stable against self-aggregation in typical freshwater environments, but should aggregate and settle in solutions with high salinity (e.g., marines and estuaries) or low pH (e.g., acid rain droplets) or both. In particular, the observation of a distinct crossover from the reaction- (high concentrations of single soot NP) to the diffusion- (high concentrations of soot aggregates) limited aggregation regimes with decrease in solution pH should not be overlooked.

In Chapter 5, the influence of presence of environmental and biological macromolecules on the colloidal stability of soot NPs in aqueous systems are examined. The same soot sample from Chapter 4 was studied here. Five macromolecules were employed in this study, including two natural organic matter (NOM) [Suwannee River humic acid (HA) and fulvic acid (FA)], a polysaccharide (sodium alginate), a protein [bovine serum albumin (BSA)], and a microbial culture medium [Luria-Bertani (LB) broth]. Results indicated that the presence of all macromolecules retarded the aggregation rates of soot NPs, with BSA protein showing the strongest effect, followed by HA, alginate, LB, and FA. Alginate enhanced soot stability in the presence of NaCl salt, but promoted soot aggregation in the presence of high concentrations of Ca^{2+} cations due to alginate bridging effect. The aggregation mechanisms of soot NPs in the presence of each macromolecules were elucidated, which suggested that the stability and hence mobility of soot NPs may be enhanced by macromolecules in aqueous systems.

In Chapter 6, the major findings of this dissertation and recommended future research needs in relevant directions to facilitate understandings in the fate, transport, and application of NACs and soot NPs in aqueous environment are summarized. Further

development of NACs as treatment agents being injected into groundwater systems for remediation will require column studies and field assessments. Meanwhile, the ubiquity and significant impact of soot NPs in aqueous environments necessitates more systematic studies on their aggregation behavior under a variety of solution conditions and in heterogeneous systems where soot NPs interact with environmental colloids and aquatic organisms.

2. CHAPTER II. COLLOIDAL STABILITY OF NANOSIZED ACTIVATED CARBONS AGAINST AGGREGATION IN AQUEOUS ENVIRONMENTS
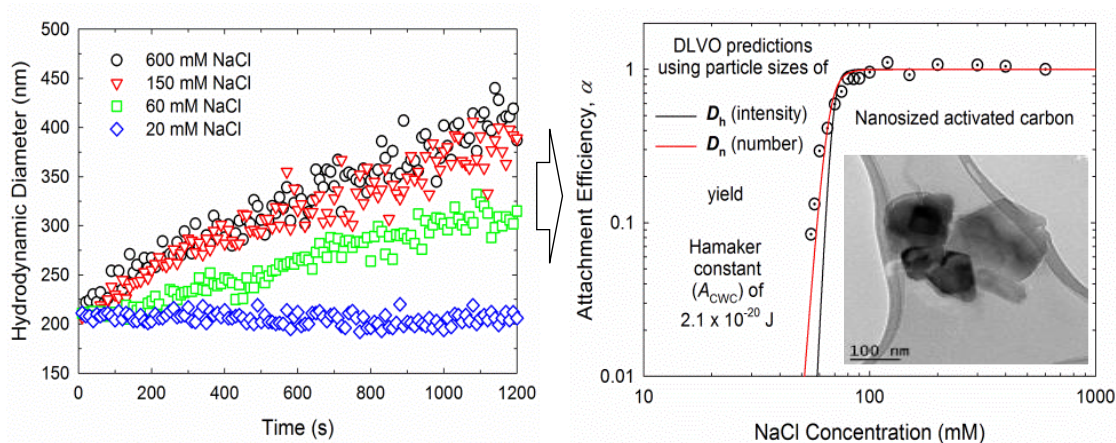
PROJECT TITLE: AGGREGATION KINETICS OF NANOSIZED ACTIVATED CARBONS IN AQUATIC ENVIRONMENTS

The work in this chapter has been published in the title of "Aggregation Kinetics of Nanosized Activated Carbons in Aquatic Environments" in Chemical Engineering Journal (Volume 313, Pages 882-889) on April 1, 2017.

Abstract

Nanosized activated carbons (NACs) are emerging as a new class of manufactured nanomaterials, but their colloidal stability governing the fate and transport in aquatic environments has not yet been evaluated. We have characterized four representative NAC materials and examined their colloidal stability and early-stage aggregation kinetics under

various water chemistry conditions. The results showed that these NAC particles had intensity-weighted hydrodynamic diameters (D_h) and number-weighted averaged diameters (D_n) of approximately 200 and 100 nm, respectively, and that their aggregation kinetics exhibited both reaction- and diffusion-limited regimes in the presence of monovalent (NaCl) or divalent ($CaCl_2$) salt with distinct critical coagulation concentrations (CCC), indicating that their colloidal stability under the tested aqueous conditions was consistent with the classic Derjaguin-Landau-Verwey-Overbeek (DLVO) theory. The fitting of the aggregation kinetics with predictions based on DLVO theory yielded the Hamaker constant of 2.1-2.7 $\times$ 10^{-20} J (A_{CWC}, aqueous medium). The study demonstrated that NACs may be relatively stable under typical freshwater chemistry conditions, suggesting their potential applications as reactive agents for remedy of contaminated water and soil systems where long-time suspension of introduced particles is desired. The observed strong colloidal stability may also indicate high possibility of NACs being nanosized pollutants in natural and engineered environmental systems.

2.1. Introduction

Nanosized activated carbons (NACs) are recently developed nanomaterials with major reactivities such as adsorbability similar to traditional granular and powdered activated carbon (GAC and PAC) materials [10, 77]. The unique nano-size feature of NAC, along with its enormous porosity and great specific surface area (SSA), makes it potential candidates for catalyst support [45], drug carriers [43], disease tracers [46], and adsorbents for water reclamation [47]. The anticipated growth in production and use of

NACs will inevitably lead to their release into natural or engineered aquatic systems [11]. Although limited studies have demonstrated insignificant cytotoxicity after short-term exposure to NACs [43, 44], their potential impact on human and the environment remains unknown. Indeed, the increasing public concern over manufactured nanomaterials as emerging environmental pollutants involves not only their inherent toxicity but also how they may interact with each other or with environmental solids [15]. Upon release to aquatic environments, potential risks from exposure to nanoparticles may be largely dependent on their fate and transport processes, which are strongly influenced by their aggregation tendency under different aquatic conditions [12]. It is therefore of particular interest to investigate the colloidal stability of NACs against aggregation in various aquatic systems.

Prior studies focused on the fate and transport of several important carbonaceous nanoparticles such as fullerenes [36-38], carbon nanotubes [39-41], and graphene oxide [42] in aquatic systems, but little is known for NACs. One goal of this study was to quantitatively investigate the colloidal stability of well-characterized NACs using various state-of-art instruments and the theories of particle-particle interactions. In prior studies, time-resolved dynamic light scattering (TRDLS) has been widely used to measure the aggregation kinetics of colloidal particles (fullerenes, carbon nanotubes, and graphene) under the influence of different solution chemistry [36, 41, 42]. The early-stage aggregation rates at different electrolyte concentrations were used to construct the attachment efficiency profiles, which often exhibited a reaction- (slow) and diffusion-limited (fast) aggregation regimes. The critical coagulation concentrations (CCC) were determined by extrapolating from both the fast and slow aggregation regimes. These

studies showed that the aggregation behavior of fullerenes, carbon nanotubes, and graphene nanoparticles generally followed the predictions from the classic Derjaguin-Landau-Verwey-Overbeek (DLVO) theory with strong effects from background electrolytes [25, 42].

The second goal of this study was to derive the Hamaker constant for general activated carbon (AC) materials from the colloidal stability measurements made directly for NACs. The Hamaker constant, which is highly dependent on both the external surface properties of interacting bodies and the intervening medium, provides a means for assessing the relative strength of van der Waals attractive interactions [78]. It is a key physicochemical parameter for predicting interactions of surfaces and interfaces involving particles of various sizes. For example, with the Hamaker constant, the adsorption equilibria of organic contaminants on ACs could be predicted [79] and the colloidal stability and aggregation process of nanoparticles in aquatic environments could be simulated [80, 81]. The currently available Hamaker constant data for ACs, however, were either estimated from surrogate materials (e.g., carbon fibers, 5.2-6.2 $\times 10^{-20}$ J [82]) [79] using the contact angle method or calculated from adsorption data (5.0-7.8 $\times 10^{-20}$ J) [83]. However, inaccuracy could be expected for these published data. For instance, AC has high surface roughness and is not suitable for the contact angle method. Surrogate materials such as carbon fibers used in contact angle measurements may have surface chemistry properties that are not well representative of AC. Meanwhile, the Hamaker constant calculated from adsorption data was presumably representative of the dispersive interactions at the external surfaces, but the measured adsorption data were indeed averaged from overall adsorption at both internal and external surfaces of AC. Hence,

the Hamaker constant derived from direct measurements is much needed for better predicting particle-particle and particle-molecule interactions for AC materials.

In this study, four NACs derived from different biogenic materials were chosen for investigating their colloidal stability under various aquatic chemistry conditions. Their aggregation kinetics and electrophoretic mobilities (EPMs) were measured over a wide range of solution chemistry conditions, and their CCC values were quantified accordingly. The measured aggregation kinetics agreed with DLVO predictions, and the Hamaker constant was derived. The study provided insight to the aggregation mechanism of NACs and suggested the potential application of NACs as reactive agents for contaminated environmental systems. The strong colloidal stability observed for NACs also draws attention to their potential adverse environmental effects as an emerging nanosized pollutant.

2.2. Materials and Methods

2.2.1. Preparation of NACs

The four types of NACs (purity > 95%) with high SSA were purchased from US Research Nanomaterials, Inc. (Houston, TX) and assigned as NAC1, NAC2, NAC3, and NAC4. They were analyzed for elemental compositions and examined with a scanning electron microscope (SEM). The aqueous NAC suspensions were prepared following a published procedure [36]. In brief, the NACs were weighed into double deionized water (DDI) (resistivity > 18 MΩ·cm) and the suspensions were mixed for 30 d then allowed to settle for 7 d. Aliquots of 20 mL were collected at 2 cm below the suspension surface

and combined to form a 200-mL stock suspension for each sample. The stock suspensions after 24-h sonication were monitored to remain thermodynamically stable over the experimental time period.

2.2.2. *Characterization of Aqueous NAC Suspensions*

The concentrations of NACs in stock suspension (0.1-mL samples) were measured gravimetrically using an ultramicro-balance (Sartorius M2P, Goettingen, Germany). To examine the NACs on a transmission electron microscope (TEM), a drop of sonicated NAC stock suspension was placed on 200 mesh carbon coated copper grids and left to adsorb for 5 min. Then the samples were observed with a Topcon 002B (Topcon Corp., Tokyo, Japan) operating at 200 kV.

Potentiometric titration was conducted to identify titratable functional groups of the NACs. In brief, a 100-mL stirred suspension prior to gravitational settling was retained for potentiometric titration, which contained 1 g/L of NACs. The suspension was purged with nitrogen gas (N_2) for 15 min to remove dissolved CO_2 before HCl was added to lower the solution pH to 3. The suspension was subsequently kept in a nitrogen atmosphere as being titrated with 0.1 M NaOH to pH 10 with an autotitrator (702 SM Titrino, Metrohm, Herisau, Switzerland). The amount of NaOH required to raise the pH from 3 to 10 of each NAC suspension was compared to that required to raise the pH of a blank solution to identify the presence of titratable functional groups on the given NAC.

The EPMs of the NAC suspensions were measured at 25°C using a Zetasizer Nano ZS (Malvern Instruments, Worcestershire, UK) which employs phase analysis light

scattering (PALS). Electrolyte stock solutions were prepared by dissolving ACS grade NaCl or $CaCl_2$ in DDI and filtered through 0.1-μm filters (Puradisc 25 TF, Whatman), with desired final solution pH adjusted with HCl and NaOH. The NAC concentration was diluted to 10 mg/L for each EPM measurement. For a given solution condition, three independent samples of the same NAC were each measured 10 times for EPM values which were converted to zeta (ζ) potentials using the Smoluchowski approximation [36].

2.2.3. *Dynamic Light Scattering Measurements*

The effective particle sizes of NAC suspensions were measured on a Brookhaven 90Plus Dynamic Light Scattering (DLS) instrument (Holtsville, NY), which employed a 35-mW solid state laser operated at a wavelength of 635 nm and was calibrated with NIST-certified standards (Fisher Scientific). Prior to aggregation test, the intensity averaged hydrodynamic diameter (D_h) was determined as the initial D_{h0} ($t = 0$) using the scattered light intensity which was scanned for 15 s with a photo-detector positioned at 90 °. Here the scanned data was fitted with autocorrelation to a second-order cumulant analysis (MAS software) and D_{h0} was determined with a polydispersity index (PDI). The Non-Negatively constrained Least Squares (NNLS) algorithm was used to generate the intensity-weighted size distribution. With the Mie scattering coefficient, the results were also converted to number-weighted size distribution with a number-weighted mean diameter (D_{n0}).

The aggregation kinetics at $t > 0$ was measured with TRDLS at 25 °C and under different solution conditions by recording the D_h values over time. For each aggregation

experiment, an aliquot of 2-mL NAC suspension at 20 mg/L was introduced into a pre-cleaned glass vial (VWR, Chester, PA), followed by addition of 2 mL of a given electrolyte solution to induce NAC aggregation. After vortexed for 1 s (Vortex Genie, Fisher Scientific), the vial was immediately inserted into the DLS instrument to start the measurement. Each autocorrelation function was accumulated for 10 s, and the measurements lasted between 20 to 480 min. This measurement was run in triplicates for each aggregation test.

The equation below depicts the dependence of the initial aggregation rate constant (k) upon initial rate of linear increase and initial particle concentration (N_0) [39]:

$$k \propto \frac{1}{N_0} \left(\frac{dD_h(t)}{dt} \right)_{t \to 0} \tag{2.1}$$

where the initial rate of linear increase was determined from the slope up to the point where D_h had increased to $1.25 D_{h0}$. In cases where the linear regime ends before reaching $1.25 D_{h0}$, the slope of the linear regime was approximated similarly. The fitted line was verified to intercept the y axis no more than 5% from D_{h0} for all aggregation experiments.

The aggregation attachment efficiency (α, equivalent to the inverse stability ratio) ranging from 0 to 1 was used to quantify the aggregation kinetics under different solution conditions. Assuming $N_0 = 10$ mg/L, α was calculated by normalizing the initial slope of aggregation under different solution conditions to the slope obtained under diffusion-limited (fast) aggregation conditions [39, 41]:

$$\alpha = \frac{k}{k_{fast}} = \frac{\frac{1}{N_0} \left(\frac{dD_h(t)}{dt} \right)_{t \to 0}}{\frac{1}{(N_0)_{fast}} \left(\frac{dD_h(t)}{dt} \right)_{t \to 0, fast}} = \frac{\left(\frac{dD_h(t)}{dt} \right)_{t \to 0}}{\left(\frac{dD_h(t)}{dt} \right)_{t \to 0, fast}} \tag{2.2}$$

2.2.4. DLVO Calculations

According to the DLVO theory, the attachment efficiency can be predicted for spherical particles having both colloidal and hydrodynamic interactions using the following equation [37, 38, 84]:

$$\alpha = \frac{\int_0^\infty \beta(h) \frac{exp\left[\frac{V_A(h)}{k_B T}\right]}{(2R+h)^2} dh}{\int_0^\infty \beta(h) \frac{exp\left[\frac{V_T(h)}{k_B T}\right]}{(2R+h)^2} dh} \tag{2.3}$$

where h is the surface-to-surface separation distance [m] between two particles having identical radius (R [m]), and k_B and T are the Boltzmann constant (1.38×10^{-23} [m^2 kg s^{-2} K^{-1}]) and the absolute temperature [K], respectively. The total colloidal interaction potential energy between two particles, $V_T(h)$ in [$1/k_B T$], is the sum of the van der Waals attraction potential energy, $V_A(h)$, and the electrical double layer (EDL) repulsion potential energy, $V_R(h)$:

$$V_T(h) = V_A(h) + V_R(h) \tag{2.4}$$

The hydrodynamic interaction between two approaching particles, which causes slower motion of the two particles due to restricted removal of the liquid between two rigid interfaces, is corrected with the dimensionless function $\beta(h)$ according to Honig, Roeberse and Wiersema [85]:

$$\beta(h) = \frac{6\left(\frac{h}{R}\right)^2 + 13\left(\frac{h}{R}\right) + 2}{6\left(\frac{h}{R}\right)^2 + 4\left(\frac{h}{R}\right)} \tag{2.5}$$

$V_A(h)$ is calculated using the expression proposed by Gregory [86] that accounts for the electromagnetic retardation effect between two spherical particles of the same size:

$$V_A(h) = -\frac{A_{CWC}R}{12h}\left[1 - \frac{bh}{\lambda}\ln\left(1 + \frac{\lambda}{bh}\right)\right] \qquad (2.6)$$

where A_{CWC} is the Hamaker constant [J] between the interacting carbon nanoparticles through water, $b = 5.32$ and λ is the "characteristic wavelength" of the interaction often assumed to be about 100 nm [24].

$V_R(h)$ is calculated using the constant potential approximation (CPA) expression [81, 87] between two spherical particles of the same size and surface potential both in the fitting procedure and DLVO interaction energy profiles:

$$V_R(h) = \frac{2\pi R n_\infty k_B T \Phi^2}{\kappa^2}\left[\ln\left(\frac{1+exp(-\kappa h)}{1-exp(-\kappa h)}\right) + \ln\left(1 - exp(-\kappa h)\right)\right] \qquad (2.7)$$

where n_∞ is the bulk number density of ions [m^{-3}] given by:

$$n_\infty = 1000 N_A C_s \qquad (2.8)$$

where N_A is the Avogadro's constant (6.02×10^{23} [mol^{-1}]) and C_S is the electrolyte molar concentration [mol dm^{-3}]; Φ is the reduced potential [V] given by:

$$\Phi = ze\varphi/k_B T \qquad (2.9)$$

where φ is the surface potential [V] of NACs, and is assumed as the ζ potential [V] obtained from experiment changing as a function of NaCl concentration as shown in Figure 2.8; e is the elementary charge (1.602×10^{-19} [C]); and κ is the Debye-Hückel

parameter or the inverse Debye length [m^{-1}] which in aqueous solutions at 25 ℃ was approximated as [24]:

$$\kappa = 2.32 \times 10^9 (\sum c_i z_i^2)^{\frac{1}{2}} \tag{2.10}$$

Other than the CPA expression, the linear superposition approximation (LSA) and constant charge approximation (CCA) expressions are also commonly employed to calculate $V_R(h)$ between two spherical particles of the same size and surface potential. The LSA expression is given by [88]:

$$V_R(h) = \frac{64\pi R n_\infty k_B T}{\kappa^2} \gamma^2 exp(-\kappa h) \tag{2.11}$$

where $\gamma = tanh\left(\frac{ze\varphi}{4k_BT}\right)$.

The CCA expression is given by [89, 90]:

$$V_R(h) = \frac{2\pi R n_\infty k_B T \Phi^2}{\kappa^2} \left[ln\left(\frac{1+exp(-\kappa h)}{1-exp(-\kappa h)}\right) - ln\left(1 - exp(-\kappa h)\right) \right] \tag{2.12}$$

The Poisson-Boltzmann equation is solved at the boundary condition of the maintenance of surface-chemical equilibrium for the CPA expression, and at the boundary condition of a fixed surface charge density during particle approach for the CCA expression; whereas the LSA expression assumes that the contributions of the potential from each interacting surface can be added towards the overall potential [24, 91]. The Derjaguin integration method (DIM) [92] of interacting spheres is applied throughout. The DLVO predictions were calculated with MATLAB R2014a software (MathWorks, Natick, MA).

2.3. Results and Discussion

2.3.1. Physical Characteristics

The four pristine NAC samples as received were characterized for pore size distributions (Table 2.1), elemental compositions (Table 2.2), and SEM (Figure 2.1) presented below. The pore structures of NACs will be discussed in Chapter III to correlate with their adsorption behavior. The NAC elemental compositions will be discussed later in this chapter when the pH effects on the aggregation kinetics are studied. The SEM images demonstrated that the pristine NACs had very polydispersed (non-uniformed) size distributions, with some particle sizes in nano-dimension and others around one micron. The pristine NACs particles were irregular and angular, which could be attributed to the arbitary grinding process during manufacturing.

After extended stirring, gravitational settling, and sonication processes, the NACs in stock suspensions had much decreased particle according to results obtained by TEM and DLS. As shown in Table 2.3 and Figures 2.2a and b, the four NACs in stock suspensions had similar D_{h0} values of 200 nm and D_{n0} of 100 nm. The large difference between D_{h0} and D_{n0} is expected for colloids with high PDI since larger particles scatter more light [93]. The TEM images shown in Figures 2.2c to f confirmed that the NACs were irregular yet roughly spherical in shape with diameters mostly ~100 nm. It appears that D_{n0} may be a better approximation for the actual particle size of NACs compared to D_{h0}. Note that the major properties listed in Table 2.3 did not change over the experimental time period, indicating that the suspensions were kinetically stable. Overall, the first three

NAC samples exhibited very similar characteristics on the SSA (Table 2.1), elemental

compositions (Table 2.2), and ζ potentials (Table 2.3) that were different from NAC4.

Table 2.1 Material properties, surface area and pore size distributions for the pristine NACs as received from the manufacturer[a].

Sample	Raw Material[b]	Particle Density[b]	Specific Surface Area	Total Pore Volume	Average Pore Radius	Surface Area Distribution		
						<20Å	20-100Å	>100Å
		(g/cm^3)	(m^2/g)	(cm^3/g)	(Å)	(%)	(%)	(%)
NAC1	perennial mountain bamboo and holly trees	0.44	909	0.482	19.92	87.33	11.75	0.92
NAC2	perennial mountain bamboo and holly trees	0.46	879	0.448	19.86	87.05	12.08	0.87
NAC3	Indonesian coconut shell charcoal	0.42	933	0.473	17.08	87.56	11.72	0.72
NAC4	bamboo charcoal	0.43	307	0.180	20.37	79.80	17.68	2.53

[a] The specific surface area and pore volume distribution were determined from the adsorption-desorption isotherm of N_2 at 77 K (TriStar II 3020, Micromeritics Instrument Corp., Norcross, GA).

[b] From the manufacturer.

Table 2.2 Elemental compositions of the pristine NAC materials determined by energy dispersive X-ray (EDX), X-ray photoelectron spectroscopy (XPS), and elemental analysis (EA).

Sample	EDX[a] (weight %)								XPS[b] (atomic %)			EA[c] (weight %)			
	C	O	Al	Si	K	Ca	Fe	Total	C	O	Total	C	O	H	Total
NAC1	85.86	11.77		0.92	0.47	0.57	0.42	100	93.22	6.78	100	74.8	11.4	3.7	89.9
NAC2	87.21	11.84		0.23	0.44	0.27		100	93.39	6.61	100	79.5	11.7	2.51	93.7
NAC3	88.77	9.38		0.46	1.39			100	93.38	6.62	100	79.9	11.6	2.66	94.2
NAC4	87.65	9.28	0.27	0.62	0.62	1.28	0.27	100	91.11	8.89	100	78.6	9.83	2.27	90.7

[a] Determined by scanning electron microscope (SEM) equipped with EDX (MERLIN, Zeiss, Oberkochen, Germany).

[b] Thermo Fisher K-Alpha.

[c] Vario EL III Element Analyzer.
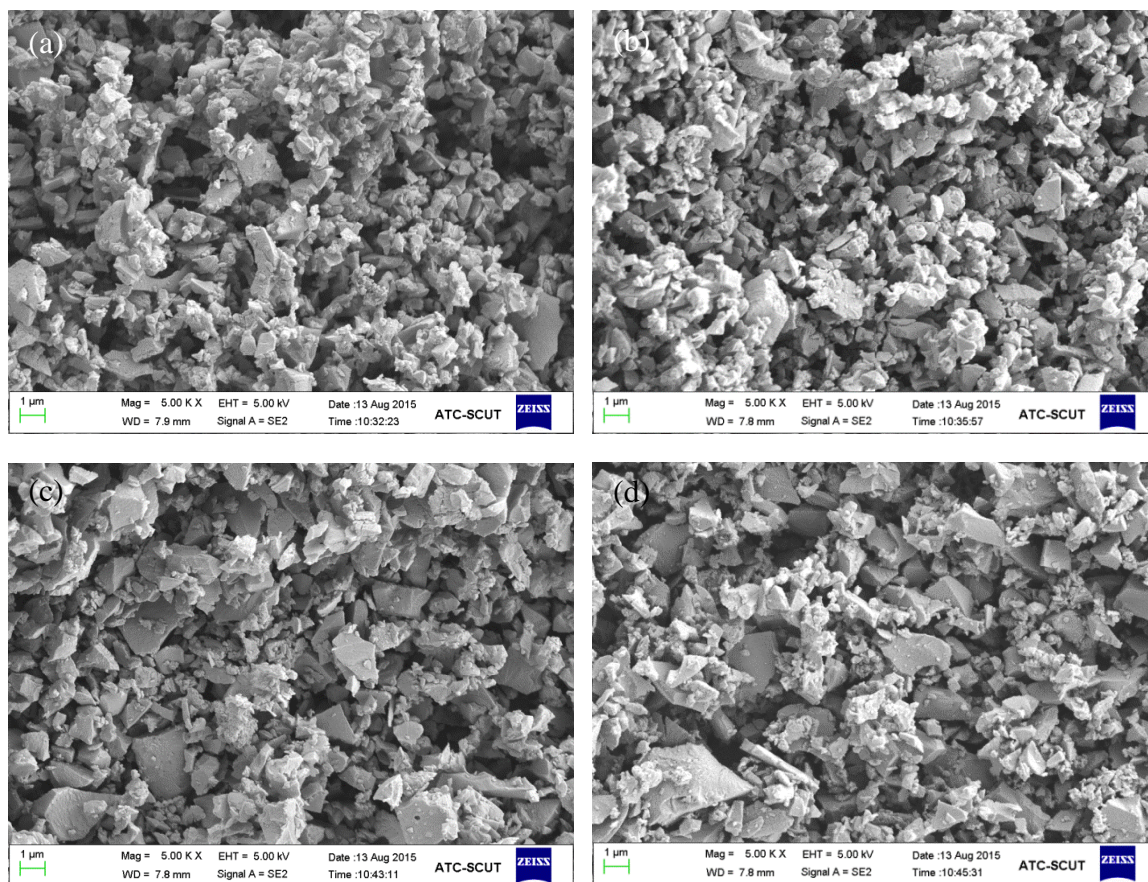
Figure 2.1 Representative scanning electron microscope (SEM) images of (a) NAC1, (b) NAC2, (c) NAC3, and (d) NAC4 pristine samples as received from the manufacturer. The images were acquired by a MERLIN SEM instrument (Zeiss, Oberkochen, Germany).

Table 2.3 Summary of major parameters determined for the four NACs.

Sample	Stock Suspension					CCC			Hamaker constant		Isoelectric Point
	C_{NAC}[a,b]	D_{h0}[b]	PDI	D_{n0}[b]	ζ potential[c]	NaCl	$CaCl_2$	ratio[d]	A_{CWC}	A_{CC}	pI[e]
	(mg/L)	(nm)		(nm)	(mV)	(mM)	(mM)		$[(\times 10^{-20}), J]$		
NAC1	217 ± 12	203 ± 3	0.219	113 ± 5	-44.4 ± 0.7	69.1	3.7	$z^{-4.23}$	2.6	12.5	1.82 ± 0.07
NAC2	246 ± 15	211 ± 4	0.136	133 ± 8	-45.8 ± 0.7	76.2	4.5	$z^{-4.10}$	2.1	11.4	1.83 ± 0.06
NAC3	196 ± 6	184 ± 2	0.169	108 ± 5	-43.3 ± 0.5	66.4	3.3	$z^{-4.32}$	2.7	12.7	1.97 ± 0.07
NAC4	188 ± 5	204 ± 3	0.216	115 ± 3	-30.6 ± 0.4	42.4	2.6	$z^{-4.05}$	2.5	12.3	2.12 ± 0.05

[a] Concentration of NACs in stock suspensions.

[b] Mean ± standard deviation from three measurements at pH 6.

[c] Mean ± standard deviation from 10 measurements in the presence of 1 mM NaCl and at pH 6.

[d] $z = 2$ for the valence of calcium cation.

[e] Mean ± 95% confidence limits for pI, which was extrapolated at the point where the ζ potential $= 0$.
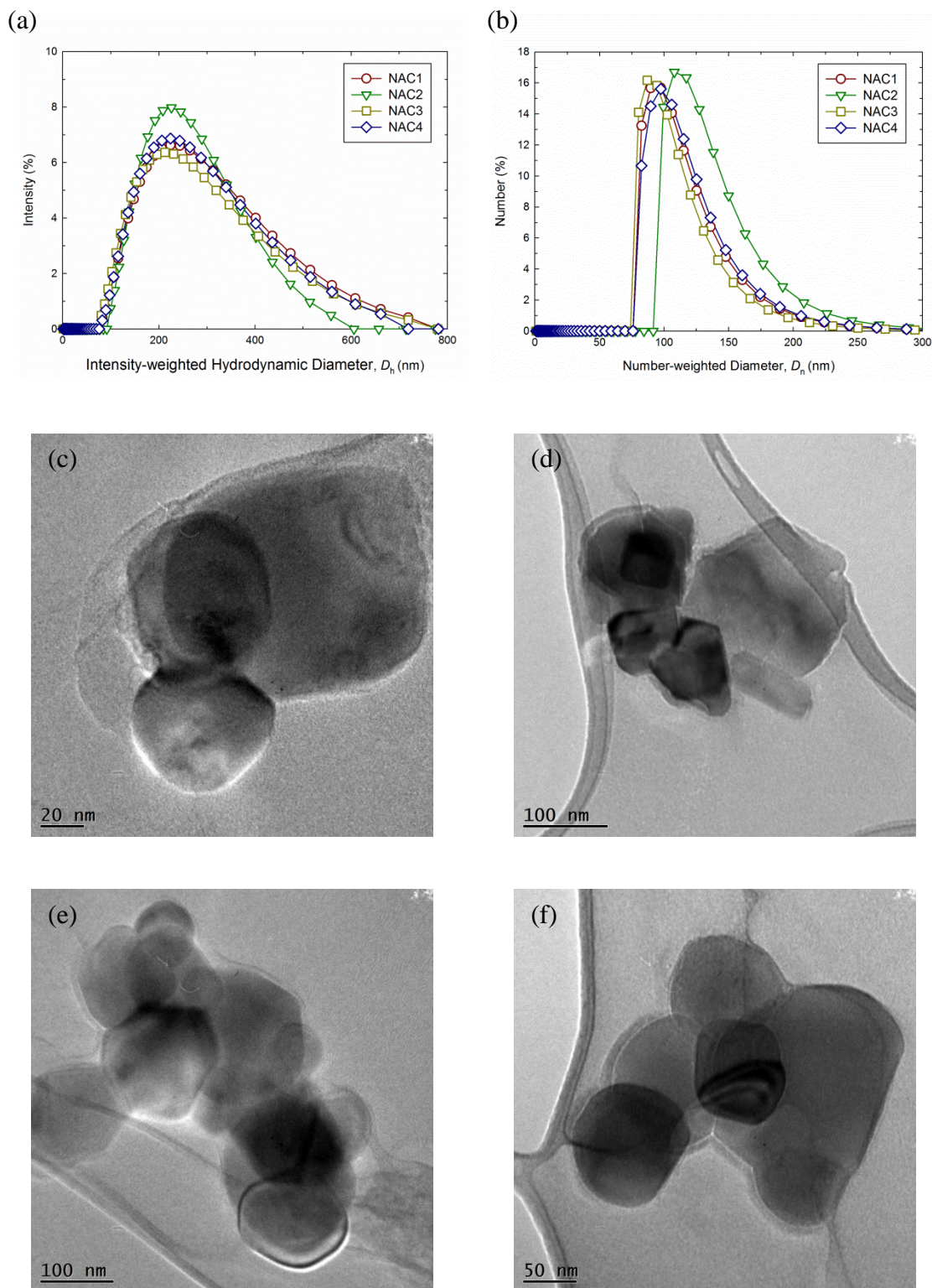
Figure 2.2 Size distributions of (a) intensity-weighted hydrodynamic diameter (D_h), and

(b) number-weighted diameter (D_n) for the NACs determined by DLS; and representative

TEM images of (c) NAC1, (d) NAC2, (e) NAC3, and (f) NAC4. Sonicated NAC stock suspensions were dropped onto 200 mesh carbon coated copper grids.

2.3.2. Zeta Potentials

Negatively charged surfaces were observed for the four NACs with ζ potential values lower than -30 mV in the presence of 1 mM NaCl and at pH 6 (Table 2.3), indicating they were stable suspensions [94]. The ζ potentials of the four NACs over wide ranges of NaCl or $CaCl_2$ concentrations were determined at pH 6 (Figure 2.3), with the corresponding EPMs presented in Figure 2.4. The results showed that the four NACs remained negatively charged over the tested concentration ranges of both electrolytes. The ζ potential values for the first three NACs remained overlapped throughout, which were generally more negative than those determined for NAC4. The increase in concentrations of both electrolytes resulted in less negative ζ potentials for all NACs due to charge screening, as is widely observed for common colloidal particles [24]. The divalent salt ($CaCl_2$) was more effective in reducing the ζ potentials of the NACs than the monovalent salt (NaCl), which could be attributed to much stronger interactions of calcium ions with particle surface [38]. The findings are similar to those reported for other carbonaceous materials such as carbon nanotubes [39], fullerenes [38], and graphene oxides [42] and other natural colloids including vermiculite [95], pumice [96], and bentonite [96].
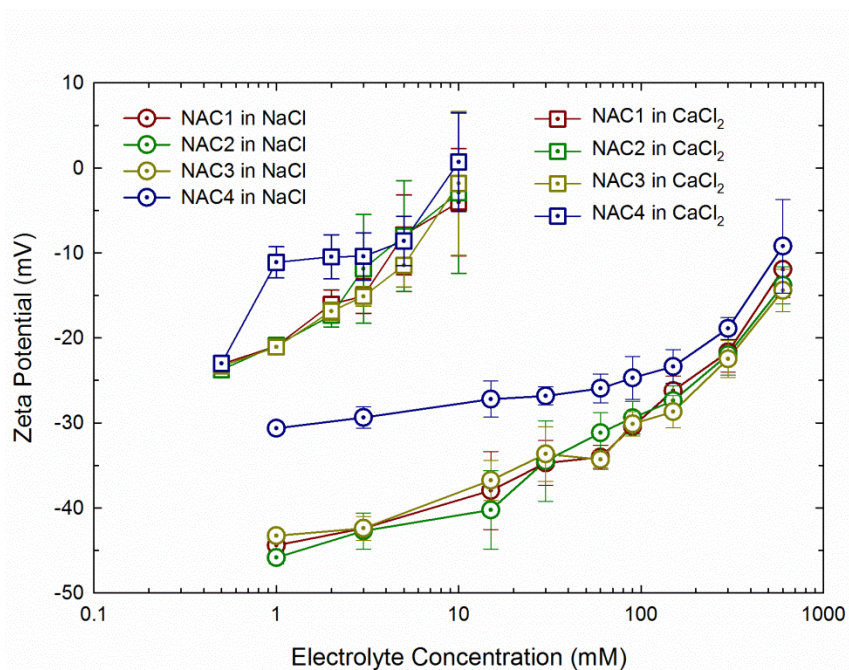
Figure 2.3 ζ potentials of the four NACs (10 mg/L) as a function of electrolyte concentration at pH 6 and 25 °C. Each error bar represents one standard deviation from three independent samples each with 10 measurements.
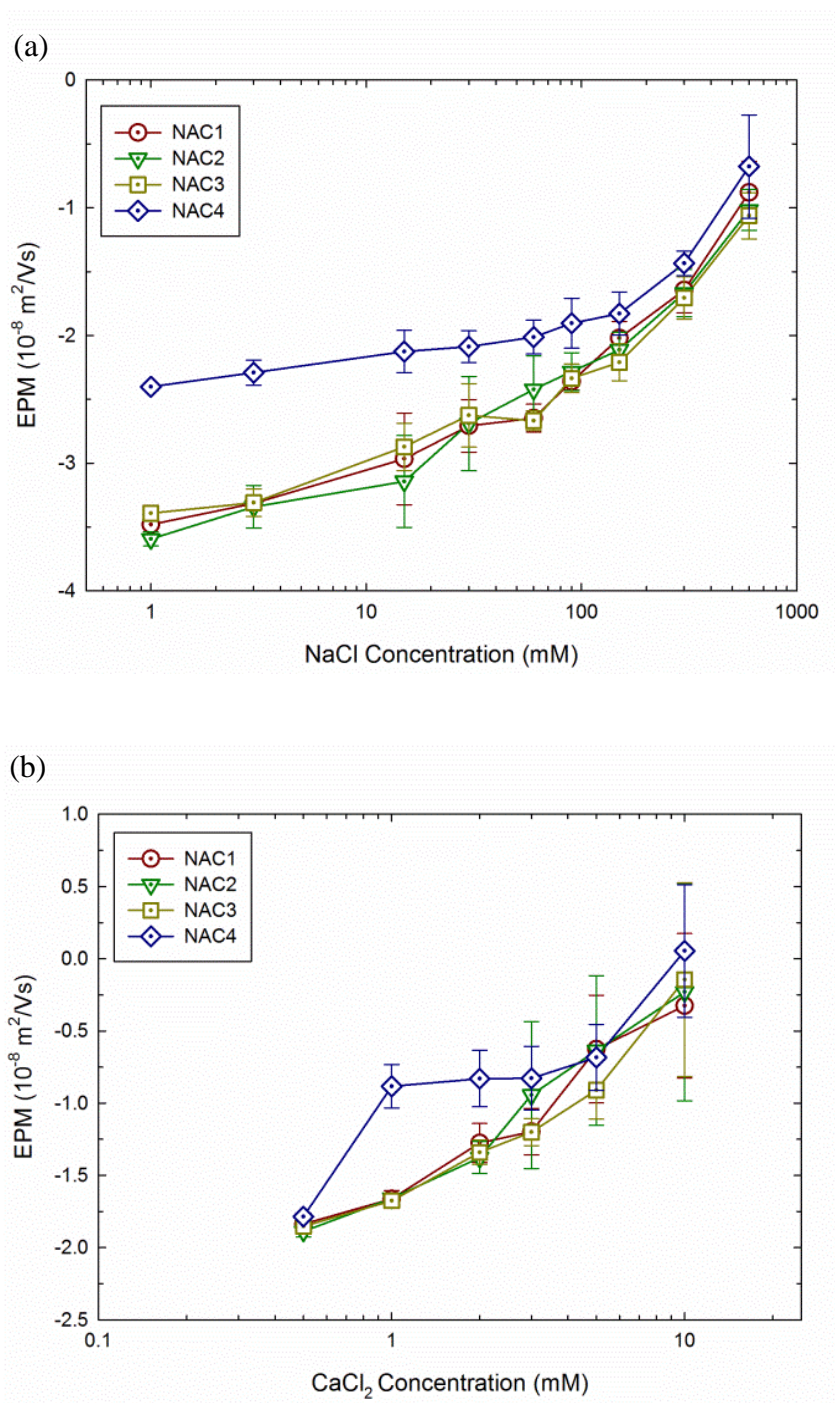
Figure 2.4 Electrophoretic mobilities (EPM) of NACs as a function of (a) NaCl and (b) CaCl$_2$ concentrations at pH 6 and 25°C. The error bars represent standard deviations from three independent samples each with 10 measurements.

2.3.3. Colloidal Stability

The aggregation profile showing the rate of increase in D_h of NAC1 in the presence of 500 mM NaCl at pH 6 over 8 hours is presented in Figure 2.5. In general, the non-linear increase in hydrodynamic diameter with time could be fitted by power-law [97] or exponential [98] functions. At the initial stage of aggregation, however, the hydrodynamic diameter increases linearly with time and the slope of the linear region could be determined as the aggregation rate.
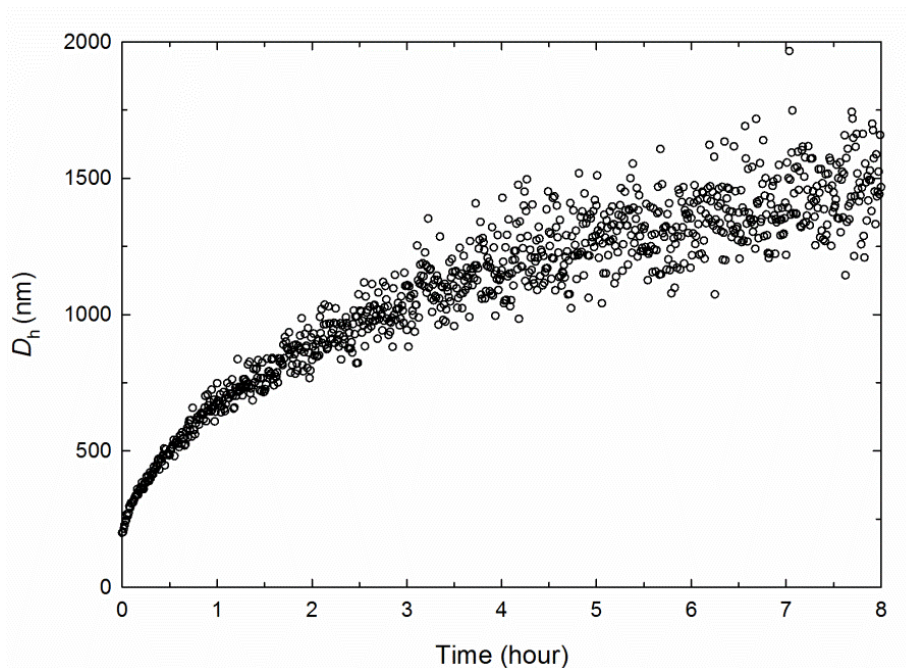
Figure 2.5 Aggregation profile showing the increase in hydrodynamic diameter (D_h) with time for NAC1 in the presence of 500 mM NaCl at pH 6 and 25 ℃.

The representative aggregation profiles showing the early-stage aggregation kinetics of NACs in the presence of NaCl and CaCl$_2$ at pH 6 are presented in Figure 2.6.

Consistent with the ζ potential results, divalent salt (CaCl$_2$) was much more effective in inducing aggregation of NACs than monovalent salt (NaCl). Meanwhile, NACs 1-3 were relatively more stable against aggregation compared to NAC4 in both electrolyte solutions.
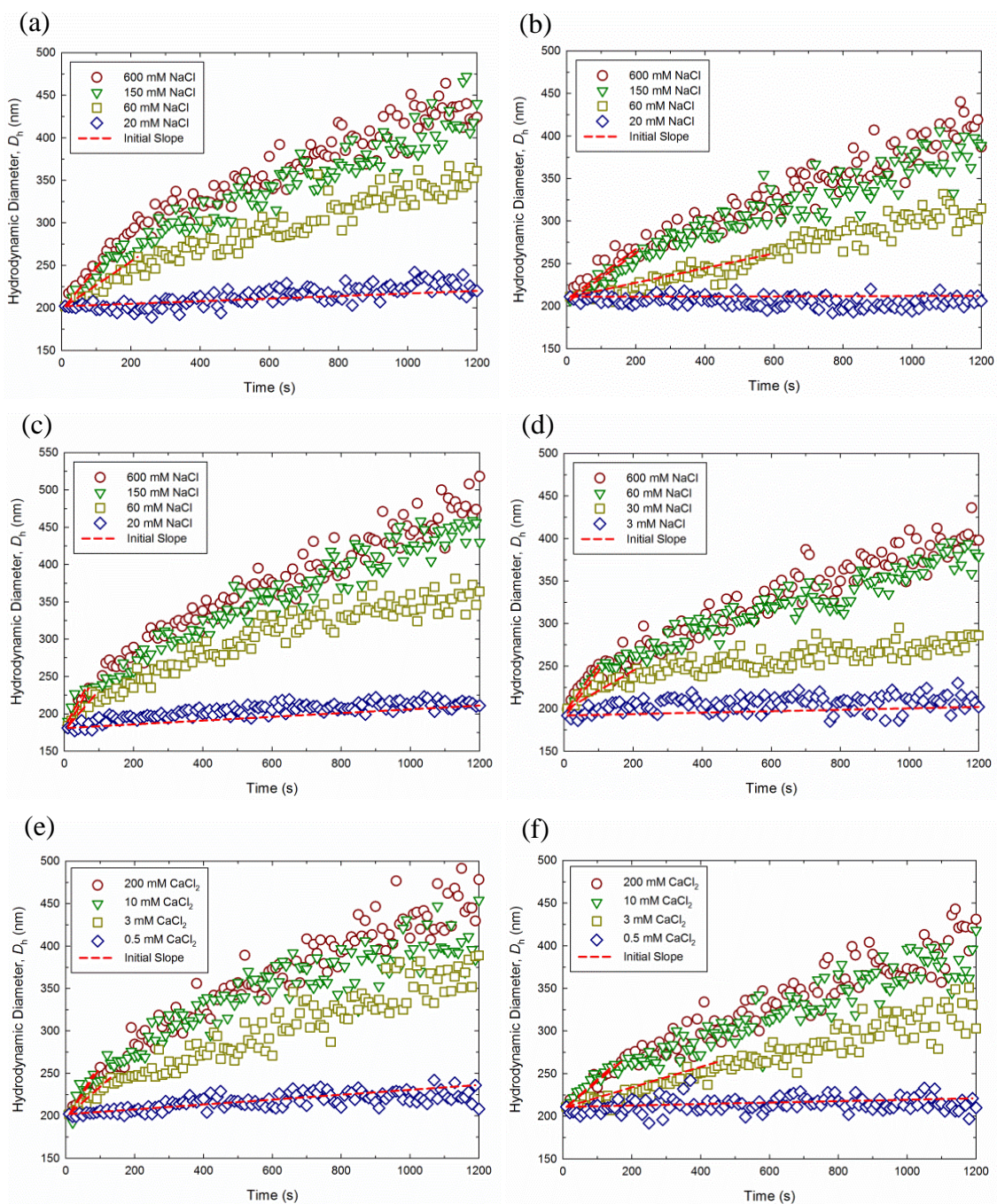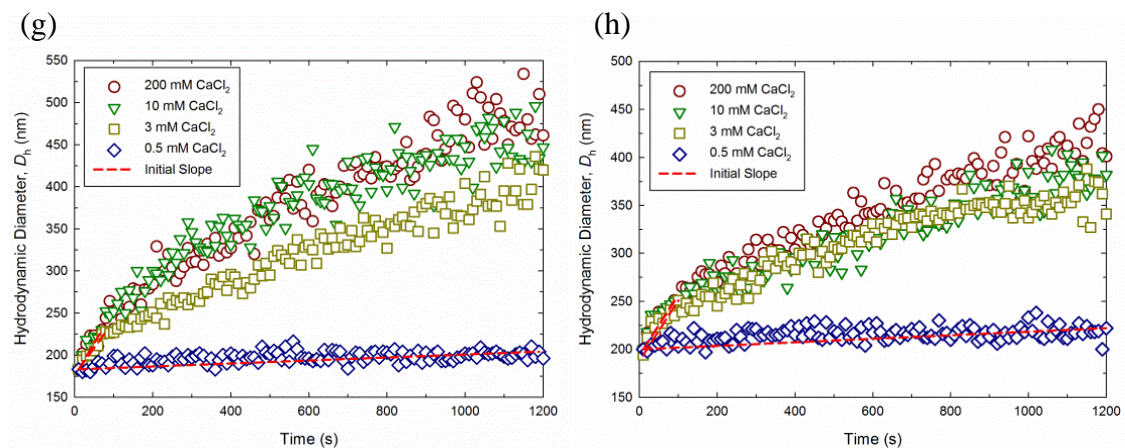
Figure 2.6 Representative aggregation profiles showing the increase in D_h with time for (a) NAC1, (b) NAC2, (c) NAC3, and (d) NAC4 in the presence of NaCl, and (e) NAC1, (f) NAC2, (g) NAC3, and (h) NAC4 in the presence of CaCl$_2$ at pH 6 and 25 °C. Each aggregation profile was measured in triplicates to ensure data quality. The slopes of red dashed lines were determined as the aggregation rates.

By normalizing the initial slopes of the aggregation profiles, the attachment efficiencies (α) were obtained to quantify the stability of NACs under the tested solution conditions (Figure 2.7). The attachment efficiency profiles demonstrated two distinct regimes, suggesting that the aggregation kinetics of the four NACs could be explained with the classic DLVO theory for colloidal stability [24]. At the electrolyte concentrations below the critical coagulation concentrations (CCC), increase of electrolyte concentrations resulted in charge screening on particle surface and lowering of the energy barrier to aggregation, as was evident from the measured concentration-dependent change of the ζ potentials shown in Figure 2.3. The attachment efficiencies increased accordingly with electrolyte concentrations in the reaction-limited aggregation

regime ($\alpha < 1$). At the electrolyte concentrations over CCC, however, the energy barrier to aggregation was completely screened and the van der Waals forces dominated the interaction of the particles. The attachment efficiencies became independent of electrolyte concentrations in the diffusion-limited aggregation regime ($\alpha = 1$), where the same average k_{fast} value was observed for each type of NACs in the presence of NaCl or CaCl$_2$.

The CCC values for each type of NACs in both NaCl and CaCl$_2$ solutions were determined, as shown graphically in Figure 2.7, by extrapolating from the reaction-limited and diffusion-limited regimes. In general, a higher CCC value indicated a higher colloidal stability. The resulting CCC data listed in Table 2.3 suggested that NACs 1-3 were more stable than NAC4 in the presence of both electrolytes, and that CaCl$_2$ was more effective than NaCl in inducing aggregation of NACs, which were consistent with the ζ potential measurements. Meanwhile, the results also showed that the ratio of the CCC values for the NACs in divalent salt to monovalent salt were proportional to near z^{-4} (Table 2.3), where $z = 2$ for the valence of the calcium ion. The weak dependence of the NACs CCC values on counterion valence was consistent with colloidal particles, where the proportionality was observed to range from z^{-2} to z^{-6} (Schulze-Hardy Rule) in practice [24, 25]. Note that the CCC values (42-76 mM NaCl and 2.6-4.5 mM CaCl$_2$) determined for the four NACs were considerably lower than those reported for aqueous fullerene nanoparticles (FNPs) (120 mM NaCl and 4.8 mM CaCl$_2$) [38] - but slightly higher than those for single-walled carbon nanotubes (SWNTs) [40] (37 mM NaCl and 0.20 mM CaCl$_2$) and multi-walled carbon nanotubes (MWNTs) (25 mM NaCl and 2.6 mM CaCl$_2$) [39], which corresponded to their respective ζ potentials of -35 [38], -12 [40], and -30

mV [39] measured under similar solution conditions. It appears that the differences of the CCC values reported for the carbonaceous nanoparticles were largely due to the difference in surface charge as indicated by the ζ potentials. Nevertheless, the CCC values obtained for the four NACs were considerably higher than the NaCl and $CaCl_2$ concentrations in typical freshwater environments (see Table 2.4), suggesting that these nanomaterials may remain relatively stable against aggregation in these aquatic systems.

(a)
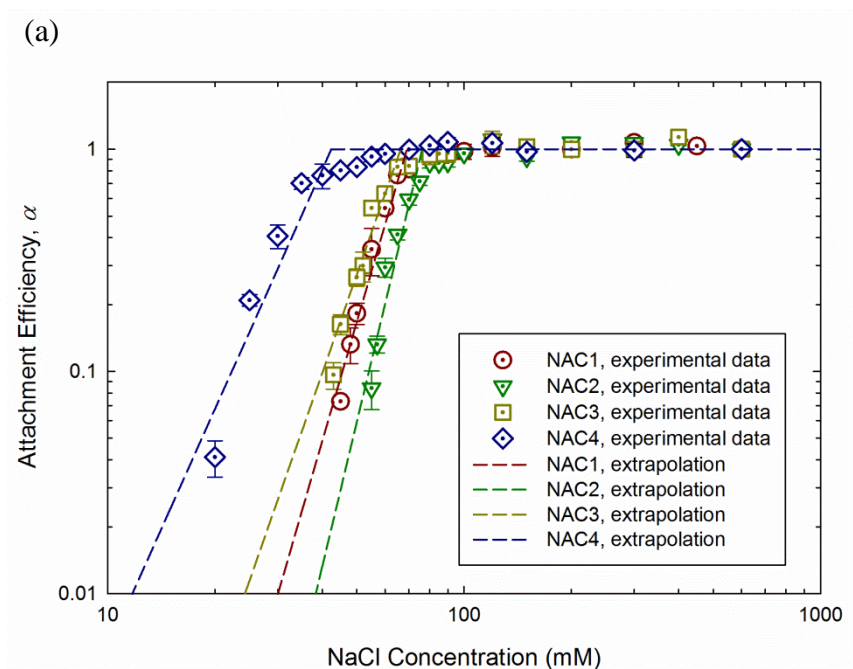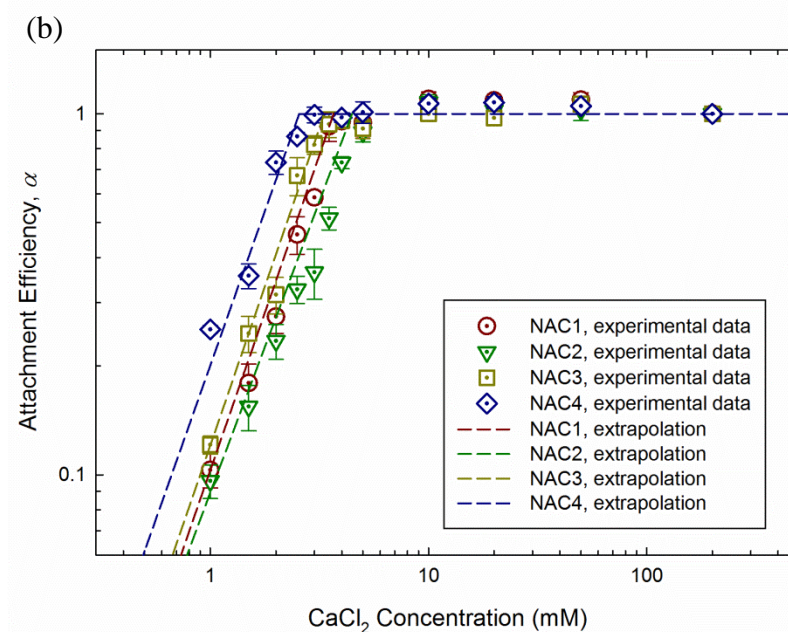
Figure 2.7 Attachment efficiency (α) profiles of the four NACs as a function of the aqueous concentration of (a) NaCl and (b) CaCl$_2$ at pH 6 and 25 °C. Each error bar represents one standard deviation from three independent samples each with 10 measurements. The NAC concentration was at 10 mg/L. The lines extrapolated from the reaction-limited and diffusion-limited regimes were for vision guidance, and their intersections yielded the respective CCC value.

Table 2.4 Typical concentrations of sodium and calcium ions and the corresponding ionic strengths in natural water bodies.

Types of Water Bodies		Na^+ (mM)	Ca^{2+} (mM)	Ionic Strength (mM)[a]
		Surface Water		
Streams[b]	Minimum	0.0026	0.0015	0.014
	Maximum	15.2	5.3	50.1
Rivers[b]	Minimum	0.35	0.05	0.49
	Maximum	1.1	1.25	7.04
Global average (MCNC)[b]		0.16	0.2	1.09
Olentangy River, Ohio, USA[c]		1.85	1.81	9.4
Meadow complex stream water, Nevada, USA[d]		0.74	0.48	3.5
South Han-river, Korea[e]		0.12	1.27	6.39
		0.17	0.48	2.62
		Groundwater		
Typical natural groundwater[b]		<8.7	<2.5	20.1
		8.9	1.6	14.4
Meadow complex stream water, Nevada, USA[d]		1.13	0.58	3.8
South Han-river, Korea[e]		0.33	0.58	4.63
		3.71	1.08	8.56
		Seawater		
Typical seawater[f]		456.5	10.25	690

[a] Ionic strength (I) was calculated by $I = \frac{1}{2}\sum c_i z_i^2$ by accounting for all ions from the data source including Na^+ and Ca^{2+}.

[b] Data from UNESCO, WHO and UNEP [99]; streams: 1-100 km^2; rivers: 100,000 km^2; MCNC (most common natural concentrations) corresponding to the median value obtained for 60 major rivers.

[c] Data from Li and Lenhart [100].

[d] Data from Atekwana and Richardson [101].

[e] Data from Kim, Lee, Yum and Chang [102].

[f] Data from Hem [103].

2.3.4. Comparison with DLVO Theory

The attachment efficiencies obtained experimentally for each NAC were fitted with the DLVO model predictions following the DLVO calculations described in the experimental section (eqs 2.3 to 2.12), which yielded the optimal Hamaker constants (A_{CWC}) for the NACs. Note that the ζ potentials values used for DLVO calculations were represented by a logarithm function as shown in Figure 2.8. In the fitting procedure, A_{CWC}, which affected the intersection between the fast and slow aggregation regimes (the position of CCC), was the sole fitting parameter. Therefore, the A_{CWC} values were optimized for NACs in NaCl solutions such that the CCC values estimated theoretically matched the ones obtained experimentally and listed in Table 2.3.

(a)

$$\zeta = -79.9037 + 10.3142 \times \ln(C + 35.5461)$$

(b)

$$\zeta = -65.5416 + 7.8139 \times \ln(C + 13.651)$$

(c)

$$\zeta = -72.0789 + 8.7163 \times \ln(C + 30.6197)$$

(d)

$$\zeta = -319.37 + 41.9471 \times \ln(C + 1017.07)$$
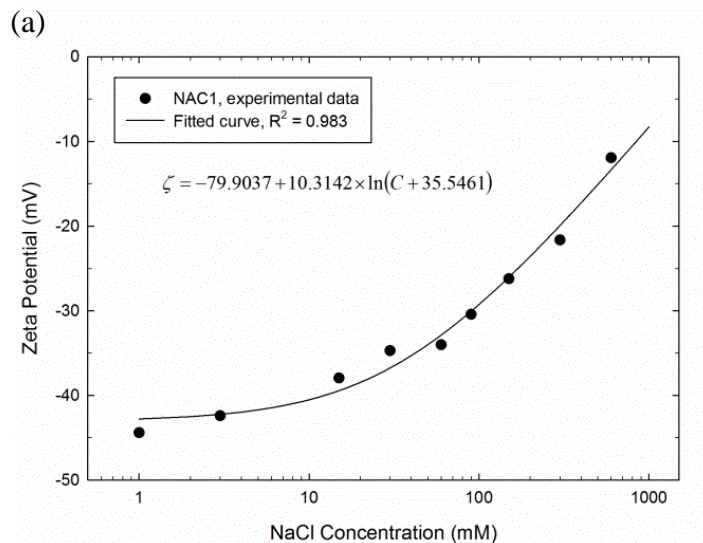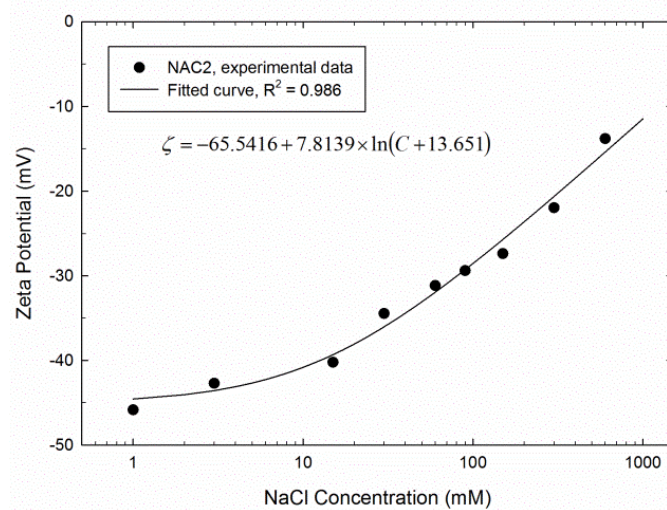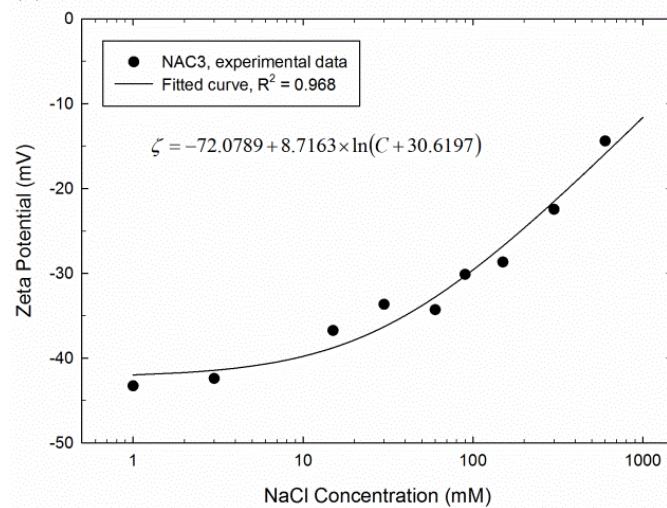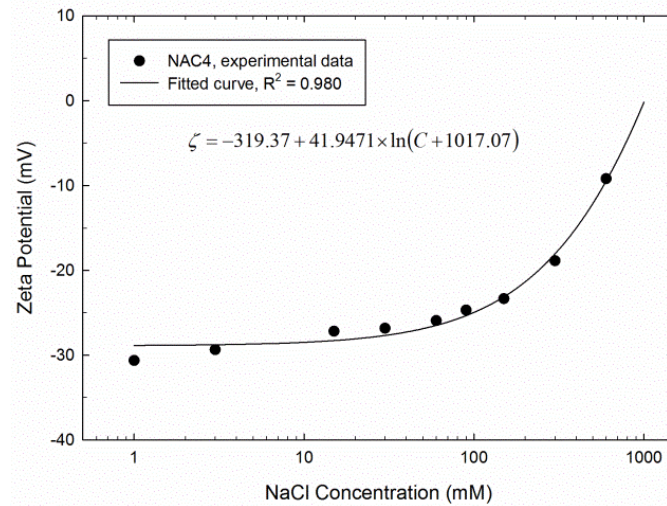
Figure 2.8 The ζ potentials of (a) NAC1, (b) NAC2, (c) NAC3, and (d) NAC4 as a function of NaCl concentration at pH 6. The experimental data points were reproduced from Figure 2.3, which were fitted by a logarithm 3 parameter function for DLVO calculations.

Figure 2.9 compares the attachment efficiency curves predicted theoretically with the experimental α values in the presence of NaCl. It shows that, in the slow aggregation regime, the slope of the α curve depends upon both the particle radius (R) and the theoretical expressions employed for computing $V_R(h)$. Here, both R_{h0} (solid lines) and R_{n0} (dashed lines) were utilized as the R value during computation. Figure 2.9 demonstrates that, when R_{h0} was utilized, the theoretical α curves (solid lines) in the slow aggregation regime deviated considerably from the experimental data for all four NACs. More specifically, the α curves predicted using R_{h0} as R were much steeper than those measured experimentally for the same NAC, which is consistent with the reports for other colloidal particles [24, 104]. Such deviations could be due to the fact that these NACs were irregularly shaped and polydispersed particles as observed in the TEM images, which was far from the assumed spherical shape with monodispersity. When R_{n0} was utilized, however, the theoretical α curves (dashed lines) showed fairly good agreement with the experiment data for all four NACs. This fitting exercise suggested that the actual sizes of these polydispersed NAC particles could be much better approximated by R_{n0} compared to R_{h0}.
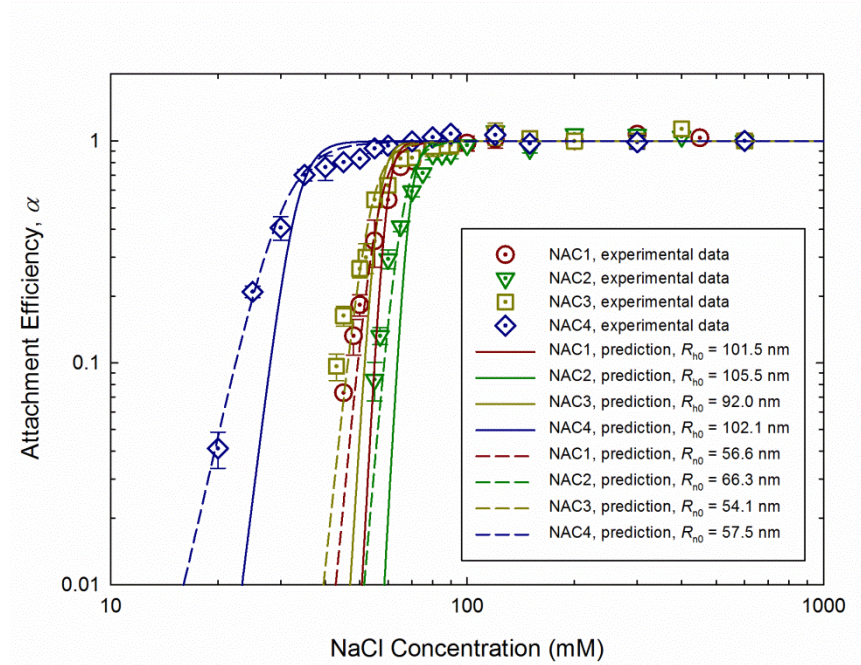
Fig. 2.9. The theoretical DLVO predictions and the experimentally derived attachment efficiencies for the four NACs as a function of NaCl concentration at pH 6 and 25 °C. Each error bar represents one standard deviation from three independent samples each with 10 measurements. The data points were reproduced from Figure 2.7a. The concentration of NACs was at 10 mg/L. The DLVO predictions utilizing R_{h0} (solid lines) and R_{n0} (dashed lines) for approximation of the particle radius both yielded the same value for the Hamaker constant (A_{CWC}) for each type of NAC. The derived A_{CWC} values were 2.1-2.7 × 10^{-20} J for the four NACs (Table 2.3).

In addition to the particle radius, the expression employed for calculating the $V_R(h)$ value was the other factor affecting the slope of the theoretical α curves. Figure 2.10 shows that compared to the CCA and LSA expressions, the CPA expression always provided the shallowest slope of theoretical curve by predicting the minimum repulsion

energy. This is consistent with theoretical expectations [24]: the CPA expression predicts the minimum repulsion that is more likely for surfaces developing charge by ion adsorption, while the CCA expression predicts the maximum repulsion and fits closest for surfaces that develop charge through dissociation. For a real system, intermediate prediction by the LSA expression with both surface charge density and the surface potential changing may be more likely to occur. However, our fitting exercise indicated that the CPA expression was the most suitable for all four NACs, which supported its underlying assumptions that NACs may develop surface charges by rapid sorption of the potential-determining ions, thus the surface potentials remained constant when two surfaces approach to each other [91]. The CPA expression yielding the best fitting for all four NACs compared to other two commonly used expressions could also be attributed to the polydispersity of particles as suggested by Chen and Elimelech [37].

(a)

(b)

(c)

(d)
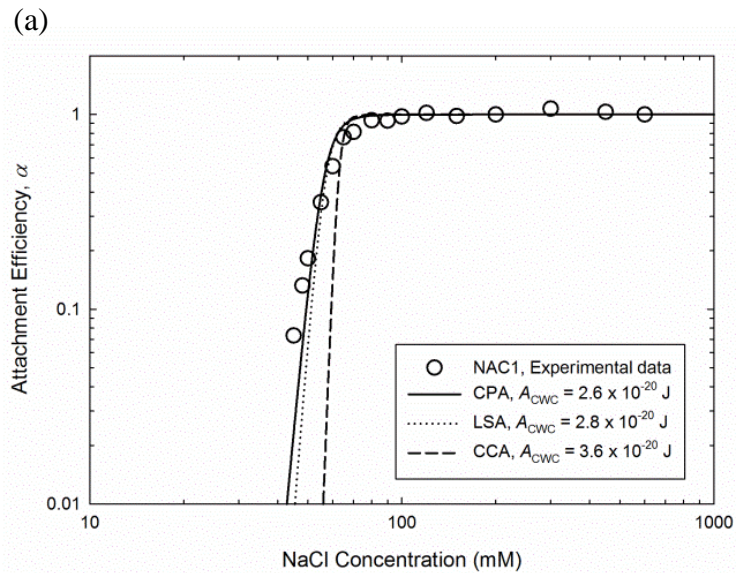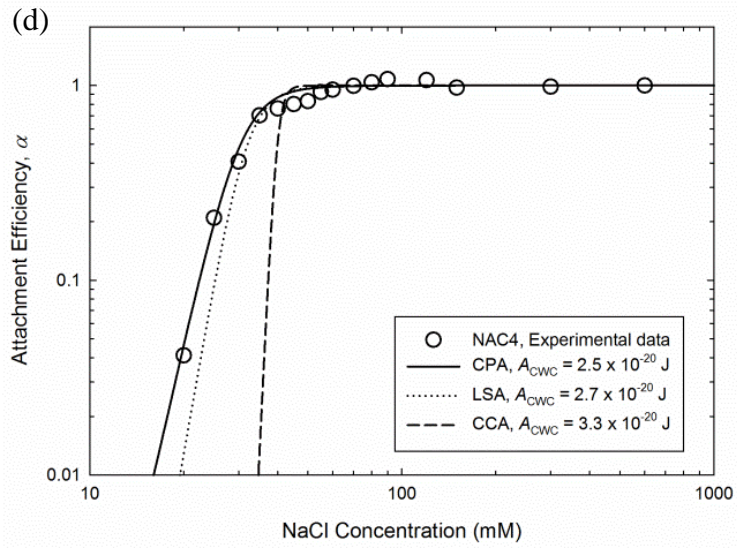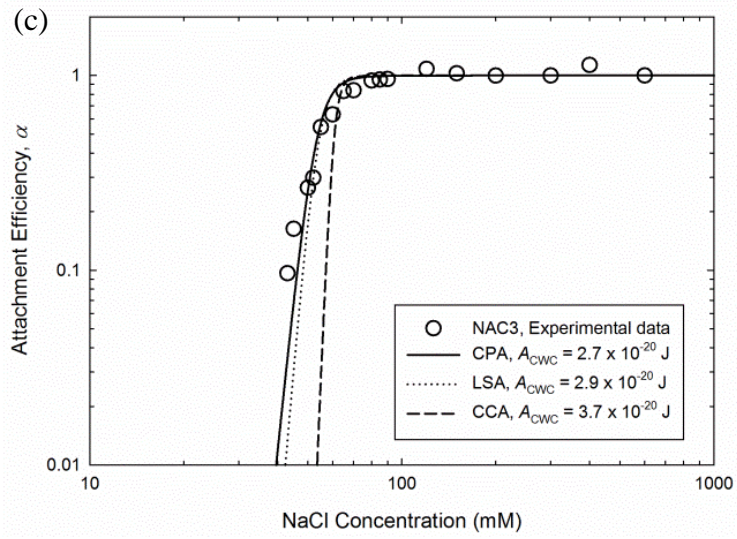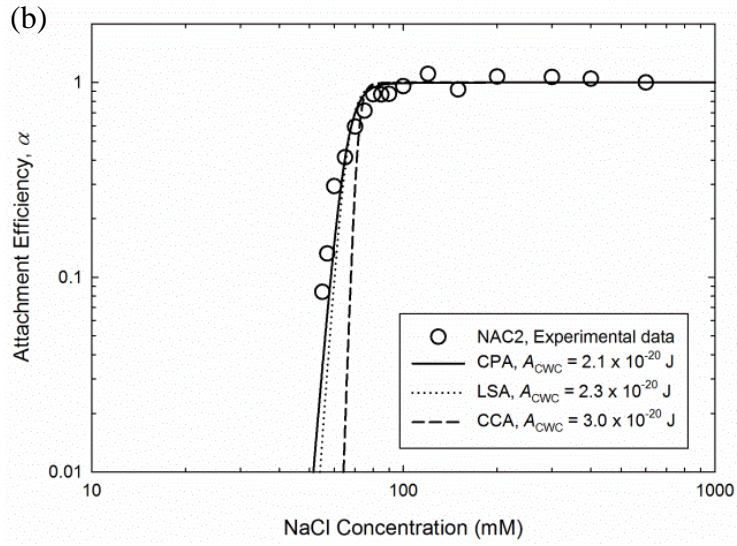
Figure 2.10 The effect of charge regulation on theoretical DLVO prediction of attachment efficiency for (a) NAC1, (b) NAC2, (c) NAC3, and (d) NAC4 at pH 6 and 25 ℃. The CPA, LSA, or CCA expressions was employed to calculate $V_R(h)$. R_{n0} was utilized throughout to approximate the particle radius. The Hamaker constants were fitted for each expression such that the critical coagulation concentrations (CCC) of theoretically prediction matched the ones obtained from experiments in Table 2.3.

2.3.5. *Hamaker Constants for NACs*

Figure 2.11 shows that the change of the Hamaker constant renders horizontal shifting of a given α curve, hence affects only the position of CCC. As a result, the fitting procedures using either R_{h0} or R_{n0} and eq 2.3 yielded a singular Hamaker constant for each type of NACs. The A_{CWC} values listed Table 2.3 are the effective Hamaker constants for the NACs under aquatic conditions. Note that, regardless of the differences in their original materials, the four NACs had very similar Hamaker constants of 2.1-2.7 × 10^{-20} J, which were greater than those measured similarly for aqueous FNPs (0.67-0.85 × 10^{-20} J [37, 38]), but smaller than that for graphite in water (3.7 × 10^{-20} J [105]). The Hamaker constant of NAC particles interacting under the vacuum condition (A_{CC}) can be approximated from the following relationship [78]:

$$A_{cwc} \approx \left(\sqrt{A_{cc}} - \sqrt{A_{ww}} \right)^2 \tag{2.13}$$

where A_{WW} is the Hamaker constant for water-water interaction in a vacuum. Given the A_{WW} value of 3.7 × 10^{-20} J [78], the A_{CC} values calculated for the four NACs ranged from

11.4-12.7 $\times$ 10^{-20} J (Table 2.3). It should be noted that these A_{CC} values obtained in this study for the NACs were much smaller than the A_{CC} values reported for carbon nanotubes (23-60 $\times$ 10^{-20} J [38]), but they were approximately twice as large as the Hamaker constants (A_{CC}) widely used for AC materials, such as 5.2-6.2 $\times$ 10^{-20} J estimated from carbon fibers [79, 82] or 5.0-7.8 $\times$ 10^{-20} J calculated from the adsorption data ACs [83]. A relatively larger value of the effective Hamaker constant could be expected in our study using the colloidal chemistry approach, because a hypothetical hydrophobic attraction may be lumped into the van der Waals forces [104]. Nevertheless, the Hamaker constants reported here based on the colloidal chemistry approach should be a valuable addition to the database on the characteristics of AC materials.

(a)

(b)

(c)

(d)
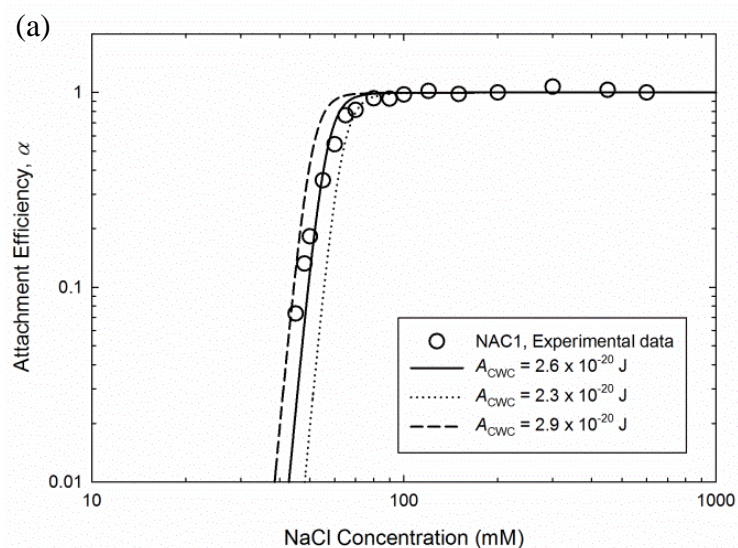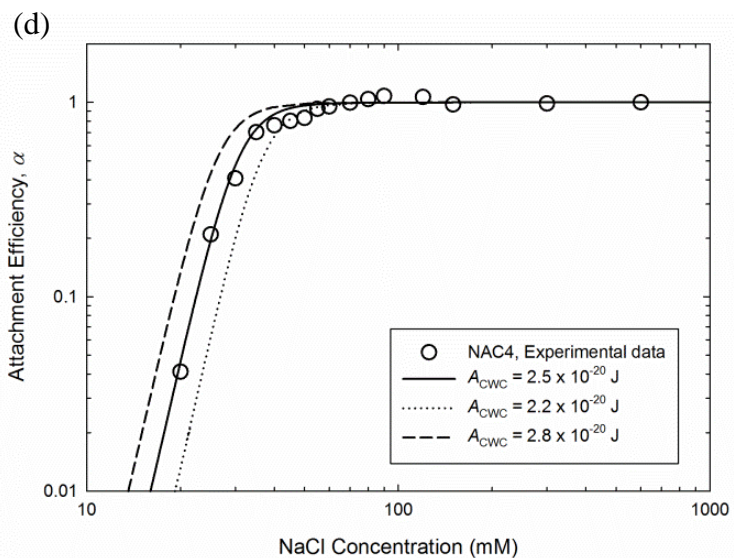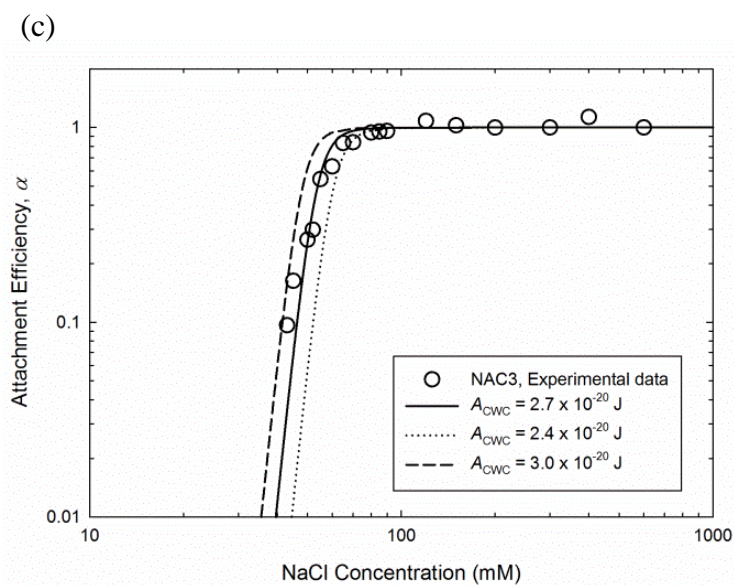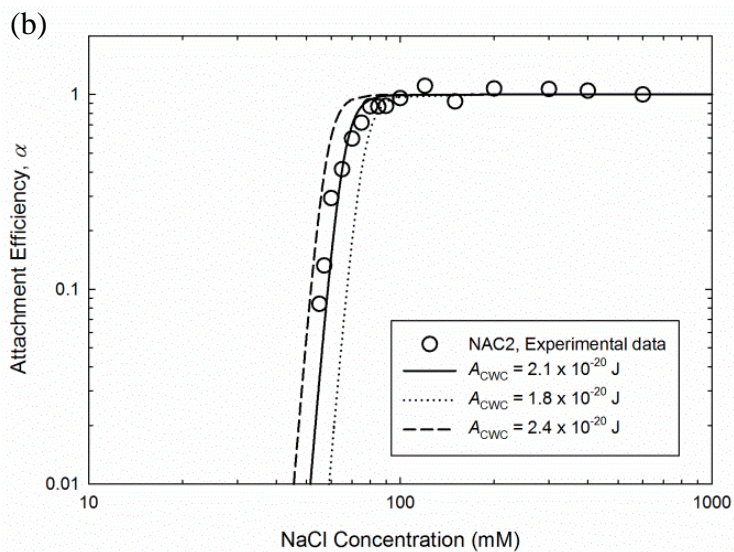
Figure 2.11 Sensitivity of the Hamaker constants for (a) NAC1, (b) NAC2, (c) NAC3, and (d) NAC4 on the theoretical DLVO prediction of attachment efficiency curves at pH 6 and 25 ℃. The CPA expression and R_{n0} as the particle radius were used for quantifying $V_R(h)$.

2.3.6. DLVO Interaction Energy Profiles

Since the Hamaker constant depends only on material properties [24], it is a key parameter for elucidating and predicting the particle interactions and stability of the AC materials in aquatic environments. For instance, the total DLVO interaction energy profiles of two approaching NAC particles as a function of NaCl concentration could be computed for explanation and prediction of the NACs stability upon entering aquatic systems with different ionic strengths (Figures 2.12 and 2.13).

Figure 2.12 presents the calculated DLVO interaction energies between two nearby NAC particles as a function of their separation distance in the presence of 1 mM NaCl at pH 6 and 25 °C, using eq 2.4, 2.6, and 2.7. The shape of the interaction profile directly influences the kinetics of the particles aggregation and thus, the stability of the colloidal system. At small separations, the attractive energy outweighs the repulsive energy giving rise to an infinitely deep primary minimum, which in practice could be restricted by short-range effects such as ion hydration and particle surface roughness. At intermediate separations, the repulsive energy predominates such that a maximum in the total interaction energy, V_{max}, is observed. The attachment efficiency (α) could be described here as the fraction of effective collisions made by particles overcoming this energy

barrier for close contact. Since particles in Brownian motion have energies less than a few k_BT, relatively stable colloids will be found if V_{max} exceeding a few k_BT. For instance, only 1 out of 10^6 particle collisions is effective ($\alpha = 10^{-6}$) if $V_{max} \cong 15\ k_BT$ [106]. At NaCl concentration of 1 mM, even NAC4 having the lowest V_{max} among all NACs of about 20 k_BT is indicative of stable NAC colloids in freshwater environments.

(a)

(b)
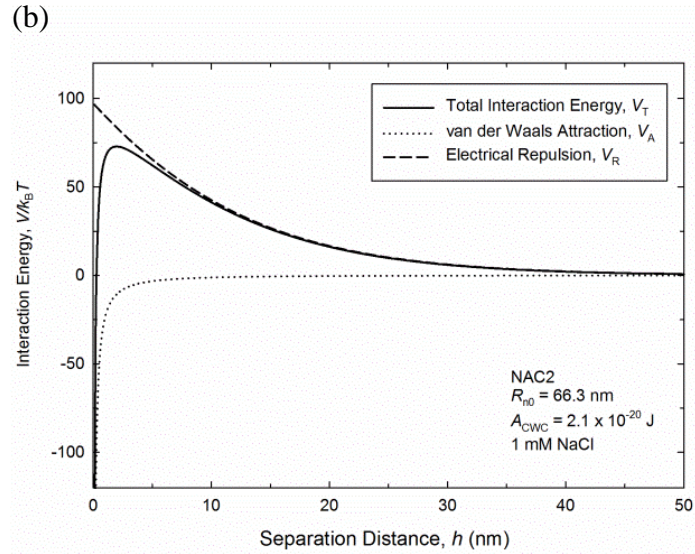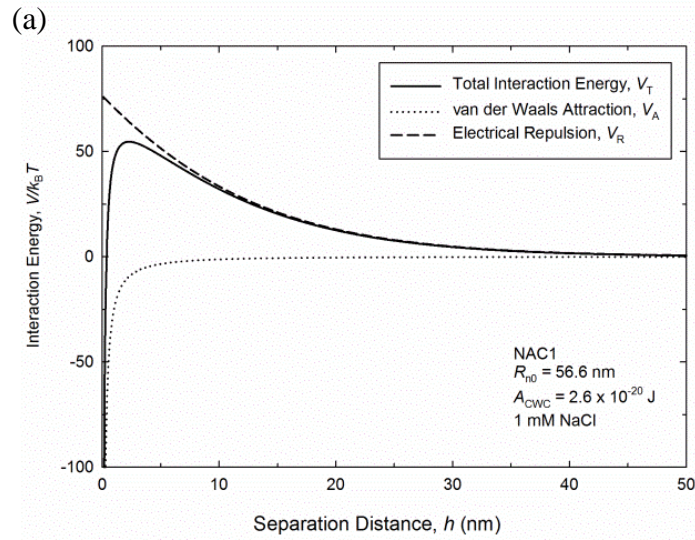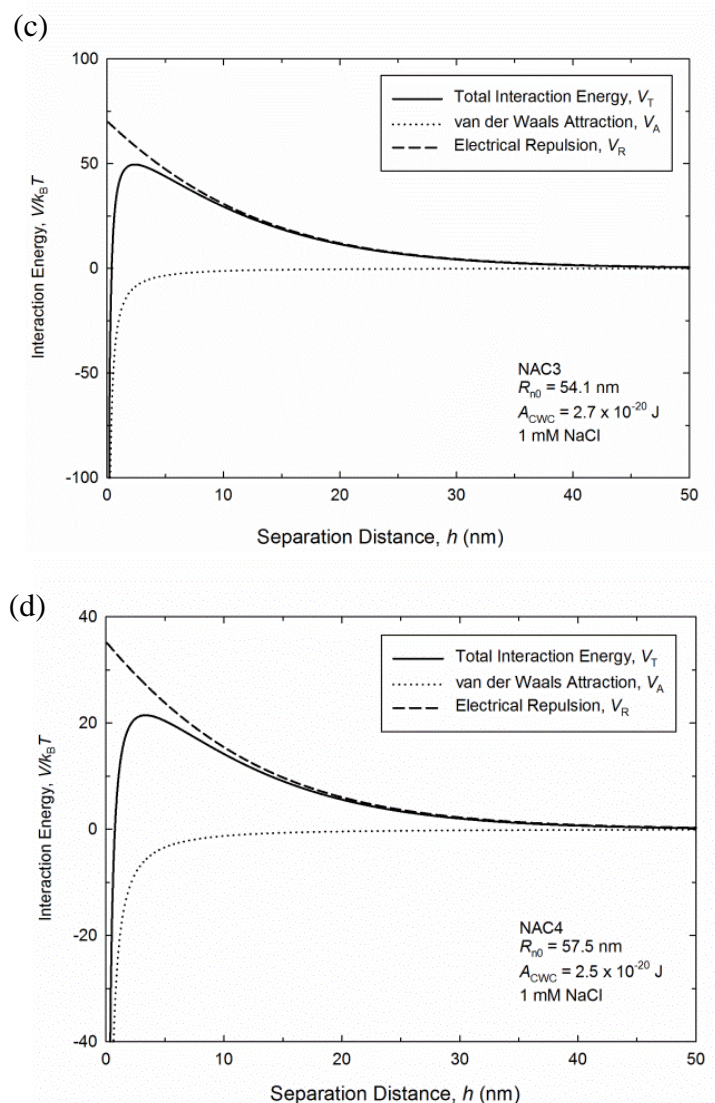
Figure 2.12 DLVO interaction energies (V_T, V_R, and V_A) between two approaching particles of (a) NAC1, (b) NAC2, (c) NAC3, and (d) NAC4 as a function of separation distance in the presence of 1 mM NaCl and at pH 6 and 25 °C. The Hamaker constants (A_{CWC}) derived for the NACs were used in the calculations. The sum of V_R and V_A yielded V_T, which determines the likelihood of fast aggregation of NACs.

Figure 2.13 depicts the lowering of the energy barrier maximum at increasing ionic strength due to charge screening. In fact, the effect of increase in ionic strength on the

repulsive force is two-fold: a decrease in the double layer thickness (κ^{-1}, also known as the inverse Debye length), e.g., from 9.64 nm at 1 mM NaCl to 2.15 nm at 20 mM NaCl for NAC1 (eq 2.10); and a decrease in the ζ potential especially for particle surfaces adsorbing specific counterions. The arrows in Figure 2.13 indicate that the increase of NaCl concentrations up to the CCC not only lowered the maximum energy barrier (V_{max}), but also decreased the separation distance between the two spheres at V_{max} due to double layer compaction. For example, the separation distances between NAC1 particles at V_{max} shortened from 2.3 nm ($V_{max} = 54.7\ k_BT$) at 1 mM NaCl to 1.4 nm ($V_{max} = 20.4\ k_BT$) at 20 mM NaCl (Figure 2.13a). As the NaCl concentration further increased to near the CCC (69 mM), the energy barrier between NAC1 particles disappeared such that they would adhere each time they collide. The NaCl concentrations at which the energy barrier was lowered to 0 are in good agreement with the experimental CCC values, again indicating the consistency between DLVO predictions and experimental results.

The increase of ionic strength also resulted in the deepening of the secondary minimum, such that the attractive energy preponderated over longer distance. In Figure 2.13a at 1 mM NaCl, for example, the secondary minimum started from a separation distance of 76 nm where the total interaction energy (V_T) fell below 0, and reached the minimum V_T of -0.0217 k_BT at separation distance of 96.3 nm. Stable NAC particles were observed experimentally due to the presence of strong repulsive force extending over long distance which prevented particles from aggregation. As the ionic strength increased to 20 mM NaCl, the effect of double layer compression was obvious that the minimum V_T was deepened to -0.66 k_BT at a much shorter separation distance of 12.9 nm in the secondary minimum. This minimum V_T of -0.66 k_BT calculated at 20 mM NaCl was

slightly greater than the Brownian energy of 0.5 $k_B T$ (compared in absolute value) which acts in random directions [107]. But here the attractive energy was still not strong enough to cause rapid particles flocculation due to reaction-limited aggregation occurring near vicinity of the energy barrier, so we have observed relatively slow aggregation for NAC1 in Figure 2.6a. Further increase in NaCl concentration above the CCC (69 mM) would cause disappearance of the secondary minimum leaving only a deep primary minimum in the energy profile, which ultimately approaches the pure van der Waals attraction curve. Such conditions corresponded to the fast aggregation regime, where particles aggregated each time they collide and the diffusion-limited aggregation was achieved such that aggregation rates did not further increase at higher ionic strength. It should be noted that while particles overcoming V_{max} in the primary minimum (coagulation) may not be separated, those held together by weaker forces in the secondary minimum (flocculation) could be easily redispersed [24].

(a)

(b)

(c)

(d)
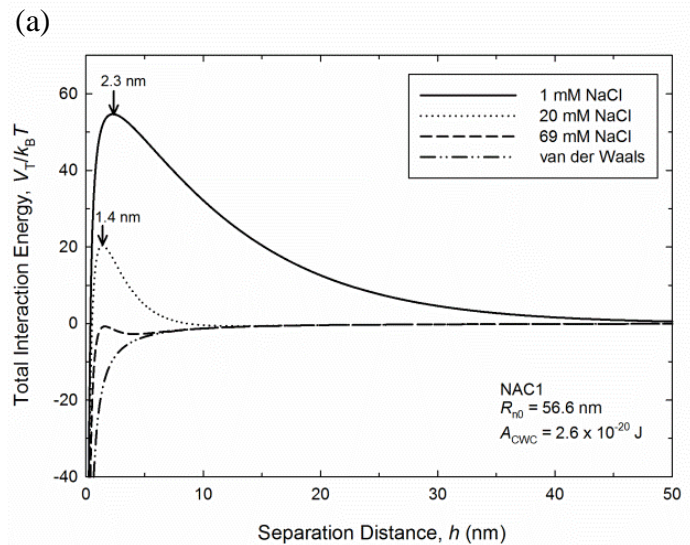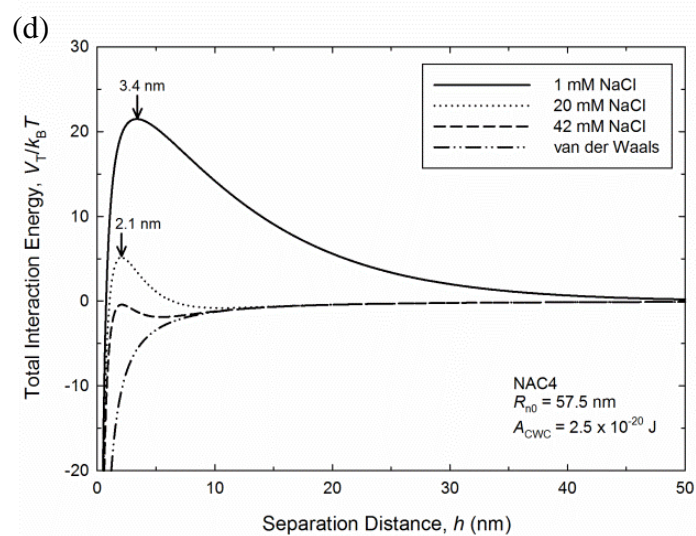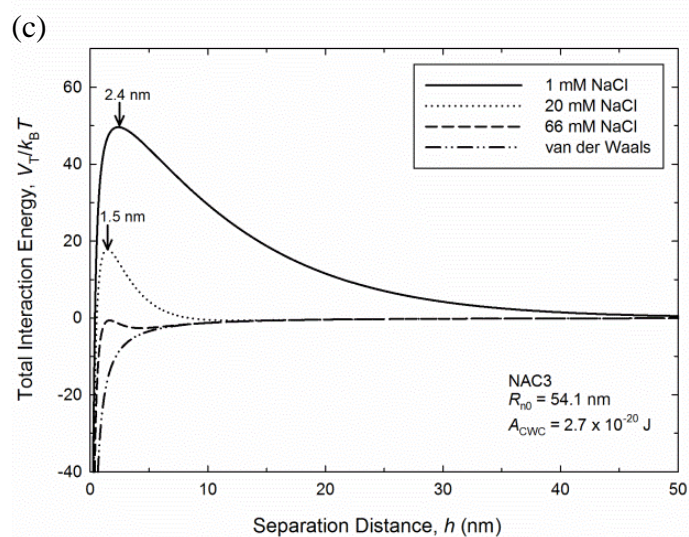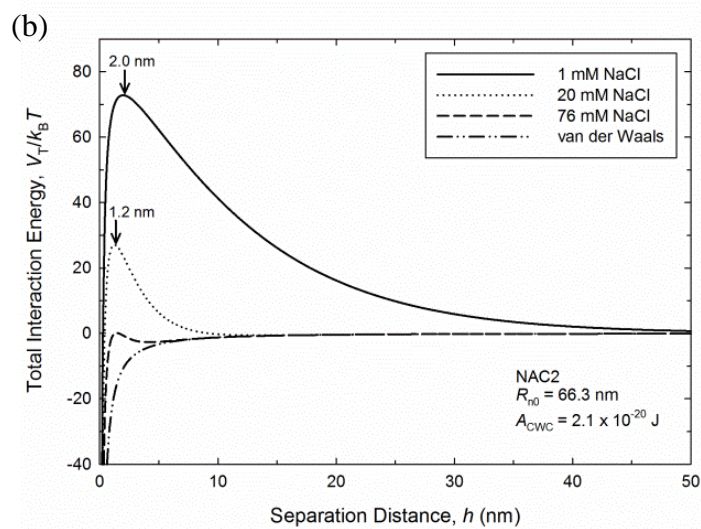
Figure 2.13 DLVO interaction energy profiles for two approaching identical spheres of (a) NAC1, (b) NAC2, (c) NAC3, and (d) NAC4 as a function of NaCl concentration at NAC concentration of 10 mg/L, pH 6, and 25 °C. Here the pure van der Waals interaction profile is shown. The total interaction energy profiles were calculated using R_{n0} as the particle radius, $V_R(h)$ obtained from the CPA expression, and the Hamaker constants (A_{CWC}) listed in Table 2.3 of the text. The arrows indicated the distance from the particle surface where the energy barrier reached the maximum.

2.3.7. Influence of Solution pH on NACs Stability

The role of pH on NACs stability was investigated by measuring their ζ potentials from pH 2 to 12 in the presence of 1 mM NaCl (Figure 2.14a). The results showed that the ζ potentials measured for all NACs were pH-dependent over the tested pH range, with greater negative ζ potentials at higher pH. This pH dependence was consistent with the observations for other charged colloids, such as aqueous FNPs [36], MWNTs [39, 41], carboxyl latex nanoparticles [104], and TiO$_2$ nanoparticles [108]. As the solution pH decreased from 4 to 2 where strong proton activity was present, however, the ζ potentials of all NACs increased sharply and converged to 0 at pH ~3.75, with NAC4 reaching pH 0 slightly faster than other NACs. Therefore, the values of the isoelectric points (pI) determined by extrapolating at the pH where the ζ potential = 0 were very close for the four NACs (Table 2.3).

Potentiometric titration was conducted to investigate the origin of surface charge on aqueous NACs (Figure 2.14b). The titration curves demonstrate that all NACs contained

titratable functional groups, indicating that deprotonation of surface functional groups may be responsible for the charge acquisition. It is known that AC materials contain acidic functional groups that may dissociate at higher pH and result in negatively charged surfaces [109].

Fourier transform infrared (FTIR) spectra was obtained for the four NACs to elucidate their charge acquisition in water (Figure 2.14c), which indicated that their oxygen-containing functionalities mainly included carboxyl and hydroxyl groups. The FTIR spectra of the four NACs had very similar oxygen functional groups, which are typical for activated carbons [110, 111]. According to the literatures [110-115], the intense and broad absorption bands at 3438 cm^{-1} are associated with the stretching vibration of hydroxyl groups [112]. The peaks at 1618 cm^{-1} are characteristics of C=O stretching vibration of carbonyl group in ketone [113, 114]. The bands appear at 1384 cm^{-1} can be ascribed either to carboxyl-carbonate structure or aromatic C=C bond [115]. The two peaks occur at 1109 cm^{-1} only for NAC3 and NAC4 can be assigned to vibration of the CC group in lactones and due to –COH stretching and –OH deformation [111]. The bands at 669 cm^{-1} are related to out-of-plane vibration of C-H groups in aromatic structures [112, 115].

(a)

(b)

(c)
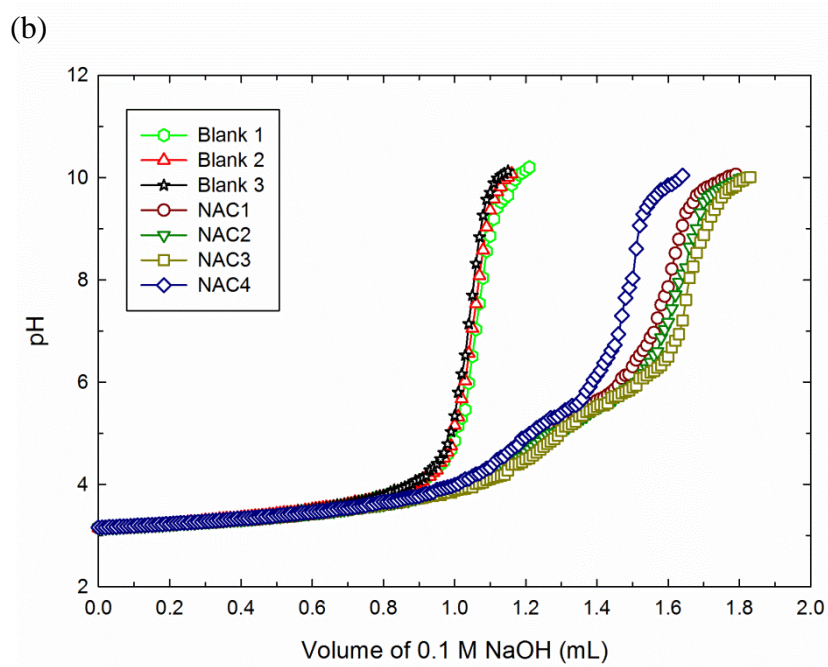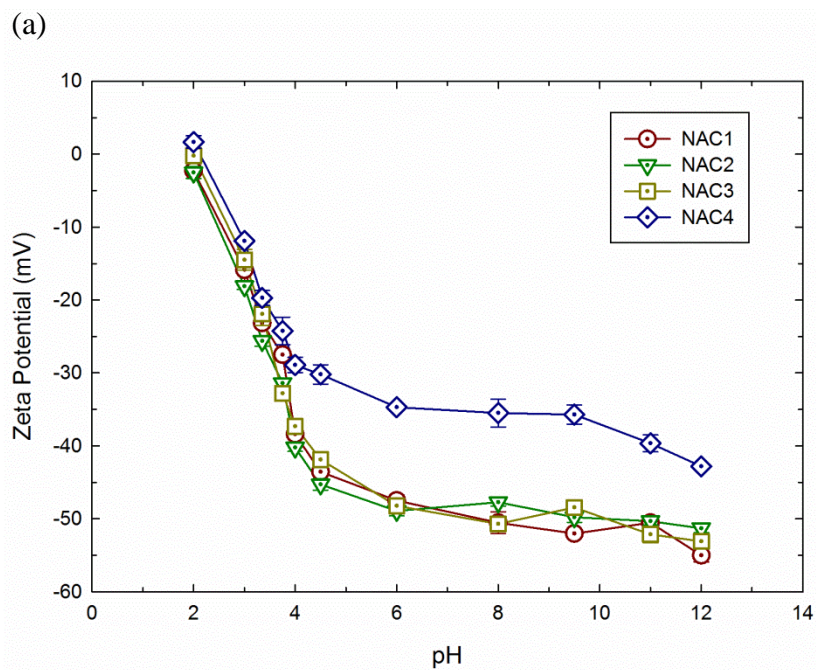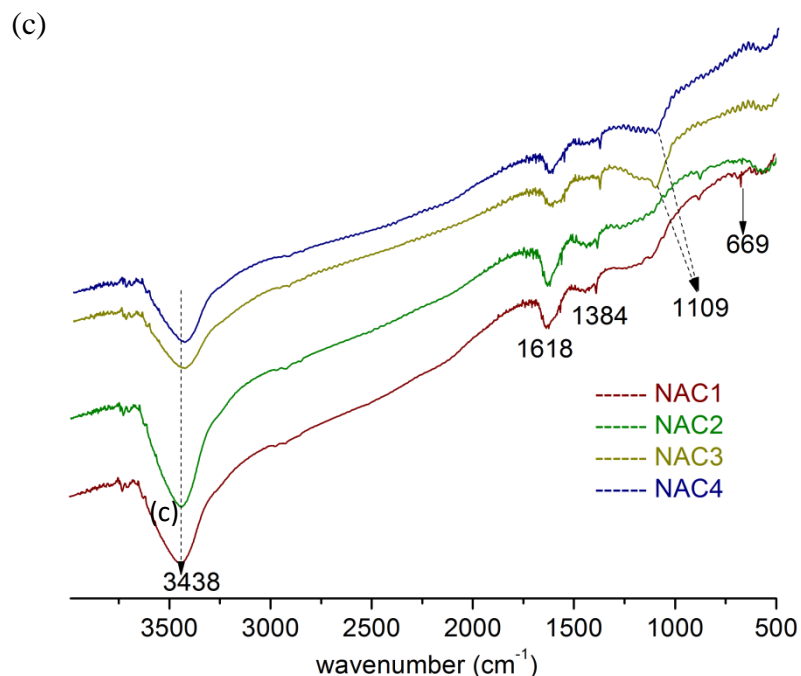
Figure 2.14 Investigation of charge acquisition of aqueous NACs: (a) Effect of pH on the ζ potentials of 10 mg/L NACs measured in the presence of 1 mM NaCl and at 25 ℃. Each data point represents the mean of three independent samples and the error bars represent standard deviations. (b) Potentiometric titration profiles measured at 25 ℃ for NACs from pH 3 to 10. The suspension concentrations of NACs were 1.0 g/L. The blanks contained double deionized water (DDI) without NACs. (c) Fourier transform infrared (FTIR) spectra of the four NACs. The original samples as received from the manufacturer were analyzed using a FTIR spectrometer (Bruker Vector 33, Germany).

The pH effects on the stability of NACs were further illustrated in the aggregation profiles measured in the presence of NaCl at pH 3, 6, and 10 (Figure 2.15). The NaCl concentrations were chosen for each NAC material to induce relatively fast aggregation.

The attachment efficiencies determined for NAC3 in 90 mM NaCl, for instance, were 1.07, 0.88, and 0.24 at pH 3, 6, and 10, respectively. It was evident that the stability of all NACs increased with pH due to deprotonation of surface functional groups as seen by slower aggregation rates.

(a)

(b)

(c)

(d)
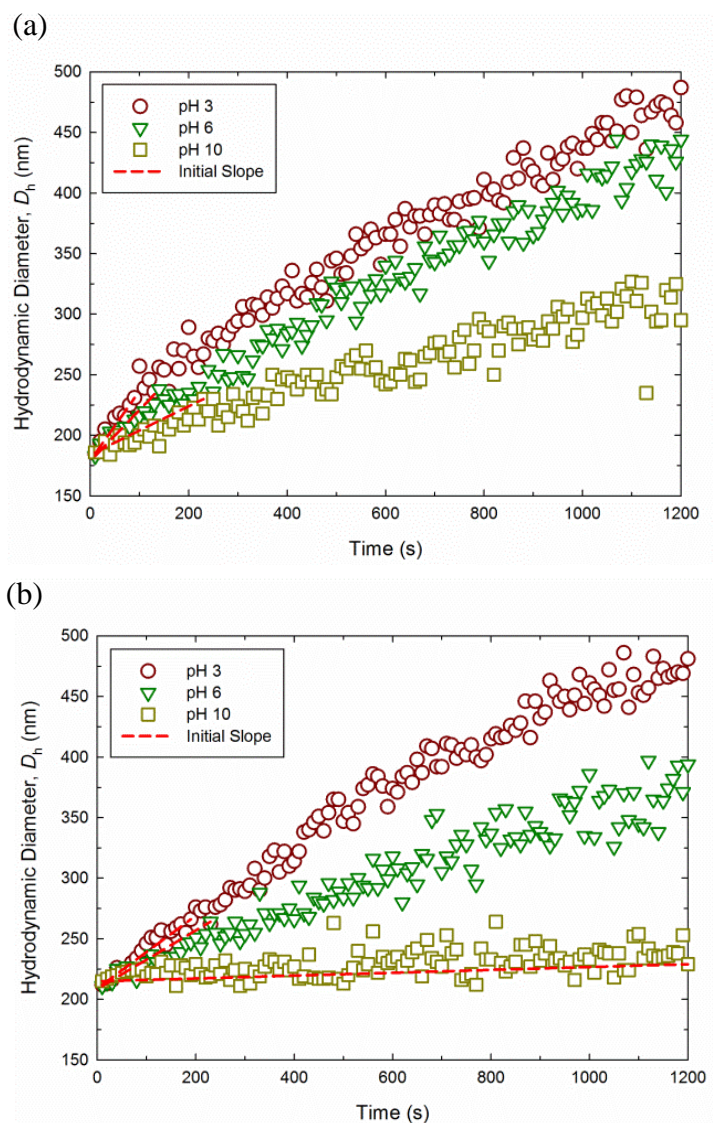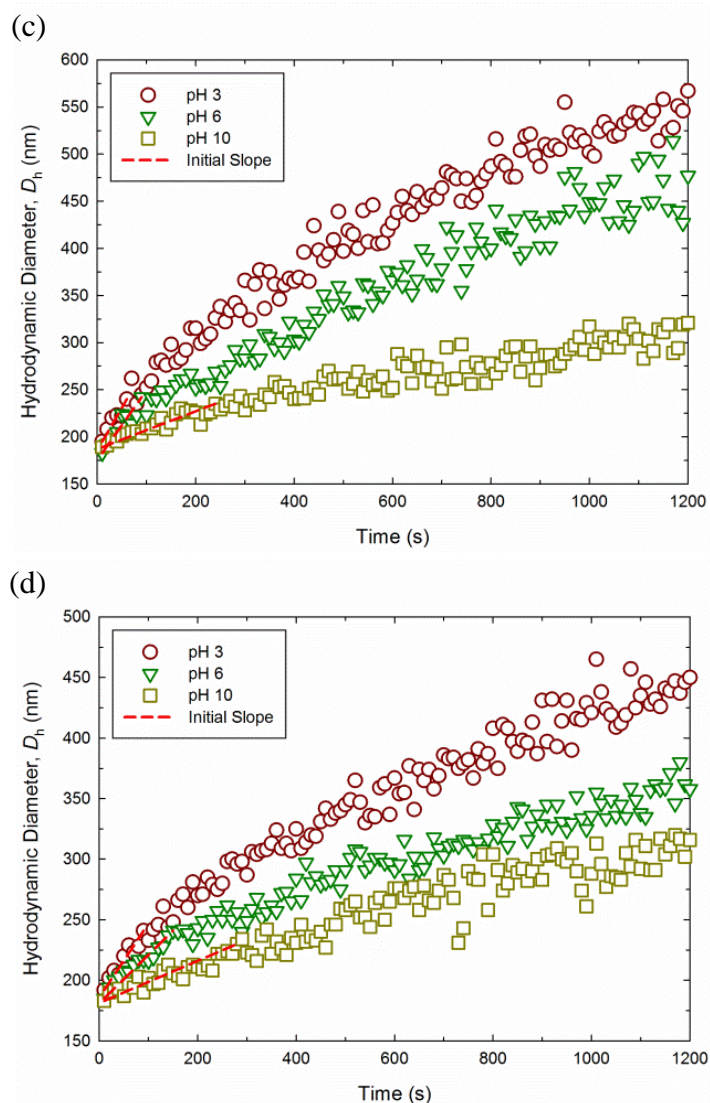
Figure 2.15 Aggregation profiles of (a) NAC1, (b) NAC2, and (c) NAC3 in the presence of 90 mM NaCl, and (d) NAC4 in the presence of 45 mM NaCl at pH 3, 6, and 10 at 25 ℃. The aqueous NAC concentrations were 10 mg/L. The slopes of red dashed lines were determined as the initial aggregation rates, which decreased with increasing pH for all NACs.

2.4. Conclusions

The results of this study indicated that NACs may be very stable against aggregation in freshwater environments, but they likely aggregate and settle out in highly saline aquatic systems. Such high stability in low salinity water may make NAC an ideal engineered adsorbent for in situ remediation of contaminated groundwater systems where long-term suspension of introduced particulate agents is desired due to strong particle-particle interactions and very slow flow rates. In particular, NACs may be suited for in situ treatment of polluted groundwater of coastal regions where NAC particles could remain highly dispersed in the upstream of low salinity and aggregated in the downstream of high salinity. With the Hamaker constant reported here, the transport of the introduced NACs and the treatment efficiency could be quantified with established modeling approaches.

The strong colloidal stability observed for NACs also calls attention to their potential adverse environmental effects as an emerging nanosized pollutant. Increasing use of engineered NACs may cause spreading of these nanoparticles in aquatic environments, and the wide use of PAC materials for emergent water treatment may release a fraction of nano-sized PAC particles to the water. The fate and transport of these NACs in aquatic systems, especially in drinking water systems, should be further studied in order to assess their environmental and health risks.

2.5. Acknowledgements

3. CHAPTER III. APPLICATION OF NANOSIZED ACTIVATED CARBONS AS ADSORBENTS WITH STRONG COLLOIDAL STABILITY FOR GROUNDWATER REMEDIATION

Adsorption of 4-chlorophenol by nanomaterials: NACs (this study) vs. graphene and CNTs (reported)
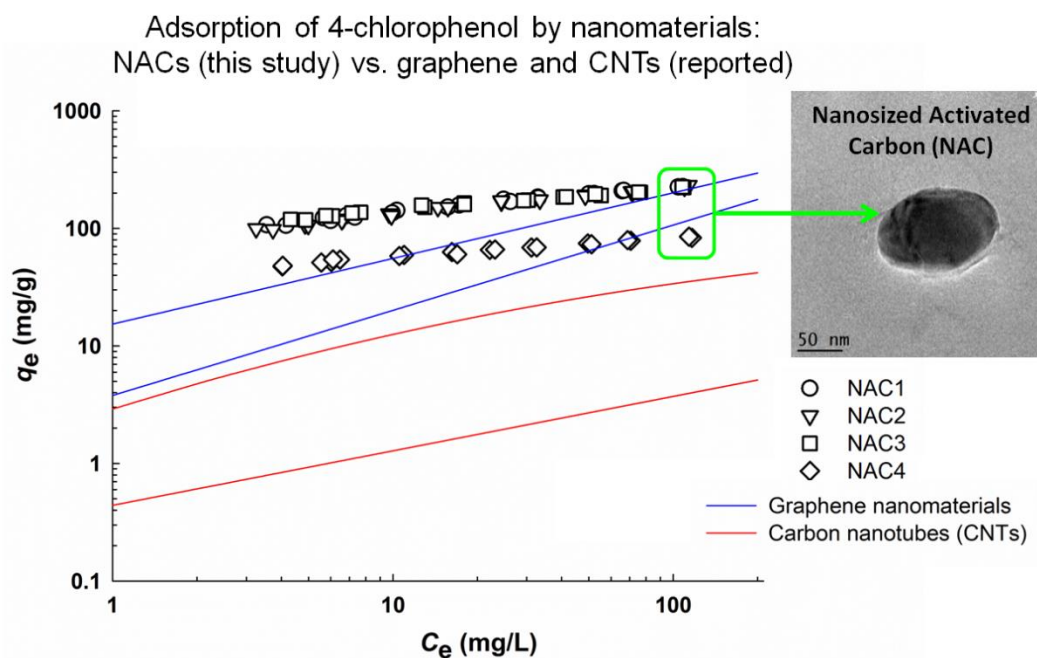
PROJECT TITLE: ADSORPTION OF 4-CHLOROPHENOL AND ANILINE BY NANOSIZED ACTIVATED CARBONS

The work in this chapter has been published in the title of "Adsorption of 4-Chlorophenol and Aniline by Nanosized Activated Carbons" in Chemical Engineering Journal, In Press, https://doi.org/10.1016/j.cej.2017.06.183.

Abstract

Reactive solids injected into aquifers for *in situ* groundwater remediation should possess both high mobility and great reactivity or adsorption for targeted contaminants.

We have shown in a prior study that nanosized activated carbons (NACs) had strong colloidal stability in aquatic environments. The present study investigated the adsorption behavior for the four NACs and two typical aromatic contaminants, 4-chlorophenol (4-CP) and aniline. The adsorption capacities measured for the NACs were compared with those reported for other nanosized adsorbents which were considered as potential candidates for groundwater remediation. Our results indicated that NACs had large specific surface areas (SSAs) and microporosities, and exhibited rapid rates of adsorption that could be quantified with both the pseudo-second-order rate equation and the intra-particle diffusion model. The adsorption equilibria were adequately described with the Freundlich isotherm equation, and hydrophobic interactions were likely the dominating mechanism for the adsorption. The adsorption processes were influenced by solution pH and temperature, whereas background electrolytes showed negligible effect. The tested NACs exhibited adsorption capacities 10-100 times greater for the respective adsorbates when compared to other carbonaceous nano-adsorbents such as carbon nanotubes (CNTs) and graphene derivatives. Such strong adsorbability, along with their high colloidal stability, makes NACs potentially suitable for remedy of aquifers contaminated with organic pollutants.

Keywords: NACs; nanosized carbonaceous adsorbents; aromatic contaminants; adsorption rate model; Freundlich equilibrium isotherm; groundwater remediation.

3.1. Introduction

Injecting strongly sorptive and/or reactive solids into aquifers is a widely used engineering scheme for *in situ* remedy of groundwater systems contaminated with toxic organic and inorganic chemicals [116]. The injected solids presumably not only are highly reactive, but also can remain suspended and can travel along with groundwater in polluted aquifers over long periods of operating time [58]. Searching for innovative nanomaterials that meet the two criteria has long remained a top priority in the field of groundwater remediation.

Manufactured carbonaceous nanomaterials have recently been considered as potential adsorbents for serving such remedial purposes because they have nano-structures, large specific surface areas (SSAs), controlled pore size distribution, and tunable surface chemistry, which overcome various intrinsic limitations of conventional carbonaceous adsorbents [117, 118]. Indeed, their high sorption capacities and more stable colloidal properties may be better suited for decontamination of groundwater systems. Prior studies have quantified and compared the aqueous adsorption of pollutant onto various carbonaceous nanomaterials, such as carbon nanotubes (CNTs) (single-walled, SWCNTs or multi-walled, MWCNTs), graphene and derivatives (graphene oxides, GO or reduced graphene oxides, RGO), fullerenes (C_{60}), and carbon nanospheres (CNS) [48, 118]. CNTs were shown to have more efficient adsorption of large size molecules due to their larger pore sizes compared to conventional activated carbons (ACs). However, due to their strong inter-particle interactions, pristine CNTs are prone to aggregation, forming settleable aggregates in aqueous solutions, which significantly reduces both the SSA available for pollutant adsorption and their mobility in porous media [119]. Surface functionalization of CNTs may alleviate their aggregation in water, but can lower their

adsorption capacity for organic pollutants. For instance, the adsorption capacities of MWCNTs for synthetic organic compounds were reduced by 25-30% after surface functionalization [56]. With different structures and functional groups, two-dimensional graphene and its derivatives such as GO have adsorption capacities comparable to CNTs for both organic compounds and heavy metals, and are also more stable against aggregation compared to CNTs [116]. However, the reported toxicity and high costs of CNTs and GO nanomaterials are the major roadblocks preventing their potential application as adsorbents in water treatment [116, 117]. Other manufactured carbonaceous nano-adsorbents, such as fullerene and CNS, have low SSAs of 0.07-10 [48] and 1.2-100 m^2/g [120], respectively, and thus exhibit much lower adsorption capacities compared to AC materials with large SSAs. For example, the adsorption capacity for naphthalene by fullerene was about 1000-fold lower than ACs [121].

Conventional AC materials are among the best adsorbents for water treatment due to their high adsorption capacities for a broad spectrum of pollutants, well understood adsorption mechanisms, and high cost-effectiveness [122]. Powdered activated carbon (PAC) materials with particle sizes ranging from a few to 40 μm are known as strong sorbents for various contaminants, but they could be readily immobilized in aquifer due to filtration mechanisms. They are apparently not ideal reactive solids for *in situ* groundwater remediation. Two prior studies proposed to utilize AC suspensions having particle sizes of 800 nm as a stable mobile adsorbent that could be injected into contaminated aquifers [123, 124]. Nanosized activated carbons (NACs) with properties and adsorbability likely similar to conventional ACs may be better candidates. Meanwhile, NACs may have no obvious toxicity or adverse effect as revealed by clinical

and biological studies using NACs as drug carriers and as disease tracers during surgery treatments [125-128]. However, few studies have examined their adsorption properties for organic (e.g., methyl orange dye [129] and organophosphorus malathion pesticide [130]) and inorganic pollutants (e.g., arsenic [131] and copper [132]) from aqueous solutions.

The goal of this study was to quantify the adsorption properties for four NACs in an effort to assess their applicability in groundwater remediation. In a prior study [133], we found that NACs have high colloidal stability against aggregation under typical freshwater chemistry conditions. Herein, the four types of NACs investigated in that prior study were chosen to investigate their adsorption behavior for two aromatic pollutants, 4-chlorophenol (4-CP) and aniline, in aqueous solutions. These two target pollutants were chosen because chlorophenols and anilines are toxic, carcinogenic, and environmentally related contaminants commonly found in groundwater [50, 134-137]. The results showed that their adsorption capacities were one or two orders of magnitude greater when compared with other nanosized adsorbents that were considered in prior studies as potential active reagents. The strong adsorption, along with high colloidal stability, makes NACs better candidates for remedy of contaminated groundwater systems.

3.2. Materials and Methods

3.2.1. Adsorbents

The four NACs purchased from US Research Nanomaterials, Inc. (Houston, TX) were assigned as NAC1, NAC2, NAC3, and NAC4, which were the same nanomaterials

investigated in our prior study [133]. According to the supplier, the four NACs were produced from a selection of different plant materials (Table 3.1) through carbonization, activation, grinding, and classification. For better comparison with the four NACs, a commercial Hydrodarco©C PAC produced via steam activation of lignite coal was also obtained from Norit Americas Inc. (Marshall, TX) and used as the fifth adsorbent. These five AC adsorbents were stored in a desiccator prior to use.

3.2.2.   *Characterization of Adsorbents*

The porous structures of the adsorbents were characterized using the methods of N_2 gas adsorption-desorption isotherms obtained at 77 K on a Micromeritics TriStar II 3020 instrument (Micromeritics Instrument Corp., Norcross, GA), yielding results of the SSA and the pore distribution using the Brunauer-Emmett-Teller (BET) and Barrett–Joyner–Halenda (BJH) methods, respectively. The size and morphology of the adsorbents were examined on a scanning electron microscope (SEM) (MERLIN, Zeiss, Oberkochen, Germany) and on a transmission electron microscope (TEM) (Topcon 002B, Topcon Corp., Tokyo, Japan) operating at 200 kV. The hydrodynamic sizes of NACs were measured in water by dynamic light scattering (DLS) using a Malvern Zetasizer Nano ZS instrument (Malvern Instruments, Worcestershire, UK).

3.2.3.   *Chemicals and Solutions*

Aniline (ACS grade, +99%) and 4-CP (+99%) were purchased from Sigma-Aldrich Chemical Co. (St. Louis, MO) and Alfa Aesar (Ward Hill, MA), respectively, as the target pollutants. The selected physicochemical properties of the adsorbate chemicals are presented in Table 3.2. Calcium chloride, sodium azide, acetic acid, hydrochloric acid, and sodium hydroxide of ACS grade were obtained from Sigma-Aldrich Chemical Co. (St. Louis, MO). Methanol and acetonitrile of HPLC grade were purchased from Honeywell International, Inc. (Morris Plains, NJ) and EMD Millipore (Billerica, MA), respectively.

Stock solutions of the adsorbates at 1000 mg/L were prepared by dissolving their pure liquids in background solution containing 10 mM $CaCl_2$ in Milli-Q water (resistivity of 18.2 MΩ·cm) with 200 mg/L sodium azide (NaN_3) as a biocide. All working solutions of desired solute concentrations were prepared by successive dilution of respective stock solutions with the background solution. Most solutions used in adsorption experiments were adjusted to pH 7.0 using HCl (1 M) or NaOH (1 M) to ensure 4-CP and aniline remained in their protonated forms. A neutral solution pH facilitates the adsorption performance of aniline and 4-CP on various ACs [138, 139] and enables comparison of the adsorption behavior of 4-CP and aniline onto the tested AC materials with other reported adsorbents in the literature.

3.2.4. Adsorption Rates

Batch experiments were conducted for quantifying adsorption rates and the times required to reach adsorption equilibria for 4-CP or aniline by each adsorbent. Erlenmeyer

flasks (500 mL) sealed with PTFE-lined cap were used as the completely mixed batch reactors (CMBRs), which contained 500 mL of initial aqueous solution of 100 mg/L 4-CP or aniline with pH adjusted to 7. At time 0, a predetermined amount of pre-wetted adsorbent was added to the reactor in order to achieve approximately 80% reduction of the target adsorbate from aqueous solution at equilibrium (i.e., $C_e = 0.2\ C_o$; here C_o and C_e are designated as the initial and equilibrium aqueous concentrations of the adsorbate, respectively). The mixtures were immediately agitated on a thermostated shaker (VWR Orbital Shaking Incubator 1575, VWR International, Radnor, PA) at 150 rpm and at $25 \pm 1\ °C$. For each adsorbent-adsorbate system, duplicate reactors and a control reactor without adsorbent were set up and were run simultaneously to ensure data quality. At a designated time, an aliquot of suspension was withdrawn at predesigned time intervals from each reactor, filtered and analyzed for the residual adsorbate concentrations as described later in this paper.

3.2.5. Adsorption Equilibrium Tests

Adsorption isotherms were measured using amber glass bottles (50 mL) with PTFE-lined screw caps (Qorpak, Bridgeville, PA) as the CMBR systems for the five AC adsorbents and the two adsorbates at pH 7. A preliminary test was performed to determine appropriate adsorbent-to-solution ratios for each adsorbent-adsorbate system that allowed reduction of C_o by approximately 50% after attainment of adsorption equilibrium. The final isotherm data were collected using a total of 30 50-mL CMBRs and at 10 different C_o levels. At each C_o level, two CMBRs with adsorbent materials

were set up identically as duplicates and a third CMBR containing no adsorbent was used

the control. The adsorbent dosage, ranging from 0.034 to 1.7 g/L for adsorption of 4-CP

and from 0.085 to 2.3 g/L for adsorption of aniline by different adsorbents, were

weighted using an ultramicro-balance (Sartorius M2P, Goettingen, Germany). The

CMBRs were mixed on a thermostated shaker at 150 rpm and at controlled temperature

(25 ± 1 °C). After mixed for approximately 14 days, aqueous suspension was sampled

from each CMBR, filtered, and analyzed for the C_e using the method described below.

Batch experiments were also conducted to quantify the factors including solution

background electrolytes, pH, and temperature that may affect the adsorption equilibria.

The experiments on pH and temperature effects were run using the above background

solution with pH adjusted to the desired level with NaOH or HCl whereas the

experiments on background electrolyte effect had NaCl or $CaCl_2$ at desired concentration

levels.

3.2.6. Chemical Analysis

To analyze the aqueous solute concentrations, samples were taken from the

supernatant and filtered using a 5-mL glass syringe (Poulten and Graf Fortuna, Air-Tite

Products Co., Inc., Virginia Beach, VA) with a 0.20 μm PTFE syringe filter (Thermo

Scientific, Waltham, MA), and the filtrates were analyzed to determine the residual solute

concentrations. Preliminary experiment showed less than 2% loss of the adsorbates after

the filtration process. Both 4-CP and aniline aqueous concentrations were quantified with

a reversed phase high performance liquid chromatography (HPLC) (Agilent 1100, Santa

Clara, CA) equipped with a diode array UV detector and with a Luna® 5 μm C18(2) 100

Å (250 $\times$ 2.00 mm) LC column (Phenomenex, Torrance, CA). For the analysis of 4-CP, a

mixture of water + methanol + acetic acid at 15:80:5% (v/v/v) was used as the mobile

phase at a flow rate of 0.330 mL/min and the UV detector was set at wavelength of 280

nm. For the analysis of aniline, a mixture of water + acetonitrile at 45:55% (v/v) was used

as the mobile phase at a flow rate at 0.330 mL/min, and the UV detector was set at

wavelength of 244 nm. The aqueous-phase solute concentrations were quantified using

calibration curves of absorbance area versus known concentrations of 4-CP or aniline.

The calibration curves exhibited linear variation ($R^2 > 0.99$) for concentrations from 1

mg/L to 250 mg/L. The solid-phase solute concentrations (q_e) were computed based on

the mass balance of the solute between the solid and aqueous phases. The control

experiments showed that average system losses were consistently less than 4% of initial

aqueous-phase concentrations for both sorbates. Hence, no correction was made during

reduction of the adsorption data.

3.3. Results and Discussion

3.3.1. Adsorbent Characterization

3.3.1.1. Physiochemical Properties

The TEM (Figure 3.1) and SEM (Figure 3.2) images show that the four NACs were

roughly spherical nanoparticles with diameters from 50 to 200 nm, which was attributed

to the arbitrary grinding process during manufacturing. The size distributions determined

for NACs in water by DLS (Figure 3.1e) indicated that their hydrodynamic diameters

(D_h) were approximately 200 nm, while the number-weighted average diameters (D_n) were ~100 nm (Table 3.1). Our previous study [133] demonstrated that D_n of ~100 nm were indeed more appropriate than D_h of ~200 nm for representing the actual particle sizes of all NACs. This is because DLS often overestimates particle sizes, especially for polydispersed particles, as larger particles may scatter more light [93]. So the studied NACs are nanoparticles by the size-definition. Typical PAC particles are observed in Figure 3.1f with sizes <45 μm, which were much larger than the NACs.

The elemental compositions of NACs presented in Table 3.3 indicate high oxygen content of ~10%, which were primarily identified as hydroxyl and carboxyl functional groups by Fourier transform infrared (FTIR) analysis (Figure 3.3). The deprotonation of these acidic functional groups from NACs in water were responsible for their observed negatively charged surfaces and strong colloidal stability (Table 3.1) [133]. As a result, NACs were more stable against aggregation and sedimentation compared to other nanomaterials proposed for potential water remediation (Figure 3.4, Figure 3.5, and Table 3.4). These chemical properties of NACs were also important for their adsorption of 4-CP and aniline, which will be discussed later in this paper.
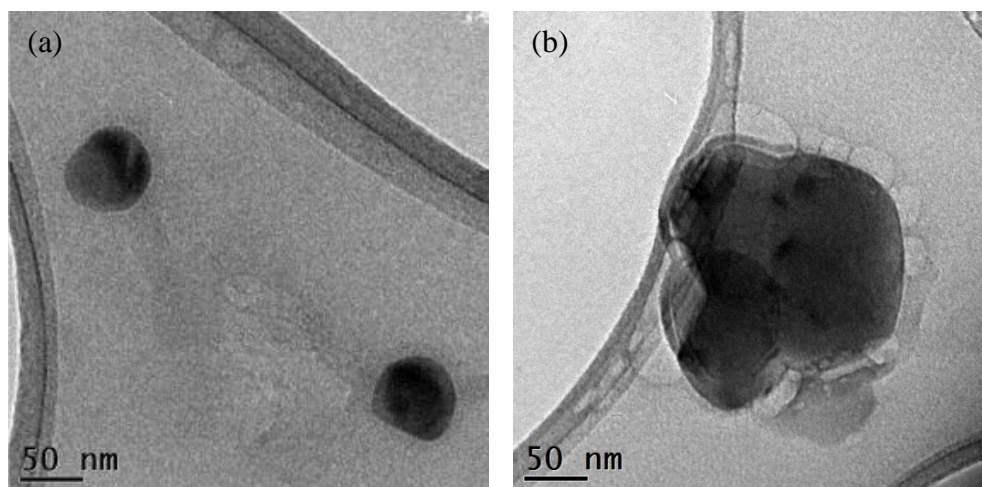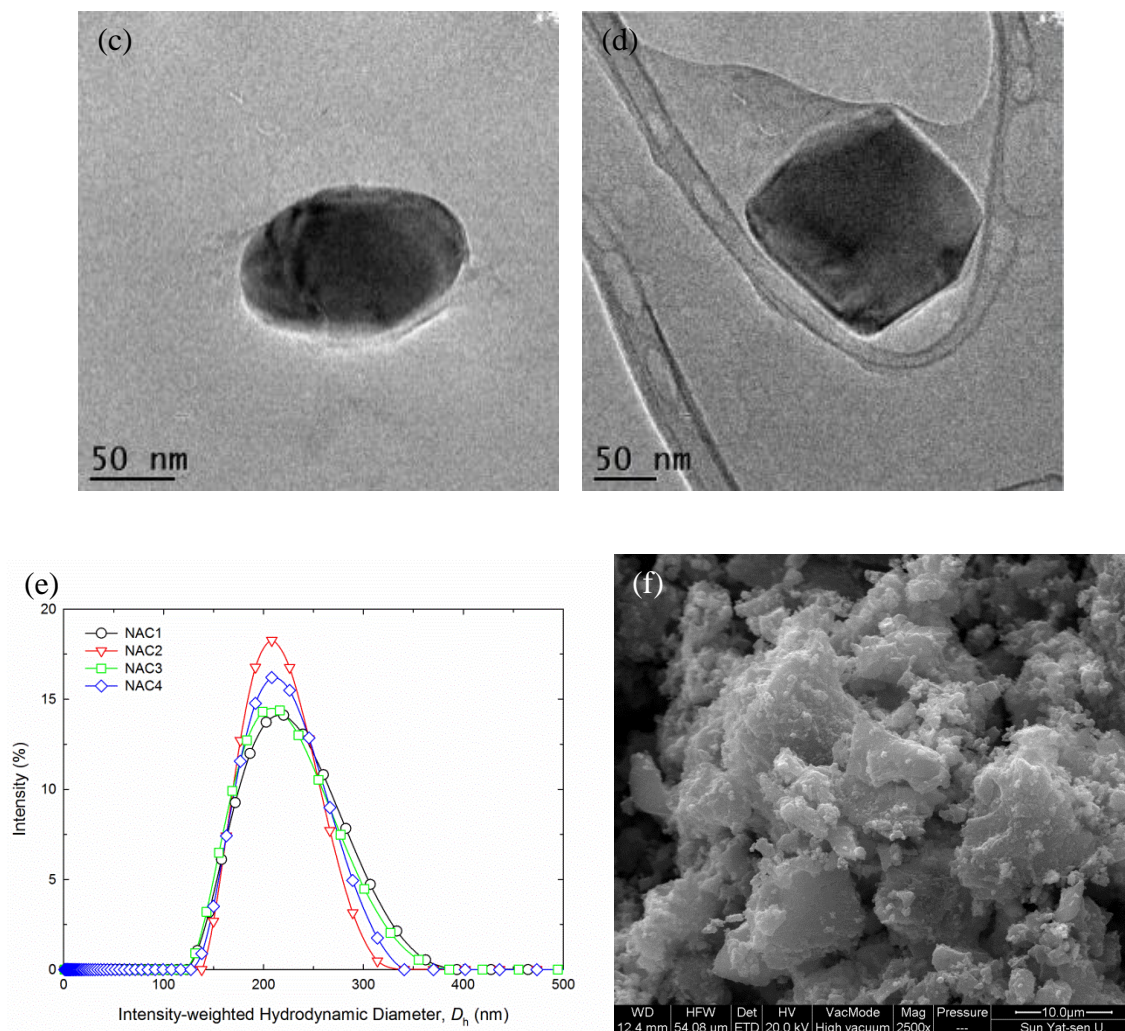
Figure 3.1 Transmission electron microscope (TEM) images for (a) NAC1, (b) NAC2, (c) NAC3, and (d) NAC 4; (e) size distributions for nanosized activated carbons (NACs) determined by dynamic light scattering (DLS); (f) scanning electron microscope (SEM) image for powdered activated carbon (PAC).
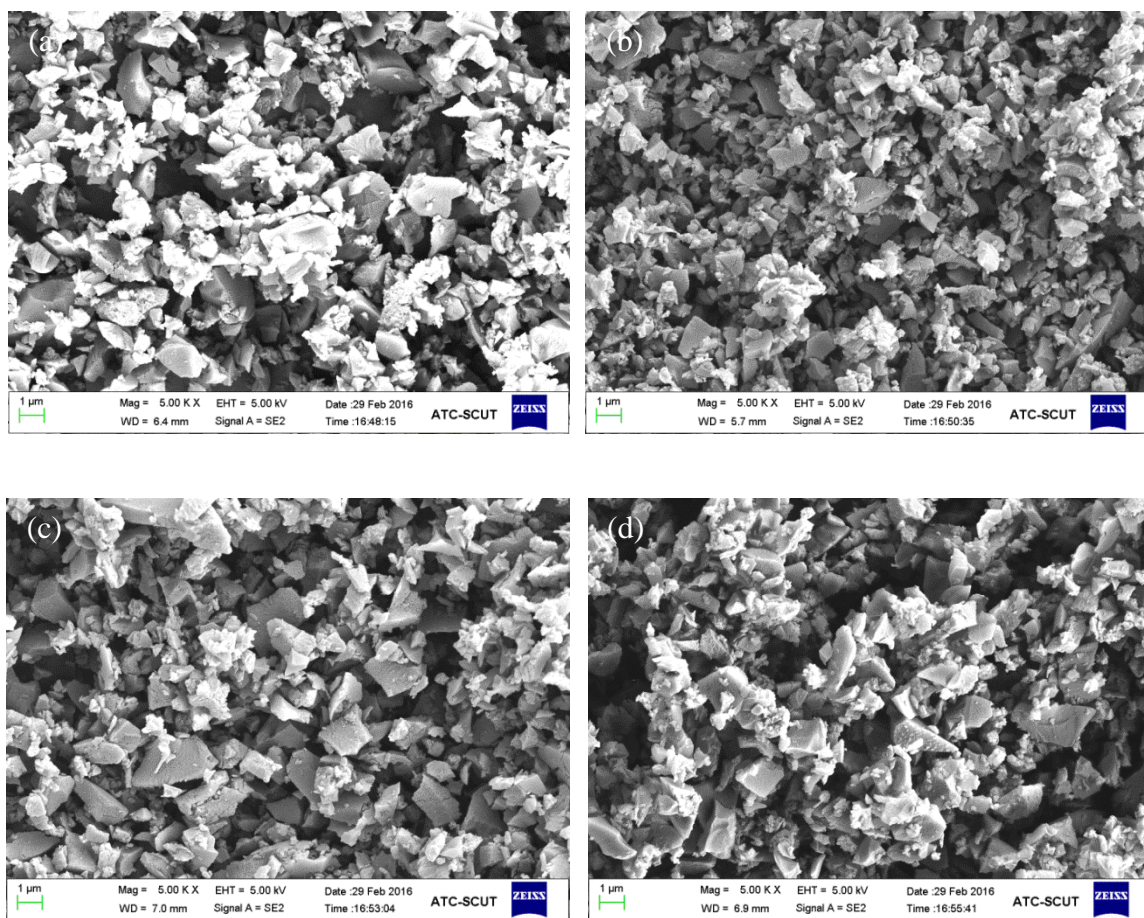
Figure 3.2 Representative SEM images of (a) NAC1, (b) NAC2, (c) NAC3, and (d) NAC4 original samples as received from the manufacturer. The images were acquired by a MERLIN SEM instrument (Zeiss, Oberkochen, Germany).

Table 3.1 Physicochemical properties of NACs and PAC adsorbents.

Adsorbent	General properties				Pore structure[d]						Colloidal stability[e]	
	Raw material[a]	Density[a] (g/cm^3)	Particle size		SSA (m^2/g)	A_{micro} (m^2/g)	D_{pore} (Å)	V_{micro} (cm^3/g)	V_{meso} (cm^3/g)	V_{total} (cm^3/g)	ζ potential (mV)	CCC (mM NaCl)
			D_h^{b} (nm)	D_n^{c} (nm)								
NAC1	bamboo and trees	0.32	221	113	909	874	18.1	0.307	0.145	0.482	-44	69
NAC2	bamboo and trees	0.34	212	133	879	869	18.0	0.305	0.110	0.448	-46	76
NAC3	coconut shell charcoal	0.28	223	108	933	868	18.1	0.303	0.132	0.473	-43	66
NAC4	bamboo charcoal	0.30	215	115	307	146	23.2	0.050	0.056	0.180	-31	42
PAC	lignite coal	0.64	65% min. < 45 μm (325US mesh)[a]		588	305	38.7	0.118	0.526	0.596		

[a] From the supplier.

[b] Intensity-weighted hydrodynamic diameter (D_h) determined by DLS.
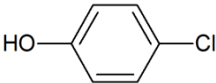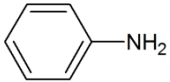
[c] Number-weighted average diameter (D_n) determined by DLS.

[d] Specific surface area (SSA) was determined with nitrogen by multi-point Brunauer-Emmett-Teller (BET) method. Micropore surface area (A_{micro}), average pore diameter (D_{pore}), mesopore volume (V_{meso}), and micropore volume (V_{micro}) were determined by Barrett–Joyner–Halenda (BJH) desorption method. The pores were divided into micropores ($D_{pore} < 2$ nm) and mesopores ($2 < D_{pore} < 50$ nm). Single point total pore volume (V_{total}) was measured at relative pressure of 0.995.

[e] Data from [133]. Data were obtained under neutral pH conditions. The zeta (ζ) potentials were measured in the presence of 1 mM NaCl. The more negative ζ potentials and the higher critical coagulation concentrations (CCC) for NACs compared to those reported for other nanosized adsorbents (Table 3.4) indicate the higher colloidal stability of NACs against aggregation and sedimentation.

Table 3.2 Chemical structures and selected properties of the adsorbates[a].

Adsorbate	Structure[b]	S^c (mg/L)	ρ^d (g/cm^3)	$M_W{}^b$ (g/mol)	$M_V{}^b$ (cm^3/mol)	$D_m{}^b$ (Å)	$A_m{}^e$ (Å^2)	$\log K_{ow}{}^f$	$pK_a{}^c$	π^{*c}	$\beta_m{}^c$	$\alpha_m{}^c$
4-CP	HO—⬡—Cl	26300	1.306	128.56	99.8	6.42	36.14	2.16	9.38	0.72	0.23	0.67
Aniline	⬡—NH$_2$	34160	1.0217	93.13	91.7	5.89	34.34	1.08	4.60	0.73	0.5	0.16

[a] 4-CP: 4-chlorophenol; S: water solubility; ρ: density; M_W: molecular weight; M_V: molecular volume; D_m: molecular diameter; A_m: projecting area of a single adsorbate molecule; $\log K_{ow}$: logarithmic octanol-water partition coefficient; pK_a: acid dissociation constant. π^*: polarity/polarizability parameter; β_m: hydrogen-bonding acceptor parameter; α_m: hydrogen-bonding donor parameter.

[b] Advanced Chemistry Development-ACDLabs 12.01 software, Toronto, Canada.

[c] Data from [50].

[d] Data from the supplier.

^{e} Data estimated by $\pi \times (3M_{W}/(4\pi \times \rho \times N))^{2/3}$, where N is the Avogadro constant.

^{f} Data from [140].

Table 3.3 Elemental compositions of NACs.[a]

Adsorbent	EDX[b] (weight %)							XPS[c] (atomic %)		EA[d] (weight %)			
	C	O	Al	Si	K	Ca	Fe	C	O	C	O	H	Others
NAC1	85.86	11.77		0.92	0.47	0.57	0.42	93.22	6.78	74.8	11.4	3.7	10.1
NAC2	87.21	11.84		0.23	0.44	0.27		93.39	6.61	79.5	11.7	2.51	6.3
NAC3	88.77	9.38		0.46	1.39			93.38	6.62	79.9	11.6	2.66	5.8
NAC4	87.65	9.28	0.27	0.62	0.62	1.28	0.27	91.11	8.89	78.6	9.83	2.27	9.3

[a] Data from [133].

[b] Energy dispersive X-ray (EDX) determined by scanning electron microscope (SEM) equipped with EDX (MERLIN, Zeiss, Oberkochen, Germany).

[c] X-ray photoelectron spectroscopy (XPS) determined by Thermo Fisher K-Alpha (Thermo Fisher Scientific, Waltham, MA).

[d] Elemental analysis (EA) determined by Vario EL III Element Analyzer (Elementar Americas Inc., Mt Laurel, NJ).

Table 3.4 Physicochemical properties of other reported nanosized carbonaceous adsorbents.[a]

| Adsorbent | Particle size | Pore structure | | | | | | Colloidal stability[d] | | Reference |
		SSA (m²/g)	A_{micro} (m²/g)	D_{pore} (Å)	V_{micro} (cm³/g)	V_{meso} (cm³/g)	V_{total} (cm³/g)	ζ potential (mV)	CCC (mM NaCl)	
MWCNTs[b]	60-100 nm (diameter), 5-15 μm (length)[c]	43	11.8	73.7	0.004	0.096	0.115	-30[d]	25[e]	This study
Graphene oxide (GO)	~400 nm (D_h)	939		31.58				-45	44	
Reduced graphene oxide (RGO)	~1500 nm (D_h)	974		18.51				-20		[42, 141, 142]
Fullerene	~1.0 nm (outer diameter)	7.21			0.0022			-40	120	[38, 48]

[a] SSA: specific surface area; A_{micro}: micropore surface area; D_{pore}: average pore diameter; V_{meso}: mesopore volume; V_{micro}: micropore volume; V_{total}: single point total pore volume; ζ potential: zeta potential; CCC: critical coagulation concentration.

[b] This sample was obtained from TCI America, which was characterized for its pore structure along with the NACs and PAC samples in this study for comparison.

[c] From the supplier.

[d] Reported data were measured at neutral pH solution conditions.

[e] Data from [143].
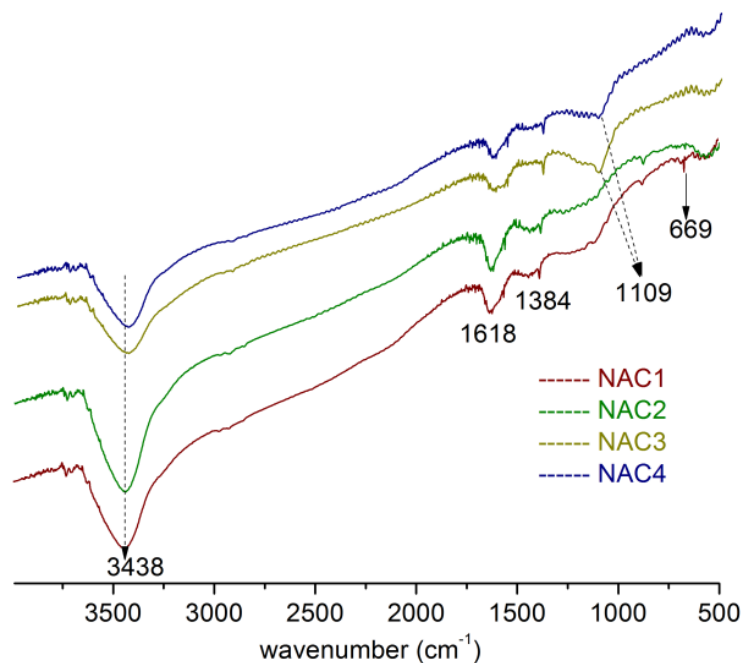
Figure 3.3 Fourier transform infrared (FTIR) spectra of the four NACs (Data from [133]).
The original samples as received from the manufacturer were analyzed using a FTIR
spectrometer (Bruker Vector 33, Germany). The FTIR spectra of the four NACs had very
similar oxygen functional groups, such as hydroxyl (3438 cm^{-1}), carbonyl (1618 cm^{-1}),
and carboxyl (1384 cm^{-1}) groups, which are typical for activated carbons [133].
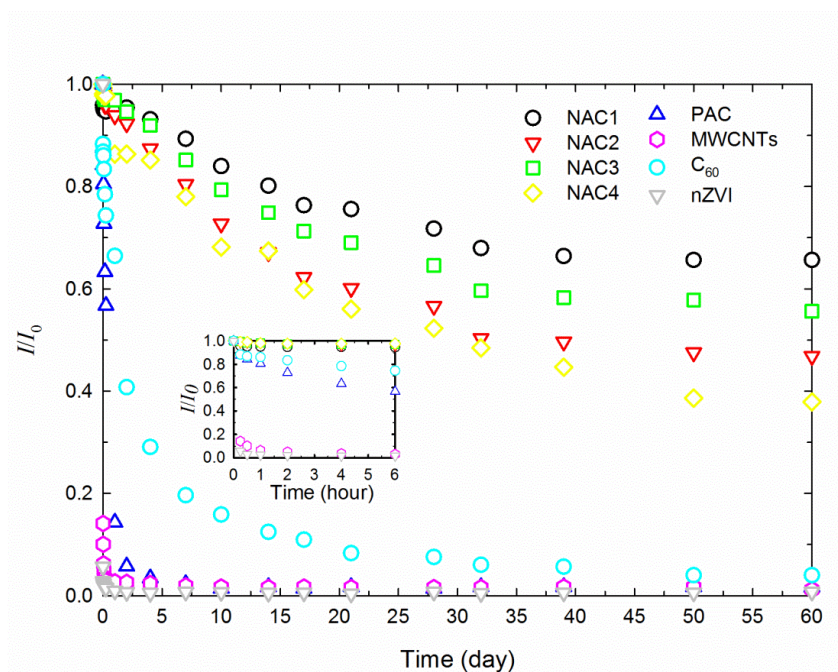
Figure 3.4 Comparison of sedimentation rates of NACs with other potential water treatment agents by light absorption. Experiments were conducted in Milli-Q water at pH 7 and the light absorption of suspensions was measured periodically over 6 hours (inset) and 2 months with a Spectronic 200 spectrophotometer (Thermo Scientific, Waltham, MA). The compared materials are commonly proposed for use in water remediation [57, 144, 145], including the powdered activated carbon (PAC) characterized for adsorption study in this paper as well as the multi-walled carbon nanotubes (MWCNTs), fullerene nanoparticles (C_{60}), and nano zerovelent iron (nZVI) obtained from TCI America for comparison. The pristine samples introduced into Milli-Q water were dispersed prior to experiment. The portion of particles remaining suspended in water over time were quantified by the ratio of light absorption at time t (I) over the light absorption at time 0 (I_o). It shows that NACs compared to other materials should be more stable and thus mobile in water, which is desired for remediation purpose.
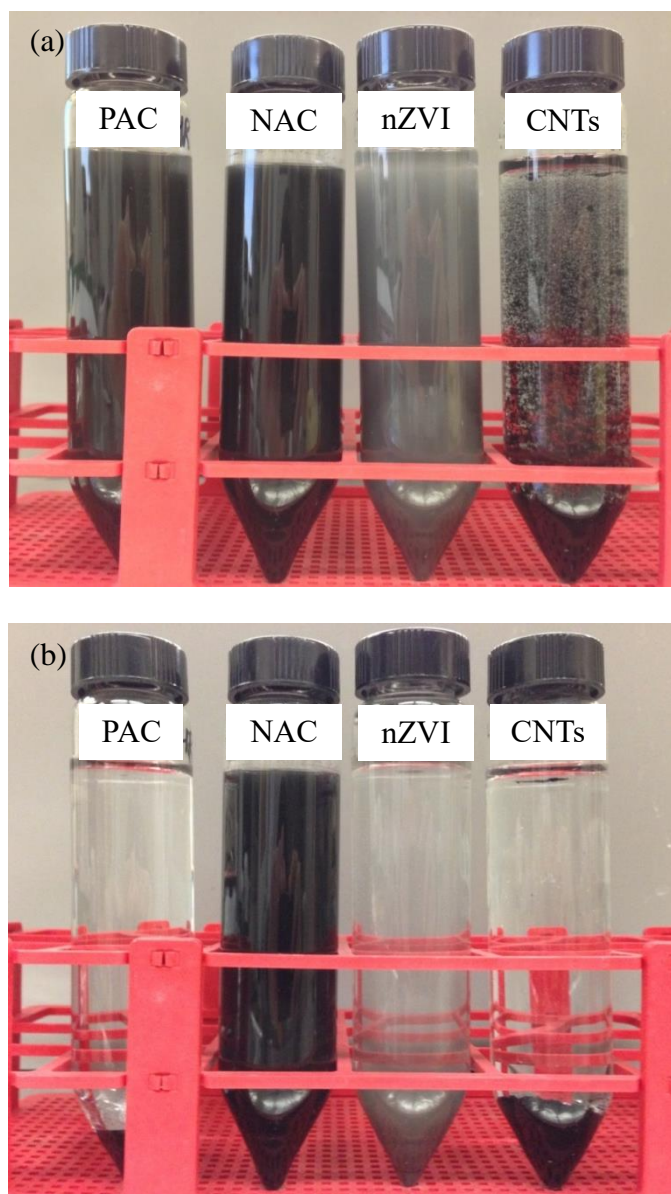
Figure 3.5 Comparison of sedimentation rates of NACs with other potential water treatment agents by visual observation. Experiments were conducted in Milli-Q water at pH 7 and photos were taken (a) on day 1 and (b) after 2 months. The compared materials are widely proposed or used for water remediation processes, including the PAC characterized for adsorption study in this paper as well as the carbon nanotubes (CNTs) and nZVI obtained from TCI America for comparison. The pristine samples introduced into Milli-Q water were dispersed prior to experiment. It shows that NACs have strong

stability against sedimentation.

3.3.1.2. *Pore Structures*

The pore structures were characterized for NACs and PAC (Table 3.1, Figure 3.6, and Figure 3.7), and the results were compared with literature data for other carbonaceous adsorbents, such as GO, RGO, and fullerene (Table 3.4). In general, similar pore structures were observed for NAC1, NAC2, and NAC3, which had smaller pore diameters and larger SSAs than NAC4. The first three NACs had the largest overall SSAs (~900 m^2/g) and micropore-based SSAs (~870 m^2/g) and the smallest pore diameters (18 Å) compared to other carbonaceous adsorbents. The SSA values for NAC1, NAC2, and NAC3 were similar to GO and RGO, twice as large as PAC, and two orders of magnitude higher than fullerene. Pore size distribution analyses presented in Table 3.1 and Figure 3.6 indicate that the first three NACs had dominantly micropores (<2 nm), with microporous volume constituting 65% of the total volumes. In comparison, NAC4 had evenly distributed micropores and mesopores (2-50 nm), and PAC was dominated by mesopores. The average pore sizes (D_{pore}) for NACs were about half of PAC and were similar to RGO. Since micropores have higher surface-area-to-volume ratio than mesopores and macropores, the first three NACs exhibited larger SSA values than PAC.
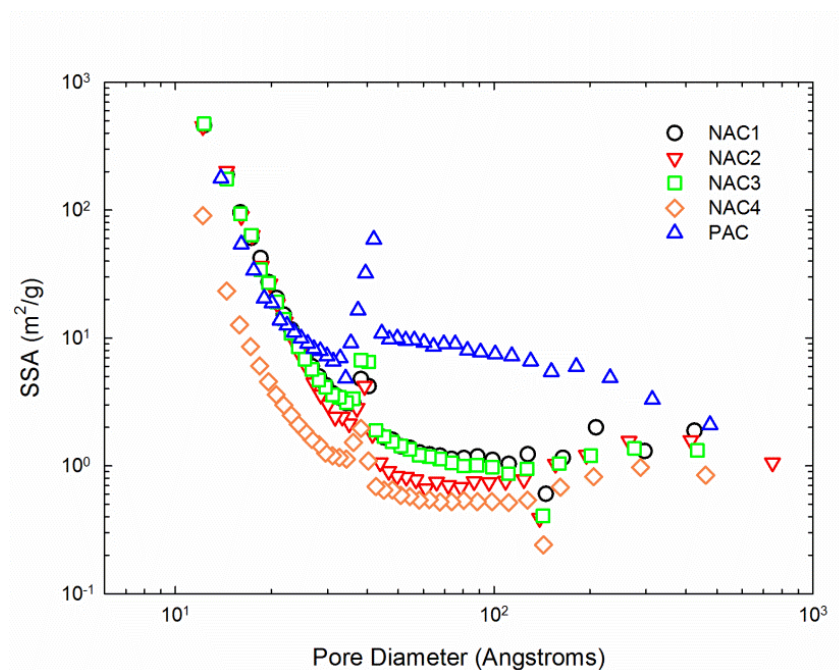
Figure 3.6 Pore size distributions for NACs and PAC.

Figure 3.7 shows that all adsorbents tested in this study exhibited adsorption hysteresis, which was generally associated with capillary condensation in mesopore structures. The N_2 adsorption isotherms obtained for the AC materials could be classified as type IV isotherms with H4 type hysteresis loops [146], which are characteristics of AC materials with two-dimensional slit pores and three-dimensional cross-linked spaces [147]. The first three NACs similarly exhibited slight hysteresis, whereas NAC4 showed apparent desorption hysteresis at low relative pressure, which was likely due to the swelling of a non-rigid porous structure [146]. The wide hysteresis loop observed for PAC could be explained by the presence of relatively more complex pore network with longer paths, which retarded N_2 desorption rate if the only exit was through a narrow channel [148]. A common hysteresis feature for AC materials was observed for the first

three NACs and PAC, where the lower closure points of desorption branch joining the adsorption branch were located at p/p° ~0.42 for N_2 at 77 K [146].

(a)

(b)
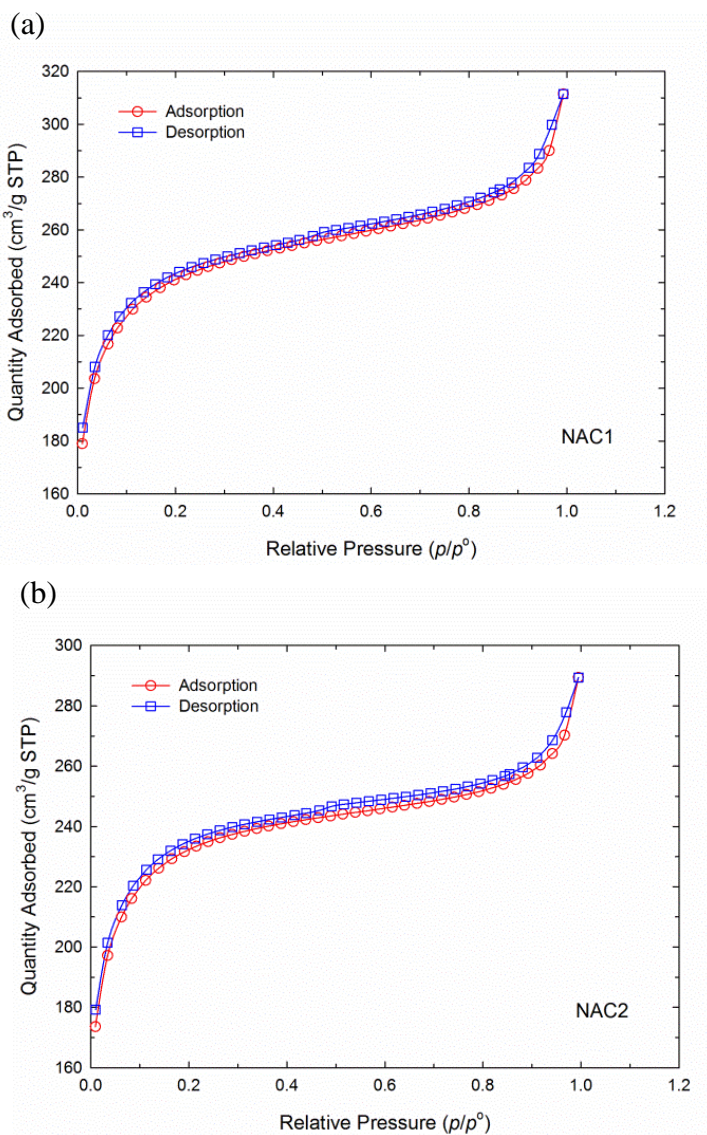
(c)
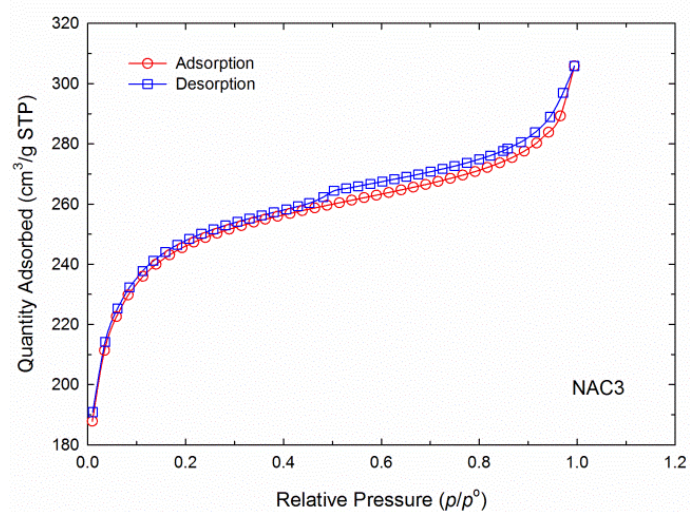
(d)
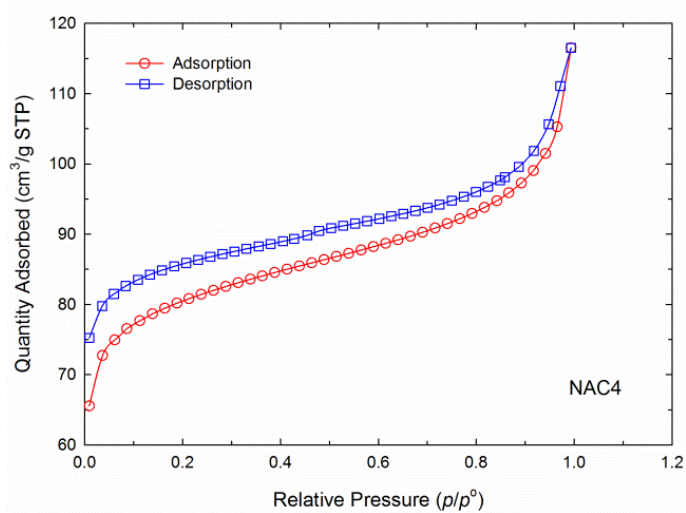
(e)
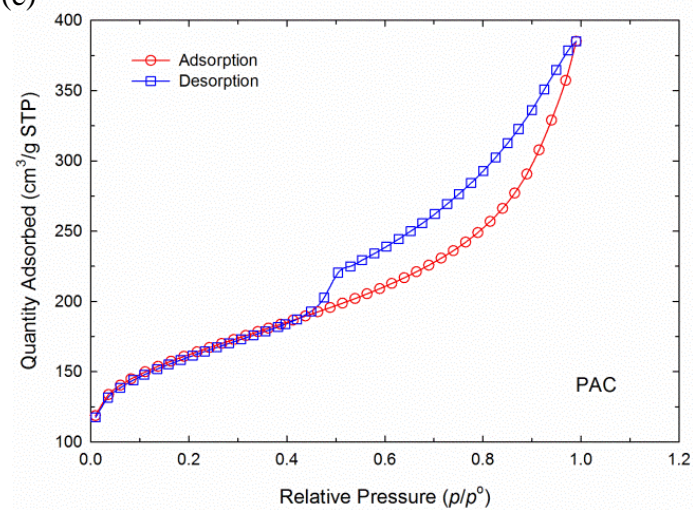
Figure 3.7 Nitrogen adsorption-desorption isotherms at 77 K by NACs and PAC.

3.3.2. Adsorption Rates

3.3.2.1. Overall Rates

Figure 3.8 presents the uptake percentages of the adsorbate as a function of the contact time for the ten adsorbent-adsorbate systems, which showed very rapid adsorption rates as expected. For example, within the first 3 minutes, 53% of 4-CP and 66% of aniline were adsorbed by NAC2 from aqueous solution, and 71% removal of 4-CP and 70% removal of aniline were achieved after only 15 minutes. Figure 3.8 also shows that, after an initial fast adsorption phase, the rates became relatively slower to approach apparent equilibria as 30 and 45 minutes were needed for aniline and 4-CP, respectively, to achieve the maximal 80% uptake by NAC2.

The rate phenomena observed for the ten adsorbent-adsorbate systems appeared to be slightly different. For a given adsorbent, aniline exhibited faster rates of adsorption than 4-CP likely due to the difference of molecular sizes between the two adsorbates (Table 3.2). For a given adsorbate, NAC4 had the slowest rate of adsorption among the five adsorbents whereas NAC1, NAC2, and NAC3 had slightly faster rates than PAC. Such slightly different rates among the five adsorbents may be correlated with their differences in physicochemical characteristics such as internal pore diameters and pore size distribution. Other factors such as temperature, solution pH, and mixing conditions that also influence the rate of adsorption may be identical for the tested systems as the CMBRs were run at similar conditions.

The NACs tested in this study had far faster rates of adsorption than conventional AC materials (e.g., PAC and GAC) due to their much smaller particle sizes. The adsorption rates onto the NACs were also similar or faster compared to CNTs and activated carbon fibers (ACFs), which have direct opening pore structures on the surface [119]. For instance, the reported equilibrium time for adsorption of phenolic compounds were 30 min by ACFs [149], 1 h by MWCNT polymers [150], 1-5 h by PAC and GAC [139], and 5 h by MWCNTs [151]. The reported equilibrium time for adsorption of aniline were 20 min to 3 h by MWCNTs [152, 153] and 5-20 h by PAC and GAC [139, 154]. The rapid adsorption on NACs suggested the high potential of these novel carbon nanomaterials for applications such as emergent water remediation agents for organic pollutants.

(a)

(b)
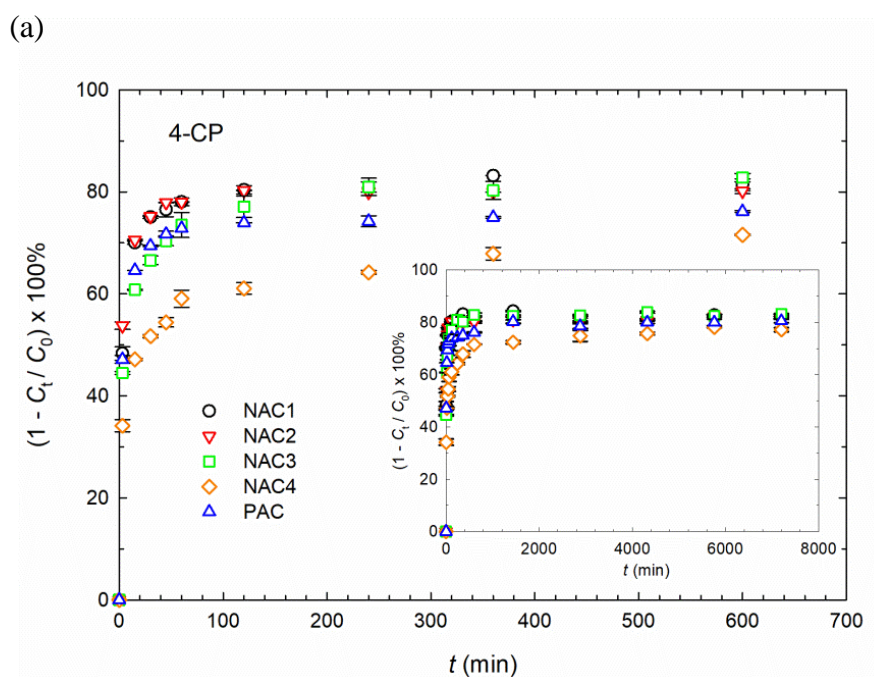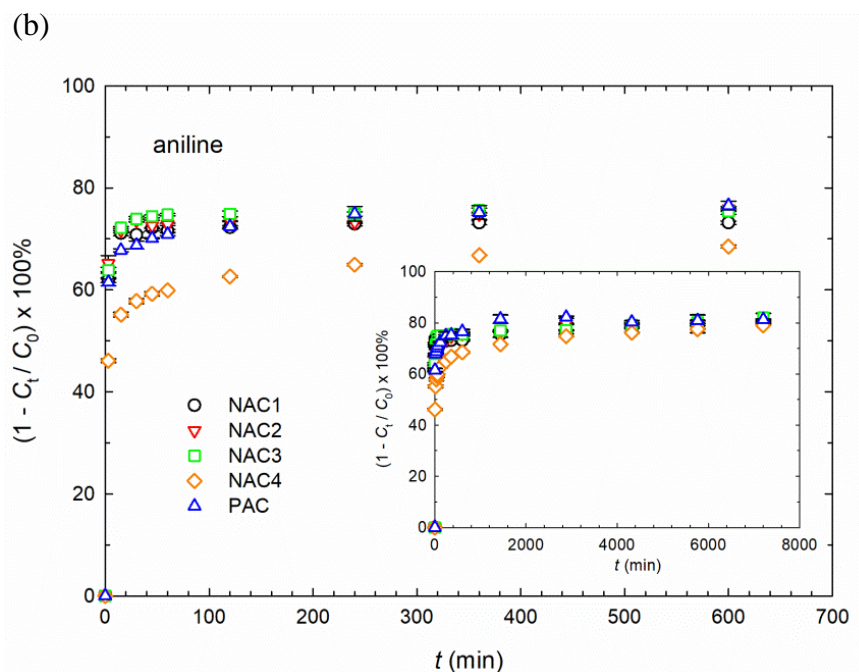
Figure 3.8 The rates of (a) 4-CP and (b) aniline adsorption from aqueous solution by NACs and PAC adsorbents in 10 hours and 5 days (insets). The experiments were run at $C_0 = 100$ mg/L, $C_e \cong 20$ mg/L, $V = 500$ mL, 150 rpm, pH 7, and $T = 25$ °C. The removal percentage of adsorbates from aqueous solution was calculated by $(1 - C_t / C_0) \times 100\%$, where C_t is the aqueous solute concentration at time, t. Data point and error bars represent the means and standard deviations, respectively, of duplicate samples.

3.3.2.2. Rate Modeling

The adsorption rate data from Figure 3.8 were processed to understand the adsorption process in terms of the order of the rate constant. Two rate models, namely pseudo-first-order [155] and pseudo-second-order rate models [156], were used to fit the sorption rate

data of the first 10 hours. The Lagergren pseudo-first-order rate model being one of the most widely used equations for liquid-phase adsorption processes is given by:

$$q_t = q_e[1 - exp(-k_f t)] \tag{3.1}$$

where q_e and q_t are the amount of adsorbate adsorbed (mg/g) at equilibrium and time t (min), respectively, and k_f is the pseudo-first-order rate constant (1/min).

The pseudo-second-order rate model, which assumes that (i) the adsorbate concentration is constant over time and (ii) the total number of binding sites depends on the amount of adsorbate adsorbed at equilibrium, has been interpreted as a special kind of Langmuir rate [51] and is given as follows:

$$q_t = \frac{t k_s q_e^2}{1 + t k_s q_e} \tag{3.2}$$

where k_s is the pseudo-second-order rate constant (g/(mg min)).

The adsorption capacity (q_t) as a function of contact time was fitted with the two rate models (eq 3.1 and eq 3.2) by a commercial software (SigmaPlot 12.5) with a nonlinear regression program, and the results were plotted in Figure 3.9. The corresponding fitting parameters and correlation coefficients are given in Table 3.5 below. The results demonstrated that the theoretical $q_{e,cal}$ values predicted by the pseudo-second-order rate model fit better to the experimental rate data compared to those predicted by the pseudo-first-order rate model. Furthermore, the much higher correlation coefficients obtained for the fittings by the pseudo-second-order rate model also indicated the suitability of using the pseudo-second-order rate model for phenomenological description of the adsorption of both adsorbates by the NACs and PAC adsorbents in this study. This was in agreement

with previous reports that the rates of 4-CP and aniline adsorption by GAC and PAC could be quantitatively described with a pseudo-second-order rate model [139, 154, 157].

(a)
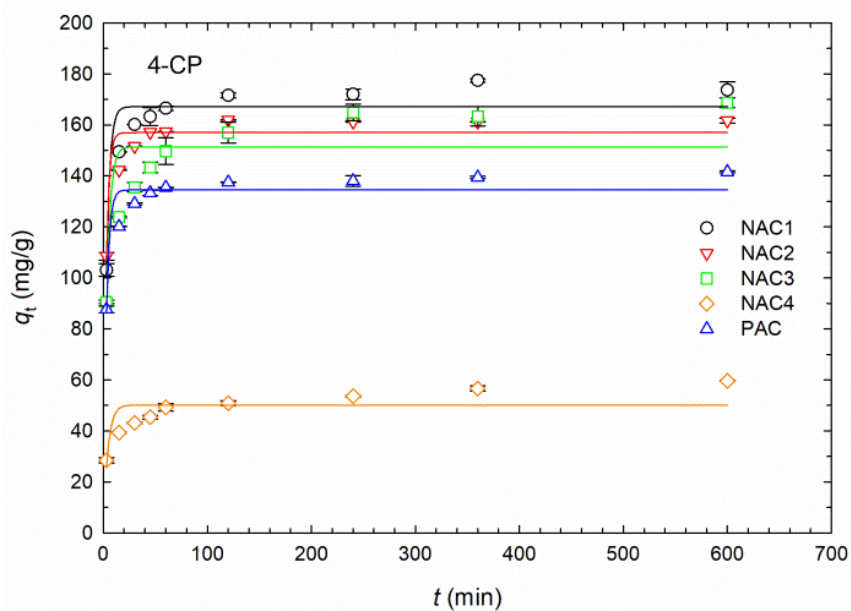
(b)
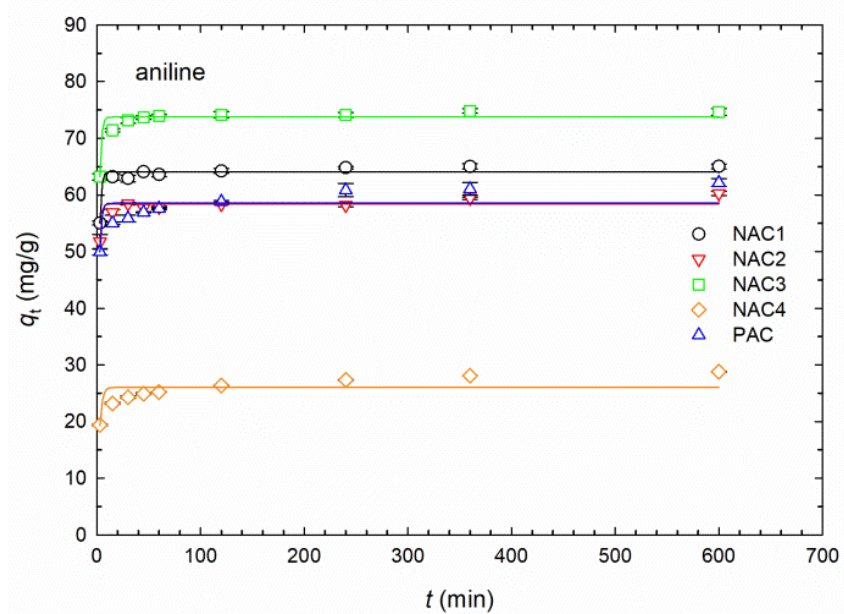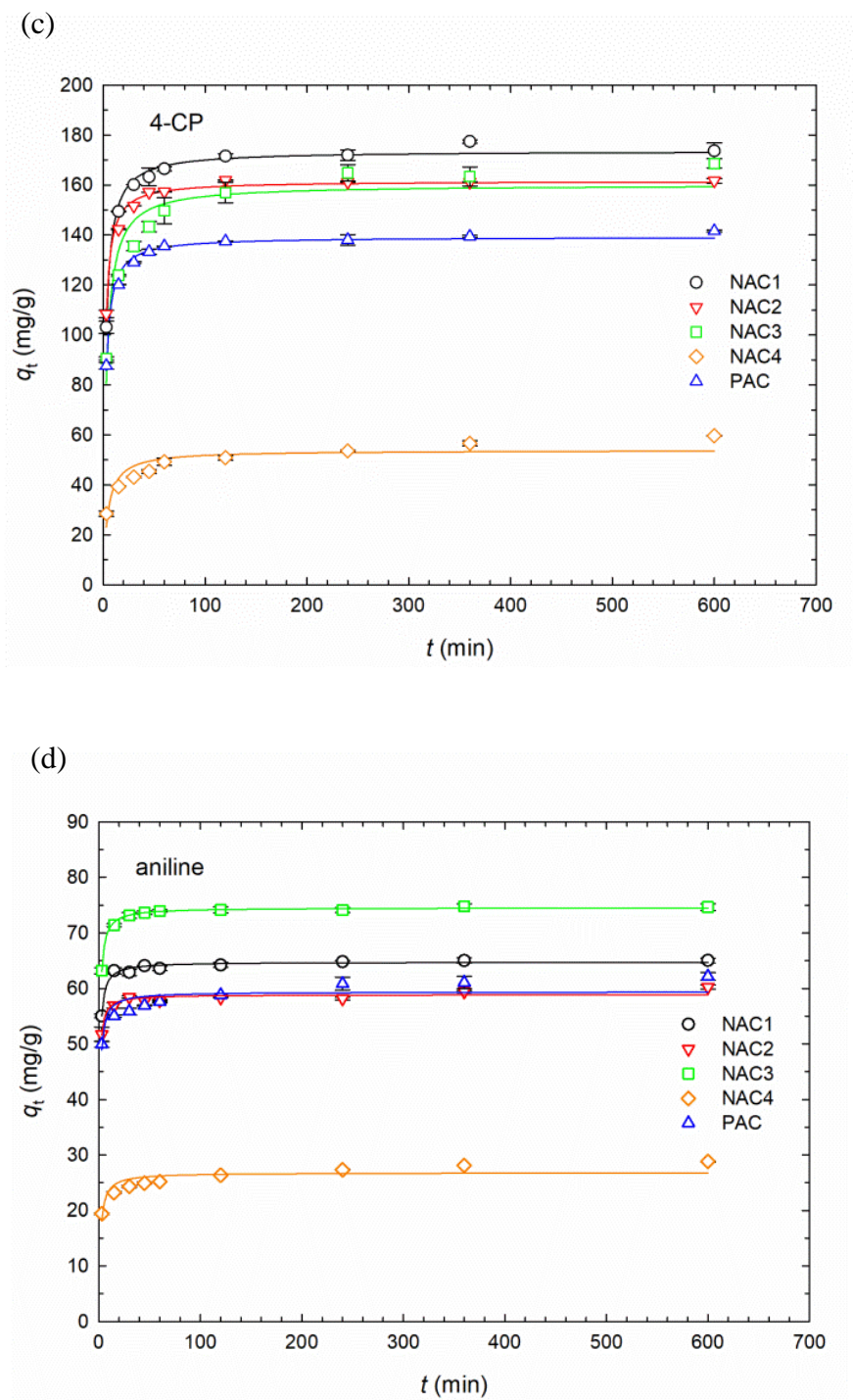
Figure 3.9 Adsorption rate data (Figure 3.8) fitted by pseudo-first-order rate model for (a) 4-CP and (b) aniline and by pseudo-second-order rate model for (c) 4-CP and (d) aniline on NACs and PAC.

Table 3.5 Fitting parameters of the pseudo-first-order and pseudo-second-order rate models (Figure 3.9) for the adsorption rate data (Figure 3.8) of 4-CP and aniline on NACs and PAC at C_0 = 100 mg/L, $C_e \cong$ 20 mg/L, V = 500 mL, 150 rpm, pH 7, and T = 25 °C.

Adsorbate	Adsorbent	Pseudo-first-order			Pseudo-second-order		
		k_f (1/min)	$q_{e,cal}$ (mg/g)	R^2	k_s (g mg^{-1} min^{-1})	$q_{e,cal}$ (mg/g)	R^2
4-CP	NAC1	0.296	170.6	0.841	0.00257	174.8	0.997
	NAC2	0.373	159.7	0.838	0.00384	162.7	0.998
	NAC3	0.243	158.5	0.629	0.00175	164.7	0.973
	NAC4	0.0703	57.49	0.514	0.00229	59.45	0.916
	PAC	0.315	140.0	0.734	0.00310	142.5	0.974
Aniline	NAC1	0.599	65.98	0.528	0.0218	66.58	0.982
	NAC2	0.660	60.02	0.477	0.0290	60.50	0.984
	NAC3	0.605	75.48	0.606	0.0197	76.15	0.989
	NAC4	0.375	28.30	0.351	0.0147	29.22	0.897
	PAC	0.559	61.40	0.356	0.0168	62.29	0.957

To further identify the rate-limiting step that may control the observed adsorption phenomena, the rate data were fitted to an intra-particle diffusion model [158]:

$$q_t = k_d t^{1/2} + I \tag{3.3}$$

where q_t (mg/g) is the amount of adsorbed solutes on the adsorbent at time t (min), k_d is the intra-particle diffusion rate constant (mg/(g min$^{1/2}$)), and I (mg/g) is a constant proportional to the thickness of the boundary layer.

The intra-particle diffusion (Weber-Morris) plots (Figure 3.10) show that, for each of the tested adsorbate-adsorbent system, the adsorption rate exhibited two linear regimes, suggesting that adsorption may follow two sequential processes. The first linear portion with a steep slope appears to be the fast surface adsorption attributed to the boundary layer effect, whereas the second linear portion with a much smaller slope corresponds to the gradual attainment of adsorption equilibrium due to intra-particle diffusion of the adsorbates within ACs [158]. The intra-particle diffusion parameters obtained from the slope and intercept of the second linear portion were presented in Table 3.6. It shows that the first three NACs had greater I values than PAC, indicating the adsorption on the three NACs may have greater impact from boundary layer effect (i.e., greater rate limiting from adsorption to external surfaces) due to larger specific external surface area. The deviation of all q_t versus $t^{1/2}$ plots from the origin suggested that intra-particle diffusion was not the singular rate-controlling step [153]. Nevertheless, it is true that the adsorption processes of 4-CP and aniline onto NACs and PAC were controlled by both external mass transfer and intra-particle diffusion [159].

(a)

(b)
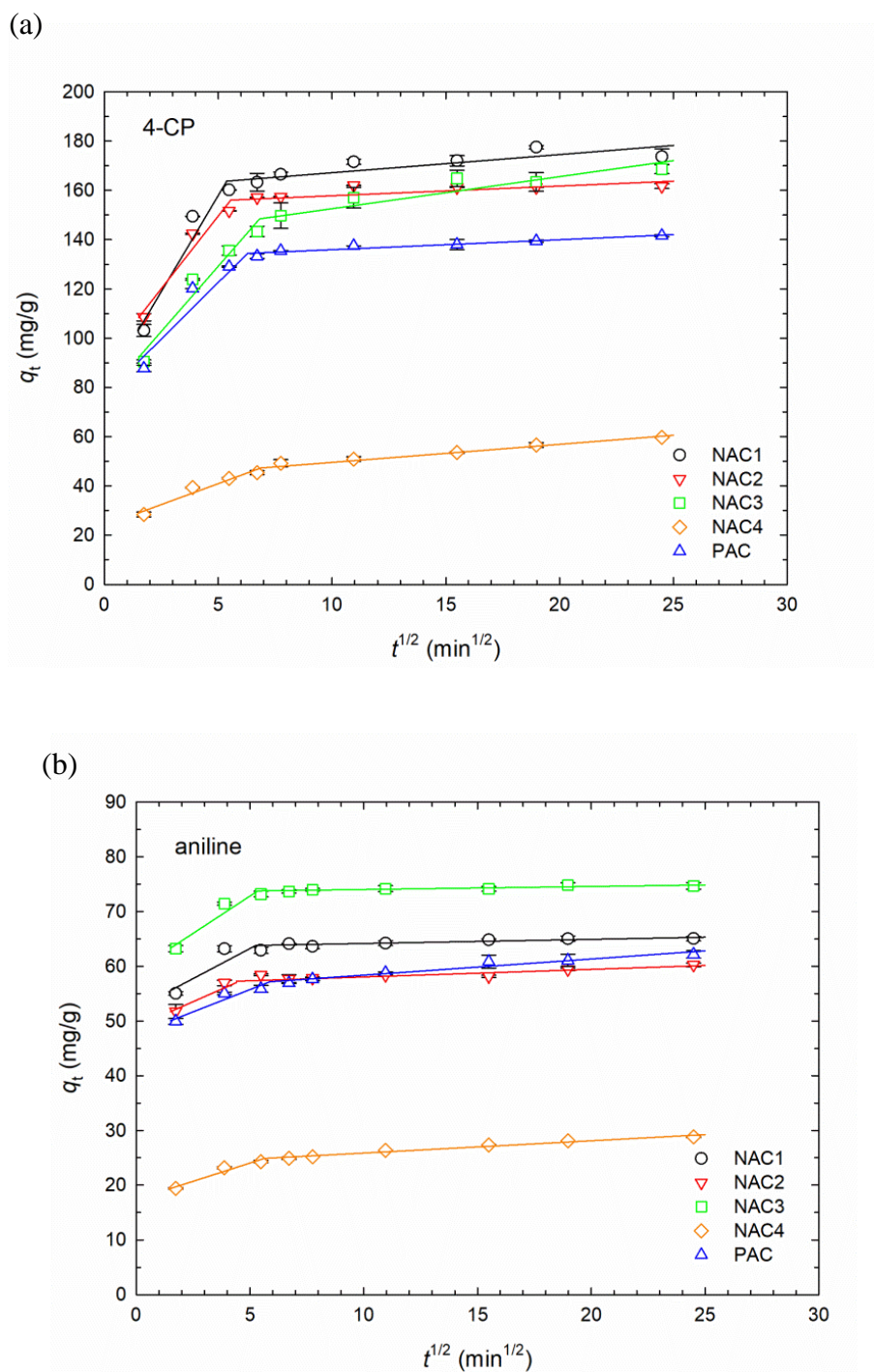
Figure 3.10 Fitting of the adsorption rate data to the intra-particle diffusion (Weber-Morris) model.

Table 3.6 Intra-particle diffusion parameters for the adsorption of 4-CP and aniline from aqueous solution by NACs and PAC at $C_0 = 100$ mg/L, $C_e \cong 20$ mg/L, $V = 500$ mL, 150 rpm, pH 7, and $T = 25$ °C.

Adsorbate	Adsorbent	k_d (mg/(g min$^{1/2}$))	I (mg/g)	R^2
4-CP	NAC1	0.7377	159.8	0.726
	NAC2	0.3948	153.9	0.551
	NAC3	1.303	139.5	0.853
	NAC4	0.7299	42.28	0.957
	PAC	0.4049	131.9	0.922
Aniline	NAC1	0.07533	63.41	0.809
	NAC2	0.1392	56.66	0.899
	NAC3	0.05622	73.44	0.786
	NAC4	0.2242	23.62	0.974
	PAC	0.2950	55.43	0.944

3.3.3. Adsorption Isotherms

3.3.3.1. Isotherm Modeling

The equilibrium adsorption data were fitted to both the Langmuir (eq 3.4) and Freundlich (eq 3.5) equations having the following forms [160]:

$$q_e = \frac{q_{max}K_L C_e}{1+K_L C_e} \tag{3.4}$$

$$q_e = K_F C_e{}^n \tag{3.5}$$

where q_{max} and K_L are the maximum monolayer adsorption capacity (mg/g) and the adsorption energy related constant (L/mg), respectively in eq 3.4, and K_F and n are adsorption capacity related constant (mg^{1-n} L^n/g) and the adsorption energy heterogeneity related constant, respectively in eq 3.5.

The best fits of the isotherm data are presented in Figure 3.11, with the fitting model parameters listed in Table 3.7. It is apparent from Figure 3.11 that the Freundlich model fits better (Figure 3.11a and b) to the data than the Langmuir model (Figure 3.11c and d) as the R^2 values for the Freundlich model fit are near or above 0.990 for all isotherm datasets, indicating that the Freundlich model is more appropriate for the tested adsorption systems because AC materials have heterogeneous distributions of surface energies for adsorption [160]. Further inspection of Figure 3.11 showed that, among the five adsorbents tested, NAC1, NAC2 and NAC3 had highest adsorption capacities whereas PAC had moderate and NAC4 the lowest capacities, respectively for 4-CP or aniline. This appears to be consistent with their relative SSA values (Table 3.1). The adsorption affinity of all NACs and PAC adsorbents for 4-CP was about 2-3 times as

high as aniline, which is consistent with the results reported on MWCNTs [50]. The determined n values were between 0.1 and 0.5, indicating the adsorption of both 4-CP and aniline onto all tested adsorbents to be a favorable process and the presence of a great proportion of active sites with a high energy [161].

(a)

(b)

(c)
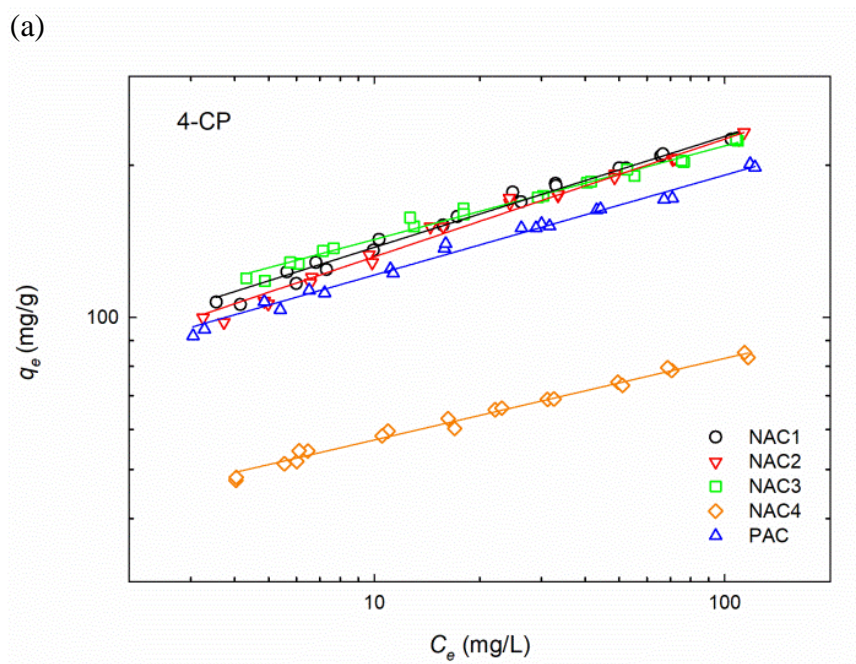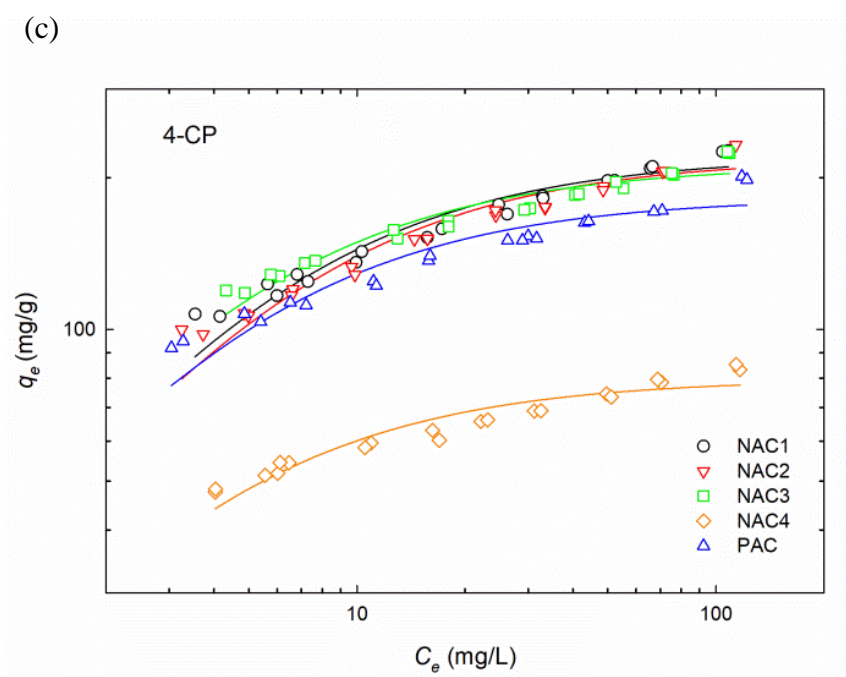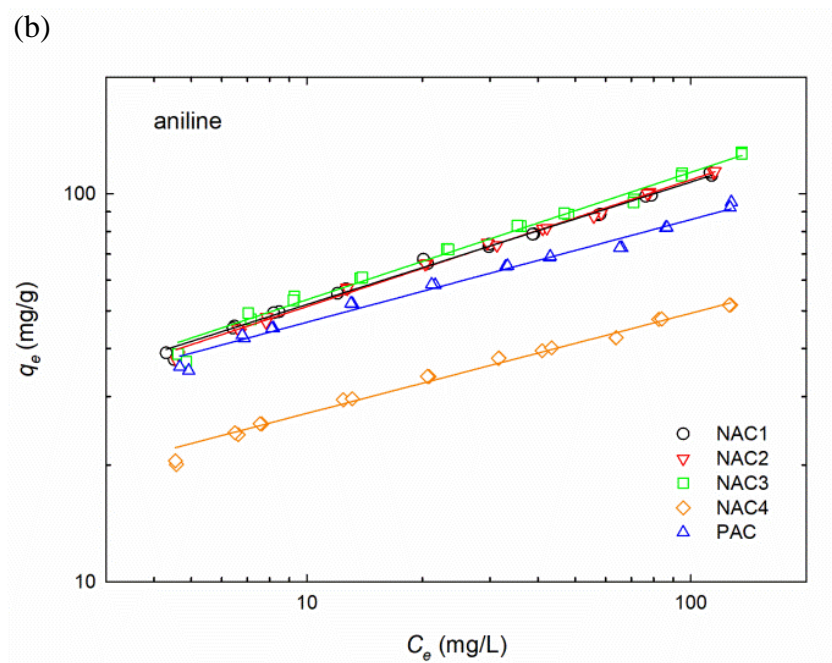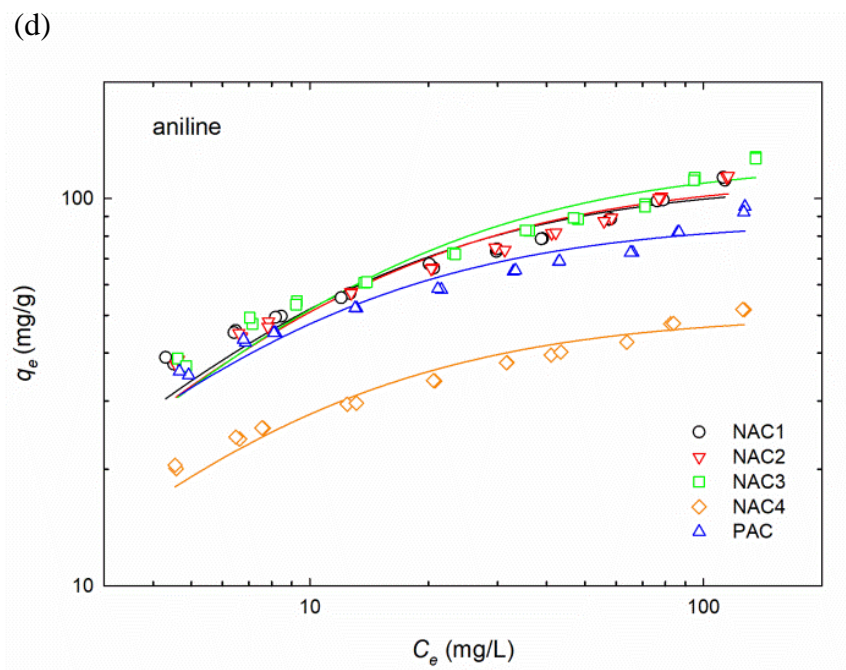
Figure 3.11 The best fits of the equilibrium adsorption data obtained at pH 7 and 25 ℃

to the Freundlich (a and b) and Langmuir (c and d) isotherm equations.

Table 3.7 Isotherm parameters for adsorption of 4-CP and aniline by NACs and PAC adsorbents at pH 7 and 25 °C.[a]

Adsorbate	Adsorbent	Freundlich isotherm			Langmuir isotherm		
		K_F (mg^{1-n} L^n/g)	n	R^2	q_{max} (mg/g)	K_L (L/mg)	R^2
4-CP	NAC1	83.03 ± 1.72	0.2195 ± 0.0058	0.989	220.6 ± 4.8	0.189 ± 0.017	0.940
	NAC2	77.08 ± 1.69	0.2331 ± 0.0060	0.989	218.9 ± 5.4	0.176 ± 0.018	0.936
	NAC3	93.13 ± 1.66	0.1852 ± 0.0049	0.988	211.7 ± 4.3	0.237 ± 0.024	0.917
	NAC4	39.44 ± 0.53	0.1615 ± 0.0038	0.990	79.69 ± 1.63	0.307 ± 0.033	0.897
	PAC	76.97 ± 1.42	0.1977 ± 0.0052	0.989	182.5 ± 4.9	0.242 ± 0.031	0.888
Aniline	NAC1	25.08 ± 0.45	0.3158 ± 0.0047	0.997	111.1 ± 3.9	0.0877 ± 0.0106	0.931
	NAC2	24.18 ± 0.44	0.3266 ± 0.0046	0.997	113.9 ± 3.9	0.0809 ± 0.0094	0.939
	NAC3	25.08 ± 0.82	0.3283 ± 0.0080	0.991	125.3 ± 4.7	0.0701 ± 0.0090	0.929
	NAC4	15.00 ± 0.36	0.2584 ± 0.0063	0.991	50.31 ± 1.24	0.123 ± 0.012	0.945
	PAC	25.40 ± 0.79	0.2646 ± 0.0080	0.986	88.02 ± 2.77	0.117 ± 0.014	0.914

[a] All estimated parameter values and their standard errors were determined by a commercial software (SigmaPlot 12.5) with a nonlinear regression program.

3.3.3.2.   *Factors affecting adsorption*

Physical and chemical conditions may affect equilibrium adsorption of organic pollutants by ACs [162]. Figure 3.12 presents three sets of the adsorption data measured at different levels of NaCl or $CaCl_2$ concentrations, different solution pH, and different temperatures for NAC3 and the two adsorbates. As shown in Figure 3.12a, variations in concentrations of background electrolytes have little or no effects on the adsorption of both adsorbates on the NAC. This is expected since hydrophobic interactions are the dominant mechanism for the adsorption.

As shown in Figure 3.12b, the background solution pH has significant effect on the adsorption. The measured single-point adsorption capacities, q_e (mg/g), remain the highest and constant in the solution pH range where either 4-CP (pH < 9) or aniline (pH > 5) is in non-ionized forms. As 4-CP deprotonates and becomes negatively charged at pH close to pK_a (9.38) or higher (Table 3.2) [139], its adsorption on NAC3 becomes progressively lowered due to much less hydrophobic feature of the charged 4-CP molecule. Similarly, aniline protonates and becomes positively charged at pH close to pK_a (4.60) or lower, and its adsorption is lowered accordingly.

It is known that the adsorption of organic pollutants on carbonaceous materials is exothermal, with higher capacity at lower temperature conditions [160, 161, 163]. As shown in Figure 3.12c and d and summarized in Table 3.8, the adsorption isotherms measured at 15, 25, and 35 °C for 4-CP and aniline have capacities increasingly higher as the temperature decreases.

(a)

(b)

(c)

(d)
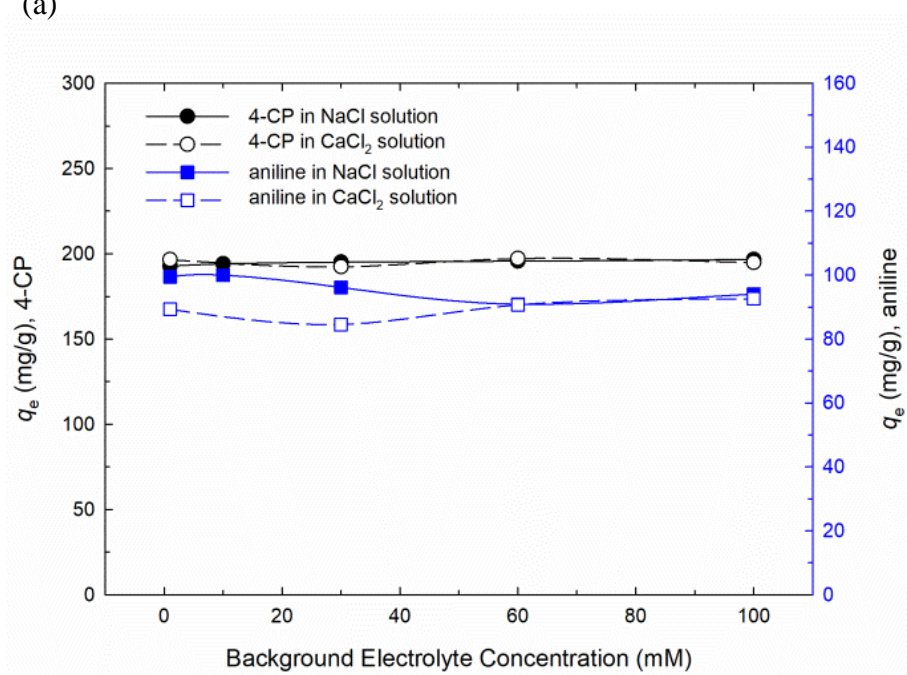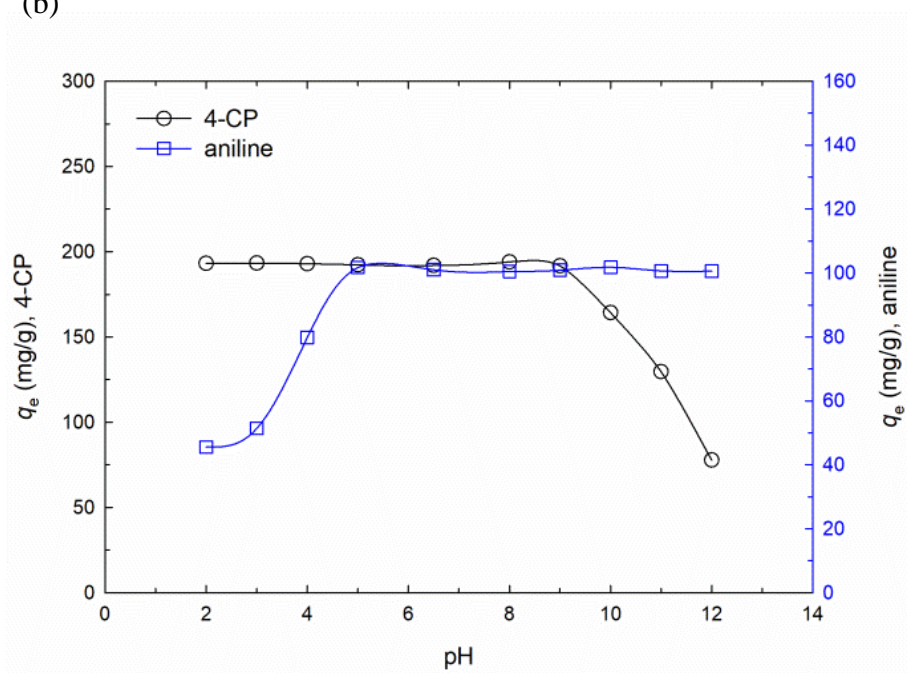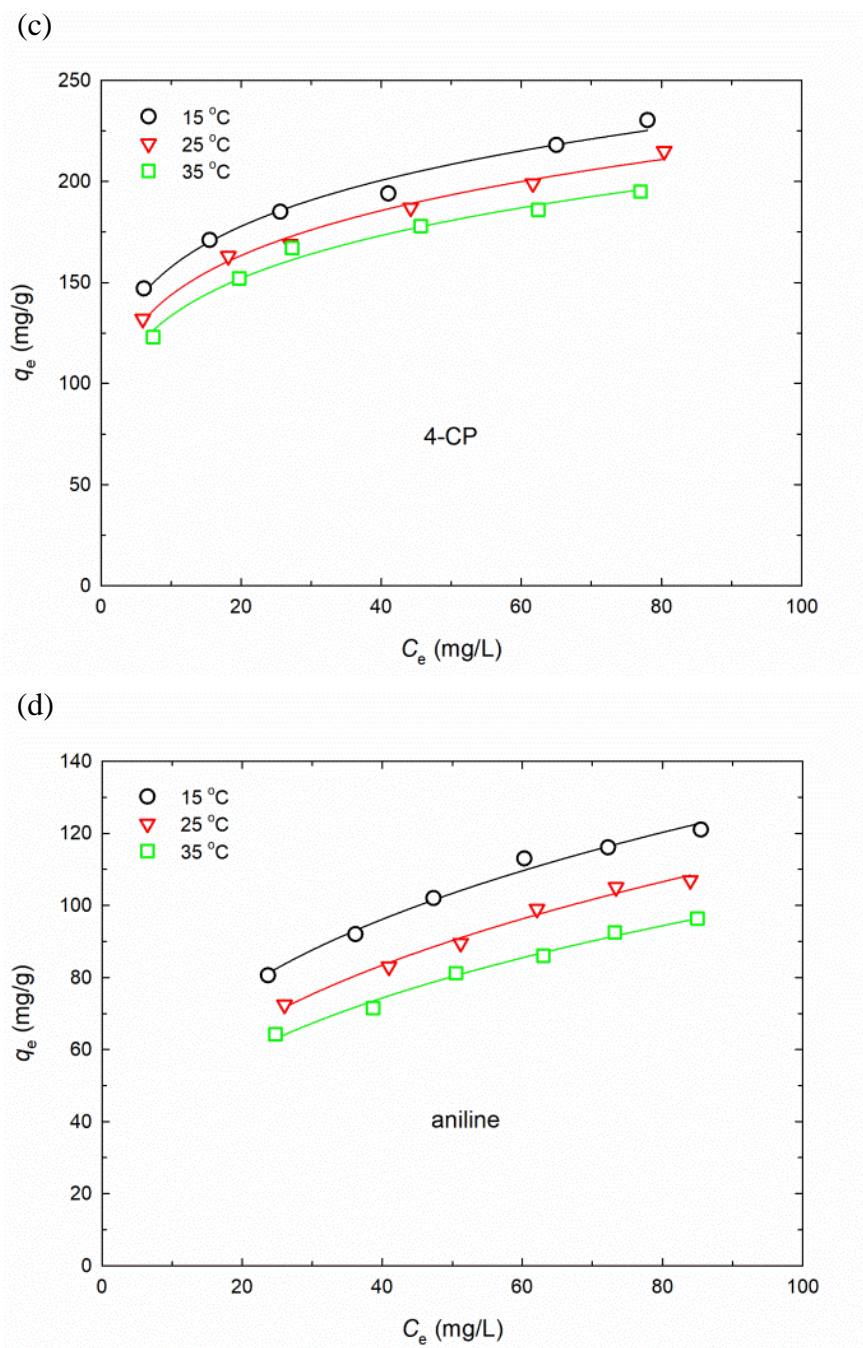
Figure 3.12 Factors affecting the adsorption of 4-CP and aniline onto NAC3: (a) effect of background electrolyte (0.26 g/L NAC3 for 4-CP C_0 = 100 mg/L or 0.33 g/L NAC3 for aniline C_0 = 100 mg/L, pH = 7, T = 25 °C); (b) effect of pH (condition: 0.26 g/L NAC3 for 4-CP C_0 = 100 mg/L or 0.33 g/L NAC3 for aniline C_0 = 100 mg/L, 10 mM CaCl$_2$, T =

25 °C); and effect of temperature on the adsorption of (c) 4-CP and (d) aniline (condition:

10 mM $CaCl_2$, pH = 7).

Table 3.8 Freundlich isotherm parameters obtained for the adsorption of 4-CP and aniline by NAC3 at different temperatures (Figure 3.12c and d).[a]

Adsorbate	T (°C)	K_F (mg^{1-n} L^n/g)	n	R^2
	15	105.8 ± 4.9	0.1735 ± 0.0126	0.9812
4-CP	25	94.22 ± 3.51	0.1838 ± 0.0100	0.9895
	35	86.66 ± 3.95	0.1878 ± 0.0123	0.9852
	15	29.23 ± 2.29	0.3227 ± 0.0194	0.9870
Aniline	25	22.69 ± 1.90	0.3530 ± 0.0206	0.9878
	35	20.88 ± 1.53	0.3443 ± 0.0180	0.9902

[a] pH = 7; all estimated parameter values and their standard errors were determined by a commercial software (SigmaPlot 12.5) with a nonlinear regression program.

3.3.3.3.   Adsorption mechanisms

Hydrophobic and π-π dispersion interactions may dominate the adsorption of 4-CP and aniline aromatic molecules onto NACs from aqueous solution, whereas electrostatic interactions, electron donor-acceptor interactions, and hydrogen-bonding interactions may play minor roles in the adsorption process [162]. Hydrophobic interactions between organic pollutants and the hydrophobic carbon surfaces often control the adsorption process, especially for aromatic contaminants with higher hydrophobicity [163, 164]. The observed adsorption capacity 2-3 times stronger for 4-CP than aniline by all NACs should be primarily attributed to the higher hydrophobicity ($\log K_{ow} = 2.16$) and lower aqueous solubility of 4-CP (Table 3.2). Meanwhile, NAC exhibited the highest adsorption affinity for both aromatic molecules in their neutral forms (Figure 3.12b), suggesting the important contribution of hydrophobic interactions to the adsorption process. Similar observation was reported for the adsorption of these two aromatic molecules by MWCNTs [50].

The interactions between π-electrons in the graphene layers of ACs and those in the aromatic rings of 4-CP [160, 165] or aniline [138, 166] may play a secondary role in the adsorption of aromatic contaminants onto AC materials. Such π-π interactions may include charge transfer, dispersive force, and polar electrostatic components [163]. For a given adsorbent, the magnitude of π-π interactions is determined by the π-electron polarizability parameter (π^*) of the adsorbate. As shown in Table 3.2, both 4-CP and aniline have similar π^* values, hence both chemicals may exhibit comparable π-π interactions with each NAC. The contribution of the π-π interactions to the overall adsorption of both adsorbates on each NAC is expected to be the same. As a result, in

natural water with pH 5.5-8.5, both 4-CP and aniline are neutral aromatic molecules and their differences in adsorption onto each NAC are attributable mainly to their difference of the dispersive or van der Waals interactions or their $\log K_{ow}$ values [139].

Note that electrostatic interactions, electron donor-acceptor complex, and hydrogen bonding may contribute variously at even smaller magnitudes to the overall adsorption [138]. In this study, electrostatic interactions should be insignificant in aqueous solutions of neutral pH under which both 4-CP ($pK_a = 9.38$) and aniline ($pK_a = 4.60$) (Table 3.2) are neutral molecules. Electron donor-acceptor complex could form between NACs and either adsorbate that may enhance the adsorption. As indicated by the results of FTIR spectra (Figure 3.3), the carbonyl oxygen groups on the basal plane of these four NACs could act as electron donors and the aromatic ring of the adsorbates as electron acceptors. This should favor stronger adsorption for 4-CP having an electron withdrawing -Cl group than aniline having an electron donating -NH$_2$ group [159]. Meanwhile, as indicated by their hydrogen-bonding coefficients (α_m and β_m in Table 3.2), both the amino group (-NH$_2$) on aniline and the hydroxyl group (-OH) on 4-CP could form hydrogen bonds with the -OH group on NACs (Figure 3.3), which may further enhance their adsorptive interactions [138].

3.3.4. *Comparison of adsorption with other carbonaceous adsorbents*

The NAC adsorbents have superior adsorption capacities for 4-CP and aniline when compared to other nanosized carbonaceous adsorbents potentially used for groundwater remediation. A thorough comparison of the adsorption capacities between the NACs

tested in this study and other carbonaceous adsorbents reported in the literature, including nanosized carbonaceous adsorbents and conventional AC adsorbents, was achieved based on the isotherms generated from the adsorption model parameters. Figure 3.13 presents the comparison using isotherm plots with mass-based adsorption capacities (q_e, mg/g) (Figure 3.13a and b) and SSA-based adsorption capacities (q_e/SSA, mg/m^2) (Figure 3.13c and d). Other adsorbents unavailable for generating isotherm plots were compared based on their maximum adsorption capacities (q_{max}) (Table 3.9).

A comparison with other reported nanosized adsorbents showed that the mass-based adsorption capacities for 4-CP or aniline by NAC1, NAC2, and NAC3 were about an order of magnitude higher than graphene derivatives (e.g., GO and RGO) and about one to two orders of magnitudes higher than CNTs (e.g., MWCNTs) (Figure 3.13a and b and Table 3.9). Such an advantage of NACs was especially pronounced at low solute concentrations of environmental relevance (e.g., C_e < 10 mg/L), and was still significant at high solute concentrations of pollution level tested in the experiment. For instance, the concentrations of chlorophenols and aniline can reach 100 mg/L or above in contaminated groundwater [135, 136, 167], where the introduction of NACs could be advantageous over other reported nanosized adsorbents such as CNTs [50]. The greater mass-based adsorption capacities of NACs correlated with their larger SSAs compared to other nanosized adsorbents. The greater mass-based adsorption capacities of NACs correlated with their larger SSAs compared to other nanosized adsorbents. A prior study also reported that AC materials having large SSAs and micropore volumes generally exhibit greater mass-based adsorption capacities for low-molecular-weight aromatic compounds when compared to CNTs, which are dominated by mesopores and

macropores [147]. This was attributed to the micropore effects that adsorption of small adsorbate molecules into the microporous region is enhanced by overlap of potential forces.

The adsorption capacity normalized to adsorbent SSA values provides further insights to the adsorption affinity and energy of adsorbate molecules onto adsorbent surface. It was found that the SSA-based adsorption capacities of NACs were higher than other nanosized adsorbents for the adsorption of 4-CP or aniline (Figure 3.13c and d), yet were slightly lower than the MWCNTs adsorption for 4-CP as shown in Table 3.9. Note that a large fraction of internal surfaces of NACs (with D_{pore} of ~18 Å) can be accessed by smaller N_2 molecules (with diameter of 3.86 Å and cross-sectional area of 16.2 Å^2), but not by the larger 4-CP or aniline molecules (with diameter of ~6 Å and cross-sectional area of ~ 35 Å^2) (Tables 3.1 and 3.2 and Figure 3.14). For instance, although the first three NACs had higher mass-based adsorption capacities than PAC, the SSA-based adsorption capacities of NACs were indeed smaller than PAC having larger pore sizes (Table 3.1).

The surface coverage (%) of 4-CP and aniline molecules adsorbed onto the adsorbents (Figure 3.14) was calculated by dividing the adsorbed amount with monolayer adsorption capacity Q_m (mg/g) [51]:

$$Surface\ Coverage = \frac{q_e}{Q_m} \times 100\% \tag{3.6}$$

where $Q_m = (SSA/(A_m \times N)) \times 10^{23}$ using the SSAs of the adsorbents (m^2/g) (Table 3.1), A_m (Å^2) of the adsorbates (Table 3.2), and N (Avogadro constant).

Within the tested concentrations, most adsorbents including NACs showed adsorption lower than monolayer coverage for both 4-CP and aniline molecules. There may be a portion of vacant sites on the NAC adsorbents (with D_{pore} of ~18 Å (Table 3.1)) that could be accessed by N_2 gas molecules (with diameter of 3.86 Å and cross-sectional area of 16.2 Å^2 at 77 K), but not by the larger 4-CP or aniline molecules (with diameter of ~6 Å and cross-sectional area of ~ 35 Å^2 (Table 3.2)). The only compared adsorbents exhibiting multilayer adsorption were the adsorption of 4-CP on tea leaves based AC [168] and polymerized MWCNTs [150], and the adsorption of aniline on polystyrene sulfonate based AC [169].

Over the tested aqueous concentration range of 4-CP or aniline, NAC1, NAC2, and NAC3 had similar or higher mass-based adsorption capacities compared to conventional AC adsorbents, including the PAC in this study, coconut shell based AC [170], and pitch based ACFs [163] in Figure 3.13a, the bamboo based AC [138] and GAC [166] in Figure 3.13b, and the coal based AC [171] in Table 3.9. This indicated that the reduction of particle sizes for conventional AC adsorbents to NAC nanomaterials may preserve or enhance their SSAs and mass-based adsorption capacities [47, 129, 130], which are much greater than other reported nanosized adsorbents such as CNTs and GO. Apparently, the NACs have both strong adsorbability and great colloidal stability while other nanomaterials or AC materials often possess one of such properties [133]. As such, NACs may be superior nanosized adsorbents for wide applications, including remediation of groundwater contaminated with organic pollutants.

(a)

(b)

(c)

(d)
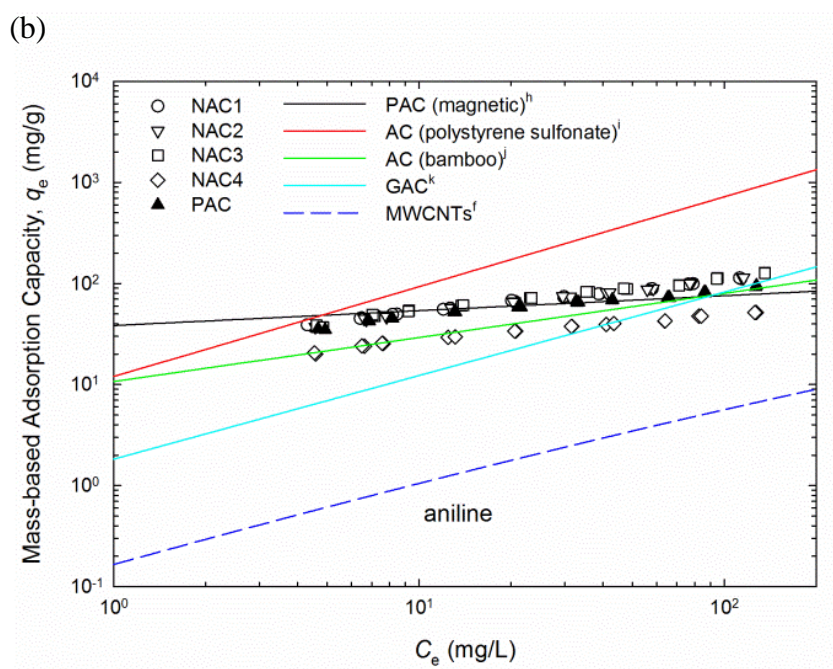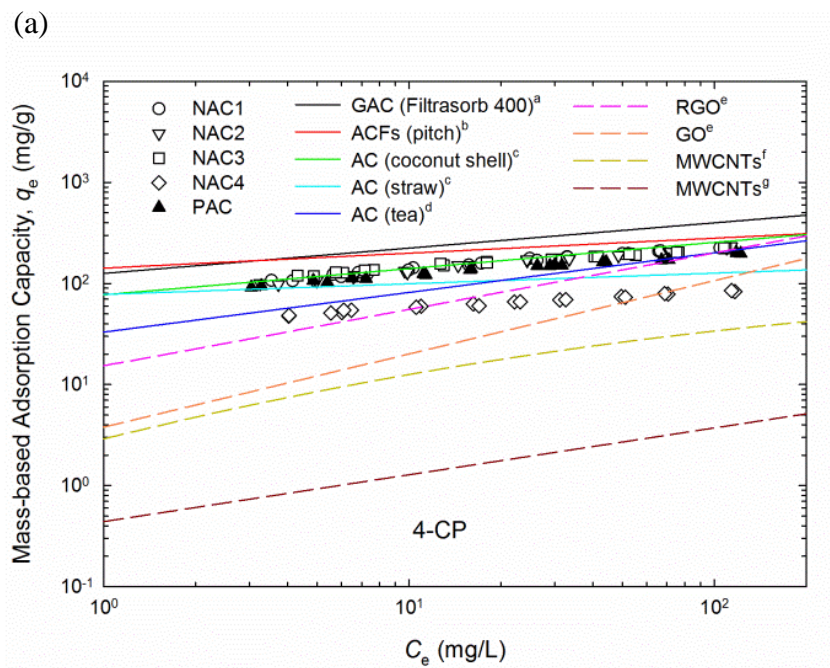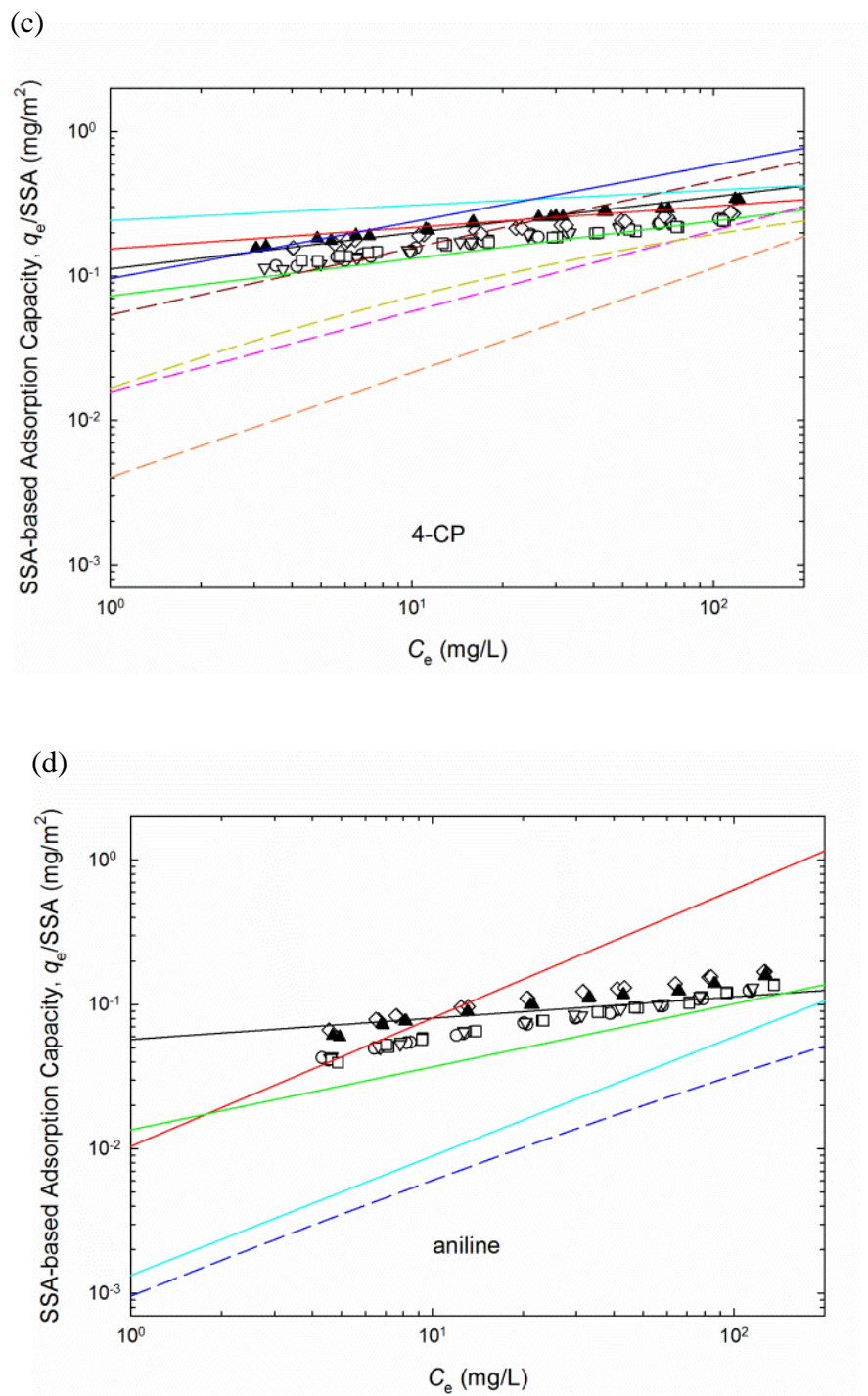
Figure 3.13 Comparison of mass-based (a and b) and SSA-based (c and d) adsorption

capacities of NACs with other adsorbents. Data points are the adsorption data measured

in this study for NACs and PAC (pH = 7, T = 25 °C) and lines represent adsorption

isotherms calculated from reported adsorption isotherm parameters for the same adsorbates. [a] granular activated carbon (GAC), T = 20 °C [172]; [b] activated carbon fibers (ACFs), T = 25 °C [163]; [c] T = 21 °C [170]; [d] pH = 6 [168]; [e] reduced graphene oxide (RGO-1) and graphene oxide (GO), pH = 7, T = 25 °C [141]; [f] MWCNT15, pH = 7, T = 25 °C [50]; [g] phosphorylated MWCNT-cyclodextrin polymer, pH = 5-6, room temperature [150]; [h] pH = 6, T = 20 °C [154]; [i] pH = 6.5, T = 25 °C [169]; [j] pH = 7, T = 25 °C [138]; and [k] pH = 7.5, T = 25 °C [166].

Table 3.9 Comparison of mass-based and SSA-based adsorption capacities of NACs and PAC in this study with other reported adsorbents in the literature, including conventional ACs adsorbents and nanosized carbonaceous adsorbents, for 4-CP and aniline.

4-CP						Aniline					
Adsorbent	q_{max} (mg/g)	SSA (m²/g)	q_{max}/SSA (mg/m²)	Condition	Reference	Adsorbent	q_{max} (mg/g)	SSA (m²/g)	q_{max}/SSA (mg/m²)	Condition	Reference
NAC1	220.6	909	0.243	pH 7	This	NAC1	111.1	909	0.122	pH 7	This
NAC2	218.9	879	0.249	25 °C	study	NAC2	113.9	879	0.130	25 °C	study
NAC3	211.7	933	0.227			NAC3	125.3	933	0.134		
NAC4	79.69	307	0.260			NAC4	50.31	307	0.164		
PAC (Norit)	182.5	588	0.310			PAC (Norit)	88.02	588	0.150		
PAC (Riedel-de Haen)	300.9	3000-3500	0.093	30 °C	[173]	GAC (Merck)	177.8			20 °C	[174]
GAC (Prolabo)	256-323	929	0.276-0.347	pH 5.5 21 °C	[160]	PAC (BDH)	126.6			pH 7.2 25 °C	[175]
AC (rattan sawdust)	188.7	1083	0.174	28 °C	[157]	AC (aloe vera)	106.4			pH 3 25 °C	[176]
PAC (commercial grade coconut shell)	134.1	838.5	0.160	pH 2 30 °C	[177]						
PAC (waste coconut shell)	72.77	935.2	0.078								
GAC (coal)	119	637	0.187	pH < 6.5 25 °C	[171]						
MWCNTs (pristine)	43.19[a]	157	0.275	25 °C	[178]	MWCNTs (ball-milled)	36.2			23 °C	[179]
MWCNTs (NH₃ treated)	53.31[a]	195	0.273			MWCNT30 (oxidized)	9.82-46.7			25 °C	[180]
						MWCNTs (magnetic)	2.00	50.84	0.0393	pH 8 25 °C	[152]

[a] Determined by fitting the reported isotherm data with the Langmuir isotherm model by a commercial software (SigmaPlot 12.5).
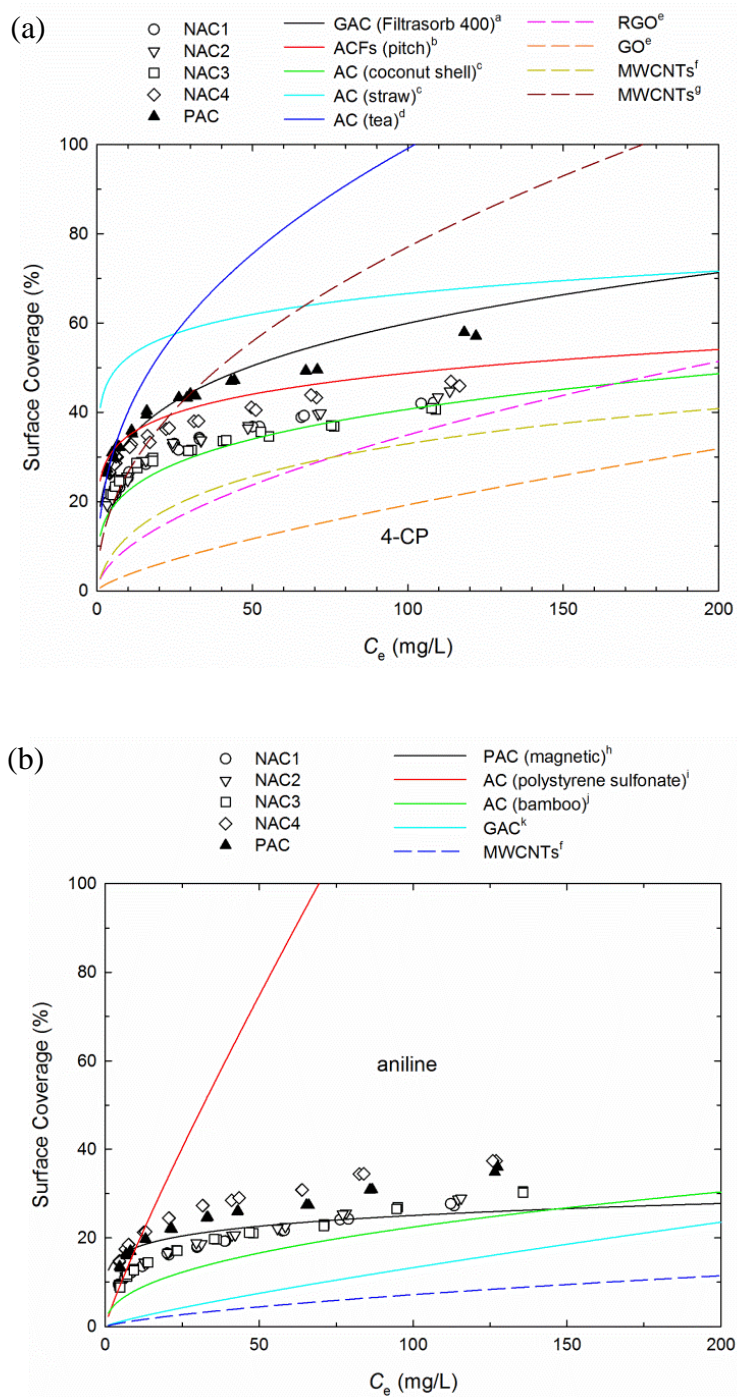
Figure 3.14 Comparison of surface coverage (eq 3.6) for (a) 4-CP and (b) aniline molecules adsorbed onto NACs with other adsorbents. Data points are the adsorption data measured in this study for NACs and PAC (pH = 7, T = 25 °C) and lines represent

adsorption isotherms calculated from reported adsorption isotherm parameters for the same adsorbates. [a] granular activated carbon (GAC), $T = 20$ °C [172]; [b] activated carbon fibers (ACFs), $T = 25$ °C [163]; [c] $T = 21$ °C [170]; [d] pH = 6 [168]; [e] reduced graphene oxide (RGO-1) and graphene oxide (GO), pH = 7, $T = 25$ °C [141]; [f] MWCNT15, pH = 7, $T = 25$ °C [50]; [g] phosphorylated MWCNT-cyclodextrin polymer, pH = 5-6, room temperature [150]; [h] pH = 6, $T = 20$ °C [154]; [i] pH = 6.5, $T = 25$ °C [169]; [j] pH = 7, $T = 25$ °C [138]; and [k] pH = 7.5, $T = 25$ °C [166].

3.4. Conclusions

Ideal nanomaterials that could be injected into groundwater systems for remedy of contamination should have both high mobility and strong reactivity or adsorbability. We have previously demonstrated that NACs could remain stable as dispersed nanoparticles in natural aquatic environments. This study further demonstrated that these NAC nanomaterials are much stronger adsorbents than other reported nanosized adsorbents such as CNTs and GO that were considered in prior studies as potential candidates for removal of typical aromatic contaminants. Our results showed that the four NACs had large SSAs and great microporosities, and exhibited fast rates of adsorption for 4-CP and aniline that followed both pseudo-second-order rate model and intra-particle diffusion model. The equilibrium adsorption could be described with the Freundlich isotherm equation and hydrophobic interactions were likely the dominating mechanism for the observed adsorption. The adsorption of both target adsorbates on NACs was influenced by solution pH and temperature, whereas background electrolytes showed negligible effect. More importantly, the tested NACs had adsorption capacities one to two orders of magnitudes greater than other potential nanosized adsorbents. Such strong adsorbability, along with their high colloidal stability, suggests that NACs may be superior adsorbents for broad environmental applications, including as injected agent for *in situ* treatment of groundwater contaminated with organic pollutants. However, further flow-through column experiments and proof-of-concept field demonstrations are needed to evaluate such engineering applications.

Acknowledgements

4. CHAPTER IV. EFFECT OF SOLUTION CHEMISTRIES ON THE AGGREGATION OF SOOT NANOPARTICLES IN AQUEOUS ENVIRONMENTS
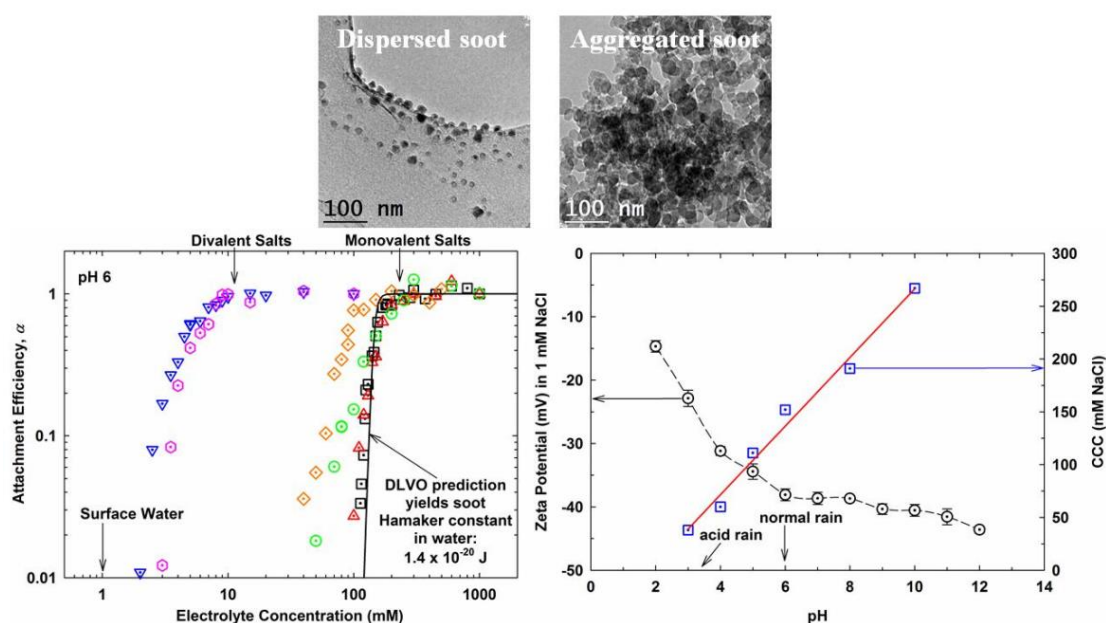
PROJECT TITLE: AGGREGATION KINETICS OF DIESEL SOOT NANOPARTICLES IN WET ENVIRONMENTS

The work in this chapter has been published in the title of "Aggregation Kinetics of Diesel Soot Nanoparticles in Wet Environments" in Environmental Science & Technology (Volume 51, Pages 2077-2086) on January 16, 2017.

Abstract

Soot produced during incomplete combustion consists mainly of carbonaceous nanoparticles (NPs) with severe adverse environmental and health effects, and its

environmental fate and transport are largely controlled by aggregation. In this study, we examined the aggregation behavior for diesel soot NPs under aqueous condition in an effort to elucidate the fundamental processes that govern soot particle-particle interactions in wet environments such as rain droplets or surface aquatic systems. The influence of electrolytes and aqueous pH on colloidal stability of these NPs was investigated by measuring their aggregation kinetics in different aqueous solution chemistries. The results showed that the NPs had negatively charged surfaces and exhibited both reaction- and diffusion-limited aggregation regimes with rates depended upon solution chemistry. The aggregation kinetics data were in good agreement with the classic Derjaguin-Landau-Verwey-Overbeek (DLVO) theory. The critical coagulation concentrations (CCC) were quantified and the Hamaker constant was derived for the soot (1.4×10^{-20} J) using the colloidal chemistry approach. The study indicated that, depending upon local aqueous chemistry, single soot NPs could remain stable against self-aggregation in typical freshwater environments and in neutral cloud droplets, but are likely to aggregate under salty (e.g., estuaries) and/or acidic (e.g., acid rain droplets) aquatic conditions.

4.1. Introduction

Soot particles are airborne carbonaceous particulate matter produced from incomplete combustion of fuel and biomass. They are often of sizes <100 nm and consist of a graphitic core and an organic component [181]. Each year, approximately 8 million tons of soot particles were released to the environment due to fuel combustion and wild fires

[14]. They are ubiquitously distributed in both atmosphere and hydrosphere, possessing broad environmental concerns.

Upon released to the atmosphere, soot particles have various adverse effects on human health [17, 19, 59, 60], visibility reduction [61], soiling of buildings [62], agricultural productivity [63], and global climate change [64-66]. They may also impact aquatic environments as they eventually reach water bodies via atmospheric dry and wet deposition or fluvial discharge [67-69]. Contaminants such as persistent organic pollutants (POPs) are carried by soot into the water column and sediments of surface water and the ocean [33-35]. Recent studies also indicate that the interactions of soot particles with marine biological species and nutrients could have strong impact on ecosystems and the global carbon cycle [20, 21].

Size of soot particles is a key factor controlling their fate and transport in both the atmosphere and hydrosphere. Freshly produced soot contains a fraction of particles having sizes <100 nm. To evaluate the environmental fate and transport of these soot nanoparticles (NPs) and their potential interactions with the ambient environment, it is crucial to understand the factors governing their aggregation behavior under both atmospheric and aquatic conditions [22]. The aggregation behavior of soot under dry atmospheric conditions has been well studied with model simulations [70, 71, 182] and laboratory measurements [72, 73, 183-186]. With respect to soot particles in humid atmosphere, previous studies mainly focused on the effects of cloud water processing (soot-water interactions [74, 187, 188]) and photochemical aging processes (UV exposure and mixing/coating with other aerosol components [75, 189-193]) of soot aggregates on their hygroscopic, morphological and optical properties. Few studies examined

aggregation of soot or its surrogate, carbon black, under aqueous conditions. For example, Growney et al. [194] measured the zeta (ζ) potentials of diesel soot NPs in aqueous solution under different pH conditions. Mari et al. [20] reported the decrease in concentration of marine organic particles due to their adsorption by soot particles, and hypothesized that soot particles deposited onto the ocean may act as aggregation nuclei to form large marine aggregates. Shiu et al. [21] recently observed that carbon black with a negative surface charge in water enhances the stability of marine polymers. Others studies have evaluated the stability of carbon black in various solvents including water [195, 196]. However, the aggregation kinetics and colloidal stability of soot NPs in wet environments such as under aqueous or rain droplet conditions are not well characterized.

The objective of this study was to investigate the early stage aggregation kinetics of soot NPs under the influence of aqueous solution chemistries in an effort to elucidate the fundamental processes that control soot particle-particle interactions in wet environments. Diesel soot particulate matter (standard reference material (SRM-1650b)), which was widely used in prior studies as a representative soot sample due to its environmental relevance [33, 197, 198], was obtained from National Institute of Standards and Technology (NIST, Gaithersburg, MD) for use in this study. The aggregation kinetics and electrophoretic mobilities (EPM) of the soot NPs were measured under various environmentally relevant electrolyte composition/concentration and pH, from which the respective critical coagulation concentrations (CCC) were determined. The stability curves constructed from the aggregation data were in good agreement with predictions from the classic Derjaguin-Landau-Verwey-Overbeek (DLVO) theory, yielding the Hamaker constant for diesel soot NPs first determined using the colloidal chemistry

approach. Potentiometric titration coupled with material characterization conducted on soot NPs were used to elucidate their charge acquisition and aggregation mechanisms.

4.2. Materials and Methods

4.2.1. Preparation of Aqueous Soot NPs

According to NIST [199], SRM 1650b was produced by a diesel engine and was collected from the heat exchangers of a dilution tube facility following 200 hours of particulate accumulation. The soot sample is representative of typical diesel particulate matter emitted from heavy-duty diesel engines. The NIST-certified sample was characterized for its contents of polycyclic aromatic hydrocarbons (PAHs) and nitro-substituted PAHs (nitro-PAHs) and its specific surface area of 108 m^2/g. After received, the soot sample was further characterized in this study for its elemental compositions and examined by scanning electron microscope (SEM).

Aqueous soot NPs were prepared by stirring 10 mg of SRM 1650b in 500 mL of Milli-Q water (resistivity > 18 MΩ·cm) for 24 h on a magnetic stirrer, followed by 24 h sonication in the dark. The resulting stock suspension contained 20 mg/L soot NPs which was monitored over the experimental time period; and the result showed that the soot NPs remained well dispersed and kinetically stable at a solution pH of 3.99 ± 0.01. Prior to the use in experiments, the stock suspension was divided into several batches and stored in the dark at room temperature.

4.2.2. Characterization of Aqueous Soot NPs

The particle size of soot suspensions after 1 h and 24 h sonication at pH 6 were examined using transmission electron microscope (TEM), high resolution TEM (HRTEM), and dynamic light scattering (DLS). Measurements for the stock suspension at pH 4 yielded the same results as those at pH 6. For TEM analyses, sonicated soot suspension was dropped onto 200 mesh carbon coated copper grids, and the images were acquired on either TEM (Topcon 002B, Topcon Corp., Tokyo, Japan) or HRTEM (JEM 2010F, JOEL USA Inc., MA) operating at 200 kV. DLS measurements were conducted to determine the hydrodynamic size distribution using a Zetasizer Nano ZS (Malvern Instruments, Worcestershire, UK) set at a refractive index of 1.5 and absorption index of 0.1, which allowed comparisons with the reference information provided by NIST.

The electrophoretic mobilities (EPM) of aqueous soot NPs were measured over a range of electrolyte (NaCl or $CaCl_2$) concentrations and pH using the same Zetasizer Nano ZS instrument by phase analysis light scattering (PALS). The concentration of soot NPs was maintained at 10 mg/L for all EPM measurements. For each solution condition, triplicate suspension samples were each measured for 10 times. The EPM values were converted to zeta (ζ) potentials using the Smoluchowski approximation [200], which were later used to calculate the electrostatic interaction energies between the soot NPs in this study.

Potentiometric titration measurement was conducted on a 100-mL suspension containing 0.5 g/L of soot NPs, which was prepared following the same procedure for preparation of the stock suspension. The suspension was purged with nitrogen (N_2) gas for 15 min to remove any dissolved CO_2 before HCl was added to lower the solution pH to 3. The suspension was subsequently kept in a nitrogen atmosphere as being titrated

with 0.1 M NaOH to pH 10 with an autotitrator (702 SM Titrino, Metrohm, Herisau, Switzerland). The amount of NaOH required to raise the pH from 3 to 10 of the suspension containing soot NPs was compared to that required to raise the pH of a soot-free blank solution to identify the presence of titratable functional groups on soot NPs.

4.2.3. Solution Chemistry

Electrolyte stock solutions were prepared by dissolving ACS-grade electrolytes in Milli-Q water and filtering them through 0.1-μm filters (Puradisc 25 TF, Whatman) before use. The concentrations for the electrolyte stock solutions were prepared in 0.5 M and 2 M for monovalent salts, and 0.04 M and 0.2 M for divalent salts. HCl and NaOH were used to adjust the solution pH in this study.

4.2.4. Soot NPs Aggregation Kinetics

Time-resolved dynamic light scattering (TRDLS) was used to measure the increase in the intensity weighted hydrodynamic diameter (D_h) of soot NPs with time in different solution chemistries following the protocol published in prior studies [201-203]. A Brookhaven 90Plus DLS instrument (Holtsville, NY) was employed for the measurement, which uses a 35 mW solid state laser operating at a wavelength of 635 nm. Each autocorrelation function was accumulated for 15 s with a photo-detector positioned at 90°. The instrument performance was verified using NIST-polystyrene nanosphere size standards. In each aggregation experiment, separate aliquots containing soot NPs, Milli-Q water, and electrolyte were prepared. Each aliquot was adjusted to the same pH condition.

1 mL of aliquot containing 20 mg/L of soot NPs from the stock suspension was first introduced into a new glass vial (VWR, Chester, PA), which had been thoroughly cleaned and oven-dried under dust-free conditions. To initiate the aggregation, aliquots containing varying volume of electrolyte and Milli-Q water were combined in the vial to form a total solution volume of 2 mL at a predesigned electrolyte concentration. This protocol ensured that the initial soot NPs concentration (N_0) remains constant at 10 mg/L (see eq 4.1) in each aggregation experiment. The vial was vortexed for 1 s (Vortex Genie, Fisher Scientific) before being immediately inserted into the DLS instrument to start the measurement. The soot NPs were left to aggregate between 20 min to 100 min. All aggregation experiments were conducted in triplicates to ensure data quality.

The initial aggregation rate constant (k) for the soot NPs is proportional to the initial rate of linear increase in D_h with time (t) and the inverse of initial soot NPs concentration (N_0) [204]:

$$k \propto \frac{1}{N_0}\left(\frac{dD_h(t)}{dt}\right)_{t \to 0} \tag{4.1}$$

Here k was determined from the slope up to the point where D_h has increased to $1.5D_{h0}$. In cases where the linear regime ended before reaching $1.5D_{h0}$, the slope of linear regime was still determined. The fitted line was verified to intercept the y axis no more than 5 % from D_{h0} for all aggregation experiments.

The aggregation attachment efficiency (α), which is equivalent to the inverse stability ratio and ranges from 0 to 1, was used to quantify the aggregation kinetics of soot NPs under different solution conditions. Given that N_0 was kept constant in all aggregation experiments, α was calculated by normalizing the initial slope of aggregation in different

solution chemistries by the slope obtained under diffusion-limited (fast) aggregation conditions [39]:

$$\alpha = \frac{k}{k_{fast}} = \frac{\frac{1}{N_0}\left(\frac{dD_h(t)}{dt}\right)_{t\to0}}{\frac{1}{(N_0)_{fast}}\left(\frac{dD_h(t)}{dt}\right)_{t\to0,fast}} = \frac{\left(\frac{dD_h(t)}{dt}\right)_{t\to0}}{\left(\frac{dD_h(t)}{dt}\right)_{t\to0,fast}} \tag{4.2}$$

4.2.5. DLVO Calculations

The Derjaguin-Landau-Verwey-Overbeek (DLVO) predicted attachment efficiency curve was calculated using the following governing equation [37, 38, 84] :

$$\alpha = \frac{\int_0^\infty \beta(h)\frac{exp\left[\frac{V_A(h)}{k_BT}\right]}{(2R+h)^2}dh}{\int_0^\infty \beta(h)\frac{exp\left[\frac{V_T(h)}{k_BT}\right]}{(2R+h)^2}dh} \tag{4.3}$$

where h is the distance between the surface of two approaching particles, R is the particles radius taken as the hydrodynamic radius (R_h), k_B is the Boltzmann constant, and T is the absolute temperature. The total colloidal interaction potential energy between two particles, $V_T(h)$, is the sum of the van der Waals attraction potential energy, $V_A(h)$, and the electrical double layer (EDL) repulsion potential energy, $V_R(h)$:

$$V_T(h) = V_A(h) + V_R(h) \tag{4.4}$$

The hydrodynamic resistance (interaction) between two approaching particles, which causes slower motion of close particles due to restricted removal of the liquid between two rigid interfaces, was corrected by calculating the dimensionless function $\beta(h)$ according to Honig et al. [85]:

$$\beta(h) = \frac{6\left(\frac{h}{R}\right)^2 + 13\left(\frac{h}{R}\right) + 2}{6\left(\frac{h}{R}\right)^2 + 4\left(\frac{h}{R}\right)} \tag{4.5}$$

$V_A(h)$ was calculated using the expression proposed by Gregory [86] that accounts for the electromagnetic retardation effect between two approaching spherical particles of the same size:

$$V_A(h) = -\frac{A_{CWC}R}{12h}\left[1 - \frac{bh}{\lambda}\ln\left(1 + \frac{\lambda}{bh}\right)\right] \tag{4.6}$$

where A_{CWC} is the Hamaker constant between the interacting soot NPs through water, $b = 5.32$, and λ is the "characteristic wavelength" of the interaction often assumed to be about 100 nm [24]. Please note that eq 4.6 is an approximate expression for the van der Waals interaction energy between sphere-sphere that is derived from the corresponding flat plate-plate expression by the Derjaguin integration method (DIM) [92]. Thus, eq 4.6 remains connected with the plate-plate geometry and this expression is applied strictly to separations between particles that are much smaller than the particle radius ($h \ll R$). Nevertheless, previous studies [37, 38, 205] have successfully applied this expression to simulate the van der Waals interaction energy between aggregating spherical nanoparticles.

$V_R^{\psi}(h)$ was calculated using the constant potential approximation (CPA) expression [87] between two spherical particles of the same size and surface potential both in the fitting procedure and DLVO interaction energy profiles:

$$V_R^{\psi}(h) = \frac{2\pi R n_\infty k_B T \Phi^2}{\kappa^2}\left[\ln\left(\frac{1+e^{-\kappa h}}{1-e^{-\kappa h}}\right) + \ln(1 - e^{-2\kappa h})\right] \tag{4.7}$$

where n_∞ is the bulk number density of ions given by:

$$n_\infty = 1000 N_A C_s \tag{4.8}$$

where N_A is Avogadro's constant and C_S is the electrolyte molar concentration [mol dm^{-3}]; and Φ is the reduced potential given by:

$$\Phi = ze\varphi/k_B T \tag{4.9}$$

where φ is the surface potential of soot NPs, and is assumed as the ζ potential [81, 206, 207] obtained from experiment changing as a function of NaCl concentration as shown in Figure 4.5c; and κ is the Debye-Hückel parameter or the inverse Debye length, which in aqueous solutions at 25 ℃ was approximated as [24]:

$$\kappa = 2.32 \times 10^9 (\textstyle\sum c_i z_i^2)^{\frac{1}{2}} \tag{4.10}$$

In addition to the CPA expression, both the linear superposition approximation (LSA) and constant charge approximation (CCA) expressions are also commonly employed to calculate the EDL repulsion potential energy between two spherical particles of the same size and surface potential. The LSA expression is given by [88]:

$$V_R(h) = \frac{64\pi R n_\infty k_B T}{\kappa^2} \gamma^2 exp(-\kappa h) \tag{4.11}$$

where $\gamma = tanh\left(\frac{ze\varphi}{4k_B T}\right)$.

The CCA expression is given by [90, 208]:

$$V_R^\sigma(h) = \frac{2\pi R n_\infty k_B T \Phi^2}{\kappa^2} \left[ln\left(\frac{1+e^{-\kappa h}}{1-e^{-\kappa h}}\right) - ln(1 - e^{-2\kappa h}) \right] \tag{4.12}$$

By assuming the potential to be sufficiently small for slightly charged particles ($\Phi = ze\varphi/k_B T \ll 1$ or φ less than about 25 mV in 1-1 electrolytes), the Poisson-Boltzmann equation is solved in its linear form known as the Debye-Hückel approximation [91]. The linear Poisson-Boltzmann equation (LPB) is solved at the boundary condition of the maintenance of surface-chemical equilibrium for the CPA expression, and at the boundary condition of a fixed surface charge density during particle approach for the CCA expression; whereas the LSA expression assumes that the contributions of the potential from each interacting surface can be added towards the

overall potential [24]. The DIM [92] approximation for interacting spheres is applied throughout. The data of DLVO prediction were computed with MATLAB R2014a software (MathWorks, Natick, MA).

4.3. Results and Discussion

4.3.1. Characterization of Aqueous Soot NPs

The pristine diesel soot sample upon received was examined by SEM (Figure 4.1) and was analyzed for elemental compositions (Table 4.1). The TEM images showing the size and morphology of diesel soot particles in suspensions after 1 h and 24 h sonication treatments were presented in Figures 4.2 and 4.3, respectively. Meanwhile, DLS was employed to measure the hydrodynamic size of soot particles in water (Figure 4.4). After 1 h sonication, chain-like aggregates of 10-50 nm spherules of soot particles were observed in Figure 4.2, with Figure 4.2d showing the microstructure consisting of turbostratic graphitic layers [209]. Comparison of TEM images in Figures 4.2 and 4.3 indicated that 24 h sonication broke up most soot agglomerates into detached primary spherules, hence exhibiting a more uniform and smaller particle size distribution profile (Figure 4.4a), which is typical for combustion engine emissions and is similar to measurements conducted by NIST [199] (Figure 4.4b). Note that this intensity weighted size distribution determined by DLS was actually dominated by the larger particles that were low in number as they scatter more light [93] (Figure 4.4c). The intensity weighted average (Z-average) hydrodynamic diameter (D_h) after 24 h sonication was 169 ± 3 nm, with a polydispersity index (PDI) of 0.117 ± 0.015 (Figure 4.4a). These values did not

change significantly over the experimental time period, indicating that diesel soot NPs dispersed in water were kinetically stable. It should be noted that the detached primary soot particles studied in this paper were only relevant to their aqueous phase study of aggregation and were unlikely representative of airborne diesel soot particles present as chain-shaped aggregates [210-212] in the atmosphere where liquid water is not the dominant phase.
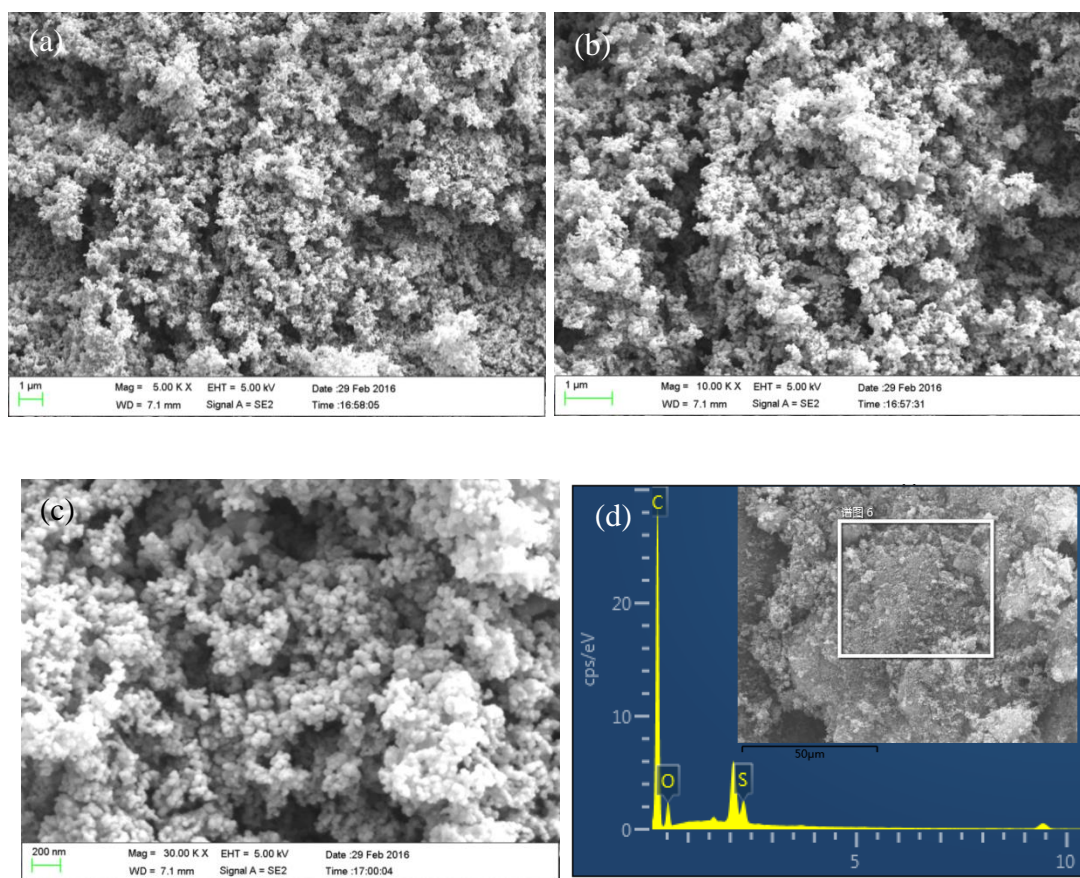
Figure 4.1 (a) (b) (c) Representative scanning electron microscope (SEM) images and (d) SEM-EDX analysis of pristine soot material as received from the supplier. Results of SEM-EDX analysis are presented in Table 4.1. The instrument used for analysis was MERLIN, Zeiss, Oberkochen, Germany.

Table 4.1 Elemental Compositions of Pristine Soot Material Determined through Energy Dispersive X-ray (EDX), X-ray Photoelectron Spectroscopy (XPS), and Elemental Analysis (EA)

	EDX[a] (atomic %)	XPS[b] (atomic %)	EA[c] (weight %)
C	86.72	87.15	76.17
O	12.31	12.85	17.95
H			2.15
N			1.27
S	0.97		2.14
Total	100	100	99.68

[a] Determined by scanning electron microscope (SEM) equipped with EDX (MERLIN, Zeiss, Oberkochen, Germany).

[b] Thermo Fisher K-Alpha.

[c] Vario EL III Element Analyzer.
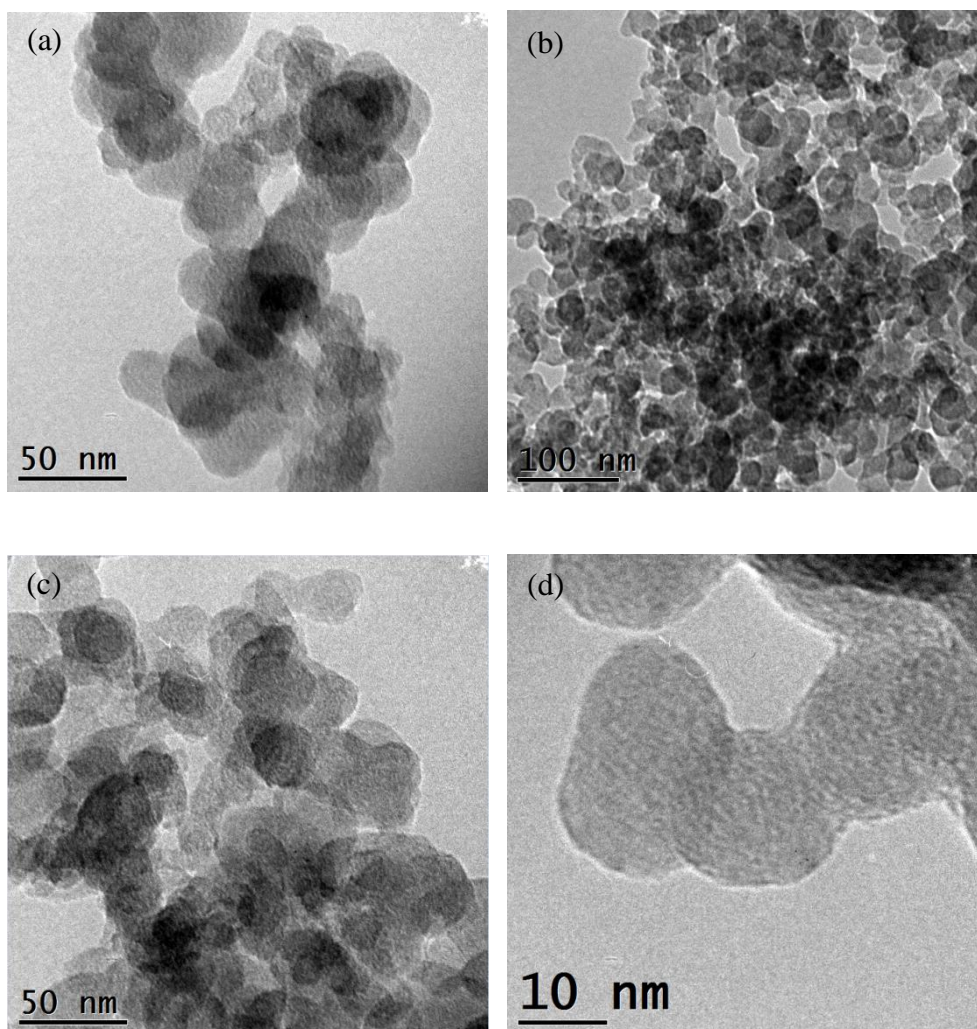
Figure 4.2 Representative TEM images of soot NPs dropped on 200 mesh carbon coated copper grids after sonication in water for 1 h. Images were acquired on a TEM (Topcon 002B, Topcon Corp., Tokyo, Japan).
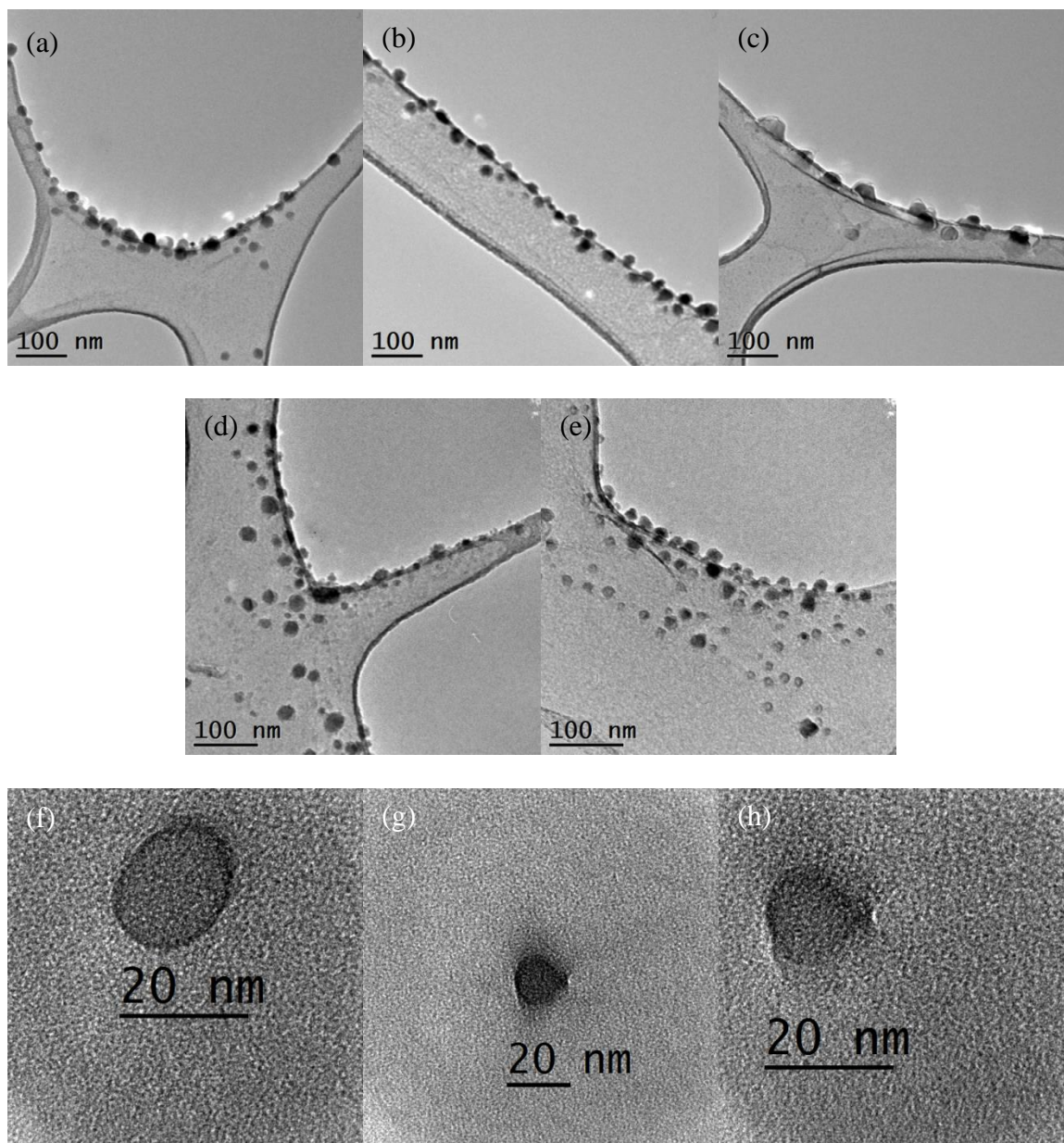
Figure 4.3 Representative TEM images of soot NPs dropped on 200 mesh carbon coated copper grids after sonication in water for 24 h. Images (a) to (e) were acquired on a TEM (Topcon 002B, Topcon Corp., Tokyo, Japan) and (f) to (h) on a HRTEM (JEM 2010F, JOEL USA Inc., MA) operating at 200 kV.

(a)
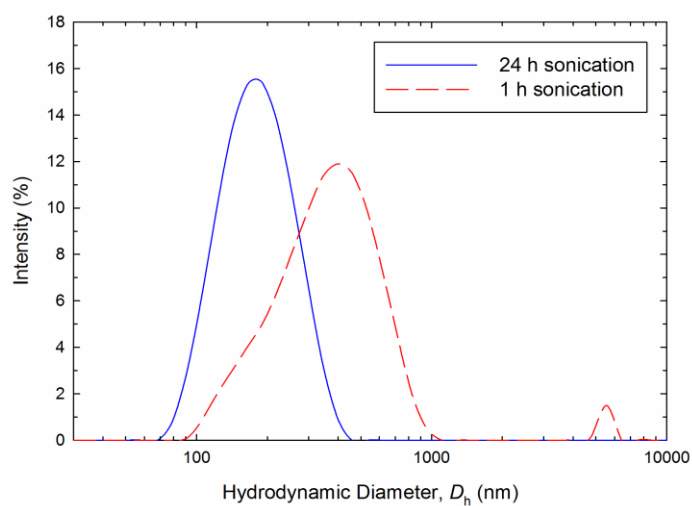
(b)
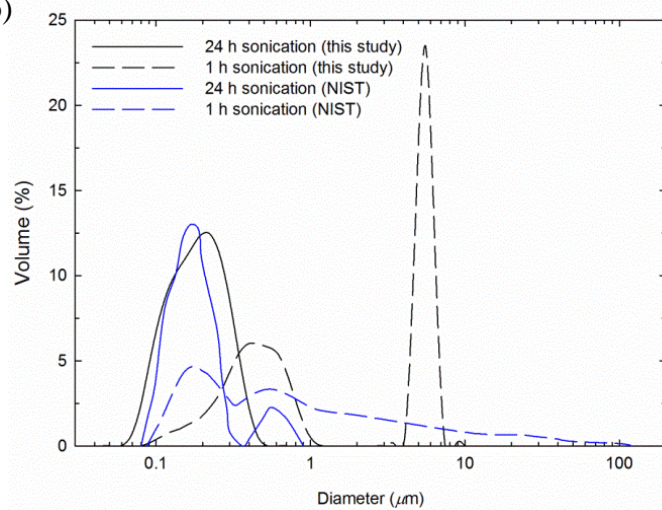
(c)
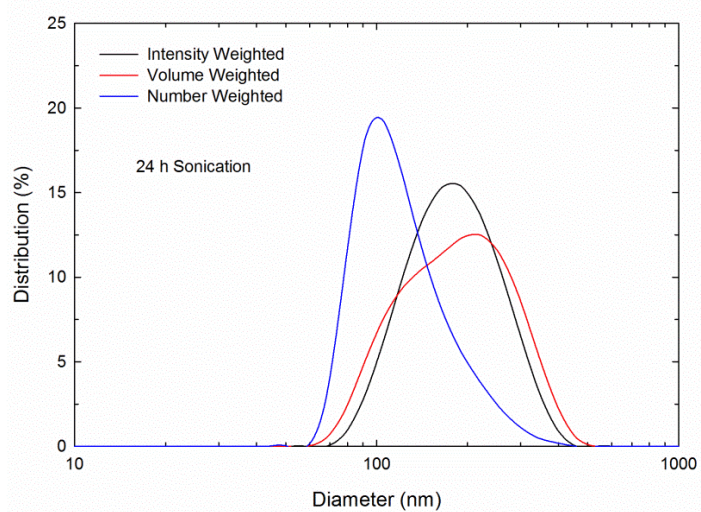
Figure 4.4 (a) Intensity weighted size distribution of soot NPs after 1 h and 24 h sonication measured by DLS in this study. The intensity-weighted average (Z-average) hydrodynamic diameter (D_h) after 24 h sonication was 169 ± 3 nm, with a polydispersity index (PDI) of 0.117 ± 0.015. It indicates that extended sonication broke up most agglomerates, showing a soot profile typical for combustion engine emissions. (b) Volume weighted size distribution of soot NPs in suspensions sonicated for 1 h and 24 h measured in this study (black lines) and by National Institute of Standards and Technology (NIST) (blue lines, data extrapolated from NIST [199]). It demonstrates that the size measurement results reported by NIST for SRM 1650b soot samples were reproduced in this study following the same treatments. (c) Intensity/volume/number weighted size distributions of soot NPs in suspension sonicated for 24 h in this study. It suggests that the size distribution was dominated by the largest soot particles of the sample that were actually low in number.

The ζ potentials of diesel soot NPs in the presence of electrolyte were determined at pH 6 over a range of monovalent or divalent salt concentrations (Figure 4.5a), with the corresponding EPM values presented in Figure 4.5b. In general, particles in suspensions having greater ζ potentials (absolute values) will tend to repel each other and to form stable suspensions, whereas particles having lower ζ potentials may aggregate due to mutual attraction. The soot NPs remained negatively charged over the concentrations examined in both electrolytes. The ζ potential of soot NPs in Milli-Q water or at very low concentrations of monovalent salt (e.g., 1 mM NaCl) was near -40 mV, indicating a

stable suspension [213, 214]. The gradual increase in concentration of both electrolytes generally resulted in lower negative ζ potential due to charge screening by Na^+ and Ca^{2+} counterions, as is commonly observed for other colloidal particles [24]. The greater efficiency of Ca^{2+} in screening the surface charges of soot NPs compared to Na^+ is possibly due to specific adsorption of calcium ions [39]. The magnitude and variation of ζ potentials measured in this study for the soot NPs were consistent with those observed for other diesel soot particles [194] and carbon black [21] under similar aqueous conditions.
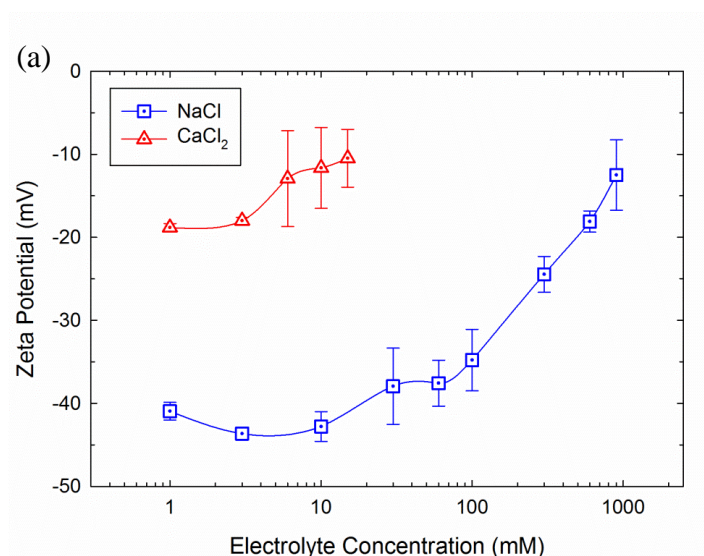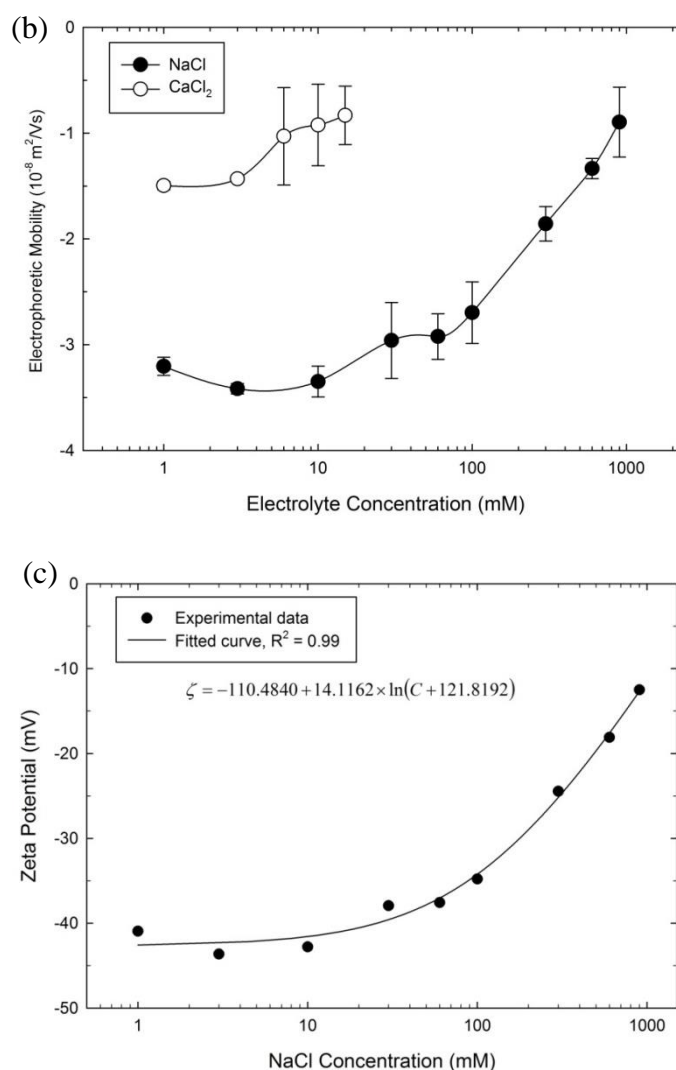
Figure 4.5 (a) ζ potentials and (b) electrophoretic mobilities (EPM) of soot NPs as a function of monovalent and divalent salts concentration measured at pH 6 and 25 °C. The concentration of soot NPs was 10 mg/L. The lines are meant for vision guidance. (c) ζ potentials of soot NPs as a function of NaCl concentration (C) at pH 6 extrapolated with the fitted curve. The experimental data points reproduced from (a) are fitted by a logarithm-3-parameter function for DLVO calculations.

4.3.2. Aggregation Kinetics Influenced by Electrolytes

TRDLS was employed to study the aggregation kinetics of soot NPs in the presence of 40-1,000 mM monovalent electrolytes (NaCl, NaNO$_3$, NH$_4$Cl, and Na$_2$SO$_4$) and 2-100 mM divalent electrolytes (CaCl$_2$ and MgCl$_2$) at pH 6. Representative aggregation profiles showing the initial rates of increase in D_h as a function of NaCl concentration are presented in Figure 4.6a. No significant aggregation was observed at 100 mM NaCl, from which a small increase in electrolyte concentration to 130 or to 150 mM NaCl resulted in a corresponding small increase in the aggregation rate. This is characteristic of the reaction-limited (slow) aggregation regime, where the electrostatic repulsion preventing particles from aggregation was reduced by charge screening as revealed in Figure 4.5a. At higher concentrations (e.g., 300 and 600 mM), however, increase in the electrolyte concentration did not further increase the aggregation rate because the energy barrier was completely eliminated in this diffusion-limited aggregation regime. The results indicated that the aggregation behavior of soot NPs was dominated by DLVO-interactions by the interplay between electrostatic and van der Waals interactions, as has been widely reported for other natural or engineered colloidal particles [202, 215-219].

By normalizing the initial slopes of the aggregation profiles using eq 4.2, the attachment efficiencies α were determined to construct the soot NPs stability curves in the presence of different electrolytes in Figure 4.6b. For each electrolyte, the soot NPs exhibited DLVO aggregation behavior in which both distinct reaction-limited ($\alpha < 1$) and diffusion-limited ($\alpha = 1$) aggregation regimes were observed. It was verified that the average k_{fast} values obtained at high ionic strength for all electrolytes were the same (within 10% experimental error), indicating the diffusion-controlled aggregation kinetics under such conditions. The critical coagulation concentrations (CCC), which are the

minimum electrolyte concentration to induce diffusion-limited aggregation, were determined for each electrolyte by fitting the attachment efficiency profile using eq 4.13 [220]:

$$\alpha = \frac{1}{1+\left(\frac{CCC}{C_S}\right)^{\beta}}$$ (4.13)

where C_S is the molar salt concentration, and β is the slope of dlog(α)/dlog(C_S) in the reaction-limited aggregation regimes.

All the stability profiles shown in Figure 4.6b could be well quantified with eq 4.13. The determined CCC values were 152, 157, 160, 91, 4.6, and 5.7 mM for NaCl, NaNO$_3$, NH$_4$Cl, Na$_2$SO$_4$, CaCl$_2$, and MgCl$_2$, respectively. In general, a higher CCC value indicates greater colloidal stability of particles against aggregation. The CCC values for the first three monovalent electrolytes are about the same and are slightly greater than that for Na$_2$SO$_4$, but are roughly 30 times of the values quantified for both divalent cationic electrolytes (CaCl$_2$ and MgCl$_2$). The data indicate that the anion type (Cl$^-$, NO$_3^-$, and SO$_4^{2-}$) may have insignificant influence on the soot NPs stability, which is consistent with prior report for other carbonaceous NPs such as multiwalled carbon nanotubes (MWNT) [201] and fullerene NPs [37, 221]. The CCC values for divalent electrolytes being 30 times lower than those for monovalent electrolytes is consistent with the ζ potential results in Figure 4.5a. The ratio of CCC values for the soot NPs in divalent salts (CaCl$_2$) to monovalent (NaCl) is proportional to $z^{-5.05}$ (where $z = 2$ is the counterion valence). This proportionality is reasonable because the CCC dependence on couterion valence for colloidal particles may range from z^{-2} to z^{-6} (Schulze-Hardy Rule) in practice [24, 25]. The soot CCC values of ~150 mM for monovalent salts and ~5 mM for divalent

salts are somewhat higher than those reported for fullerene NPs (120 mM NaCl and 4.8 mM CaCl$_2$ [38]) and considerably higher than the acid-treated MWNT (~90 mM monovalent salts and ~2 mM divalent salts [201]). The higher CCC values determined for soot NPs compared to other carbonaceous particles are likely due to the more negative ζ potential of soot NPs.

Note the CCC values determined are much higher than the equivalent ionic strengths (*I*) of average freshwater [222] and cloud water [223], but are much lower than *I* of average seawater [224] (Table 4.2). Meanwhile, considering the typical concentrations of soot particles in wet environments (Table 4.3), it is likely that soot NPs could remain stable against self-aggregation under typical salinity conditions in freshwater and in cloud droplet environments, but they should aggregate and settle out in estuaries.

(a)

(b)
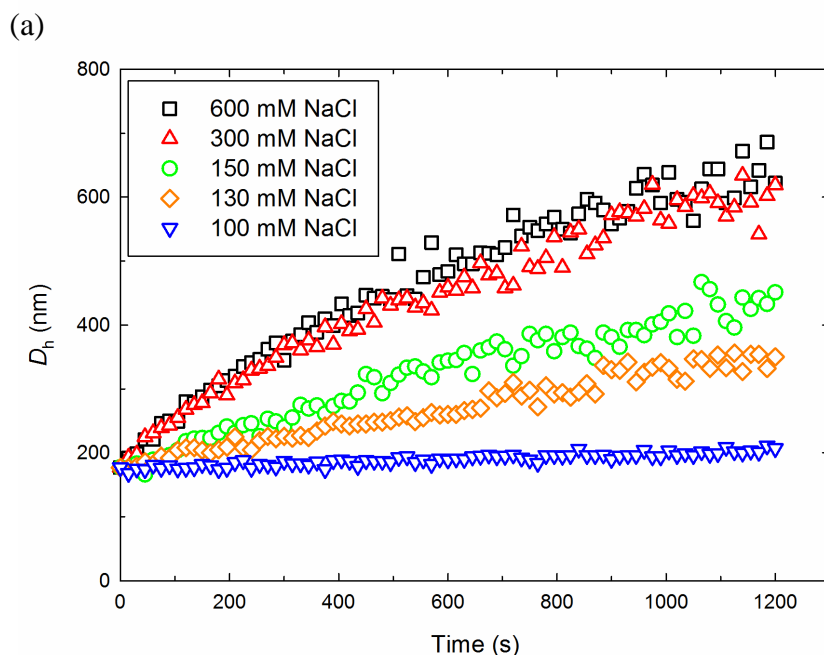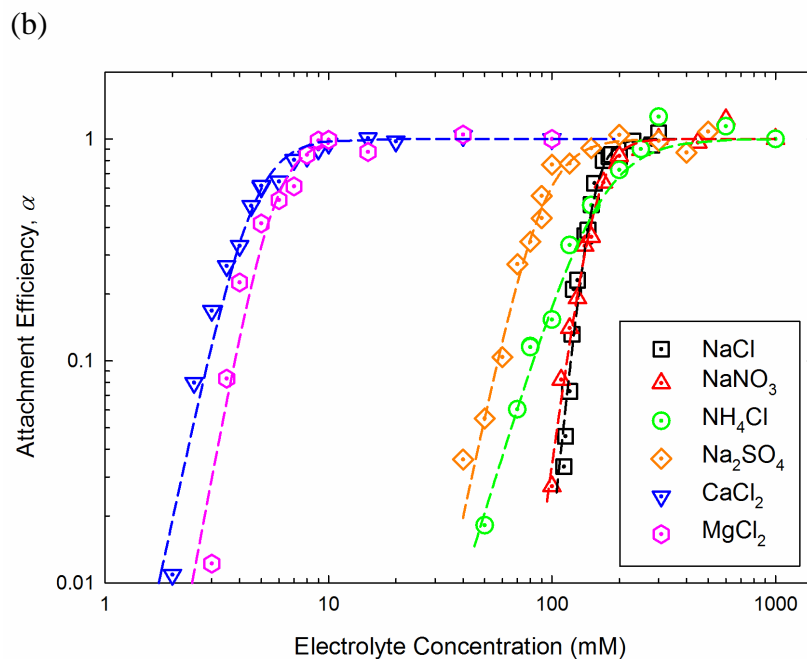
Figure 4.6 Influence of electrolyte on aggregation kinetics of soot NPs. (a) Aggregation profiles of soot NPs at various NaCl concentrations; (b) Influence of electrolyte composition on attachment efficiencies of soot NPs. Dashed lines represent fits to eq 4.13. All experiments were conducted at an soot NPs concentration of 10 mg/L and at pH 6.

Table 4.2 Compiled typical ionic concentrations in natural wet environments.

Wet Environments	pH	Na^+	K^+	NH_4^+	Ca^{2+}	Mg^{2+} (mM)	Cl^-	HCO_3^-	NO_3^-	SO_4^{2-}	I^a
Surface Water[b]											
Rivers (global average)	6.5-8.5	0.16	0.0256	0.00008	0.2	0.099	0.11	0.5	0.0016	0.05	1.1
Streams (minimum)	4.7	0.0026	0.0026		0.0015	0.0021	0.0025			0.0015	0.014
Streams (maximum)	8.5	15.2	0.16		5.24	3.29	14.9	5.74		7.49	50
Rivers (minimum)	6.2	0.35	0.013	0.0003	0.05	0.035	0.017	0.164	0.0008	0.023	0.49
Rivers (maximum)	8.2	1.10	0.102	0.0022	1.25	0.498	0.704	2.79	0.0032	0.604	7.05
Groundwater[b]											
Groundwater (typical)	6-8.5	8.70	0.256		2.49	2.06	0.282	8.2	0.161	3.12	24.1
Seawater[c]											
Seawater (typical)	7.5-8.4	457	9.97		10.2	55.6	535	2.33	0.0108	28.1	690
Cloud Water											
India[d]	6	0.204	0.017	0.028	0.098	0.05	0.234		0.068	0.099	0.674
USA[e]		0.038	0.005	0.17	0.033	0.011	0.023		0.11	0.113	0.424
China[f]	3.7	0.06	0.083	1.376	0.313	0.036	0.156		0.772	0.666	3.08
Poland[g]	4.6	0.1	0.045	0.21	0.007	0.025	0.1		0.24	0.1	0.897
Poland[h]	4.4	0.101	0.021	0.19	0.016	0.007	0.097		0.177	0.034	0.605
Puerto Rico[i]	6.14	0.477	0.01	0.005	0.012	0.055	0.446		0.011	0.027	0.626
NC, USA[j]	3.85-4.21	0.016	0.004	0.259	0.015	0.006	0.044		0.255	0.381	0.713

[a] Ionic strength (I) was calculated by $I = \frac{1}{2}\sum c_i z_i^2$ for the electrolytes listed in this table.

[b] Data from [222]. Rivers: 100,000 km^2; streams: 1-100 km^2.

[c] Data from [103].

[d] Data from [225].

[e] Data from [223].

[f] Data from [226].

[g] Data from [227].

[h] Data from [228].

[i] Data from [229].

[j] Data from [230].

Table 4.3 Compiled concentrations of refractory black carbon nanoparticles (rBC) or particulate BC (PBC) in wet environments. Note that aggregation experiments in this study have used soot NPs aqueous concentration of 10 mg/L (10,000 μg/L).

Water Sample	BC Concentration	Reference
Freshwater		
Lake Tahoe	0.02 – 0.45 μg/L	[231]
Stormwater runoff	100 – 600 μg/L	
Delaware river	100 – 400 μg/L	[232]
Poudre River water following the occurrence of wild fires	0.034 – 5.5 mg/L	[233]
Seawater		
Central Arctic Ocean	0.252 ± 0.192 μg/L	[234]
Gulf of Maine	<0.1 – 16 μg/L	[235]
Gulf of Mexico	~800 – 3700 μg/L	[236]
Chesapeake Bay	~90 – 280 μg/L	[232]
Rainwater[a]		
India	132 – 228 μg/L	[237]
Maldives	24 – 84 μg/L	[238]
Europe	2.4 – 44.4 μg/L	[239]
Lithuania	99.6 μg/L	[240]
Cloud Water[a]		
India	408 – 636 μg/L	[237]
Austria	1068 – 1404 μg/L	[241]
Austria	1152 μg/L	[242]

[a] Concentrations were converted from μmol/L to μg/L by multiplying the molecular weight of carbon (12 g/mol).

4.3.3. Good Agreement of Soot NPs Stability with DLVO Theory

The experimental attachment efficiencies (α) obtained above for soot NPs were compared with the theoretical stability curves predicted by the DLVO theory, from which the Hamaker constant of soot NPs can be derived. The change of theoretical α of the aggregating soot NPs as a function of symmetrical monovalent salt (e.g., NaCl) can be predicted for two identical sphere-sphere interactions following the DLVO calculations described in the experimental section (eqs 4.3 to 4.12) and using Figure 4.5c [38, 206, 207].

Figure 4.7 shows the theoretical DLVO prediction fitted to the experimentally derived attachment efficiencies in the presence of NaCl at pH 6. The results demonstrated good agreement between DLVO prediction and experimental data for the aqueous soot NPs. Slight deviation in the reaction-limited regime was observed, however. Such deviation may be attributed to the facts that the tested soot NPs are polydisperse and may not be strictly spherical (Figure 4.3).
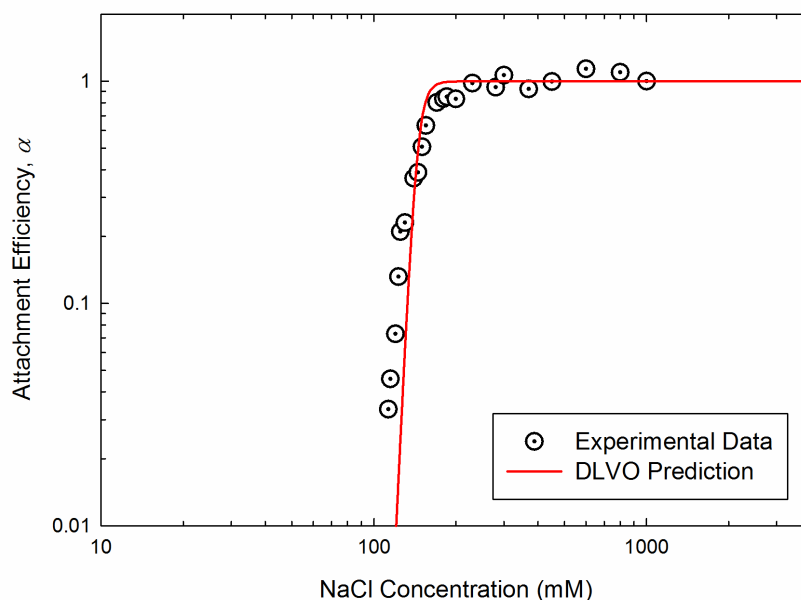
Figure 4.7 Comparison of soot NPs stability in the presence of NaCl with the DLVO theory at soot NPs concentration of 10 mg/L, pH 6, and 25 °C. Theoretical DLVO prediction (line, calculated using eq 4.3) and experimentally derived attachment efficiencies (data points, reproduced from Figure 4.6b) of soot NPs as a function of NaCl concentration. The fitting procedure yields the Hamaker constant of soot NPs in aqueous medium, A_{SWS}, of 1.4×10^{-20} J.

The slope of theoretical stability curve (Figure 4.7) in the reaction-limited regime is affected by R and the expression employed to calculate $V_R(h)$ (Figure 4.8); but the position of CCC is sensitive to A_{SWS} (Figure 4.9). Figure 4.8 shows that the calculations employing CPA expression (eq 4.7) always provided theoretical curve with the shallowest slope because CPA expression predicts the minimum repulsion energy among the three expressions [24]. The CPA expression provided the best fit to the experimental

data compared to the LSA (eq 4.11) and CCA (eq 4.12) expressions, indicating its underlying assumption that soot NPs may develop surface charges by rapid sorption of the potential-determining ions and that the surface potentials remain constant when two surfaces approach to each other [91]. Therefore, A_{SWS} was the only fitting parameter in this fitting procedure such that the CCC value of the theoretical curve matches the experimental result (i.e., 152 mM NaCl).
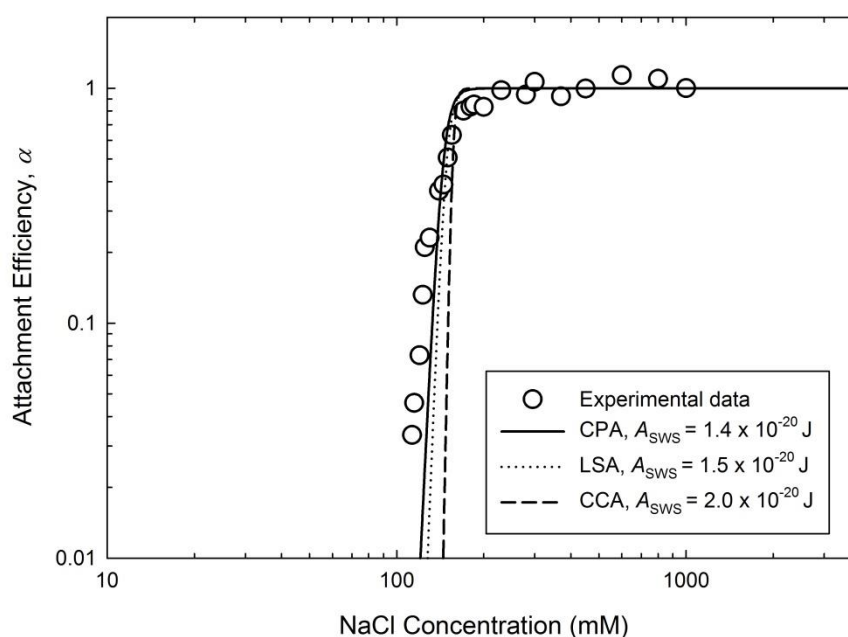
Figure 4.8 The effect of charge regulation on theoretical DLVO prediction of attachment efficiency for soot NPs in the presence of NaCl at pH 6 and 25 ℃. The CPA (eq 4.7), LSA (eq 4.11), and CCA (eq 4.12) expressions are employed to calculate the electrical double layer (EDL) repulsion potential energy. R_h is utilized throughout to approximate the particle radius. The Hamaker constants are fitted for each expression such that the critical coagulation concentrations (CCC) of theoretically prediction match the experimental result (152 mM NaCl).
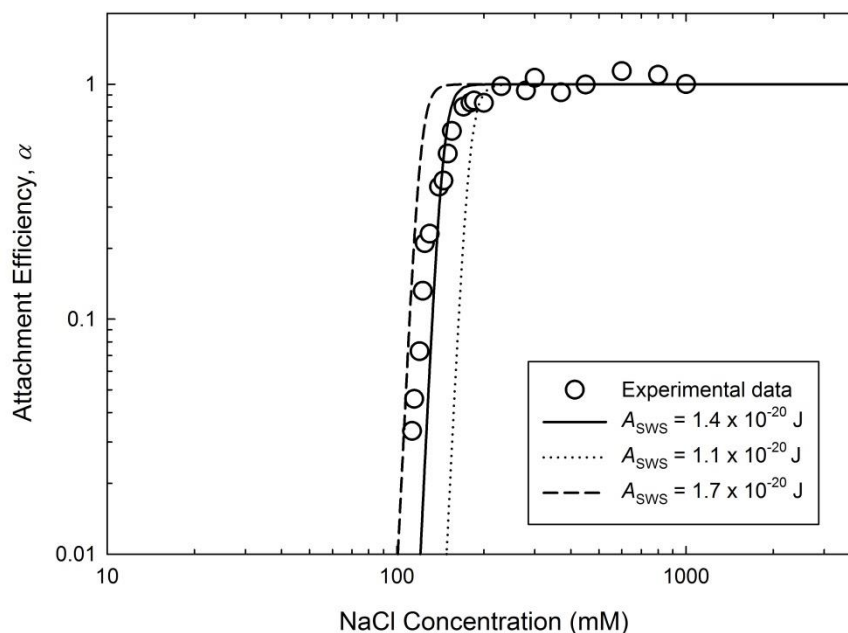
Figure 4.9 Sensitivity of the Hamaker constant on the theoretical DLVO prediction of attachment efficiency curves of soot NPs in the presence of NaCl at pH 6 and 25 ℃. The CPA expression is utilized throughout to calculate the $V_R(h)$. R_h is used to approximate the particle radius.

The value of A_{SWS} employed for the theoretical prediction, which is the effective Hamaker constant of soot NPs in aqueous medium, was 1.4×10^{-20} J. This is the first report of the Hamaker constant for soot particles determined using the colloidal chemistry approach. For comparison, our derived A_{SWS} value for soot is greater than those for aqueous fullerene NPs (0.67-0.85×10^{-20} J [37, 38]) and is smaller than the A_{SWS} for graphite in water (3.7×10^{-20} J [105]) measured using the same colloidal chemistry approach. By employing the following relationship [23]:

$$A_{SWS} \approx \left(\sqrt{A_{SS}} - \sqrt{A_{ww}}\right)^2 \qquad (4.14)$$

where A_{SS} and A_{WW} are the Hamaker constants of soot and water interacting in a vacuum, respectively, and by assuming A_{WW} to be 3.7×10^{-20} J [23], the calculated Hamaker constant of diesel soot in a vacuum, A_{SS}, is 9.7×10^{-20} J. Previous studies demonstrated that diesel particles can differ significantly from proposed surrogates such as flame-formed soot particles or manufactured carbon blacks [243, 244]. Note that, however, the A_{SS} value (9.7×10^{-20} J) derived in this study for the diesel soot NPs with colloidal chemistry approach is very close to those recently measured for flame-formed soot particles using atomic force microscopy ($9.5\text{-}9.8 \times 10^{-20}$ J [245]) and those assumed for soot particles (10×10^{-20} J [72] and $\sim 8.3 \times 10^{-20}$ J [246]), but is about half of the A_{SS} value traditionally estimated for soot using surrogate graphite materials (23.8×10^{-20} J [74, 247, 248]). Nevertheless, the Hamaker constant reported here should be representative for typical diesel soot freshly emitted from heavy-duty diesel engines.

The derived Hamaker constant can be used in turn to predict the stability of soot NPs in wet environments at a specific NaCl concentration. For instance, the DLVO interaction energies between soot NPs are predicted using the A_{SWS} value derived in this study (Figure 4.10). Figure 4.10b demonstrates that increase in NaCl concentration lowers the energy barrier maximum due to charge screening, leading to a higher tendency for soot NPs to aggregate. The arrows in Figure 4.10b indicate that the separation distance between two soot NPs at the maximum energy barrier also decreases at higher ionic strength. The NaCl concentration diminishing the energy barrier to 0 corresponds very

well with the experimental CCC value (i.e., 152 mM), again indicating the consistency between the DLVO theory and the experimental results.

(a)

(b)
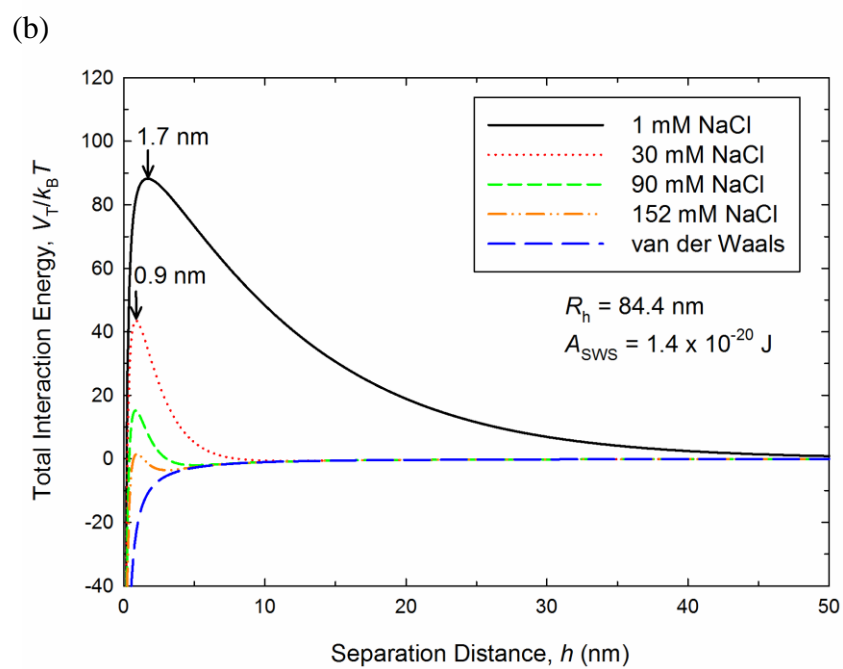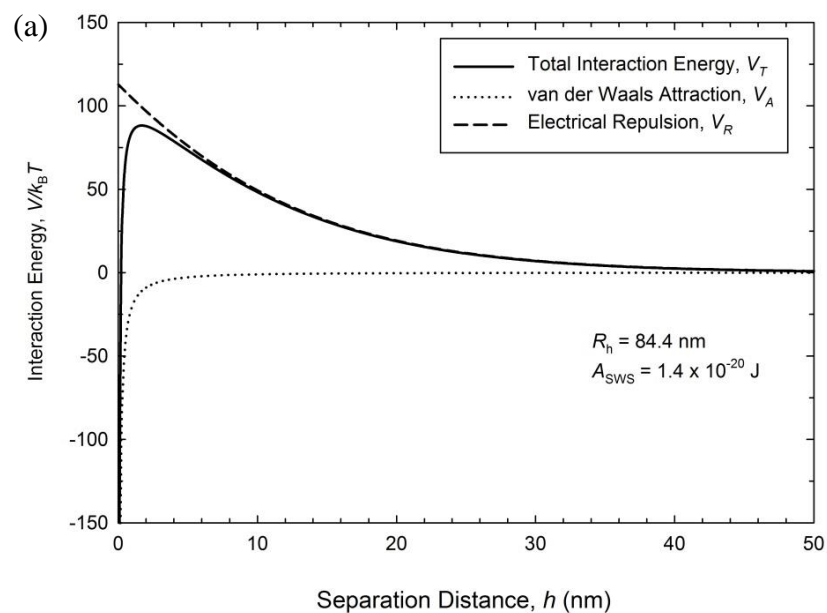
Figure 4.10 (a) DLVO interaction energies (V_T, V_R, and V_A) between two approaching soot NPs as a function of separation distance in the presence of 1 mM NaCl and at pH 6 and 25 °C. The sum of V_R and V_A yields V_T, which determines the likelihood of fast aggregation of soot NPs. (b) Theoretical DLVO prediction of interaction energy profile for two approaching soot NPs at various concentrations of NaCl. The van der Waals interaction profile is shown. The arrows indicate the distance from particle surface where the energy barrier reaches the maximum. The CPA expression is utilized to calculate the $V_R(h)$. R_h is used to approximate the particle radius. The derived Hamaker constant of soot in aqueous medium (A_{SWS}), 1.4×10^{-20} J is used for the calculations.

4.3.4. Solution pH Effects

The solution pH effects on the surface properties and aggregation kinetics of soot NPs were quantified for elucidating the aggregation mechanisms. The aggregation profiles of soot NPs at pH 3, 6, and 10 in the presence of 200 mM NaCl are compared in Figure 4.11a, which shows that the aggregation rate decreased as the pH increased. By normalizing the initial slopes of the aggregation profiles, the attachment efficiencies at pH 3, 6, and 10 were calculated to be 1.05, 0.83, and 0.16 (Figure 4.11b), respectively. The pH effects on soot NPs stability are quantitatively shown in Figure 4.11b, where the attachment efficiencies are determined as a function of NaCl concentration at pH 3, 4, 5, 6, 8, and 10. All profiles exhibited both the reaction-limited and diffusion-limited aggregation regimes. It is clear that the soot NPs stability increased as a function of

solution pH, which is consistent with prior reports for negatively-charged carbonaceous particles such as fullerene NPs [37, 249, 250] and MWNT [39, 201, 251, 252].

The stability profiles in Figure 4.11b were fitted to the empirical relationship of eq 4.13 to determine the CCC value at each pH condition. Figure 4.11c demonstrates that the CCC values determined for soot NPs increased linearly with solution pH, which is similar to the observations reported for acid-treated MWNT [201]. To better understand the role of solution pH in soot NPs stability, the particle surface charge was probed by measuring the change of ζ potentials as a function of solution pH. A monotonic decrease in ζ potentials at pH from 2 to 12 is observed in Figure 4.11c, indicating that the electrostatic repulsion was elevated at higher pH, preventing soot NPs from aggregation. Alhough some studies pointed out that ζ potential measurements may not be directly representative of the surface charge density of colloidal particles [201, 253], here, we observe a good correlation between the change in ζ potentials and the aggregation behavior of soot NPs as a function of solution pH.

(a)

(b)

(c)
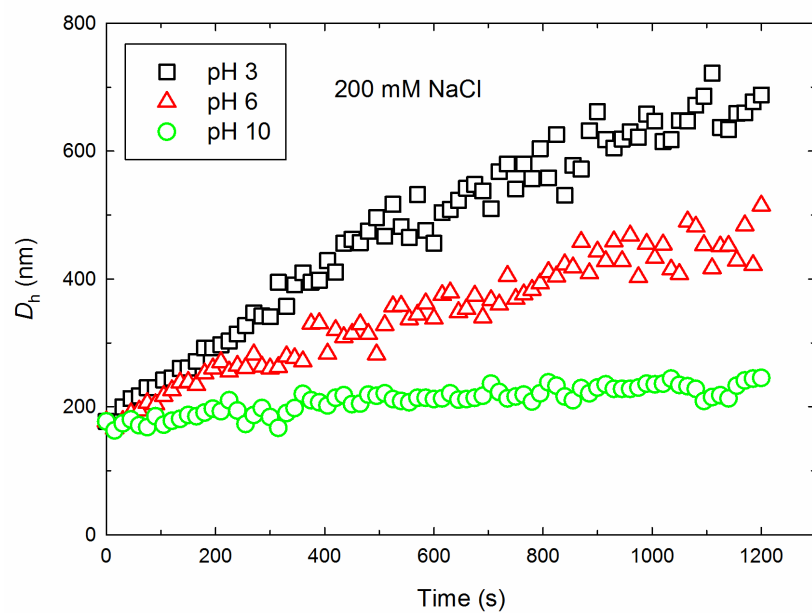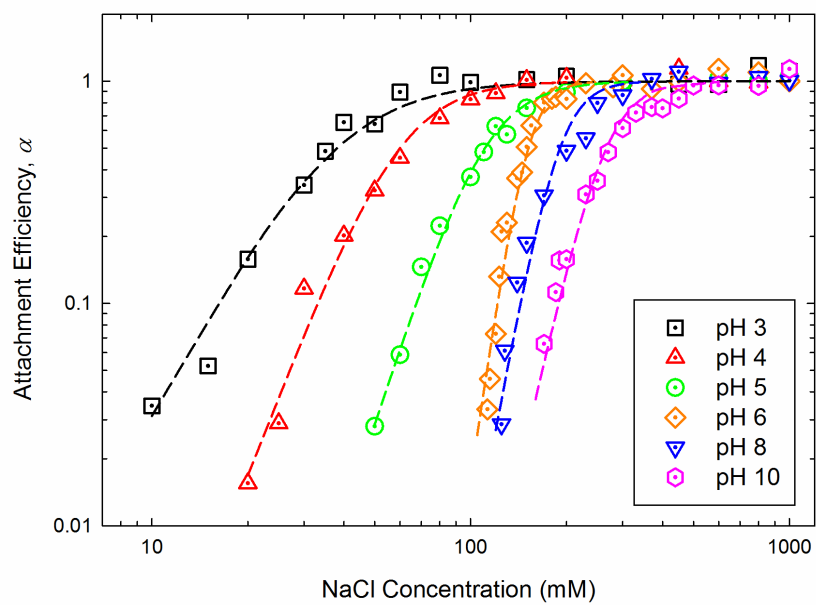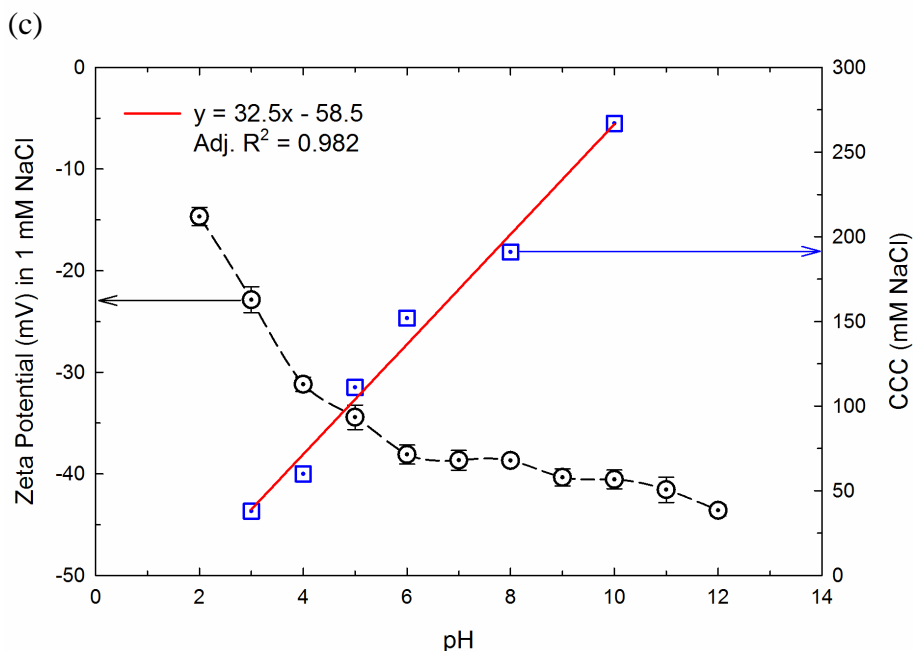
Figure 4.11 Influence of solution pH on soot NP stability. (a) Aggregation profiles of soot NPs at pH 3, 6, and 10 in the presence of 200 mM NaCl; (b) Attachment efficiencies of soot NPs as a function of NaCl concentration at pH 3, 4, 5, 6, 8, and 10. Dashed lines represent best fits to eq 4.13. The data at pH 6 were reproduced from Figure 4.6b; (c) ζ potentials of soot NPs in the presence of 1 mM NaCl (dashed line for vision guidance) and critical coagulation concentrations (CCC) of soot NPs in NaCl as a function of pH with linear regression.

To elucidate the origin of negative surface charge on the soot NPs in aqueous medium, potentiometric titration measurements were conducted for the aqueous soot suspension. Figure 4.12 shows that the titration curve of soot NPs deviates considerably from the blank curves without soot NPs, indicating the soot NPs contained acidic surface functional groups that may dissociate upon the addition of NaOH at solution pH above ~4.

This result is consistent with the chemical properties characterized for soot in prior studies [254-261], which identified surface functional groups on soot that are predominantly oxygen-based including the acidic functionalities [262, 263] such as hydroxyl (-OH) and carboxyl (-COOH) groups. These oxygen functional groups are likely located at the defective soot graphitic structure [264] and could increase the soot reactivity [256, 260, 264] and toxicity [19].

The high oxygen content (~12%) in Table 4.1 and the Fourier transform infrared (FTIR) spectroscopy in Figure 4.13 indicate the presence of these oxygen functional groups (e.g.-OH and -COOH) on the tested diesel soot NPs. The tested diesel soot sample exhibited typical FTIR spectra as those observed for soot materials in previous studies [260, 265, 266]. Apparent absorption bands appeared at 3448, 3143, 1618, 1400, 1120, and 669 cm^{-1}. The band centered at 3448 cm^{-1} with shoulders from 3268-3542 cm^{-1} originates from hydroxyl group (hydrogen-bonded O-H) stretching [267]. The band at 3143 cm^{-1} can be either assigned to –OH group associated with carboxylic acids [110, 267], or to the C-H stretching vibrations associated with C=C bonds [265]. The peaks at 1618 cm^{-1} are characteristics of an aromatic carbonyl group, which can be interpreted for the soot as an carbonyl group attached to the graphenes [260, 265]. The sharp band at 1400 cm^{-1} may arise from unsaturated C-H bending vibrations [265, 267]. The weak absorption at 1120 cm^{-1} can be due to C-O stretching in carboxylic acids [267]. Finally, the band at 669 cm^{-1} are related to out-of-plane vibration of C-H groups in aromatic structures [267].

Therefore, deprotonation of these acidic functional groups should be at least partially responsible for the acquisition of negative surface charge on the soot NPs and hence their

stability against aggregation in aqueous medium. Nevertheless, a lack of inflection point on the soot titration curve suggests that complexation of functional groups and/or other source of surface charge could also exist for the diesel particulates given their highly complex composition.
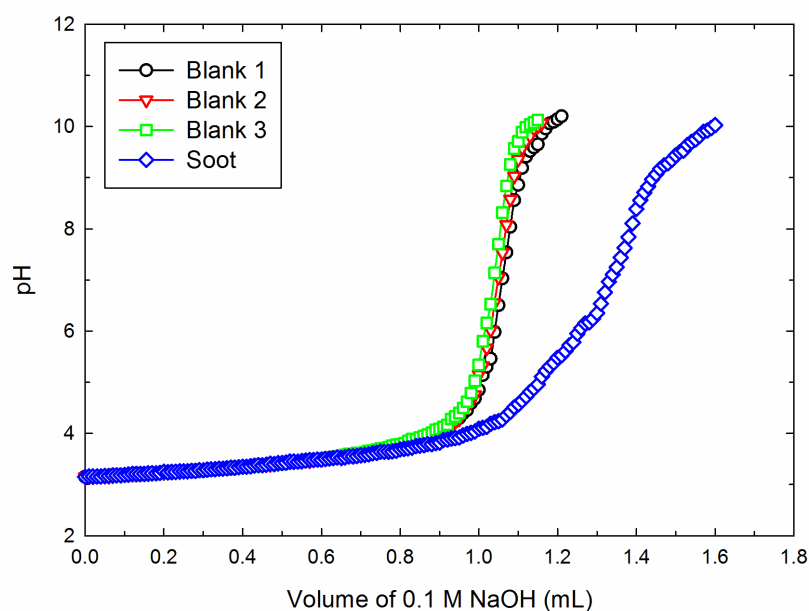
Figure 4.12 Potentiometric titration profiles of soot NPs from pH 3 to 10. The suspension concentration of soot NPs was 0.5 g/L. The blanks contained Milli-Q water without soot NPs.
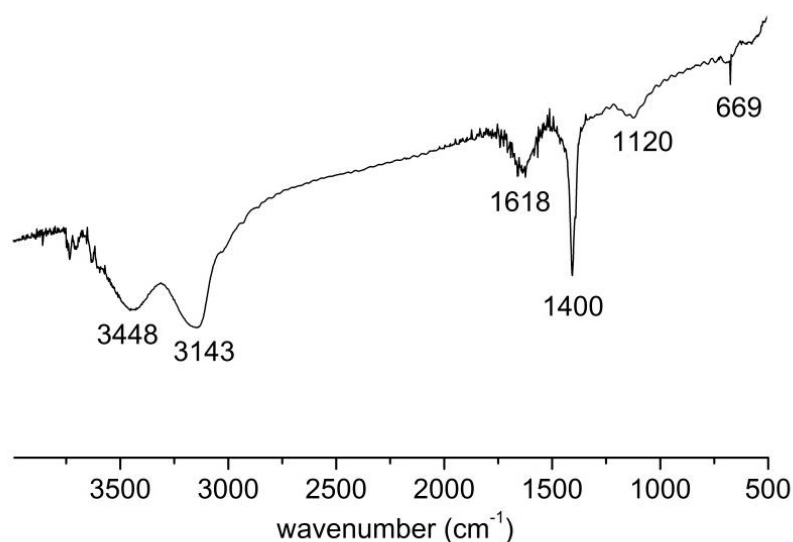
Figure 4.13 Fourier transform infrared (FTIR) spectra of the pristine soot NPs as received from the supplier using a FTIR spectrometer (Bruker Vector 33, Germany).

4.4. Environmental Implications

The results showed that soot NPs can remain dispersed in water due to their negatively charged surfaces possibly resulting from dissociation of oxygen functional groups. Their aggregation behavior was found to follow the classic DLVO theory, allowing approximation of the Hamaker constant for soot materials. This important physicochemical parameter could be used to develop predictive models for quantifying the fate and transport of soot NPs in wet environments. The study indicated that soot NPs unlikely aggregate among themselves in freshwater environments (e.g., lakes and rivers), but they should aggregate in salty aquatic environments such as estuaries. Their relative

stability in freshwater may make it difficult to be completely removed in water treatment systems. It also suggested that soot NPs may remain dispersed in regular rain droplets, but acidic conditions (such as in acid rain droplet) can increase the possibility of soot NPs aggregation as CCC <50 mM NaCl at pH 3-4 (acid rain) compared to CCC >110 mM NaCl at pH 5-6 (typical rain water). It should be noted that the soot sample used here was fresh diesel soot. Aging of soot and presence of natural organic matter and other environmental colloids may variously affect aggregation and colloidal stability of the carbonaceous NPs. Such effects should be investigated in future studies.

Acknowledgements

5. CHAPTER V. EFFECT OF MACROMOLECULES ON THE AGGREGATION OF SOOT NANOPARTICLES IN AQUEOUS ENVIRONMENTS
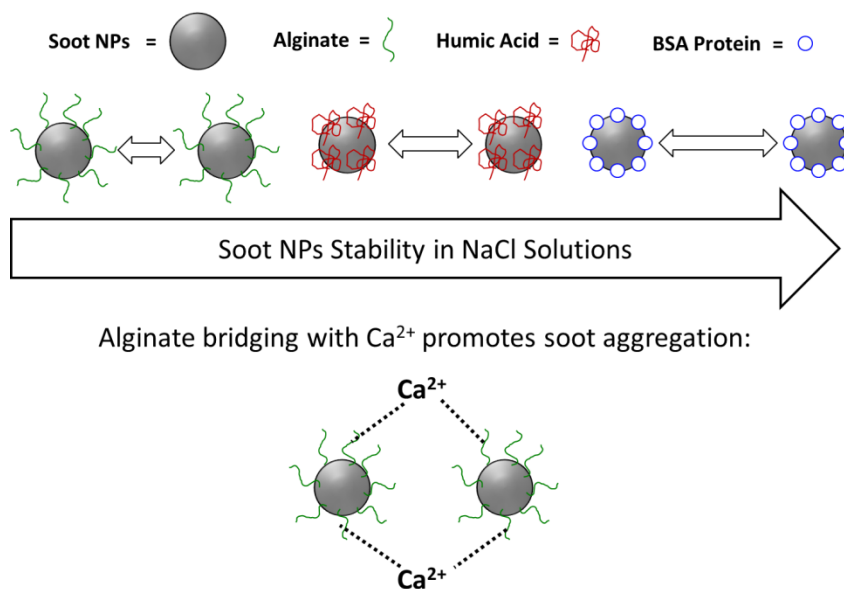
PROJECT TITLE: INFLUENCE OF MACROMOLECULES ON THE AGGREGATION KINETICS OF DIESEL SOOT NANOPARTICLES IN AQUATIC ENVIRONMENTS

The work in this chapter will be submitted in the title of "Influence of Macromolecules on the Aggregation Kinetics of Diesel Soot Nanoparticles in Aquatic Environments" to Environmental Science & Technology in 2017.

Abstract

Soot nanoparticles (NPs) produced from incomplete combustion eventually enter aquatic environments, wherein their aggregation behavior is poorly characterized. This study investigated the aggregation kinetics of soot NPs under various environmentally relevant solution chemistries, including the presence of macromolecules in varying concentrations of monovalent (NaCl) or divalent ($CaCl_2$) salts. The environmental and biological macromolecules used include natural organic matter [Suwannee River humic acid (HA) and fulvic acid (FA)], a polysaccharide (alginate), a protein [bovine serum albumin (BSA)], and a culture medium [Luria-Bertani (LB) broth]. The negatively charged soot NPs under aqueous phase exhibited both reaction- and diffusion-limited aggregation regimes with behavior similar to typical colloidal particles, allowing for determination of the critical coagulation concentrations (CCC). Results indicated that the aggregation rates of soot NPs were significantly retarded by the presence of BSA, followed by HA, alginate, LB, and FA. The stabilizing mechanism of soot NPs by macromolecules was identified as steric repulsion due to the adsorbed macromolecule layers on particle surface. BSA exhibited the strongest stabilization effect than other macromolecules since it has a more compact globular structure when attached to soot NPs, thereby imparting long-range steric repulsive forces. The presence of alginate at high calcium concentrations formed alginate gel, which significantly promoted soot NPs aggregation. The profound effects of macromolecules on the stability of soot NPs may have strong influences on their fate and transport in aquatic environments and their interactions with biological species.

5.1. Introduction

Soot particles are airborne carbonaceous particulate matter of sizes ~100 nm produced from incomplete combustion of fuel and biomass [268]. The unintentional emission of soot aerosols into the atmosphere is recognized to impact human health [19, 269], atmospheric chemistry [75, 270], and global climate change [268]. With an atmospheric lifetime varying from a few days to several weeks [271], soot particles eventually reach water bodies either directly via atmospheric deposition or indirectly along with suspended solids via fluvial discharge and soil erosion [34]. At a global scale, for instance, soot particles continuously deposit on the ocean at a rate of ~70 Tg C year^{-1} [272]. The ubiquitous distribution of soot particles in aquatic environments has strong impacts on the aquatic ecosystems [20, 21] and global carbon cycle [68]. These highly condensed carbonaceous soot nanoparticles (NPs) are potentially toxic [19] and may act as carriers for contaminants [35, 273], affect nutrient loading [21], and interact with biological species [20, 31, 32] in the water column and sediments.

Upon entering aquatic environments, the aggregation states of soot NPs will strongly influence their environmental fate, transport, and potential interactions with ambient solid surfaces [22]. Most studies to date have focused on the aggregation behavior of manufactured carbon-based NPs (MCNPs, e.g., fullerene [37, 38, 218], single-walled (SWNTs) [40, 274] and multi-walled carbon nanotubes (MWNTs) [39, 201], and graphene [42]) in aquatic environments. However, the fundamental aggregation kinetics of soot particles in aqueous phase is poorly characterized, despite the fact that the concentration of black carbon (i.e., soot) NPs is indeed 10^4 to 10^7 times greater than MCNPs in the water column and aquatic sediments [7]. There are a number of studies on the aggregation behavior of soot particles under dry [70-73] and humid [74-76]

atmospheric conditions but not in aqueous phase. Some studies reported the colloidal stability of carbon black, a surrogate for genuine soot, in various solvents [195, 196, 275], but the dissimilar surface chemistries of carbon black and soot can lead to their having substantially different colloidal stability [194]. One study examined the aggregation kinetics of engine soot particles in colloidal suspensions, but the dispersion phase was oil instead of water [276]. Based on limited information, Bisiaux et al. hypothesized that their observed rapid attenuation of soot particles in freshwater systems was attributed to unexpected aggregation of the particles [231]. In our recent study [277] we investigated the aggregation kinetics of diesel soot NPs in aqueous solutions, demonstrating that their aggregation behavior was governed by the interplay between van der Waals and electrostatic interactions as predicted by the classic Derjaguin−Landau−Verwey−Overbeek (DLVO) theory. Considering only the effects from electrolytes and solution pH, soot particles should remain stable against self-aggregation in freshwater environments but will likely aggregate under salty (e.g., marine) aquatic conditions [277].

Because of their large specific surface area and hydrophobic surface properties, soot NPs in aquatic environments will likely interact and associate with environmental and biological macromolecules. Natural organic matter (NOM), such as humic substances and polysaccharides, is ubiquitous in natural waters and has a strong affinity for the surface of soot NPs [27, 202, 278, 279]. Recent studies indicated that microorganisms such as viruses and bacteria readily attached onto reference diesel soot particles in surface waters [20, 31, 32], leading to their inevitable interaction with released biological macromolecules such as proteins [28, 280]. Likewise, experiments conducted on interaction of soot NPs with microorganisms often involve culture media that contain

biological macromolecules such as enzymes, proteins, and polysaccharides. The presence of macromolecules is expected to result in surface modification of soot NPs, thereby profoundly influencing their aggregation kinetics by steric repulsion originated from the adsorbed macromolecule layers [26, 281]. The ubiquity and impacts of soot NPs in aquatic environments necessitate a systematic understanding of their aggregation kinetics with macromolecules of environmental and biological relevance under various solution conditions.

The objective of this study was to investigate the aggregation kinetics of soot NPs in the presence of environmental and biological macromolecules under different solution chemistries relevant to aquatic environments. Diesel soot particulate matter (SRM-1650b) was selected as a reference material for soot particles due to its wide environmental relevance [33, 277, 282]. Five macromolecules were employed in this study, including two types of natural organic matter [Suwannee River humic acid (HA) and fulvic acid (FA)], a polysaccharide (sodium alginate), a protein [bovine serum albumin (BSA)], and a microbial culture medium [Luria-Bertani (LB) broth]. Aggregation experiments were conducted in solution chemistries varying in concentrations of monovalent (NaCl) or divalent ($CaCl_2$) electrolytes and macromolecules. The aggregation kinetics of soot NPs were used to construct stability curves, from which the critical coagulation concentrations (CCC) were determined. The physiochemical properties measured for soot NPs were used to elucidate their aggregation mechanisms in the presence of macromolecules.

5.2. Materials and Methods

5.2.1. Preparation of Soot NPs in Aqueous Solution

The diesel soot sample was from the same batch as the one used in our previous study [277], which is SRM 1650b obtained from NIST (Gaithersburg, MD) with representativeness of diesel particulate matter emitted from heavy-duty diesel engines. NIST has provided certified information for SRM 1650b on mass fraction values for selected polycyclic aromatic hydrocarbons (PAHs) and nitro-substituted PAHs, percent extractable mass of 20.2%, particle size distribution with a mean particle diameter of 180 nm, specific surface area of 108 m^2/g, and mutagenicity activity [199]. We have previously examined the pristine soot sample with scanning electron microscope (SEM), characterized its carbon and oxygen contents to be ~80% and 12%, respectively, and identified its surface functional groups [277].

To disperse the soot sample as NPs in aqueous solution, the same procedure used in our previous study [277] was followed. Briefly, 10 mg of SRM 1650b was introduced into 500 mL of Milli-Q water (resistivity > 18 MΩ·cm), which was stirred for 24 h on a magnetic stirrer followed by 24 h sonication in the dark. This yielded a black suspension containing 20 mg/L of well dispersed and kinetically stable soot NPs with an initial solution pH of 4.00 ± 0.01. The suspension pH was raised to 6.00 ± 0.01 and the stock suspension was stored in the dark at room temperature prior to experiments.

5.2.2. Solution Chemistry

The electrolyte stock solutions were prepared by dissolving ACS-grade monovalent (NaCl) or divalent ($CaCl_2$) salts in Milli-Q water and filtered through 0.1-μm filters

(Puradisc 25 TF, Whatman, Maidston, U.K.). The electrolyte stock solutions were diluted to desired concentrations to cover a wide range of environmental conditions. All solution pH in this study was adjusted to 6.0 using HCl and NaOH.

5.2.3. Preparation of Macromolecules

Two humic substances used in this study include a Suwannee River HA (Standard II) and a Suwannee River FA (Standard I) (International Humic Substances Society, St. Paul, MN). Other macromolecules included an alginate polysaccharide (alginic acid sodium salt, Cat. No. 180947, Sigma Aldrich), a BSA protein (Cat. No. A7030, Sigma Aldrich), and a LB broth microbial culture medium (Cat. No. BP9722, Fisher Scientific). The macromolecule stock solutions were prepared by dissolving 30 mg of dry macromolecule powders in 50 mL of Milli-Q water and stirring overnight in the dark. The solutions were then filtered under vacuum using a 0.22-μm cellulose acetate membrane (Corning Inc., Corning, NY), and the filtered stock solutions were adjusted to pH 6.0 and stored in the dark at 4 °C. The total organic carbon (TOC) content of each macromolecule stock solution was determined using a TOC analyzer (TOC-V CSN, Shimadzu, Kyoto, Japan) through high temperature oxidation at 680 °C. The TOC contents determined for the five stock solutions were 56.8% for HA, 74.7% for FA, 43.6% for alginate, 46.7% for LB, and 50.9% for BSA based on the macromolecule concentration of 600 mg/L. The macromolecule stock solutions were later diluted to desired concentrations in mg/L TOC content (mg C/L) according to these results for use in experiments.

5.2.4. Characterization of Aqueous Soot NPs

The particle size distribution of soot NPs after 24 h sonication was measured by DLS using a Zetasizer Nano ZS instrument (Malvern Instruments Ltd, Worcestershire, UK) at soot concentration of 10 mg/L, suspension pH of 6.0, and 25 °C. The DLS instrument employed a 4.0 mW He-Ne laser light operating at a wavelength of 633 nm and a scattering angle at 173° for Non-Invasive Backscatter (NIBS) optics. The performance of DLS instrument was verified with NIST-polystyrene nanosphere size standards. With the refractive index and absorption index for SRM 1650b set at 1.5 and 0.1, respectively, the DLS generated an intensity-weighted size distribution for soot NPs in the stock suspension, from which the mean intensity-weighted (Z-average) hydrodynamic diameter (D_h) was determined as the initial D_{h0} with a polydispersity index (PDI). The intensity distribution generated by DLS was further converted to a volume distribution and a number distribution using Mie theory.

The electrophoretic mobilities (EPM) of soot NPs were measured over a range of electrolyte concentrations in the presence or absence of macromolecules (i.e., alginate, HA, FA, LB, and BSA) using the Zetasizer Nano ZS instrument by phase analysis light scattering (PALS). The macromolecules were added to the soot suspension followed by addition of electrolyte, after which the EPM measurements were immediately initiated to mimic the aggregation experiments. The EPM measurements were conducted at soot concentration of 10 mg/L, macromolecule concentrations of 2.5 mg C/L for BSA and 10 mg C/L for other macromolecules, suspension pH of 6.0, and 25 °C. Triplicate samples were each measured for 10 times at each solution condition for the EPM analysis.

The soot samples were examined by a Topcon 002B (Topcon Corp., Tokyo, Japan) transmission electron microscope (TEM) operating at 200 kV. To prepare the soot stock suspension for TEM analysis, a drop of the suspension was placed on a nickel TEM grid coated with Formvar carbon and left to adsorb for 2 min. For TEM imaging of soot in the presence of alginate with $CaCl_2$, the same procedure for preparing the aqueous sample used in aggregation experiments was followed. A drop of the aggregating suspension was placed on the TEM grid 5 min after preparation of the sample suspension.

5.2.5. Determination of Soot Aggregation Kinetics

Time-resolved dynamic light scattering (TRDLS) was used to determine the aggregation kinetics of soot NPs using the same DLS instrument at pH 6 and 25 °C. The setup for the DLS instrument was the same as above except that each autocorrelation function was accumulated over a period of 15 s. The increases in D_h of soot over time in different solution chemistries were measured following the detailed aggregation experiment protocols described in prior studies [39, 277, 283]. In brief, 0.5 mL of stock suspension containing 20 mg/L of soot NPs was first introduced into a new glass vial (VWR, Chester, PA), which has been thoroughly cleaned and oven-dried under dust-free condition. A predetermined amount of Milli-Q water with pH adjusted to 6.0 was then added to the vial. For the aggregation experiments in the presence of macromolecules, aliquots containing varying volumes and concentrations of macromolecule and electrolyte were combined into the vial to form a total volume of 1 mL at their predesigned concentrations, with macromolecules added to the vial prior to the addition

of electrolyte. For the aggregation experiments in the absence of macromolecules, the procedures were the same, except that only electrolyte was added to the vial containing soot and Milli-Q water. The protocol ensured that the initial soot concentration (N_0) remained constant at 10 mg/L (see eq 5.2) for all aggregation experiments. The vial was then vortexed for 1 s (Vortex Genie 2, Fisher Scientific) before being immediately inserted into the DLS instrument to start the measurement, which lasted for a period between 20 min to 3 h. All aggregation experiments were conducted in triplicates to ensure data quality.

The initial aggregation constant (k) for the soot NPs is proportional to the initial rate of increase in D_h with time (t) and the inverse of the initial soot concentration (N_0) [204, 277]:

$$k \propto \frac{1}{N_0} \left(\frac{dD_h(t)}{dt} \right)_{t \to 0} \tag{5.1}$$

where k was determined from the slope up to the point where D_{h0} has increased to $1.5D_{h0}$. In cases where the linear regime ends before reaching $1.5D_{h0}$, the slope of the linear regime was approximated similarly. The fitted line was verified to intercept the y axis no more than 5% from D_{h0} for all aggregation experiments.

The attachment efficiency (α, equivalent to the inverse of stability ratio) ranging from 0 to 1 was used to quantify the aggregation kinetics of soot NPs under different solution chemistries. Given that N_0 was maintained constant at 10 mg/L for all aggregation experiments, α was calculated by normalizing the slope of aggregation under different solution conditions to the slope obtained under diffusion-limited (fast) aggregation conditions (i.e., at high concentrations of NaCl or $CaCl_2$ alone) [39, 284]:

$$\alpha = \frac{k}{k_{fast}} = \frac{\frac{1}{N_0}\left(\frac{dD_h(t)}{dt}\right)_{t\to0}}{\frac{1}{(N_0)_{fast}}\left(\frac{dD_h(t)}{dt}\right)_{t\to0,fast}} = \frac{\left(\frac{dD_h(t)}{dt}\right)_{t\to0}}{\left(\frac{dD_h(t)}{dt}\right)_{t\to0,fast}} \tag{5.2}$$

5.3. Results and Discussion

5.3.1. Characterization of Soot NPs in Aqueous Suspensions

The particle size of soot NPs in the stock suspension after 24 h sonication was determined by DLS and is shown as the intensity-weighted, volume-weighted, and number-weighted size distributions in Figure 5.1. The initial D_{h0} determined from the intensity-weighted size distribution was 159 ± 4 nm, with a PDI of 0.105 ± 0.018. This is very consistent with our previous results [277] and the results reported by NIST [199], indicating the reproducibility of our procedure.
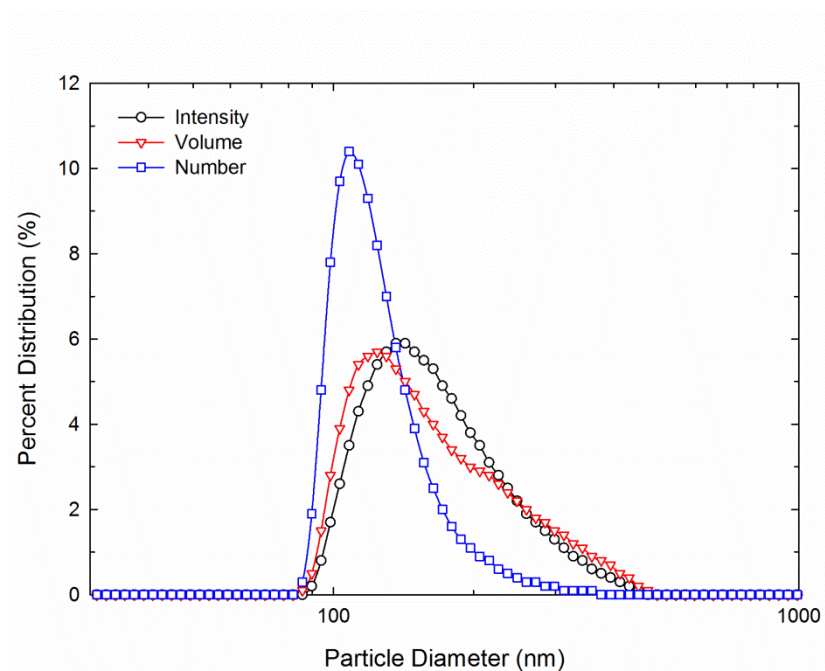
Figure 5.1 Intensity-weighted, volume-weighted, and number-weighted size distributions of soot NPs in stock suspension after 24 h sonication. The mean intensity-weighted (Z-average) hydrodynamic diameter (D_h) was determined to be 159 ± 4 nm, with a polydispersity index (PDI) of 0.105 ± 0.018. The measurement was conducted at soot NPs concentration of 10 mg/L, pH 6, and 25 °C.

The EPM of soot NPs in the presence of various macromolecules as a function of NaCl or $CaCl_2$ concentrations at pH 6 and 25 °C are presented in Figure 5.2. The measurements show that soot NPs remained negatively charged over the examined salt concentration range either in the absence or presence of macromolecules. In general, particles in suspension having highly negative or positive EPM values will tend to repel each other and form stable suspensions, which corresponds to the soot NPs with highly negative surface charge (EPM of -3.5 × 10^{-8} m^2 V^{-1} s^{-1} or zeta potential of -45 mV) in 1 mM NaCl. As is commonly observed for most colloidal particles [24], the increase in salt concentrations resulted in less negative EPM values of soot NPs due to charge screening effects by the Na^+ or Ca^{2+} cations, with Ca^{2+} divalent cation having a greater effect than Na^+ monovalent cation. The magnitude and variation of the EPMs of soot NPs as a function of salt concentrations in the absence of macromolecules were consistent with previous result for this same sample [277] and other reports for diesel soot particles [194] and carbon black [21] under similar conditions. According to our prior study [277], the soot NPs possibly acquired the negative surface charge in aqueous solution from dissociation of oxygen-based acidic functional groups such as hydroxyl (-OH) and

carboxyl (-COOH) groups that are likely located at the defective soot graphitic structure [264].

The presence of macromolecules did not significantly enhance the negative charge on soot NPs, with the most enhanced EPM value (from -2.53 to -3.68 $\times$ 10^{-8} m^2 V^{-1} s^{-1}) obtained at 0.01 mM CaCl$_2$ in the presence of alginate. This was similarly observed for single-walled carbon nanotubes (SWNTs) [274], whereas other studies is was reported that the presence of anionic surfactants and polyelectrolytes (e.g., HA and alginate) could add more negative charge to particle surfaces [285, 286]. On the other hand, BSA present at only 2.5 mg C/L effectively reduced the negative surface charge in both NaCl and CaCl$_2$ solutions. The reduction of soot surface charge in the presence of BSA was strong evidence of protein adsorption, which was also observed for other particles such as SWNTs [287] and gold NPs [288]. BSA with an isoelectric point (IEP) of 4.7-5 was negatively charged at the experimental condition of pH 6 [287, 289]. It has been documented that a negatively charged protein could spontaneously adsorb onto a negatively charged particle surface by incorporation of various cations (e.g., Na$^+$ and Ca^{2+}) into the protein-sorbent contact region [290, 291]. This process could prevent the accumulation of energetically unfavorable high electrostatic potentials [292, 293]. As a result, the adsorption of negatively charged BSA onto soot NPs of like charge has instead reduced the negative charge of soot NPs.
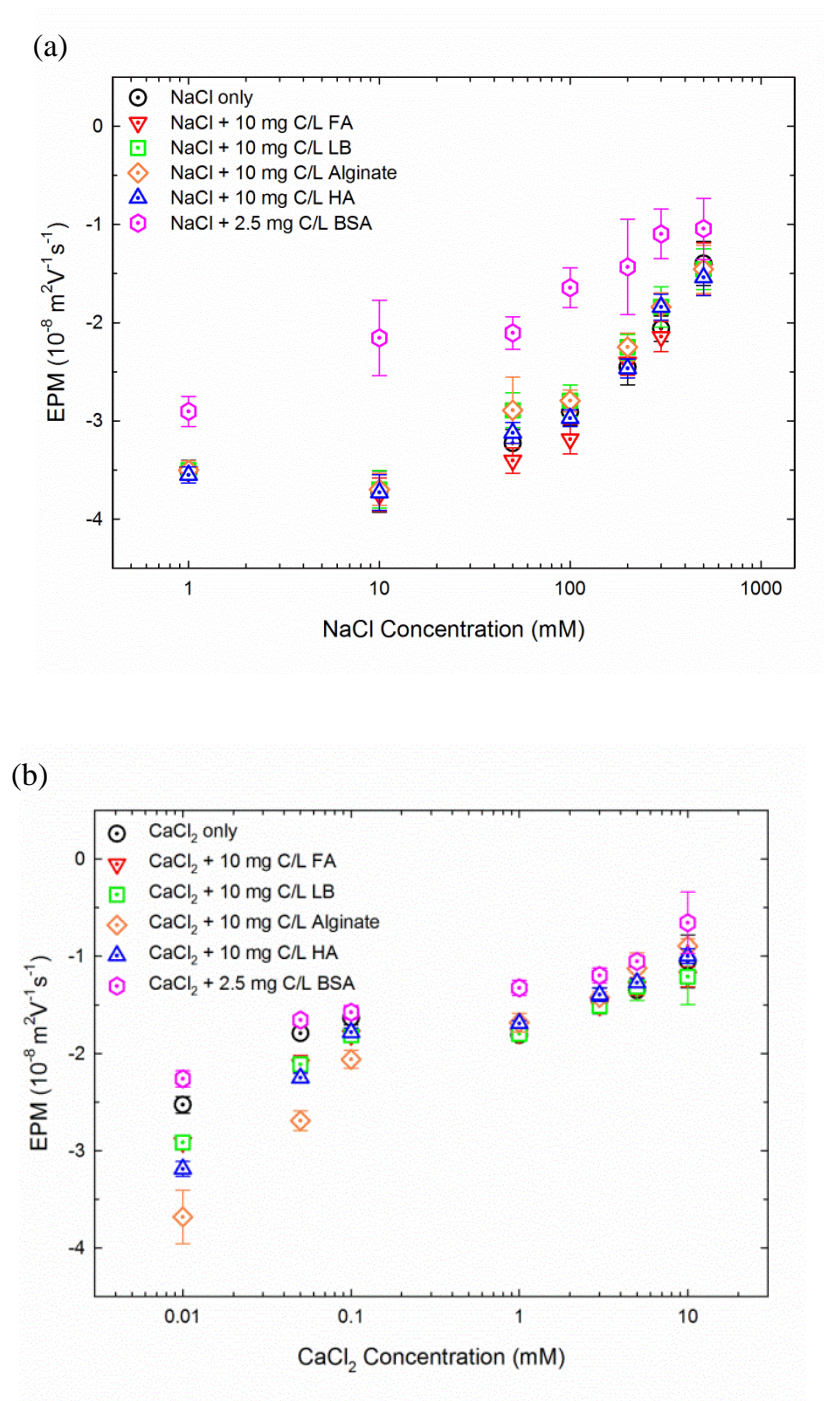
Figure 5.2 Electrophoretic mobility (EPM) of soot NPs in the presence/absence of various macromolecules as a function of (a) NaCl and (b) CaCl$_2$ concentrations at pH 6 and 25 °C. The tested macromolecules included Suwannee River fulvic acid (FA), Luria-Bertani (LB) broth, alginate, Suwannee River humic acid (HA), and bovine serum

albumin (BSA) protein. The macromolecule concentrations were maintained at 2.5 mg/L of total organic carbon (TOC) for BSA and 10 mg/L of TOC for other macromolecules. The soot NPs concentration was 10 mg/L. Each error bar represents one standard deviation from three independent samples each with 10 measurements.

5.3.2. *Aggregation Kinetics as a Function of Electrolyte Concentration*

The stability profile of soot NPs as a function of NaCl concentration in the presence or absence of various macromolecules is presented in Figure 5.3. In the absence of macromolecules, the aggregation kinetics exhibited two distinct regimes over the tested NaCl concentration range, indicating that the aggregation behavior of soot NPs was dominated by the interplay between electrostatic repulsion and van der Waals attraction forces as described by the DLVO theory [25]. At the reaction-limited (slow) aggregation regime ($\alpha < 1$), the aggregation rate increased with increasing salt concentration due to charge screening of soot NPs surface by cations. Above the critical coagulation concentration (CCC) where diffusion-limited (fast) aggregation ($\alpha = 1$) occurred, the particle surface charge was completely eliminated such that any further increase in salt concentration did not result in any increased aggregation rate. The soot NPs stability data in the absence of macromolecules were empirically fitted [220] and the determined CCC value was 167 mM NaCl, which agreed very well with our previously reported value of 152 mM NaCl [277]. This CCC value for soot NPs is similar to those for fullerene NPs (120 to 160 mM NaCl [38, 283]) and is greater than those for other carbonaceous nanomaterials such as SWNTs (20 to 37 mM NaCl [40, 274]) and multi-walled carbon

nanotubes (MWNTs) (25 to 90 mM NaCl [39, 201]). Such result is indicative of a strong colloidal stability of soot to remain as dispersed NPs in aquatic environments.

The effect of macromolecules on the aggregation kinetics of soot NPs as a function of NaCl concentration is presented in Figure 5.3. Overall, the presence of all tested macromolecules exhibited slight or significant effects on enhancing the stability of soot NPs in NaCl solutions. Over the NaCl concentration range, only slight retardation of soot aggregation rate was observed in the presence of FA at its typical environmental concentration (10 mg C/L). This is consistent with the result reported for fullerene NPs [218], although fulvic acid has been shown to have strong effects in preventing the aggregation of hematite NPs [294] and zinc sulfide NPs [295]. Compared with FA, LB broth at 10 mg C/L exhibited slightly stronger effects in retarding the aggregation. On the other hand, the presence of 10 mg C/L alginate and HA resulted in one or two orders of magnitude lower attachment efficiencies of soot NPs in NaCl solutions, respectively. The stabilizing effects of alginate or HA have also been reported for other nanomaterials such as SWNTs [274], MWNTs [39], fullerene [218, 283], and titanium oxide NPs [27]. It was also observed that the stabilization effects of soot NPs by HA became more profound at lower NaCl concentrations. The presence of BSA at only 2.5 mg C/L exhibited the most significant effect in enhancing the colloidal stability of soot NPs among all the tested macromolecules, even though BSA reduced the surface charge on soot NPs as shown in Figure 5.2a. None of the stability data in the presence of alginate, HA, or BSA over the tested NaCl concentrations exhibited diffusion-limited aggregation of soot NPs (i.e., $\alpha = 1$), indicating that these three macromolecules have important environmental implications for soot NPs by stabilization effects as discussed later.
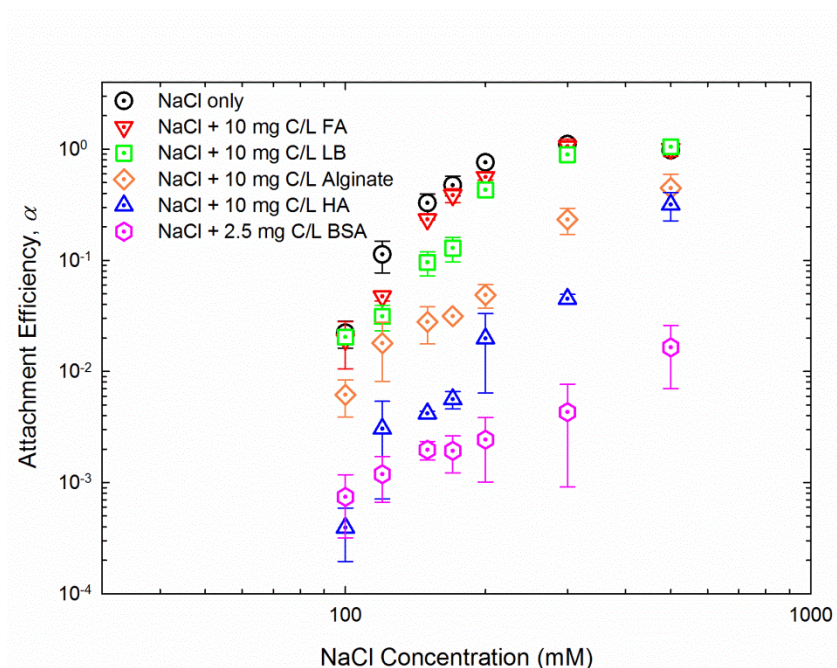
Figure 5.3 Attachment efficiency of soot NPs as a function of NaCl concentration in the presence/absence of various macromolecules. The attachment efficiencies were calculated by normalizing each aggregation rate to the fast aggregation rate obtained at high concentrations of NaCl alone. The macromolecule concentrations were maintained at 2.5 mg/L of TOC for BSA and 10 mg/L of TOC for other macromolecules. The measurement was conducted at soot NPs concentration of 10 mg/L, pH 6, and 25 °C. The error bars represent standard deviations of triplicate samples.

The aggregation kinetics of soot NPs in the presence or absence of macromolecules are presented as a function of $CaCl_2$ concentration in Figure 5.4. Similar to the NaCl treatments above, in the absence of macromolecules, the attachment efficiencies of soot NPs in aqueous solutions of $CaCl_2$ also exhibited reaction-limited and diffusion-limited aggregation regimes, allowing for empirical fitting [220] of the stability data for

determination of the CCC. The CCC of $CaCl_2$ thus obtained for soot NPs (4.5 mM) was in close agreement with that found in our previous study (4.6 mM) [277], higher than those for SWNTs (0.2 to 2 mM $CaCl_2$ [40, 274]) and for MWNTs (1.2 to 2.6 mM $CaCl_2$ [39, 201]), and lower than those for fullerene NPs (4.8 to 6.1 mM $CaCl_2$ [38, 283]). The ratio of CCC values determined for soot NPs in divalent ($CaCl_2$) and monovalent (NaCl) electrolytes (4.5/167) is equivalent to $z^{-5.21}$, where z is the counterion valence for calcium (i.e., $z = 2$). This ratio was reasonable since DLVO theory predicts that varies from z^{-2} for surfaces with low charge densities to z^{-6} (Schulze-Hardy rule) for surfaces with high charge densities [25, 201].

The overall effects of the tested macromolecules on the aggregation kinetics of soot NPs in $CaCl_2$ solution (Figure 5.4) were similar to those observed in NaCl solution (Figure 5.3). The presence of 10 mg C/L of FA and LB had negligible to weak effects on the aggregation rates of soot NPs. At $CaCl_2$ concentration below 6 mM, strong retardation of aggregation rates was observed at 10 mg C/L of HA. But as $CaCl_2$ concentration approached that of seawater 10 mM [103], the stabilization effect of HA on soot aggregation became weaker as the attachment efficiencies were close to 1. Among all tested macromolecules, BSA at only 2.5 mg C/L still exhibited the most profound effect in stabilizing soot NPs from aggregation even at high calcium concentrations. One noticeable exception was that the presence of alginate in $CaCl_2$ solution demonstrated very distinct effects on the aggregation kinetics of soot NPs from those observed with Na^+ ions. At $CaCl_2$ concentrations below the CCC value of 4.5 mM, alginate did not retard the aggregation of soot NPs as observed in NaCl solution. Above the CCC value, however, the presence of alginate in $CaCl_2$ solution significantly promoted the

aggregation of soot NPs, leading to rates of aggregate growth much greater than the rate for diffusion-limited aggregation (i.e., $\alpha > 1$). This strongly enhanced aggregation with alginate in the presence of high calcium concentrations indicated that a specific different aggregation mechanism was involved, which will be discussed later.
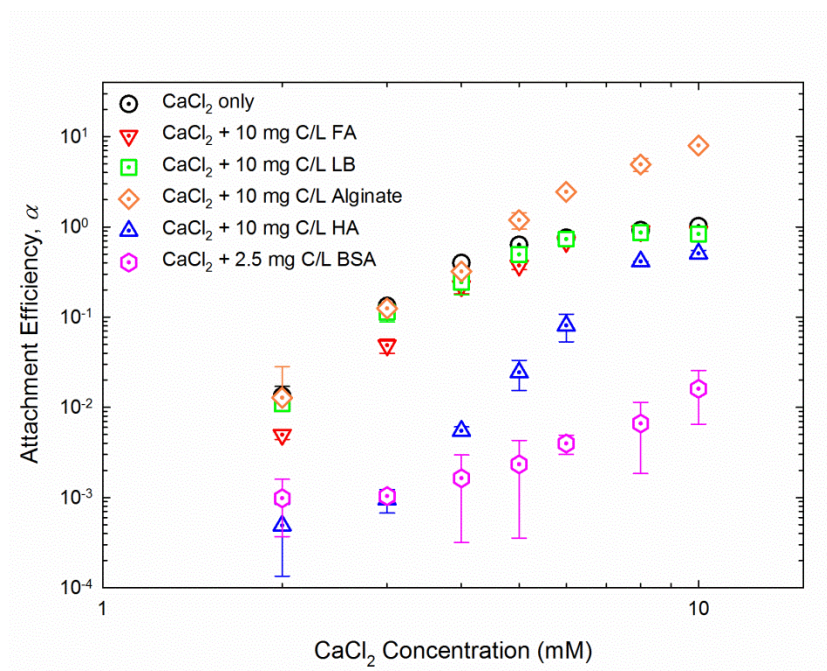
Figure 5.4 Attachment efficiency of soot NPs as a function of $CaCl_2$ concentration in the presence/absence of various macromolecules. The attachment efficiencies were calculated by normalizing each aggregation rate to the fast aggregation rate obtained at high concentrations of $CaCl_2$ alone. The macromolecule concentrations were maintained at 2.5 mg/L of TOC for BSA and 10 mg/L of TOC for other macromolecules. The measurement was conducted at soot NPs concentration of 10 mg/L, pH 6, and 25 °C. The error bars represent standard deviations of triplicate samples.

5.3.3. Aggregation Kinetics as a Function of Macromolecule Concentration

To further study the impact of macromolecules on the aggregation kinetics of soot NPs, the attachment efficiencies were determined at different macromolecule concentrations in the presence of two NaCl concentrations (Figure 5.5). The 500 mM NaCl at high salt level and the 170 mM NaCl close to the CCC level were chosen to represent seawater and estuary conditions, respectively, such that the aggregation of soot NPs in the presence of macromolecules could be observed within a reasonable time. The macromolecule concentrations were selected as 2.5, 5, 10, and 50 mg C/L as natural waters usually contain NOM concentrations ranging from 1 to 50 mg/L dissolved organic carbon (DOC) [26].

Figure 5a shows that at seawater condition of 500 mM NaCl, FA or LB had very weak impact on the aggregation even at 50 mg C/L. The trends of retarding aggregation as a function of macromolecule concentration were similar between alginate and HA at 500 mM NaCl, with HA being slightly stronger than alginate in the retardation effect. Nearly no aggregation was observed at 50 mg C/L of alginate or HA and at all tested concentrations of BSA. At the CCC level of 170 mM NaCl (Figure 5.5b), the presence of FA and LB at higher concentrations (e.g., 50 mg C/L) resulted in considerable reduction of the attachment efficiencies compared to that in the absence of macromolecules. It suggested that FA and LB may slow down the aggregation process only at high macromolecule concentrations with the presence of relatively lower ionic strength. The trend of retarding aggregation followed the order of BSA > HA > alginate > LB > FA, with their retardation effect being stronger at higher macromolecule concentration.
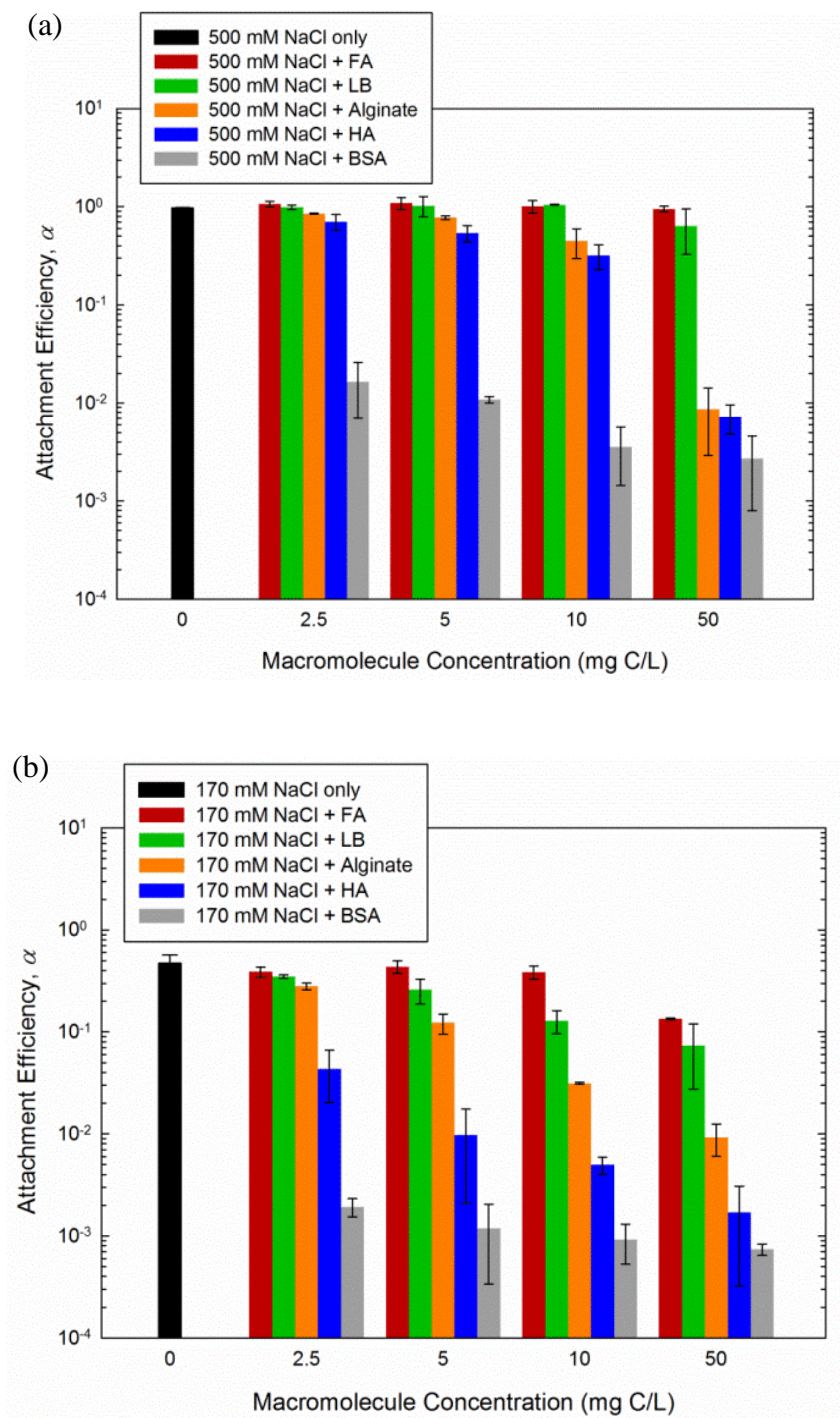
Figure 5.5 Attachment efficiency of soot NPs as a function of macromolecule

concentrations in the presence of (a) 500 mM and (b) 170 mM NaCl. The attachment

efficiencies were calculated by normalizing each aggregation rate to the fast aggregation

rate obtained at high concentrations of NaCl alone. The measurement was conducted at soot NPs concentration of 10 mg/L, pH 6, and 25 °C. The error bars represent standard deviations of triplicate samples.

The aggregation kinetics of soot NPs in the presence of 10 mM and 5 mM $CaCl_2$ were presented as a function of macromolecule concentration in Figure 5.6. Due to the stronger ability of Ca^{2+} than Na^+ to induce aggregation, the presence of FA, LB, or HA in 10 mM $CaCl_2$ solution did not exhibit much stabilization even at 50 mg C/L (Figure 5.6a). But at lower $CaCl_2$ concentration of 5 mM, the stabilization effect of soot NPs by these three macromolecules (FA, LB, and especially HA) reappeared (Figure 5.6b). It has been shown above in Figure 5.4 that the presence of alginate with Ca^{2+} promoted the aggregation of soot NPs, with more enhanced aggregation at higher $CaCl_2$ concentrations when above the CCC. Figure 5.6 demonstrated from another aspect that such enhanced aggregation effect became stronger at higher alginate concentrations. The presence of BSA again exhibited the strongest stabilization effect among all macromolecules under the tested conditions. Both the trend and magnitude of attachment efficiencies remained approximately unchanged at different BSA concentrations in NaCl solution (Figure 5.5) or $CaCl_2$ solution (Figure 5.6). Due to the strong stabilization effect of BSA on soot NPs, contributions from the electrolyte composition/concentration or the macromolecule concentration were relatively insignificant.
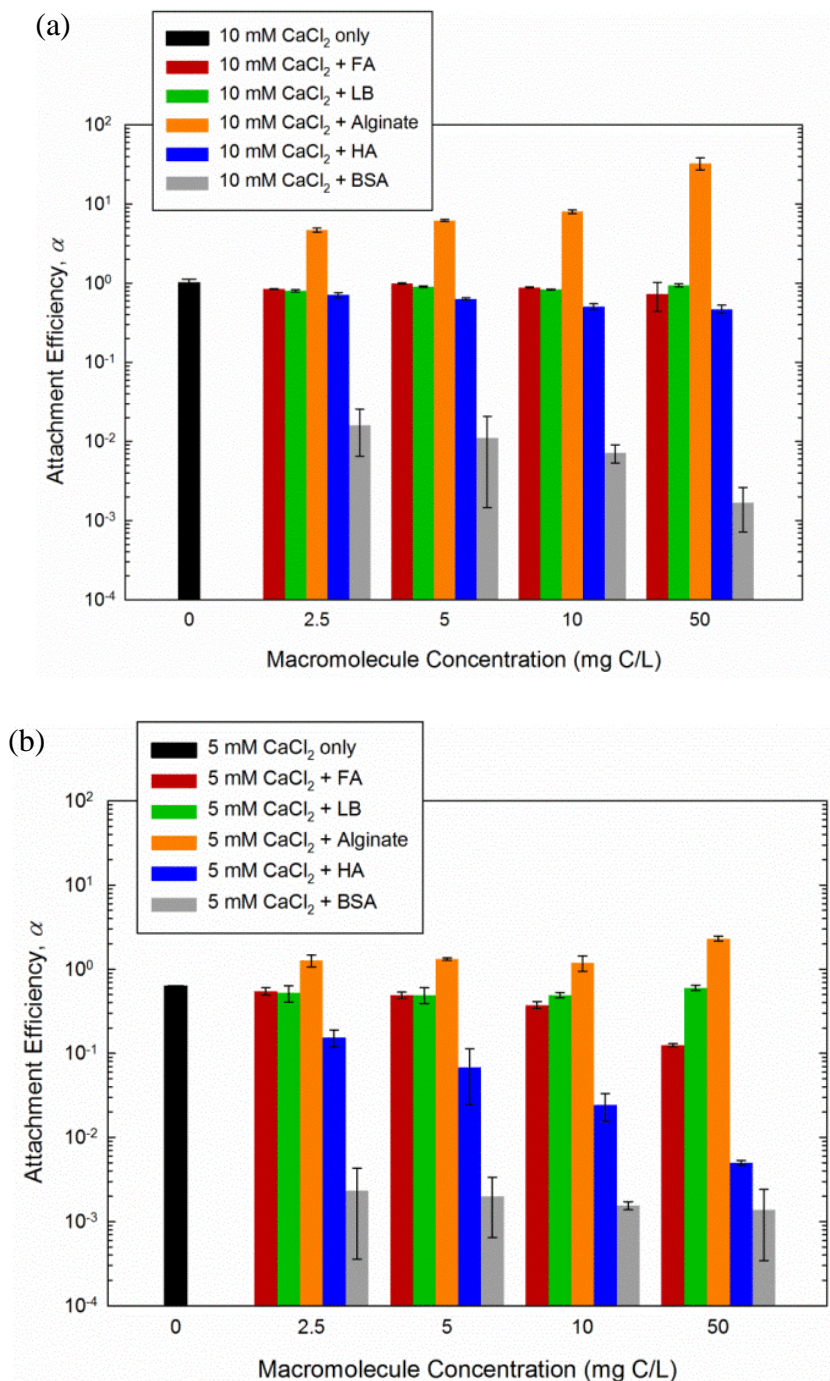
Figure 5.6 Attachment efficiency of soot NPs as a function of macromolecule concentrations in the presence of (a) 10 mM and (b) 5 mM $CaCl_2$. The attachment efficiencies were calculated by normalizing each aggregation rate to the fast aggregation rate obtained at high concentrations of $CaCl_2$ alone. The measurement was conducted at

soot NPs concentration of 10 mg/L, pH 6, and 25 °C. The error bars represent standard deviations of triplicate samples.

5.3.4. *Aggregation Mechanisms in the Presence of Macromolecules*

The presence of HA did not change the EPM of soot NPs significantly, but it has shown pronounced stabilization effect on soot NPs in solutions containing monovalent or divalent cations. This strongly suggested that electrostatic interaction was not the stabilizing factor; instead, HA adsorption onto soot NPs surface had led to steric repulsion which effectively stabilized the soot NPs suspension. The stabilizing effect of adsorbed HA macromolecules was also observed for carbonaceous NPs (e.g., fullerene [216, 218, 283], SWNTs [274], and MWNTs [39]) and metallic NPs (e.g., zinc sulfide [295], titanium oxide [27], gold [26], and hematite [215]) in the presence of monovalent salts. Although some of the studies [26, 216, 296] reported an enhanced aggregation when HA was present with divalent cations such as Ca^{2+} due to cation complexation, such effect was not observed for the soot NPs.

Some literature data indicated that FA and LB macromolecules could adsorb on particle surface and greatly retard the aggregate formation in colloidal systems [274, 294, 297]. However, this was not observed for the soot NPs in this study. The weak stabilizing effect observed for FA and LB was likely due to their low adsorption affinity to soot NPs. Compared to HA, for instance, FA has higher concentrations of negatively charged (e.g., carboxylic or phenolic) functional groups, which leads to its lower hydrophobicity and adsorption affinity to soot NPs [30, 218].

As discussed earlier, while all other macromolecules only slightly modified the EPM of soot NPs, the presence of BSA proteins has significantly lowered the particle surface charge due to spontaneous adsorption of BSA proteins onto soot NPs [290-293] (Figure 5.2 and associated discussion). The reduced surface charge in the presence of BSA could have theoretically promoted aggregation since the electrostatic repulsion between soot NPs was lowered. However, aggregation experiments have shown seemingly conflicting data that BSA proteins instead exhibited the strongest effect in retarding the soot NPs aggregation rate. It has been recognized that the adsorption of BSA protein on surfaces of carbonaceous nanomaterials [28, 280, 287] ruled by hydrophobic interactions enhances NPs stability [274, 288, 298, 299]. Compared to other tested macromolecules which are relatively more linear, BSA protein molecules have a compact globular structure after attachment onto hydrophobic solid surfaces [300, 301]. As a result, the spontaneously adsorbed layer of globular BSA molecules on soot NPs imparted long-range steric repulsive forces, which contributed to the greater stabilizing effect of BSA macromolecules.

The presence of alginate stabilized soot NPs in NaCl solutions with its effect less significant than HA and BSA macromolecules (Figures 5.3 and 5.5). Since the EPM of soot NPs in NaCl solutions was not influenced by alginate, which should also be negatively charged under low ionic conditions [27], it was unlikely that the stabilization occurred from enhanced electrostatic repulsion. Alginate adsorption onto the soot NPs has led to steric repulsion which greatly stabilized the suspensions in the presence of NaCl. The weaker stabilization effect observed for alginate was due to its more linear and semi-flexible polyelectrolyte structure compared to HA and BSA [27].

On the other hand, enhanced aggregation of soot NPs was observed in the presence of alginate at high $CaCl_2$ concentrations, resulting in attachment efficiencies greater than one (Figures 5.4 and 5.6). Figure 5.7 shows that the aggregation rates of soot NPs were dramatically increased when 2.5 mg C/L of alginate was present at $CaCl_2$ concentrations above the CCC of 4.5 mM (Figure 5.4). In the absence of alginate, diffusion-limited (fast) aggregation was attained at 6 and 10 mM $CaCl_2$ since these concentrations were above the CCC. The addition of alginate at these high $CaCl_2$ concentrations significantly enhanced the aggregation, leading to aggregation rates much greater than those possible for the fast aggregation regime (i.e., $\alpha > 1$). However, such enhanced effects were not obvious at $CaCl_2$ concentrations below CCC (e.g., 4 mM $CaCl_2$).
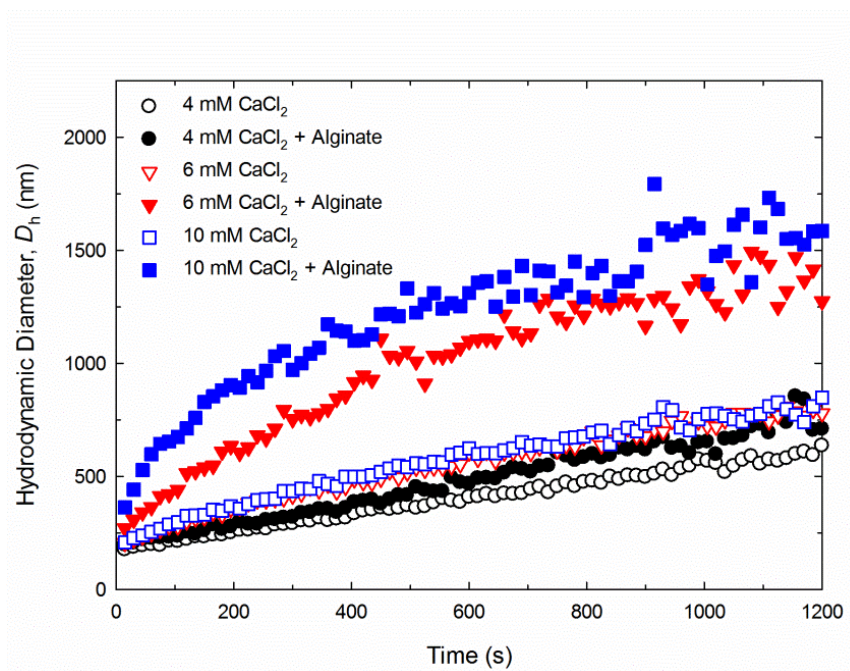
Figure 5.7 Representative aggregation profiles of soot NPs in various $CaCl_2$ solutions in the absence and presence of alginate (2.5 mg/L of TOC). Experiments were conducted at pH 6 and 25 °C.

Alginate molecules bridging in the presence of Ca^{2+} ions at high concentrations was identified as the primary mechanism responsible for the enhanced aggregation of soot NPs (Figure 5.8). It has been previously shown that divalent cations such as Ca^{2+} can complex with the guluronic acid blocks (G-blocks) of two alginate polymers, thereby crosslinking the polymers to form alginate gel with a cooperative "egg-box structure" [302, 303]. The formation of alginate gel resulting in enhanced particle aggregation was also reported for SWNTs [274] and hematite NPs [202, 304] in the presence of alginate and high calcium concentrations. Figure 5.9 provides visual observations of alginate gel formation leading to enhanced aggregation and removal of soot NPs from suspensions.
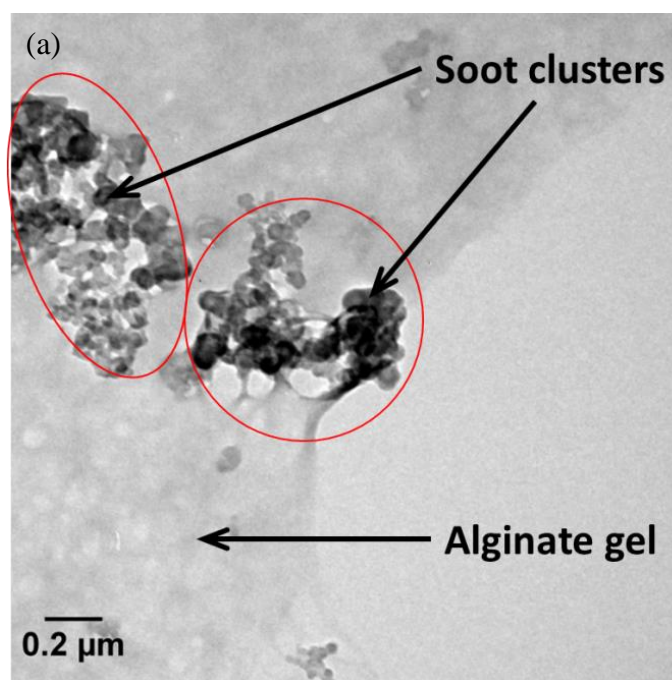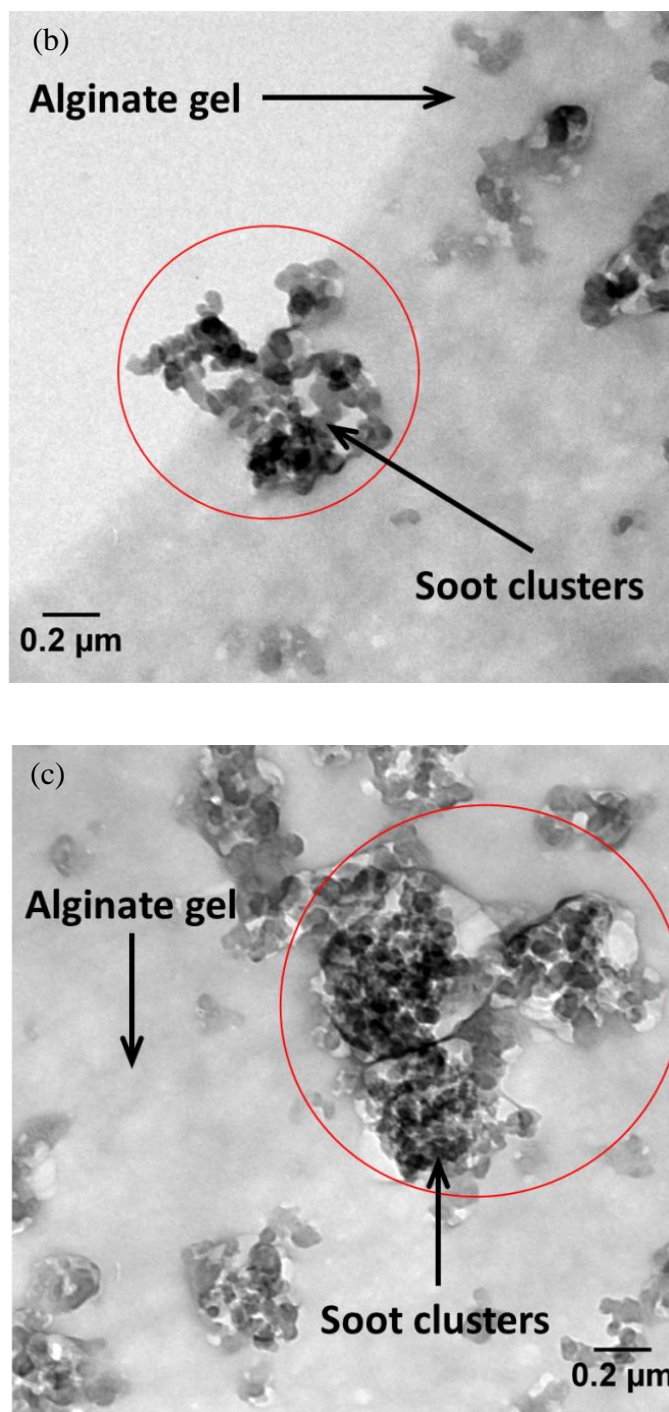
Figure 5.8 Transmission electron micrograph (TEM) image showing the alginate bridging with Ca^{2+} ion, which has resulted in the enhanced aggregation of soot NPs. The TEM grid was prepared 5 min after preparation of the aqueous sample, which contained 10 mg/L soot NPs, 10 mM $CaCl_2$, and 10 mg C/L alginate.
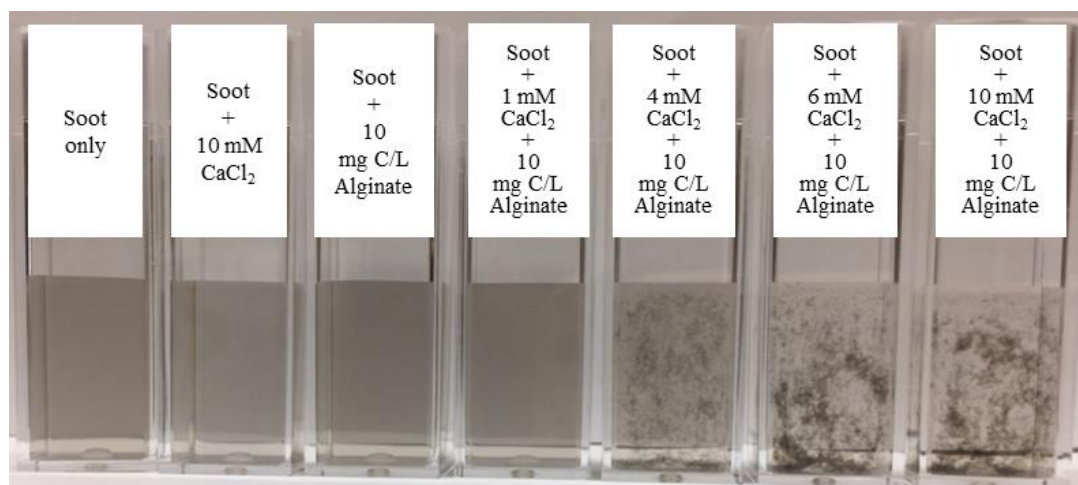
Figure 5.9 Visual observations for suspensions containing 10 mg/L soot NPs and varying concentrations of alginate and $CaCl_2$ at pH 6 and 25 °C. Photos were taken 45 min after preparation of the aqueous suspensions.

5.4. Environmental Implications

Soot particles produced from incomplete combustion of fuel and biomass may eventually enter aquatic environments in large amounts, contributing to toxic effects on aquatic ecosystems and the global carbon cycle. The fate and transport of soot particles and their interactions with ambient suspended solids and aquatic organisms are greatly dependent upon their aggregation states under various environmentally relevant solution chemistries, including monovalent and divalent salts as well as the presence of organic macromolecules. Results from this study suggest that soot NPs should remain relatively stable under solution chemistries typical of freshwater environments, and their aggregation in highly salty environments (e.g., estuaries and ocean) could be greatly suppressed by the presence of macromolecules including humic acids and proteins. The

marked stabilizing effect from protein adsorption onto soot NPs may have a strong influence on the interactions of NPs with aquatic organisms and their cytotoxicity due to their enhanced mobility when entering biological fluids. In studies involving interactions of soot NPs with bacteria or cells, use of culture media containing macromolecules such as LB broth that has minor effects on soot NPs may be desired. The ubiquitous distribution of NOM such as humic acid in aquatic environments can retard the aggregation of soot NPs, therefore enhancing their transport in natural water. While alginate polysaccharide may stabilize soot NPs, it forms alginate gel by complexation with calcium ions at high concentrations, leading to enhanced soot aggregation. Such mechanism might be taken advantage of in water treatment designs for removal of soot NPs. Other than macromolecules, soot NPs will likely interact with suspended particles and mineral surfaces in aquatic environments. Such effects should be investigated in future studies.

Acknowledgements

6. CHAPTER VI. MAJOR CONCLUSIONS AND FUTURE WORK

6.1. Major Conclusions

The overall conclusions of this dissertation are that (1) engineered NACs nanomaterials having high colloidal stability and strong adsorptivity may be utilized as promising nanosized adsorbents to be injected into groundwater systems for in situ remediation of organic pollutants; and (2) depending upon local aqueous chemistry and presence of macromolecules, combustion-generated soot NPs could remain stable against self-aggregation under typical freshwater conditions, posing high risks to the environment. Results from this dissertation may have significant implications on the fate, transport, and application of carbonaceous NPs in natural and engineered aqueous systems.

The key findings and conclusions of this dissertation are briefly summarized below:

(i) Both the four types of NACs and the soot NPs investigated in this dissertation exhibit strong negative surface charge under solution conditions typical of freshwater environments, which may be attributed to deprotonation of oxygen-containing acidic surface functional groups. The negative surface charge of studied NPs confers them a strong colloidal stability against aggregation under solution chemistries typical of freshwater, and therefore they are likely mobile in such aqueous environments. However, the NPs may aggregate and settle away under salty (e.g., marines and estuaries) or acidic (e.g., acid rain droplets for soot NPs) aqueous conditions or both.

(ii) The aggregation behavior of the studied NAC and soot NPs is governed by the

interplay between electrostatic repulsion and van der Waals attraction forces, which could be predicted by the classic DLVO theory and is in principle similar to that of most aqueous colloidal materials. Such observations allow the determination of the CCC values for NPs under different solution conditions, and more importantly, enable the derivation of Hamaker constants for the NAC and soot NPs. This important physiochemical parameter could be used to construct predictive models for describing the fate and transport of NAC and soot NPs in various aqueous environments.

(iii) The NP aggregation processes are greatly influenced by a variety of solution conditions, which include salt compositions (mainly the valence of cations), salt concentrations (ionic strengths), pH conditions, and the presence of macromolecules. General trends observed for the aggregation processes are that NP colloidal stability decreases at higher ionic strengths and lower pH conditions, and that divalent cations (e.g., Ca^{2+}) have more significant effect on reducing NP colloidal stability than monovalent cations (e.g., Na^+).

(iv) The presence of environmental and biological macromolecules has complex impacts on the aggregation processes of soot NPs. Generally, all investigated macromolecules resulted in enhanced colloidal stability of soot NPs due to steric repulsive forces imparted by the adsorbed macromolecular layers, with BSA protein showing the strongest enhancing effect followed by HA, alginate, LB, and FA. The BSA protein having the strongest effect is attributed to its more compact globular structure when attached to soot NPs, thereby imparting long-range steric repulsive forces. Although the presence of alginate enhances soot NP stability in NaCl

solutions, it promotes soot aggregation in the presence of high Ca^{2+} concentrations due to alginate bridging effect.

(v) NACs have enormous SSA mainly distributed in their microporous structure. These NPs exhibit rapid adsorption towards two model aromatic pollutants, 4-CP and aniline, from aqueous solution, with the rate data following predictions by pseudo-second-order rate model and intra-particle diffusion model. The adsorption equilibrium isotherm data of NACs could be well described by the Freundlich isotherm. Hydrophobic interactions should be mainly responsible for the adsorption of 4-CP and aniline onto NACs, with 4-CP showing stronger affinity than aniline having higher hydrophobicity. More importantly, comparison shows that the adsorption capacities of NACs are 10-100 times greater than other reported nanosized adsorbents (e.g., CNTs, fullerene, and graphene), suggesting the applicability of NACs as superior adsorbents for toxic organic compounds in aqueous systems.

6.2. Future Work

Based on the current knowledge and challenges, future work to advance the understanding of fate, transport, and application of carbonaceous NPs in aqueous environments may include the following crucial issues:

(i) Linking the aggregation behavior of NAC and soot NPs to more environmental relevance by studying the effects of environmental colloids, suspended particles, and more macromolecules. This dissertation mainly addressed the self-aggregation of NPs, however, recent studies have shown that heteroaggregation between NPs

and environmental particles can take place in natural aquatic systems that contain suspended and colloidal particles as well as minerals [305, 306]. In addition, the effects of macromolecules on aggregation of NACs have not yet been investigated in this dissertation, which will be covered in an upcoming study. Other dominant macromolecules such as chitosan may also be present with soot NPs in marine aquatic environments. Further studies on this topic may be more relevant and important to the aggregation behavior of NAC and soot NPs in natural environments.

(ii) Linking the aggregation behavior of NAC and soot NPs to more biological relevance by involving biological fluids and biological species in the aggregation experiment. It has been shown that microorganisms such as viruses and bacteria readily adsorb onto surfaces of soot NPs once they enter marine ecosystems through deposition or fluvial discharge [20, 31, 32]. Soot NPs adsorbed by microorganisms may undergo surface modification, and at the same time may interact with released biological molecules such as various enzymes, DNA, and proteins. It is expected such effects would impact the NP aggregation processes.

(iii) Investigation of colloidal stability for NAC and soot NPs having different physiochemical properties. This dissertation focused on the aggregation and adsorption behavior of NACs independently. However, the mutual influence from these two processes on each other when NACs are introduced in water as adsorbents remains unknown. For instance, it is unclear if the adsorption process for organic pollutants would impact the NAC aggregation process or vice versa. In addition, this dissertation has only examined the aggregation behavior of standard

reference diesel particulate matter collected from heavy duty diesel engine, which presumably represented freshly produced diesel soot NPs released from diesel engine. It would be interesting to study the aggregation behavior of soot particles from various sources and have different physiochemical properties.

(iv) Development of superior NAC adsorbents for practical applications in water treatment using packed column experiments and field measurements. The adsorption and aggregation behavior has only been studied in batch reactors in this dissertation, which may deviate from real environmental circumstances in practical applications. Employment of packed column experiments as well as field measurements to evaluate and develop NACs as nanosized, mobile, cost-effective, and environmentally friendly remediation agents can be of great importance.

REFERENCES

[1] P.J. Borm, D. Robbins, S. Haubold, T. Kuhlbusch, H. Fissan, K. Donaldson, R. Schins, V. Stone, W. Kreyling, J. Lademann, J. Krutmann, D. Warheit, E. Oberdorster, The potential risks of nanomaterials: A review carried out for ECETOC, Part. Fibre Toxicol. 3 (2006) 11.

[2] P. Biswas, C.-Y. Wu, Nanoparticles and the environment, J. Air & Waste Manage. Assoc. 55 (2005) 708-746.

[3] M.S. Mauter, M. Elimelech, Environmental applications of carbon-based nanomaterials, Environ. Sci. Technol. 42 (2008) 5843-5859.

[4] J. Ni, Y. Li, Carbon nanomaterials in different dimensions for electrochemical energy storage, Adv. Energy Mater. 6 (2016) 1600278.

[5] S. Shahgaldi, J. Hamelin, Improved carbon nanostructures as a novel catalyst support in the cathode side of PEMFC: A critical review, Carbon 94 (2015) 705-728.

[6] G.E. Batley, J.K. Kirby, M.J. Mclaughlin, Fate and risks of nanomaterials in aquatic and terrestrial environments, Acc. Chem. Res. 46 (2011) 854-862.

[7] A.A. Koelmans, B. Nowack, M.R. Wiesner, Comparison of manufactured and black carbon nanoparticle concentrations in aquatic sediments, Environ. Pollut. 157 (2009) 1110-1116.

[8] C.M. Long, M.A. Nascarella, P.A. Valberg, Carbon black vs. black carbon and other airborne materials containing elemental carbon: physical and chemical distinctions, Environ. Pollut. 181 (2013) 271-286.

[9] A.S. Adeleye, J.R. Conway, K. Garner, Y. Huang, Y. Su, A.A. Keller, Engineered nanomaterials for water treatment and remediation: Costs, benefits, and applicability, Chem. Eng. J. 286 (2016) 640-662.

[10] H. Ghorbani, H. Tavanai, M. Morshed, Fabrication of activated carbon nanoparticles from PAN precursor, J. Anal. Appl. Pyrol. 110 (2014) 12-17.

[11] M.R. Wiesner, G.V. Lowry, P. Alvarez, D. Dionysiou, P. Biswas, Assessing the risks of manufactured nanomaterials, Environ. Sci. Technol. 40 (2006) 4336-4345.

[12] A.L. Dale, E.A. Casman, G.V. Lowry, J.R. Lead, E. Viparelli, M. Baalousha, Modeling nanomaterial environmental fate in aquatic systems, Environ. Sci. Technol. 49 (2015) 2587-2593.

[13] F. He, D. Zhao, C. Paul, Field assessment of carboxymethyl cellulose stabilized iron nanoparticles for in situ destruction of chlorinated solvents in source zones, Water Res. 44 (2010) 2360-2370.

[14] R.A. Kerr, Soot is warming the world even more than thought., Science 339 (2013) 382.

[15] A. Nel, T. Xia, L. Madler, N. Li, Toxic potential of materials at the nanolevel, Science 311 (2006) 622-627.

[16] M. Sajid, M. Ilyas, C. Basheer, M. Tariq, M. Daud, N. Baig, F. Shehzad, Impact of nanoparticles on human and environment: Review of toxicity factors, exposures, control strategies, and future prospects, Environ. Sci. Pollut. Res. Int. 22 (2015) 4122-4143.

[17] A. Nel, Air pollution-related illness: effects of particles., Science 308 (2005) 804-806.

[18] Y. Wang, S. Wu, X. Zhao, Z. Su, L. Du, A. Sui, In vitro toxicity evaluation of graphene oxide on human RPMI 8226 cells, Biomed. Mater. Eng. 24 (2014) 2007-2013.

[19] D.S. Su, A. Serafino, J.-O. Muller, R.E. Jentoft, R. Schlogl, S. Fiorito, Cytotoxicity and inflammatory potential of soot particles of low-emission diesel engines, Environ. Sci. Technol. 42 (2008) 1761-1765.

[20] X. Mari, J. Lefèvre, J.-P. Torréton, Y. Bettarel, O. Pringault, E. Rochelle-Newall, P. Marchesiello, C. Menkes, M. Rodier, C. Migon, C. Motegi, M.G. Weinbauer, L. Legendre, Effects of soot deposition on particle dynamics and microbial processes in marine surface waters, Glob. Biogeochem. Cycles 28 (2014) 662-678.

[21] R.F. Shiu, W.C. Chin, C.L. Lee, Carbonaceous particles reduce marine microgel formation, Sci. Rep. 4 (2014) 5856.

[22] J.R. Lead, E. Valsami-Jones, Nanoscience and the Environment, 1 ed., Elsevier Ltd., Amsterdam, Netherlands, 2014.

[23] J.N. Israelachvili, Intermolecular and Surface Forces., Academic Press, London, 1991.

[24] M. Elimelech, J. Gregory, X. Jia, R.A. Williams, Particle Deposition and Aggregation: Measurement, Modelling and Stimulation., Butterworth-Heinemann, Oxford, U.K., 1995.

[25] A.R. Petosa, D.P. Jaisi, I.R. Quevedo, M. Elimelech, N. Tufenkji, Aggregation and deposition of engineered nanomaterials in aquatic environments: Role of physicochemical interactions, Environ. Sci. Technol. 44 (2010) 6532-6549.

[26] J. Liu, S. Legros, F. von der Kammer, T. Hofmann, Natural organic matter concentration and hydrochemistry influence aggregation kinetics of functionalized engineered nanoparticles, Environ. Sci. Technol. 47 (2013) 4113-4120.

[27] F. Loosli, P. Le Coustumer, S. Stoll, TiO_2 nanoparticles aggregation and disaggregation in presence of alginate and Suwannee River humic acids. pH and concentration effects on nanoparticle stability, Water Res. 47 (2013) 6052-6063.

[28] M. Bergaoui, C. Aguir, M. Khalfaoui, E. Enciso, L. Duclaux, L. Reinert, J.L.G. Fierro, New insights in the adsorption of Bovine Serum Albumin onto carbon nanoparticles derived from organic resin: Experimental and theoretical studies, Microporous and Mesoporous Materials 241 (2017) 418-428.

[29] X. Ren, C. Chen, M. Nagatsu, X. Wang, Carbon nanotubes as adsorbents in environmental pollution management: A review, Chem. Eng. J. 170 (2011) 395-410.

[30] h. Hyung, J.-H. Kim, Natural organic matter (NOM) adsorption to multi-walled carbon nanotubes: effect of NOM characteristics and water quality parameters, Environ. Sci. Technol. 42 (2008) 4416-4421.

[31] R. Cattaneo, C. Rouviere, F. Rassoulzadegan, M.G. Weinbauer, Association of marine viral and bacterial communities with reference black carbon particles under experimental conditions: An analysis with scanning electron, epifluorescence and confocal laser scanning microscopy, FEMS Microbiol Ecol. 74 (2010) 382-396.

[32] M.G. Weinbauer, Y. Bettarel, R. Cattaneo, B. Luef, C. Maier, C. Motegi, P. Peduzzi, X. Mari, Viral ecology of organic and inorganic particles in aquatic systems: avenues for further research, Aquat. Microb. Ecol.: Int. J. 57 (2009) 321-341.

[33] T.D. Bucheli, Ö. Gustafsson, Quantification of the soot-water distribution coefficient of PAHs provides mechanistic basis for enhanced sorption observations, Environ. Sci. Technol. 34 (2000) 5144-5151.

[34] S. Mitra, T.S. Bianchi, B.A. McKee, M. Sutula, Black carbon from the Mississippi river: Quantities, sources, and potential implications for the global carbon cycle, Environ. Sci. Technol. 36 (2002) 2296-2302.

[35] R. Lohmann, J. MacFarlane, P. Gschwend, Importance of black carbon to sorption of native PAHs, PCBs, and PCDDs in Boston and New York harbor sediments., Environ. Sci. Technol. 39 (2005) 141-148.

[36] D. Bouchard, X. Ma, C. Isaacson, Colloidal properties of aqueous fullerenes: isoelectric points and aggregation kinetics of fullerene and derivatives, Environ. Sci. Technol. 43 (2009) 6597-6603.

[37] K.L. Chen, M. Elimelech, Relating colloidal stability of fullerene (C_{60}) nanoparticles to nanoparticle charge and electrokinetic properties, Environ. Sci. Technol. 43 (2009) 7270-7276.

[38] K.L. Chen, M. Elimelech, Aggregation and deposition kinetics of fullerene (C_{60}) nanoparticles, Langmuir 22 (2006) 10994-11001.

[39] N.B. Saleh, L.D. Pfefferle, M. Elimelech, Aggregation kinetics of multiwalled carbon nanotubes in aquatic systems: Measurements and environmental implications, Environ. Sci. Technol. 2008 (2008) 7963-7969.

[40] M. Sano, J. Okamura, S. Shinkai, Colloidal nature of single-walled carbon nanotubes in electrolyte solution: The Schulze-Hardy rule, Langmuir 17 (2001) 7172-7173.

[41] B. Smith, K. Wepasnick, K.E. Schrote, A.R. Bertele, W.P. Ball, C. O'Melia, D.H. Fairbrother, Colloidal properties of aqueous suspensions of acid-treated, multi-walled carbon nanotubes, Environ. Sci. Technol. 43 (2009) 819-825.

[42] I. Chowdhury, M.C. Duch, N.D. Mansukhani, M.C. Hersam, D. Bouchard, Colloidal properties and stability of graphene oxide nanomaterials in the aquatic environment, Environ. Sci. Technol. 47 (2013) 6288-6296.

[43] A. Sengupta, S.C. Kelly, N. Dwivedi, N. Thadhani, M.R. Prausnitz, Efficient intracellular delivery of molecules with high cell viability using nanosecond-pulsed laser-activated carbon nanoparticles, ACS Nano 8 (2014) 2889-2899.

[44] C. Jumelle, C. Mauclair, J. Houzet, A. Bernard, Z. He, F. Forest, M. Peoc'h, S. Acquart, P. Gain, G. Thuret, Delivery of molecules into human corneal endothelial cells by carbon nanoparticles activated by femtosecond laser, PloS one 10 (2015) e0132023.

[45] G. Abdulkareem-Alsultan, N. Asikin-Mijan, H.V. Lee, Y.H. Taufiq-Yap, A new route for the synthesis of La-Ca oxide supported on nano activated carbon via vacuum impregnation method for one pot esterification-transesterification reaction, Chem. Eng. J. 304 (2016) 61-71.

[46] J. He, S. Li, W. Shao, D. Wang, M. Chen, W. Yin, W. Wang, Y. Gu, B. Zhong, Activated carbon nanoparticles or methylene blue as tracer during video-assisted thoracic surgery for lung cancer can help pathologist find the detected lymph nodes, J. Surg. Oncol. 102 (2010) 676-682.

[47] R. Saraswat, N. Talreja, D. Deva, N. Sankararamakrishnan, A. Sharma, N. Verma, Development of novel in situ nickel-doped, phenolic resin-based micro–nano-

activated carbon adsorbents for the removal of vitamin B-12, Chem. Eng. J. 197 (2012) 250-260.

[48] K. Yang, L. Zhu, B. Xing, Adsorption of polycyclic aromatic hydrocarbons by carbon nanomaterials, Environ. Sci. Technol. 40 (2006) 1855-1861.

[49] R.Q. Long, R.T. Yang, Carbon nanotubes as superior sorbent for dioxin removal, J. Am. Chem. Soc. 123 (2001) 2058-2059.

[50] K. Yang, W. Wu, Q. Jing, L. Zhu, Aqueous adsorption of aniline, phenol, and their substitutes by multi-walled carbon nanotubes, Environ. Sci. Technol. 42 (2008) 7931-7936.

[51] D. Lin, B. Xing, Adsorption of phenolic compounds by carbon nanotubes: Role of aromaticity and substitution of hydroxyl groups, Environ. Sci. Technol. 42 (2008) 7254-7259.

[52] X. Liu, M. Wang, S. Zhang, B. Pan, Application potential of carbon nanotubes in water treatment: A review, J. Environ. Sci. 25 (2013) 1263-1280.

[53] E.K. Nyer, D.B. Vance, Nano-scale Iron for Dehalogenation, GWMR (2001) 41-46.

[54] S. Zhang, T. Shao, H.S. Kose, T. Karanfil, Adsorption kinetics of aromatic compounds on carbon nanotubes and activated carbons, Environ. Toxicol. Chem. / SETAC 31 (2012) 79-85.

[55] V.K. Upadhyayula, S. Deng, M.C. Mitchell, G.B. Smith, Application of carbon nanotube technology for removal of contaminants in drinking water: A review, Sci. Total Environ. 408 (2009) 1-13.

[56] S. Zhang, T. Shao, S.S.K. Bekaroglu, T. Karanfil, The impacts of aggregation and surface chemistry of carbon nanotubes on the adsorption of synthetic organic compounds, Environ. Sci. Technol. 43 (2009) 5719-5725.

[57] T. Phenrat, N. Saleh, K. Sirk, R.D. Tilton, G.V. Lowry, Aggregation and sedimentation of aqueous nanoscale zerovalent iron dispersions, Environ. Sci. Technol. 41 (2007) 284-290.

[58] H.F. Lecoanet, J.-Y. Bottero, M.R. Wiesner, Laboratory assessment of the mobility of nanomaterials in porous media, Environ. Sci. Technol. 38 (2004) 5164-5169.

[59] C.I. Davidson, R.F. Phalen, P.A. Solomon, Airborne particulate matter and human health: A review, Aerosol Sci. Technol. 39 (2005) 737-749.

[60] EPA, Health Assessment Document for Diesel Engine Exhaust, (2002) EPA/600/608-690/057F.

[61] W.H. Su, Q.P. Zhang, W.Z. Song, C. Luo, Y.F. Siu, Problems of soot pollution and environmental effects in northern China, Aerosol Sci. Technol. 10 (1989) 231-235.

[62] M. Sleiman, T.W. Kirchstetter, P. Berdahl, H.E. Gilbert, S. Quelen, L. Marlot, C.V. Preble, S. Chen, A. Montalbano, O. Rosseler, H. Akbari, R. Levinson, H. Destaillats, Soiling of building envelope surfaces and its effect on solar reflectance – Part II: Development of an accelerated aging method for roofing materials, Sol. Energ. Mat. Sol. Cells 122 (2014) 271-281.

[63] W.L. Chameides, H. Yu, S.C. Liu, M. Bergin, X. Zhou, L. Mearns, G. Wang, C.S. Kiang, R.D. Saylor, C. Luo, Y. Huang, A. Steiner, F. Giorgi, Case study of the effects of atmospheric aerosols and regional haze on agriculture: An opportunity to enhance crop yields in china through emission controls?, Proc. Natl. Acad. Sci. U.S.A. 96 (1999) 13626-13633.

[64] W.L. Chameides, M. Bergin, Soot takes center stage., Science 297 (2002) 2214-2215.

[65] V. Ramanathan, P.J. Crutzen, J.T. Kiehl, D. Rosenfeld, Aerosols, climate, and the hydrological cycle., Science 294 (2001) 2119-2124.

[66] R. Subramanian, E. Winijkul, T.C. Bond, W. Thiansathit, N.T.K. Oanh, I. Pawarmart, K.G. Duleep, Climate-relevant properties of diesel particulate emissions: results from a piggyback study in Bangkok, Thailand., Environ. Sci. Technol. 43 (2009) 4213-4218.

[67] C.A. Masiello, E.R.M. Druffel, Black carbon in deep-sea sediments, Science 280 (1998) 1911-1913.

[68] M.S. Forbes, R.J. Raison, J.O. Skjemstad, Formation, transformation and transport of black carbon (charcoal) in terrestrial and aquatic ecosystems, Sci. Total Environ. 370 (2006) 190-206.

[69] R. Lohmann, K. Bollinger, M. Cantwell, J. Feichter, I. Fischer-Bruns, M. Zabel, Fluxes of soot black carbon to South Atlantic sediments, Glob. Biogeochem. Cycles 23 (2009) GB1015.

[70] R. Richter, Computer simulation of soot aggregation., J. Colloid Interface Sci. 100 (1984) 203-209.

[71] A. Kazakov, M. Frenklach, Dynamic modeling of soot particle coagulation and aggregation: Implementation with the method of moments and application to high-pressure laminar premixed flames., Combust. Flame 114 (1998) 484-501.

[72] S. di Stasio, A.G. Konstandopoulos, M. Kostoglou, Cluster-cluster aggregation kinetics and primary particle growth of soot nanoparticles in flame by light scattering and numerical simulations, J. Colloid Interface Sci. 247 (2002) 33-46.

[73] J. Rissler, M.E. Messing, A.I. Malik, P.T. Nilsson, E.Z. Nordin, M. Bohgard, M. Sanati, J.H. Pagels, Effective density characterization of soot agglomerates from various sources and comparison to aggregation theory, Aerosol Sci. Technol. 47 (2013) 792-805.

[74] X. Ma, C.D. Zangmeister, J. Gigault, G.W. Mulholland, M.R. Zachariah, Soot aggregate restructuring during water processing, J. Aerosol Sci. 66 (2013) 209-219.

[75] A.F. Khalizov, R. Zhang, D. Zhang, H. Xue, J. Pagels, P.H. McMurry, Formation of highly hygroscopic soot aerosols upon internal mixing with sulfuric acid vapor, J. Geophys. Res., [Atmos.] 114 (2009) D05208.

[76] E.F. Mikhailov, S.S. Vlasenko, I.A. Podgorny, V. Ramanathan, C.E. Corrigan, Optical properties of soot–water drop agglomerates: An experimental study, J. Geophys. Res., [Atmos.] 111 (2006) D07209.

[77] V. Baheti, S. Naeem, J. Militky, M. Okrasa, B. Tomkova, Optimized preparation of activated carbon nanoparticles from acrylic fibrous wastes, Fiber Polym. 16 (2015) 2193-2201.

[78] J.N. Israelachvili, Intermolecular and Surface Forces, third ed., Academic Press, USA, 2011.

[79] S. Maurer, A. Mersmann, W. Peukert, Henry coefficients of adsorption predicted from solid Hamaker constants, Chem. Eng. Sci. 56 (2001) 3443-3453.

[80] S.A. Macpherson, G.B. Webber, R. Moreno-Atanasio, Aggregation of nanoparticles in high ionic strength suspensions: Effect of Hamaker constant and particle concentration, Adv. Powder Technol. 23 (2012) 478-484.

[81] P.N. Mitropoulou, V.I. Syngouna, C.V. Chrysikopoulos, Transport of colloids in unsaturated packed columns: Role of ionic strength and sand grain size, Chem. Eng. J. 232 (2013) 237-248.

[82] M. Morra, E. Occhiello, F. Garbassi, Effect of surface treatment on the Hamaker constant of intermediate modulus carbon fibers, Colloid. Polym. Sci. 27 (1992) 58-63.

[83] W. Peukert, C. Mehler, M. Götzinger, Novel concepts for characterisation of heterogeneous particulate surfaces, Appl. Surf. Sci. 192 (2002) 30-40.

[84] D.N.L. McGown, G.D. Parfltt, Improved theoretical calculation of the stability ratio for colloidal systems, J. Phys. Chem. 71 (1967) 449-450.

[85] E.P. Honig, G.J. Roeberse, P.H. Wiersema, Effect of hydrodynamic interaction on the coagulation rate of hydrophobic colloids, J. Colloid Interface Sci. 36 (1971) 97-109.

[86] J. Gregory, Approximate expressions for retarded van der waals interaction., J. Colloid Interface Sci. 83 (1981) 138-145.

[87] R. Hogg, T.W. Healy, D.W. Fuerstenau, Mutual coagulation of colloidal dispersions., Trans. Faraday Soc. 62 (1966) 1638-1651.

[88] J. Gregory, Interaction of unequal double layers at constant charge, J. Colloid Interface Sci. 51 (1975) 44-51.

[89] G.R. Wiese, T.W. Healy, Effect of particle size on colloid stability., Trans. Faraday Soc. 66 (1970) 490-500.

[90] S.J. Usui, Interaction of electrical double layers at constant surface charge., J. Colloid Interface Sci. 44 (1973) 107-113.

[91] S. Ross, I.D. Morrison, Colloidal Systems and Interfaces, 1 edition ed., Wiley-Interscience, United States of America, April 1988.

[92] B.V. Derjaguin, Friction and adhesion IV. The theory of adhesion of small particles., Kolloid Z. 69 (1934) 155-164.

[93] M. Baalousha, J.R. Lead, Rationalizing nanomaterial sizes measured by atomic force microscopy, flow field-flow fractionation, and dynamic light scattering: Sample preparation, polydispersity, and particle structure, Environ. Sci. Technol. 46 (2012) 6134-6142.

[94] M. Larsson, A. Hill, J. Duffy, Suspension stability, dividing line of zeta potential for stable suspension, Ann. T. Nord. Rheol. Soc. 20 (2012) 209-214.

[95] O. Duman, S. Tunç, Electrokinetic properties of vermiculite and expanded vermiculite: Effects of pH, clay concentration and mono- and multivalent electrolytes, Sep. Sci. Technol. 43 (2008) 3755-3776.

[96] O. Duman, S. Tunç, Electrokinetic and rheological properties of Na-bentonite in some electrolyte solutions, Micropor. Mesopor. Mat. 117 (2009) 331-338.

[97] J. Feder, T. Jøssang, E. Rosenqvist, Scaling behavior and cluster fractal dimension determined by light scattering from aggregating proteins, Phys. Rev. Lett. 53 (1984) 1403-1406.

[98] D.A. Weitz, J.S. Huang, M.Y. Lin, J. Sung, Limits of the fractal dimension for irreversible kinetic aggregation of gold colloids, Phys. Rev. Lett. 54 (1985) 1416-1419.

[99] UNESCO, WHO, UNEP, Water Quality Assessments - A Guide to Use of Biota, Sediments and Water in Environmental Monitoring, second ed., University Press, Cambridge, Great Britain, 1996.

[100] X. Li, J.J. Lenhart, Aggregation and dissolution of silver nanoparticles in natural surface water, Environ. Sci. Technol. 46 (2012) 5378-5386.

[101] E.A. Atekwana, D.S. Richardson, Geochemical and isotopic evidence of a groundwater source in the Corral Canyon meadow complex, central Nevada, USA, Hydrol. Process. 18 (2004) 2801-2815.

[102] E.S. Kim, D.H. Lee, B.W. Yum, H.W. Chang, The effect of ionic strength and hardness of water on the non-ionic surfactant-enhanced remediation of perchloroethylene contamination, J. Hazard. Mater. 119 (2005) 195-203.

[103] J.D. Hem, Study and Interpretation of the Chemical Characteristics of Natural Water, in: U.S Geological Survey Water-Supply Paper 2254, U.S. Geological Survey, Alexandria, VA, 1985.

[104] S.H. Behrens, D.I. Christl, R. Emmerzael, P. Schurtenberger, M. Borkovec, Charging and aggregation properties of carboxyl latex particles: Experiments versus DLVO theory, Langmuir 16 (2000) 2566-2575.

[105] J. Visser, On Hamaker constants: A comparison between Hamaker constants and Lifshitz -van der Waals constants, Adv. Colloid Interface Sci. 3 (1972) 331-363.

[106] W. Stumm, in: Chemistry of the Solid-Water Interface., John Wiley & Sons, Inc., United States, 1992, pp. 266.

[107] W. Zhang, C.W. Isaacson, U.S. Rattanaudompol, T.B. Powell, D. Bouchard, Fullerene nanoparticles exhibit greater retention in freshwater sediment than in model porous media, Water Res. 46 (2012) 2992-3004.

[108] V. Sygouni, C.V. Chrysikopoulos, Characterization of TiO_2 nanoparticle suspensions in aqueous solutions and TiO_2 nanoparticle retention in water-saturated columns packed with glass beads, Chem. Eng. J. 262 (2015) 823-830.

[109] D.J. de Ridder, Adsorption of Organic Micropollutants onto Activated Carbon and Zeolites, Water Management Academic Press, the Netherlands, 2012.

[110] P.E. Fanning, M.A. Vannice, A DRIFTS study of the formation of surface groups on carbon by oxidation, Carbon 31 (1993) 721-730.

[111] S. Suresh, V.C. Srivastava, I.M. Mishra, Studies of adsorption kinetics and regeneration of aniline, phenol, 4-chlorophenol and 4-nitrophenol by activated carbon, Chem. Ind. Chem. Eng. Q. 19 (2013) 195-212.

[112] A.-N.A. El-Hendawy, Influence of HNO_3 oxidation on the structure and adsorptive properties of corncob-based activated carbon, Carbon 41 (2003) 713-722.

[113] H. Deng, G. Zhang, X. Xu, G. Tao, J. Dai, Optimization of preparation of activated carbon from cotton stalk by microwave assisted phosphoric acid-chemical activation, J. Hazard Mater. 182 (2010) 217-224.

[114] V. Boonamnuayvitaya, S. Sae-ung, W. Tanthapanichakoon, Preparation of activated carbons from coffee residue for the adsorption of formaldehyde, Sep. Purif. Technol. 42 (2005) 159-168.

[115] C. Moreno-Castilla, M.V. Lopez-Ramon, F. Carrasco-Marin, Changes in surface chemistry of activated carbons by wet oxidation, Carbon 38 (2000) 1995-2001.

[116] A.S. Adeleye, J.R. Conway, K. Garner, Y. Huang, Y. Su, A.A. Keller, Engineered nanomaterials for water treatment and remediation: Costs, benefits, and applicability, Chem. Eng. J. 286 (2016) 640-662.

[117] X. Qu, P.J. Alvarez, Q. Li, Applications of nanotechnology in water and wastewater treatment, Water Res. 47 (2013) 3931-3946.

[118] C. Santhosh, V. Velmurugan, G. Jacob, S.K. Jeong, A.N. Grace, A. Bhatnagar, Role of nanomaterials in water treatment applications: A review, Chem. Eng. J. 306 (2016) 1116-1137.

[119] X. Liu, M. Wang, S. Zhang, B. Pan, Application potential of carbon nanotubes in water treatment: A review, J. Environ. Sci. 25 (2013) 1263-1280.

[120] J.C. Lazo-Cannata, A. Nieto-Márquez, A. Jacoby, A.L. Paredes-Doig, A. Romero, M.R. Sun-Kou, J.L. Valverde, Adsorption of phenol and nitrophenols by carbon nanospheres: Effect of pH and ionic strength, Sep. Purif. Technol. 80 (2011) 217-224.

[121] X. Cheng, A.T. Kan, M.B. Tomson, Naphthalene adsorption and desorption from aqueous C_{60} fullerene, J. Chem. Eng. Data 49 (2004) 675-683.

[122] F. Çeçen, Ö. Aktas, Activated Carbon for Water and Wastewater Treatment: Integration of Adsorption and Biological Treatment, 1 ed., Wiley-VCH, Weinheim, Germany, 2011.

[123] A. Georgi, A. Schierz, K. Mackenzie, F.D. Kopinke, Colloidal activated carbon for in-situ groundwater remediation - Transport characteristics and adsorption of organic compounds in water-saturated sediment columns, J. Contam. Hydrol. 179 (2015) 76-88.

[124] K. Mackenzie, A. Schierz, A. Georgi, F.-D. Kopinke, Colloidal activated carbon and carbo-iron - novel materials for *in-situ* groundwater treatment, Global NEST J. 10 (2008) 54-61.

[125] R.P. Keshari, Z. Zhou, G. Chen, S. Yuan, A study of activated carbon nanoparticles guided dissection of lymph nodes in radical gastric cancer surgery, J. Clin. Oncol. 30 (2012) e14674-e14674.

[126] P. Chakravarty, W. Qian, M.A. El-Sayed, M.R. Prausnitz, Delivery of molecules into cells using carbon nanoparticles activated by femtosecond laser pulses, Nat. Nanotechnol. 5 (2010) 607-611.

[127] J. Du, Y. Zhang, J. Ming, J. Liu, L. Zhong, Q. Liang, L. Fan, J. Jiang, Evaluation of the tracing effect of carbon nanoparticle and carbon nanoparticle-epirubicin suspension in axillary lymph node dissection for breast cancer treatment, World J. Surg. Oncol. 14 (2016) 164.

[128] Y. Zhong, S. Ma, Y. Zhang, Using activated carbon nanoparticles to decrease the genotoxicity and teratogenicity of anticancer therapeutic agents, J. Nanosci. Nanotechnol. 10 (2010) 8603-8609.

[129] M.F. Elkady, M.M. Hussein, M.M. Salama, Synthesis and characterization of nano-activated carbon from el maghara coal, Sinai, Egypt to be utilized for wastewater Purification, Am. J. Appl. Chem. 3 (2015) 1-7.

[130] M.M. Seif, F.A. Khalil, A.A.K.A. Arab, M.A.A. Donia, S.R. Mohamed, A.S. Abdel-Aziz, The adsorptive capacity of activated carbon and its nano-particles in removal of organophosphorus malathion from aqueous solution, J. Agroaliment. Proc. Technol. 21 (2015) 116-124.

[131] A. Sharma, N. Verma, A. Sharma, D. Deva, N. Sankararamakrishnan, Iron doped phenolic resin based activated carbon micro and nanoparticles by milling: Synthesis, characterization and application in arsenic removal, Chem. Eng. Sci. 65 (2010) 3591-3601.

[132] M.F. Elkady, Preparation of nano-activated carbon from carbon based material for copper decontamination from wastewater, Am. J. Appl. Chem. 3 (2015) 31-37.

[133] C. Chen, W. Huang, Aggregation kinetics of nanosized activated carbons in aquatic environments, Chem. Eng. J. 313 (2017) 882-889.

[134] R. Cheng, J.L. Wang, W.X. Zhang, Comparison of reductive dechlorination of p-chlorophenol using Fe^0 and nanosized Fe^0, J. Hazard. Mater. 144 (2007) 334-339.

[135] R.J. Portier, G.P. Curole, R.M. Conger, L.M. Basirico, C. Metosh-Dickey, In situ bioremediation of an aniline spill in an industrial setting, Remed. J. 20 (2010) 105-117.

[136] K.T. Järvlnen, E.S. Melin, J.A. Puhakka, High-rate bioremediation of chlorophenol-contaminated groundwater at low temperatures, Environ. Sci. Technol. 28 (1994) 2387-2392.

[137] W. Sun, Y. Li, L.R. McGuinness, S. Luo, W. Huang, L.J. Kerkhof, E.E. Mack, M.M. Haggblom, D.E. Fennell, Identification of anaerobic aniline-degrading bacteria at a contaminated industrial site, Environ. Sci. Technol. 49 (2015) 11079-11088.

[138] G.-Q. Wu, X. Zhang, H. Hui, J. Yan, Q.-S. Zhang, J.-L. Wan, Y. Dai, Adsorptive removal of aniline from aqueous solution by oxygen plasma irradiated bamboo based activated carbon, Chem. Eng. J. 185-186 (2012) 201-210.

[139] S. Suresh, V.C. Srivastava, I.M. Mishra, Studies of adsorption kinetics and regeneration of aniline, phenol, 4-chlorophenol and 4-nitrophenol by activated carbon, Chem. Ind. & Chem. Eng. Q. 19 (2013) 195-212.

[140] C.L. Hansch, A; Hoekman, D, Exploring QSAR: Hydrophobic, Electronic, and Steric Constants American Chemical Society, Washington, DC, 1995.

[141] X. Wang, S. Huang, L. Zhu, X. Tian, S. Li, H. Tang, Correlation between the adsorption ability and reduction degree of graphene oxide and tuning of adsorption of phenolic compounds, Carbon 69 (2014) 101-112.

[142] M.d.l. Luz-Asunción, V. Sánchez-Mendieta, A.L. Martínez-Hernández, V.M. Castaño, C. Velasco-Santos, Adsorption of phenol from aqueous solutions by carbon nanomaterials of one and two dimensions: Kinetic and equilibrium studies, J. Nanomater. 2015 (2015) 1-14.

[143] N.B. Saleh, L.D. Pfefferle, M. Elimelech, Aggregation kinetics of multiwalled carbon nanotubes in aquatic systems: Measurements and environmental implications, Environ. Sci. Technol. 42 (2008) 7963-7969.

[144] V.K. Gupta, T.A. Saleh, Sorption of pollutants by porous carbon, carbon nanotubes and fullerene- an overview, Environ. Sci. Pollut. Res. Int. 20 (2013) 2828-2843.

[145] R.J.d. Jonge, A.M. Breure, J.G.v. Andel, Reversibility of adsorption of aromatic compounds onto powdered activated carbon (PAC), Water Res. 30 (1996) 883-892.

[146] K.S.W. Sing, D.H. Everett, R.A.W. Haul, L. Moscou, R.A. Pierotti, J. Rouquerol, T. Siemieniewska, Reporting physisorption data for gas/solid systems, Pure Appl. Chem. 57 (1985) 603-619.

[147] S. Zhang, T. Shao, H.S. Kose, T. Karanfil, Adsorption of aromatic compounds by carbonaceous adsorbents: A comparative study on granular activated carbon, activated carbon fiber, and carbon nanotubes, Environ. Sci. Technol. 44 (2010) 6377-6383.

[148] E.O. Kraemer, A Treatise of Physical Chemistry, In: Taylor, H.S. (Ed.) ed., Macmillan, New York, 1931.

[149] S. Senel, A. Kara, G. Alsancak, A. Denizli, Removal of phenol and chlorophenols from water with reusable dye-affinity hollow fibers, J. Hazard. Mater. 138 (2006) 317-324.

[150] G. Mamba, X.Y. Mbianda, P.P. Govender, Phosphorylated multiwalled carbon nanotube-cyclodextrin polymer: Synthesis, characterisation and potential application in water purification, Carbohydr. Polym. 98 (2013) 470-476.

[151] G.D. Sheng, D.D. Shao, X.M. Ren, X.Q. Wang, J.X. Li, Y.X. Chen, X.K. Wang, Kinetics and thermodynamics of adsorption of ionizable aromatic compounds from aqueous solutions by as-prepared and oxidized multiwalled carbon nanotubes, J. Hazard. Mater. 178 (2010) 505-516.

[152] M. Abdel Salam, M.A. Gabal, A.Y. Obaid, Preparation and characterization of magnetic multi-walled carbon nanotubes/ferrite nanocomposite and its application for the removal of aniline from aqueous solution, Synth. Met. 161 (2012) 2651-2658.

[153] H. Al-Johani, M. Abdel Salam, Kinetics and thermodynamic study of aniline adsorption by multi-walled carbon nanotubes from aqueous solution, J. Colloid Interface Sci. 360 (2011) 760-767.

[154] B. Kakavandi, A.J. Jafari, R.R. Kalantary, S. Nasseri, A. Ameri, A. Esrafily, Synthesis and properties of Fe_3O_4-activated carbon magnetic nanoparticles for removal of aniline from aqueous solution: Equilibrium, kinetic and thermodynamic studies., Iranian J. Environ. Health Sci. Eng. 10 (2013) 1-9.

[155] S. Lagergren, About the theory of so called adsorption of soluble substances, Ksver. Veterskapsakad. Handl. 24 (1898) 1-6.

[156] Y.S. Ho, G. McKay, Pseudo-second order model for sorption processes, Process Biochem. 34 (1999) 451-465.

[157] B.H. Hameed, L.H. Chin, S. Rengaraj, Adsorption of 4-chlorophenol onto activated carbon prepared from rattan sawdust, Desalination 225 (2008) 185-198.

[158] L.J. Kennedy, J.J. Vijaya, K. Kayalvizhi, G. Sekaran, Adsorption of phenol from aqueous solutions using mesoporous carbon prepared by two-stage process, Chem. Eng. J. 132 (2007) 279-287.

[159] L.M. Cotoruelo, M.D. Marqués, J. Rodríguez-Mirasol, T. Cordero, J.J. Rodríguez, Adsorption of aromatic compounds on activated carbons from lignin: Kinetic study, Ind. Eng. Chem. Res. 46 (2007) 2853-2860.

[160] O. Hamdaoui, E. Naffrechoux, Modeling of adsorption isotherms of phenol and chlorophenols onto granular activated carbon. Part I. Two-parameter models and equations allowing determination of thermodynamic parameters, J. Hazard. Mater. 147 (2007) 381-394.

[161] L.M. Cotoruelo, M.D. Marqués, J. Rodríguez-Mirasol, T. Cordero, J.J. Rodríguez, Adsorption of aromatic compounds on activated carbons from lignin: Equilibrium and thermodynamic study, Ind. Eng. Chem. Res. 46 (2007) 4982-4990.

[162] C. Moreno-Castilla, Adsorption of organic molecules from aqueous solutions on carbon materials, Carbon 42 (2004) 83-94.

[163] Q.-S. Liu, T. Zheng, P. Wang, J.-P. Jiang, N. Li, Adsorption isotherm, kinetic and mechanism studies of some substituted phenols on activated carbon fibers, Chem. Eng. J. 157 (2010) 348-356.

[164] H. Ding, X. Li, J. Wang, X. Zhang, C. Chen, Adsorption of chlorophenols from aqueous solutions by pristine and surface functionalized single-walled carbon nanotubes, J. Environ. Sci. 43 (2016) 187-198.

[165] T.A. Kurniawan, L. Waihung, E. Repo, M.E.T. Sillanpää, Removal of 4-chlorophenol from contaminated water using coconut shell waste pretreated with chemical agents, J. Chem. Technol. Biotechnol. 85 (2010) 1616-1627.

[166] L.E. Vĵan, M. Neagu, Adsorption isotherms of phenol and aniline on activated carbon, Acad. Română 57 (2012) 85-93.

[167] H. Zilouei, B. Guieysse, B. Mattiasson, Biological degradation of chlorophenols in packed-bed bioreactors using mixed bacterial consortia, Process Biochem. 41 (2006) 1083-1089.

[168] D. Singh, Removal of some phenols by activated carbon developed from used tea leaves, J. Ind. Pollut. Control 16 (2000) 19-30.

[169] B. Roshan, K. Kadirvelu, N.S. Kumar, Investigation of aniline adsorption onto spherical carbon: Optimization using response surface methodology, Int. J. Eng. Res. Appl. 3 (2013) 943-952.

[170] M. Streat, J.W. Patrick, M.J.C. Perez, Sorption of phenol and para-chlorophenol from water using conventional and novel activated carbons, Water Res. 29 (1995) 467-472.

[171] G. Gryglewicz, K. Grabas, E. Lorenc-Grabowska, Preparation and characterization of spherical activated carbons from oil agglomerated bituminous coals for removing organic impurities from water, Carbon 40 (2002) 2403-2411.

[172] G. Mckay, M.J. Bino, A.R. Altamemi, The adsorption of various pollutants from aqueous solutions on to activated carbon, Water Res. 19 (1985) 491-495.

[173] A.R. Khan, T.A. Al-Bahri, A. Al-Haddad, Adsorption of phenol based organic pollutants on activated carbon from multi-component dilute aqueous solutions, Water Res. 31 (1997) 2102-2112.

[174] H. Shahbeig, S.A. Ghorbanian, A. Hallajisani, N. Bagheri, S. Poorkarimi, A new adsorption isotherm model of aqueous solutions on granular activated carbon, World J. Modell. and Simul. 9 (2013) 243-254.

[175] F. Orshansky, N. Narkis, Characteristics of organics removal by PACT simultaneous adsorption and biodegradation, Water Res. 31 (1997) 391-398.

[176] H. Basiri, H. Nourmoradi, F.M. Moghadam, K.F. Moghadam, J. Mohammadian, Y.O. Khaniabadi, Removal of aniline as a health-toxic substance from polluted water by aloe vera waste-based activated carbon, Der Pharma Chem. 7 (2015) 149-155.

[177] M. Radhika, K. Palanivelu, Adsorptive removal of chlorophenols from aqueous solution by low cost adsorbent - Kinetics and isotherm analysis, J. Hazard. Mater. 138 (2006) 116-124.

[178] Q. Liao, J. Sun, L. Gao, Adsorption of chlorophenols by multi-walled carbon nanotubes treated with HNO_3 and NH_3, Carbon 46 (2008) 553-555.

[179] Y.F. Sun, A.M. Zhang, Y. Yin, Y.M. Dong, Y.C. Cui, X. Zhang, J.M. Hong, The investigation of adsorptive performance on modified multi-walled carbon nanotubes by mechanical ball milling, Mater. Chem. Phys. 101 (2007) 30-34.

[180] X. Xie, L. Gao, J. Sun, Thermodynamic study on aniline adsorption on chemical modified multi-walled carbon nanotubes, Colloids Surf., A 308 (2007) 54-59.

[181] H. Rosen, A.D.A. Hansen, R.L. Dod, T. Novakov, Soot in urban atmospheres: determination by an optical absorption technique., Science 208 (1980) 741-744.

[182] R.I.A. Patterson, M. Kraft, Models for the aggregate structure of soot particles, Combust. Flame 151 (2007) 160-172.

[183] M.M. Maricq, Coagulation dynamics of fractal-like soot aggregates, J. Aerosol Sci. 38 (2007) 141-156.

[184] R.P. Bambha, H.A. Michelsen, Effects of aggregate morphology and size on laser-induced incandescence and scattering from black carbon (mature soot), J. Aerosol Sci. 88 (2015) 159-181.

[185] Ü. Köylü, G.M. Faeth, T.L. Farias, M.G. Carvalho, Fractal and projected structure properties of soot aggregates, Combust. Flame 100 (1995) 621-633.

[186] C. Oh, C.M. Sorensen, Light scattering study of fractal cluster aggregation near the free molecular regime., J. Aerosol Sci. 28 (1997) 937-957.

[187] O.B. Popovicheva, N.M. Persiantseva, V. Tishkova, N.K. Shonija, N.A. Zubareva, Quantification of water uptake by soot particles, Environ. Res. Lett. 3 (2008) 025009.

[188] E.F. Mikhailov, S.S. Vlasenko, I.A. Podgorny, V. Ramanathan, C.E. Corrigan, Optical properties of soot–water drop agglomerates: An experimental study, J. Geophys. Res. 111 (2006) D07209.

[189] B. Zuberi, Hydrophilic properties of aged soot, Geophys. Res. Lett. 32 (2005) L01807.

[190] T. Tritscher, Z. Jurányi, M. Martin, R. Chirico, M. Gysel, M.F. Heringa, P.F. DeCarlo, B. Sierau, A.S.H. Prévôt, E. Weingartner, U. Baltensperger, Changes of hygroscopicity and morphology during ageing of diesel soot, Environ. Res. Lett. 6 (2011) 034026.

[191] T. Cheng, Y. Wu, H. Chen, Effects of morphology on the radiative properties of internally mixed light absorbing carbon aerosols with different aging status, Opt. Express 22 (2014) 15904-15917.

[192] Y. Wu, T. Cheng, X. Gu, L. Zheng, H. Chen, H. Xu, The single scattering properties of soot aggregates with concentric core–shell spherical monomers, J. Quant. Spectrosc. Radiat. Transfer 135 (2014) 9-19.

[193] C. Wittbom, A.C. Eriksson, J. Rissler, J.E. Carlsson, P. Roldin, E.Z. Nordin, P.T. Nilsson, E. Swietlicki, J.H. Pagels, B. Svenningsson, Cloud droplet activity changes of soot aerosol upon smog chamber ageing, Atmos. Chem. Phys. 14 (2014) 9831-9854.

[194] D.J. Growney, O.O. Mykhaylyk, L. Middlemiss, L.A. Fielding, M.J. Derry, N. Aragrag, G.D. Lamb, S.P. Armes, Is carbon black a suitable model colloidal substrate for diesel soot?, Langmuir 31 (2015) 10358-10369.

[195] R. Xu, C. Wu, H. Xu, Particle size and zeta potential of carbon black in liquid media, Carbon 45 (2007) 2806-2809.

[196] P. Bezot, C. Hesse-Bezot, B. Rousset, C. Diraison, Effect of polymers on the aggregation kinetics and fractal structure of carbon black suspensions in an aliphatic solvent. A static and dynamic light scattering study., Colloids Surf., A 97 (1995) 53-63.

[197] J.E. Penner, H. Eddleman, T. Novakov, Towards the development of a global inventory for black carbon emissions, Atmos. Environ. Part A, General Topics 27 (1993) 1277-1295.

[198] Q. Zhang, J. Huang, G. Yu, Prediction of soot–water partition coefficients for selected persistent organic pollutants from theoretical molecular descriptors, Prog. Nat. Sci. 18 (2008) 867-872.

[199] SRM 1650b, Diesel Particulate Matter, in, National Institute of Standards and Technology, U.S. Department of Commerce: Gaithersburg, MD, 2013.

[200] M.v. Smoluchowski, Contribution to the theory of electro-osmosis and related phenomena., Bull. Int. Acad. Sci. Cracovie 3 (1903) 184.

[201] B. Smith, K. Wepasnick, K.E. Schrote, A.R. Bertele, W.P. Ball, C. O'Melia, D.H. Fairbrother, Colloidal properties of aqueous suspensions of acid-treated, multi-walled carbon nanotubes., Environ. Sci. Technol. 43 (2009) 819-825.

[202] K.L. Chen, S.E. Mylon, M. Elimelech, Aggregation kinetics of alginate-coated hematite nanoparticles in monovalent and divalent electrolytes., Environ. Sci. Technol. 40 (2006) 1516-1523.

[203] D. Bouchard, X. Ma, C. Isaacson, Colloidal properties of aqueous fullerenes: isoelectric points and aggregation kinetics of fullerene and derivatives., Environ. Sci. Technol. 43 (2009) 6597-6603.

[204] H. Holthoff, S.U. Egelhaaf, M. Borkovec, P. Schurtenberger, H. Sticher, Coagulation rate measurements of colloidal particles by simultaneous static and dynamic light scattering., Langmuir 12 (1996) 5541-5549.

[205] K.A. Huynh, K.L. Chen, Aggregation kinetics of citrate and polyvinylpyrrolidone coated silver nanoparticles in monovalent and divalent electrolyte solutions, Environ. Sci. Technol. 45 (2011) 5564-5571.

[206] X. Zhu, H. Chen, W. Li, Y. He, P.C. Brookes, J. Xu, Aggregation kinetics of natural soil nanoparticles in different electrolytes, Eur. J. Soil Sci. 65 (2014) 206-217.

[207] C.-y. Xu, K.-y. Deng, J.-y. Li, R.-k. Xu, Impact of environmental conditions on aggregation kinetics of hematite and goethite nanoparticles, J. Nanopart. Res. 17 (2015).

[208] G.R. Wiese, T.W. Healy, Effect of particle size on colloid stability, Trans. Faraday Soc. 66 (1970) 490-500.

[209] T. Ishiguro, Y. Takatori, K. Akihama, Microstructure of diesel soot particles probed by electron microscopy: First observation of inner core and outer shell, Combust. Flame 108 (1997) 231-234.

[210] M.M. Maricq, Bipolar Diffusion Charging of Soot Aggregates, Aerosol Sci. Technol. 42 (2008) 247-254.

[211] J.P. Shi, D. Mark, R.M. Harrison, Characterization of particles from a current technology heavy-duty diesel engine, Environ. Sci. Technol. 34 (2000) 748-755.

[212] K. Park, F. Cao, D.B. Kittelson, P.H. Mcmurry, Relationship between particle mass and mobility for diesel exhaust particles, Environ. Sci. Technol. 37 (2003) 577-583.

[213] J.C. Crittenden, R.R. Trussell, D.W. Hand, K.J. Howe, G. Tchobanoglous, J.H. Borchardt, MWH's Water Treatment Principles and Design, John Wiley & Sons, Inc., Hoboken, New Jersey, 2012.

[214] M. Larsson, A. Hill, J. Duffy, Suspension stability, dividing line of zeta potential for stable suspension., Ann. T. Nord. Rheol. Soc. 20 (2012) 209-214.

[215] S.E. Mylon, K.L. Chen, M. Elimelech, Influence of natural organic matter and ionic composition on the kinetics and structure of hematite colloid aggregation: implications to iron depletion in estuaries, Langmuir 20 (2004) 9000-9006.

[216] Z. Meng, S.M. Hashmi, M. Elimelech, Aggregation rate and fractal dimension of fullerene nanoparticles via simultaneous multiangle static and dynamic light scattering measurement, J. Colloid Interface Sci. 392 (2013) 27-33.

[217] Y.T. He, J. Wan, T. Tokunaga, Kinetic stability of hematite nanoparticles: the effect of particle sizes, J. Nanopart. Res. 10 (2007) 321-332.

[218] W. Zhang, U.S. Rattanaudompol, H. Li, D. Bouchard, Effects of humic and fulvic acids on aggregation of aqu/nC_{60} nanoparticles, Water Res. 47 (2013) 1793-1802.

[219] H. Holthoff, S.U. Egelhaaf, M. Borkovec, P. Schurtenberger, H. Sticher, Coagulation rate measurements of colloidal particles by simultaneous static and dynamic light scattering, Langmuir 12 (1996) 5541-5549.

[220] D. Grolimund, M. Elimelech, M. Borkovec, Aggregation and deposition kinetics of mobile colloidal particles in natural porous media, Colloids Surf., A 191 (2001) 179-188.

[221] N.O. Mchedlov-Petrossyan, V.K. Klochkov, G.V. Andrievsky, Colloidal dispersions of fullerene C_{60} in water: some properties and regularities of coagulation by electrolytes, J. Chem. Soc., Faraday Trans. 93 (1997) 4343-4346.

[222] UNESCO, WHO, UNEP, Water Quality Assessments - A Guide to Use of Biota, Sediments and Water in Environmental Monitoring., Second ed., University Press, Cambridge, Great Britain, 1996.

[223] U.S.E.P.A. U.S. EPA, Cloud Deposition Monitoring. GreatSmoky Mountains National Park, Clingmans Dome, TN., in: Summary Report, 2012.

[224] J.D. Hem, Study and Interpretation of the Chemical Characteristics of Natural Water, 3rd ed., U.S. Geological Survey, Alexandria, VA, 1985.

[225] K.B. Budhavant, P.S.P. Rao, P.D. Safai, L. Granat, H. Rodhe, Chemical composition of the inorganic fraction of cloud-water at a high altitude station in West India, Atmos. Environ. 88 (2014) 59-65.

[226] Y. Wang, J. Guo, T. Wang, A. Ding, J. Gao, Y. Zhou, J.L. Collett, W. Wang, Influence of regional pollution and sandstorms on the chemical composition of cloud/fog at the summit of Mt. Taishan in northern China, Atmos. Res. 99 (2011) 434-442.

[227] M. Błaś, Ż. Polkowska, M. Sobik, K. Klimaszewska, K. Nowiński, J. Namieśnik, Fog water chemical composition in different geographic regions of Poland, Atmos. Res. 95 (2010) 455-469.

[228] M. Błaś, M. Sobik, R. Twarowski, Changes of cloud water chemical composition in the Western Sudety Mountains, Poland, Atmos. Res. 87 (2008) 224-231.

[229] A. Gioda, O.L. Mayol-Bracero, F. Morales-Garcń, J. Collett, S. Decesari, L. Emblico, M.C. Facchini, R.J. Morales-De Jesús, S. Mertes, S. Borrmann, S. Walter,

J. Schneider, Chemical composition of cloud water in the Puerto Rican tropical trade wind cumuli, Water, Air, and Soil Pollution 200 (2008) 3-14.

[230] D.-S. Kim, V.P. Aneja, Chemical composition of clouds at Mt. Mitchell, North Carolina, USA, Tellus 44B (1992) 41-53.

[231] M.M. Bisiaux, R. Edwards, A.C. Heyvaert, J.M. Thomas, B. Fitzgerald, R.B. Susfalk, S.G. Schladow, M. Thaw, Stormwater and fire as sources of black carbon nanoparticles to Lake Tahoe, Environ. Sci. Technol. 45 (2011) 2065-2071.

[232] A. Mannino, H.R. Harvey, Black carbon in estuarine and coastal ocean dissolved organic matter, Limnol. Oceanogr. 49 (2004) 735-740.

[233] S. Wagner, K.M. Cawley, F.L. Rosario-Ortiz, R. Jaffé, In-stream sources and links between particulate and dissolved black carbon following a wildfire, Biogeochemistry 124 (2015) 145-161.

[234] Z. Fang, W. Yang, M. Chen, M. Zheng, W. Hu, Abundance and sinking of particulate black carbon in the western Arctic and Subarctic Oceans, Sci. Rep. 6 (2016) 29959.

[235] D.X. Flores-Cervantes, D.L. Plata, J.K. MacFarlane, C.M. Reddy, P.M. Gschwend, Black carbon in marine particulate organic carbon: Inputs and cycling of highly recalcitrant organic carbon in the Gulf of Maine, Mar. Chem. 113 (2009) 172-181.

[236] T. Dittmar, The molecular level determination of black carbon in marine dissolved organic matter, Org. Geochem. 39 (2008) 396-407.

[237] K.B. Budhavant, P.S.P. Rao, P.D. Safai, C. Leck, H. Rodhe, Black carbon in cloud-water and rain water during monsoon season at a high altitude station in India, Atmos. Environ. 129 (2016) 256-264.

[238] L. Granat, J.E. Engström, S. Praveen, H. Rodhe, Light absorbing material (soot) in rainwater and in aerosol particles in the Maldives, J. Geophys. Res. 115 (2010).

[239] M. Cerqueira, C. Pio, M. Legrand, H. Puxbaum, A. Kasper-Giebl, J. Afonso, S. Preunkert, A. Gelencsér, P. Fialho, Particulate carbon in precipitation at European background sites, J. Aerosol Sci. 41 (2010) 51-61.

[240] S. Armalis, Wet deposition of elemental carbon in Lithuania, Sci. Total Environ. 239 (1999) 89-93.

[241] R. Hitzenbergera, A. Bernera, H. Giebla, K. Drobescha, A. Kasper-Gieblb, M. Loeflundb, H. Urbanb, H. Puxbaumb, Black carbon (BC) in alpine aerosols and cloud water-concentrations and scavenging efficiencies, Atmos. Environ. 35 (2001) 5135-5141.

[242] M. Löflund, A. Kasper-Giebl, B. Schuster, H. Giebl, R. Hitzenberger, H. Puxbaum, Formic, acetic, oxalic, malonic and succinic acid concentrations and their contribution to organic carbon in cloud water, Atmos. Environ. 36 (2002) 1553-1558.

[243] A.D.H.D. Clague, J. B.; Wang, T. K.; Peng, J. C. M., A comparison of diesel engine soot with carbon black, Carbon 37 (1999) 1553-1565.

[244] S.H. Kim, R.A. Fletcher, M.R. Zachariah, Difference in oxidative properties between flame and diesel soot nanoparticles: The role of metals, Environ. Sci. Technol. 39 (2005) 4021-4026.

[245] G. De Falco, M. Commodo, P. Minutolo, A. D'Anna, Flame-formed carbon nanoparticles: Morphology, interaction forces, and Hamaker constant from AFM, Aerosol Sci. Technol. 49 (2015) 281-289.

[246] M.K. Alam, The effect of van der Waals and viscous forces on aerosol coagulation, Aerosol Sci. Technol. 6 (1987) 41-52.

[247] S. Rothenbacher, A. Messerer, G. Kasper, Fragmentation and bond strength of airborne diesel soot agglomerates, Particle and fibre toxicology 5 (2008) 9.

[248] L. Isella, Y. Drossinos, Langevin agglomeration of nanoparticles interacting via a central potential, Phys. Rev. E 82 (2010) 011404.

[249] X. Ma, D. Bouchard, Formation of aqueous suspensions of fullerenes, Environ. Sci. Technol. 43 (2009) 330-336.

[250] J. Brant, H. Lecoanet, M. Hotze, M. Wiesner, Comparison of electrokinetic properties of colloidal fullerenes (n-C_{60}) formed using two procedures, Environ. Sci. Technol. 39 (2005) 6343-6351.

[251] D. Lin, N. Liu, K. Yang, L. Zhu, Y. Xu, B. Xing, The effect of ionic strength and pH on the stability of tannic acid-facilitated carbon nanotube suspensions, Carbon 47 (2009) 2875-2882.

[252] Y.-T. Shieh, G.-L. Liu, H.-H. Wu, C.-C. Lee, Effects of polarity and pH on the solubility of acid-treated carbon nanotubes in different media, Carbon 45 (2007) 1880-1890.

[253] D.E. Yates, S. Levine, T.W. Healy, Site-binding model of the electrical double layer at the oxide/water interface, J. Chem. Soc., Faraday Trans. 1 70 (1973) 1807-1818.

[254] J.-O. Müller, D.S. Su, R.E. Jentoft, U. Wild, R. Schlögl, Diesel engine exhaust emission: Oxidative behavior and microstructure of black smoke soot particulate, Environ. Sci. Technol. 40 (2006) 1231-1236.

[255] R.L. Vander Wal, V.M. Bryg, M.D. Hays, Fingerprinting soot (towards source identification): Physical structure and chemical composition, J. Aerosol Sci. 41 (2010) 108-117.

[256] J.O. Müller, D.S. Su, R.E. Jentoft, J. Kröhnert, F.C. Jentoft, R. Schlögl, Morphology-controlled reactivity of carbonaceous materials towards oxidation, Catal. Today 102-103 (2005) 259-265.

[257] J. Song, M. Alam, A.L. Boehman, Impact of alternative fuels on soot properties and DPF regeneration, Combust. Sci. Technol. 179 (2007) 1991-2037.

[258] L. Wang, C. Song, J. Song, G. Lv, H. Pang, W. Zhang, Aliphatic C–H and oxygenated surface functional groups of diesel in-cylinder soot: Characterizations and impact on soot oxidation behavior, Proc. Combust. Inst. 34 (2013) 3099-3106.

[259] J.P. Szybist, J. Song, M. Alam, A.L. Boehman, Biodiesel combustion, emissions and emission control, Fuel Process. Technol. 88 (2007) 679-691.

[260] D.M. Smith, A.R. Chughtai, The surface structure and reactivity of black carbon, Colloids Surf., A 105 (1995) 47-77.

[261] A. Braun, F.E. Huggins, A. Kubátová, S. Wirick, M.M. Maricq, B.S. Mun, J.D. Mcdonald, K.E. Kelly, N. Shah, G.P. Huffmant, Toward distinguishing woodsmoke and diesel exhaust in ambient particulate matter., Environ. Sci. Technol. 42 (2008) 374-380.

[262] A. Tapia, M.S. Salgado, M.P. Martin, M. Lapuerta, J. Rodriguez-Fernandez, M.J. Rossi, B. Cabanas, Molecular characterization of the gas-particle interface of soot sampled from a diesel engine using a titration method, Environ. Sci. Technol. 50 (2016) 2946-2955.

[263] A. Setyan, J.-J. Sauvain, M. Riediker, M. Guillemin, M.J. Rossi, Characterization of surface functional groups present on laboratory-generated and ambient aerosol particles by means of heterogeneous titration reactions, J. Aerosol Sci. 40 (2009) 534-548.

[264] D.S. Su, R.E. Jentoft, J.O. Müller, D. Rothe, E. Jacob, C.D. Simpson, Ž. Tomović, K. Müllen, A. Messerer, U. Pöschl, R. Niessner, R. Schlögl, Microstructure and oxidation behaviour of Euro IV diesel engine soot: A comparative study with synthetic model soot substances, Catal. Today 90 (2004) 127-132.

[265] J.O. Müller, D.S. Su, R.E. Jentoft, J. Kröhnert, F.C. Jentoft, R. Schlögl, Morphology-controlled reactivity of carbonaceous materials towards oxidation, Catal. Today 102-103 (2005) 259-265.

[266] E.D. Goldberg, Black carbon in the environment: properties and distribution, 1 ed., John Wiley & Sons, Inc., USA., 1985.

[267] G. Socrates, Infrared and Raman characteristic group frequencies: Tables and charts, 2 ed., John Wiley & Sons, LTD, Chister, England, 2001.

[268] R.A. Kerr, Soot is warming the world even more than thought., Science (Washington, DC, U.S.) 339 (2013) 382.

[269] A. Nel, Air pollution-related illness: Effects of particles., Science (Washington, DC, U.S.) 308 (2005) 804-806.

[270] E.G. Schnitzler, A. Dutt, A.M. Charbonneau, J.S. Olfert, W. Jager, Soot aggregate restructuring due to coatings of secondary organic aerosol derived from aromatic precursors, Environ. Sci. Technol. 48 (2014) 14309-14316.

[271] E. Vignati, M. Karl, M. Krol, J.Wilson, P. Stier, F. Cavalli, Sources of uncertainties in modelling black carbon at the global scale, Atmos. Chem. Phys. 10 (2010) 2595-2611.

[272] E. Jurado, J. Dachs, C.M. Duarte, R. Simó, Atmospheric deposition of organic and black carbon to the global oceans, Atmos. Environ. 42 (2008) 7931-7939.

[273] S. Endo, P. Grathwohl, S.B. Haderlein, T.C. Schmidt, Effects of native organic material and water on sorption properties of reference diesel soot, Environ. Sci. Technol. 43 (2009) 3187-3193.

[274] N.B. Saleh, L.D. Pfefferle, M. Elimelech, Influence of biomacromolecules and humic acid on the aggregation kinetics of single-walled carbon nanotubes, Environ. Sci. Technol. 44 (2010) 2412-2418.

[275] P. Bezot, C. Hesse-Bezot, Kinetics of clustering of carbon black suspensions by light scattering techniques, Physica A 271 (1999) 9-22.

[276] P. Bezot, C. Hesse-Bezot, C. Diraison, Aggregation kinetics of colloidal suspensions of engine soots. Influence of polymeric lubricant additives, Carbon 35 (1997) 53-60.

[277] C. Chen, W. Huang, Aggregation Kinetics of Diesel Soot Nanoparticles in Wet Environments, Environ. Sci. Technol. (2017).

[278] R.M. Allen-King, P. Grathwohl, W.P. Ball, New modeling paradigms for the sorption of hydrophobic organic chemicals to heterogeneous carbonaceous matter in soils, sediments, and rocks, Adv Water Resour. 25 (2002) 985-1016.

[279] G. Cornelissen, Ö. Gustafsson, T.D. Bucheli, M.T.O. Jonker, A.A. Koelmans, Extensive sorption of organic compounds to black carbon, coal, and kerogen in

sediments and soils: Mechanisms and consequences for distribution, bioaccumulation, and biodegradation, Environ. Sci. Tech. 39 (2005) 6881-6895.

[280] Z. Gu, Z. Yang, Y. Chong, C. Ge, J.K. Weber, D.R. Bell, R. Zhou, Surface Curvature Relation to Protein Adsorption for Carbon-based Nanomaterials, Sci. Rep. 5 (2015) 10886.

[281] C.L. Tiller, C.R. O'Melia, Natural organic matter and colloidal stability: Models and measurements, Colloids Surf., A 73 (1993) 89-102.

[282] J.E. Penner, H. Eddleman, T. Novakov, Towards the development of a global inventory for black carbon emissions, Atmos. Environ. 27A (1993) 1277-1295.

[283] K.L. Chen, M. Elimelech, Influence of humic acid on the aggregation kinetics of fullerene (C60) nanoparticles in monovalent and divalent electrolyte solutions, J. Colloid Interface Sci. 309 (2007) 126-134.

[284] C. Chen, W. Huang, Aggregation kinetics of nanosized activated carbons in aquatic environments, Chem. Eng. J. 313 (2017) 882-889.

[285] B. White, S. Banerjee, S. O'Brien, N.J. Turro, I.P. Herman, Zeta-potential measurements of surfactant-wrapped individual single-walled carbon nanotubes, J. Phys. Chem. C 111 (2007) 13684-13690.

[286] Y. Liu, L. Gao, S. Zheng, Y. Wang, J. Sun, H. Kajiura, Y. Li, K. Noda, Debundling of single-walled carbon nanotubes by using natural polyelectrolytes, Nanotechnology 18 (2007) 365702.

[287] T. Kopac, K. Bozgeyik, Equilibrium, kinetics, and thermodynamics of bovine serum albumin adsorption on single-walled carbon nanotubes, Chem. Eng. Commun. 203 (2016) 1198-1206.

[288] S. Dominguez-Medina, J. Blankenburg, J. Olson, C.F. Landes, S. Link, Adsorption of a protein monolayer via hydrophobic interactions prevents nanoparticle aggregation under harsh environmental conditions, ACS Sustainable Chem. Eng. 1 (2013) 833-842.

[289] S. Salgın, U. Salgın, S. Bahadır, Zeta potentials and isoelectric points of biomolecules: The effects of ion types and ionic strengths, Int. J. Electrochem. Sci. 7 (2012) 12404-12414.

[290] W. Norde, J. Lyklema, The adsorption of human plasma albumin and bovine pancreas ribonuclease at negatively charged polystyrene surfaces. III. Electrophoresis, J. Colloid Interface Sci. 66 (1978) 277-284.

[291] P.V. Dulm, W. Norde, J. Lyklema, Ion participation in protein adsorption at solid surfaces, J. Colloid Interface Sci. 82 (1981) 77-82.

[292] W. Norde, Ion participation in protein adsorption at solid surfaces, Colloids Surf. 10 (1984) 21-31.

[293] A.V. Elgersma, R.L.J. Zsom, W. Norde, J. Lyklema, The adsorption of bovine serum albumin on positively and negatively charged polystyrene latices, J. Colloid Interface Sci. 138 (1989) 145-156.

[294] R. Amal, J.A. Raper, T.D. Waite, Effect of fulvic acid adsorption on the aggregation kinetics and structure of hematite particles, J. Colloid Interface Sci. 151 (1992) 244-257.

[295] A. Deonarine, B.L. Lau, G.R. Aiken, J.N. Ryan, H. Hsu-Kim, Effects of humic substances on precipitation and aggregation of zinc sulfide nanoparticles, Environ. Sci. Technol. 45 (2011) 3217-3223.

[296] K.L. Chen, M. Elimelech, Influence of humic acid on the aggregation kinetics of fullerene (C_{60}) nanoparticles in monovalent and divalent electrolyte solutions, J. Colloid Interface Sci. 309 (2007) 126-134.

[297] I. Heidmann, I. Christl, R. Kretzschmar, Aggregation kinetics of kaolinite-fulvic acid colloids as affected by the sorption of Cu and Pb, Environ. Sci. Technol. 39 (2005) 807-813.

[298] A.A. Bhirde, S.A. Hassan, E. Harr, X. Chen, Role of albumin in the formation and stabilization of nanoparticle aggregates in serum studied by continuous photon correlation spectroscopy and multiscale computer simulations, J. Phys. Chem. C Nanomater. Interfaces 118 (2014) 16199-16208.

[299] A.V. Singh, B.M. Bandgar, M. Kasture, B.L.V. Prasad, M. Sastry, Synthesis of gold, silver and their alloy nanoparticles using bovine serum albumin as foaming and stabilizing agent, J. Mater. Chem. 15 (2005) 5115.

[300] W. Norde, A.C.I. Anusiem, Adsorption, desorption and re-adsorption of proteins on solid surfaces, Colloids Surf. 66 (1992) 73-80.

[301] W. Norde, C.E. Giacomelli, BSA structural changes during homomolecular exchange between the adsorbed and the dissolved states, J. Biotechnol. 79 (2000) 259-268.

[302] W.R. Gombotz, S.F. Wee, Protein release from alginate matrices, Adv. Drug Deliver. Rev. 31 (1998) 267-285.

[303] T.A. Davis, F. Llanes, B. Volesky, A. Mucci, Metal selectivity of *Sargassum* spp. and their alginates in relation to their R-Lguluronic acid content and conformation., Environ. Sci. Technol. 37 (2003) 261-267.

[304] K.L. Chen, S.E. Mylon, M. Elimelech, Enhanced aggregation of alginate-coated iron oxide (hematite) nanoparticles in the presence of calcium, strontium, and barium cations, Langmuir 23 (2007) 5920-5928.

[305] K.A. Huynh, J.M. McCaffery, K.L. Chen, Heteroaggregation of multiwalled carbon nanotubes and hematite nanoparticles: Rates and mechanisms, Environ. Sci. Technol. 46 (2012) 5912-5920.

[306] A. Praetorius, J. Labille, M. Scheringer, A. Thill, K. Hungerbuhler, J.Y. Bottero, Heteroaggregation of titanium dioxide nanoparticles with model natural colloids under environmentally relevant conditions, Environ. Sci. Technol. 48 (2014) 10690-10698.

APPENDIX: LIST OF ABBREVIATIONS

4-CP	4-chlorophenol
AC	activated carbon
ACF	activated carbon fiber
BC	black carbon
BET	Brunauer-Emmett-Teller
BJH	Barrett–Joyner–Halenda
BSA	bovine serum albumin
CCA	constant charge approximation
CCC	critical coagulation concentration
CMBR	completely mixed batch reactor
CNS	carbon nanosphere
CNT	carbon nanotube
CPA	constant potential approximation
DDI	double deionized water
DLS	dynamic light scattering
DLVO	Derjaguin-Landau-Verwey-Overbeek
DIM	Derjaguin integration method
DOC	dissolved organic carbon
EA	elemental analysis
EDL	electrical double layer
EDX	energy dispersive X-ray

EPM	electrophoretic mobility
FA	fulvic acid
FNP	fullerene nanoparticle
FTIR	Fourier transform infrared spectroscopy
GAC	granular activated carbon
G-blocks	guluronic acid blocks
GO	graphene oxide
HA	humic acid
HPLC	high performance liquid chromatography
HRTEM	high resolution transmission electron microscope
IEP	isoelectric point
LB broth	Luria-Bertani broth
LPB equation	linear Poisson-Boltzmann equation
LSA	linear superposition approximation
MCNP	manufactured carbon-based nanoparticle
MWCNT / MWNT	multi-walled carbon nanotube
NAC	nanosized activated carbon
NIST	National Institute of Standards and Technology
NNLS	Non-Negatively constrained Least Squares
NOM	natural organic matter
NP	nanoparticle

nZVI	nano zero valent iron
PAC	powdered activated carbon
PAH	polycyclic aromatic hydrocarbon
PALS	phase analysis light scattering
PBC	particulate black carbon
PDI	polydispersity index
RGO	reduced graphene oxide
RBC	refractory black carbon
SEM	scanning electron microscope
SRM	standard reference material
SSA	specific surface area
SWCNT / SWNT	single-walled carbon nanotube
TEM	transmission electron microscope
TOC	total organic carbon
TRDLS	time-resolved dynamic light scattering
XPS	X-ray photoelectron spectroscopy